

UCLA

UCLA Electronic Theses and Dissertations

Title

Novel High Gain Antennas for Emerging CubeSats: Characterization of Deployable Mesh Reflectors and Low-Profile, Metal-Only Stepped Reflectors

Permalink

<https://escholarship.org/uc/item/7rc3s6mw>

Author

Manohar, Vignesh

Publication Date

2020

Peer reviewed|Thesis/dissertation

UNIVERSITY OF CALIFORNIA

Los Angeles

Novel High Gain Antennas for Emerging CubeSats: Characterization of Deployable Mesh
Reflectors and Low-Profile, Metal-Only Stepped Reflectors

A dissertation submitted in partial satisfaction
of the requirements for the degree
Doctor of Philosophy in Electrical and Computer Engineering

by

Vignesh Manohar

2020

© Copyright by
Vignesh Manohar
2020

ABSTRACT OF THE DISSERTATION

Novel High Gain Antennas for Emerging CubeSats: Characterization of Deployable Mesh Reflectors and Low-Profile, Metal-Only Stepped Reflectors

by

Vignesh Manohar

Doctor of Philosophy in Electrical and Computer Engineering

University of California, Los Angeles, 2020

Professor Yahya Rahmat-Samii, Chair

The advent of VLSI and microelectronics has made it possible to reduce the size of electronic devices by several orders of magnitude while increasing their functional capabilities and reducing production costs. This massive scaling has enabled the development of satellites that can be as small as a cube of volume 10 cm x 10 cm x 10 cm. Such satellites, called ‘CubeSats’, have revolutionized the satellite industry today. This reduced volume makes launching CubeSats economically affordable, fostering the participation of small scale establishments and universities in space programs. Owing to their small size, it is now possible to conceive launching of multiple instances of the same CubeSat for advanced missions, which was not economically viable with conventional satellites. Even though numerous CubeSats have been launched, most of the current CubeSat missions operate at low data rates and low spatial resolution. One of the major reasons for this is the absence of compact high gain antennas that can integrate with the small CubeSat form factor while providing the required data rates for deep space missions or spatial resolution for remote sensing. This work addresses this very challenge by developing tools that can aid the integration of high gain antennas with the small CubeSat form factor. In particular, we include the following: (a) an in-depth understanding of umbrella reflector antennas with an emphasis on lower number of ribs to aid stowage, (b) analysis of complex knit mesh surfaces to understand the tradeoff between mesh density and RF transmission loss, (c) innovative feed designs that are optimized for efficient illumination of reflector antennas and minimum volume, (d) characterization of chassis in-

teraction with the antenna system, and (e) development of a metal-only, low-profile, stepped parabolic reflector that can be 3D printed and readily integrated with the CubeSat chassis, simplifying deployment. As a part of this dissertation, we describe the development of one of the largest apertures at Ka-band: a 1m mesh-deployable offset reflector that can be stowed in a volume of 10 cm x 10 cm x 30 cm. The success of this endeavor marks a major milestone in the field of CubeSats, which allows advanced space missions at lower costs to become a reality.

The dissertation of Vignesh Manohar is approved.

Aydin Babakhani

Yuanxun Wang

Tatsuo Itoh

Yahya Rahmat-Samii, Committee Chair

University of California, Los Angeles

2020

*Dedicated to my wife and parents . . .
who stood by me through this journey
and never doubted my capabilities*

TABLE OF CONTENTS

1	Introduction	1
1.1	Existing Standards for Small Satellites	3
1.2	Antenna Requirements for CubeSats	4
1.2.1	Frequency	6
1.2.2	Antenna Radiated Power, Gain and Radiation Pattern	6
1.2.3	Antenna Material	7
1.3	Representative Current Antenna Concepts for CubeSats	7
1.4	Outline of this Work: Futuristic CubeSat Antenna Concepts	10
I	Umbrella Reflector Characterization	12
2	Characterization of Umbrella Reflector Antennas: Analysis of Gain Loss and Estimation of Optimal Feed Point	13
2.1	Mathematical representation of the gore surface	14
2.2	Finding the optimum feed location	16
2.2.1	Physical intuition behind the optimal feed location	16
2.2.2	Physical Optics approach	18
2.2.3	Best Fit Paraboloid approach	19
2.2.4	Manual tuning of feed position	20
2.3	Results and discussions	20
2.4	Gain loss as a function of Number of Gores	22
2.4.1	Discussions on the Radiation Performance of Umbrella Reflectors	24

2.5	Compensating For Gain Loss due to Umbrella Reflector Topology - A Conceptual Study	29
II	Mesh Deployable Reflector Design for RainCube	32
3	RainCube 1m Ka-Band Offset Mesh Deployable Antenna - Development and Characterization	33
3.1	RainCube Mission - Needs and Objectives	33
3.2	Antenna Design for Next Generation RainCube Radar	34
3.2.1	Reflector Configuration Selection	37
3.3	Feed Horn Design	39
3.3.1	Reflector Antenna Design and Feed Horn Antenna Requirements . . .	39
3.3.2	Horn Design Optimization Approach	40
3.3.3	Simulated Results	43
3.3.4	Fabrication and Measurement	44
3.4	RainCube Reflector Characterizations	53
3.4.1	Mesh Characterization	53
3.4.2	Chassis Characterization	60
3.5	Fabrication and Measurement of the RainCube 1m Reflector	63
3.6	Characterization and Reduction of Far-Field Grating Lobes	66
3.6.1	Grating Lobe Appearance	66
3.6.2	Reduction of Grating Lobes	68
3.7	Reduction of Linear Cross-Polarization for Offset Reflectors	74
III	Metal-Only, Low-Profile, Stepped Parabolic Reflector Antenna	84

4	Synthesis and Analysis of High Gain, Metal-Only, Low Profile Stepped Parabolic Reflector Antenna	85
4.1	Existing Options for Low-Profile High Gain Antennas	86
4.2	Surface Formulations	88
4.2.1	Symmetric Stepped Reflector	89
4.2.2	Offset Stepped Reflector	90
4.3	Geometry Considerations	91
4.3.1	Estimation of Number of Rings	93
4.3.2	Width of Ring	95
4.3.3	Feed Considerations	96
4.3.4	Geometry Tradeoffs	96
4.4	Simulation Results for the Stepped Parabolic Reflector Antenna	97
4.4.1	Symmetric Configuration	97
4.4.2	Offset Configuration	98
4.5	Physical Optics vs Full Wave (MLFMM) comparison for stepped parabolic reflector	99
4.6	Frequency Response of Parabolic Stepped Reflector	102
4.6.1	Bandwidth Observations for Symmetric Configurations	102
4.6.2	Bandwidth Observations for Offset Configurations	104
4.7	Fabrication and Measurement of a Stepped Reflector Prototype	105
4.8	Investigating High Sidelobe Profile for the Stepped Reflector	107
4.8.1	Analytical Model for the near Field Distribution	118
5	Conclusions	120
A	Extending Formulation of Umbrella Reflectors for Controlling Surface Be-	

tween Ribs	123
B Computing the Normals for an Umbrella Reflector Surface	126
C Cylindrical Waveguide Modes and their Applications for Reflector Antenna Feed Development	128
D Determining the Slopes for Monotonic PCHIP spline	137
E Phase Center of Reflector Antennas	139
E.1 Phase Center Derivation	139
E.2 Formulation	140
E.3 Simulation Results and Optimization of phase center	143
E.3.1 Finding the phase center through Particle Swarm Optimization	143
E.3.2 Symmetric Reflector	144
E.3.3 Offset Reflector	145
F Focal Plane Distribution for Symmetric Reflectors	148
References	151

LIST OF FIGURES

1.1	Number of CubeSat missions launched as a function of year by different sectors (adapted from [2]). Note that this does not include CubeSat constellations that are being developed for imaging, Internet of Things, etc.	2
1.2	A graphical depiction of the various antenna types available to CubeSat designers [4].	3
1.3	Illustration of the SmallSat family. Within this family, SmallSats can be classified by their mass as minisatellites, microsatellites, nanosatellites and picosatellites (adapted from [9]). CubeSats generally fall within the NanoSat and PicoSat classification.	4
1.4	Outline of this dissertation.	11
2.1	A representative example of umbrella reflector antenna that was used for previous CubeSat applications [20]. (a) The umbrella reflector model. (b) Illustration of the reflector being deployed in space.	14
2.2	Mathematical representation of umbrella reflector surface with $N_g = 8$. (a) Parameterization in XY plane. (b) Actual 3D representation of the reflector surface.	16
2.3	Variation of F_g as a function of ϕ for $N_g=5$ and 10. Note the periodic nature of F_g as a function of ϕ' . This periodicity results in cyclical variations in the amplitude and phase at the reflector aperture, causing an ambiguity in the optimum feed point, and far-field grating lobes.	17
2.4	Finding the optimal feed position: The aim is to minimize the deviation in $r' + z'$. The dotted lines show the ray paths for an ideal parabolic reflector [60].	18
2.5	Comparison of the optimal feed positions got via (2.12), (2.17), (2.13) and manual tuning of feed position [60].	21

2.6	Gain loss variation relative to an ideal reflector as a function of feed position for $N_g = 10$, $D = 1m$ and $F_r/D = 0.5$ at 35.75GHz as predicted by PO diffraction analysis [60].	22
2.7	Comparison between optimal focal lengths predicted by (2.13), manual tuning, and the corresponding gain losses with reference to an ideal paraboloid [60]. . .	23
2.8	Variation of boresight gain loss as a function of N_g for various aperture diameters D with an F_r/D of 0.5. The analytical gain loss is calculated by numerically solving (2.22) and inserting the computed RMS error into Ruze's equation. . . .	24
2.9	Aperture distributions of an umbrella reflector of $D = 1m$, $F_r/D = 0.5$ with $N_g = 15$ at 35.75GHz. (a) Normalized copol amplitude distribution when feed is at the reference focus F_r (in dB). (b) Normalized copol amplitude distribution when feed is at the optimal focus F_{opt} (in dB). (c) Copol phase distribution when the feed is at reference focus F_r (in degrees). (d) Copol phase distribution when the feed is at reference focus F_{opt} (in degrees). Note the uniformity of phase when the feed is kept at the optimum position.	25
2.10	Comparisons between far field patterns for feed placed at F_r , F_{opt} and an ideal paraboloid for $N_g = 15$, $D = 1m$ and $F_r/D = 0.5$ at 35.75GHz.	26
2.11	Far fields for $N_g = 15$, aperture diameter $D = 1m$ and $F/D = 0.5$ at 35.75 GHz. (a) 3D representation of the normalized copolarized fields (dB) and (b) E-Plane copol pattern.	27
2.12	Far-fields of umbrella reflector as a function of N_g to illustrate the behavior of grating lobes as the number of gores increase. The details are tabulated in Table 2.1.	28
2.13	Focal plane fields at F_{opt} for $N_g = 10$, aperture diameter $D = 1m$ and $F_r/D = 0.5$ at 35.75 GHz. (a) Normalized copol amplitude distribution (dB) and (b) copol phase distribution. The dotted lines correspond to the location of the ribs, which are at $\phi = 0, 2\pi/N_g, 4\pi/N_g$ and so on.	30

2.14	Excitation coefficients for the focal plane array to conjugate match the focal plane fields of the umbrella reflector. (a) Normalized amplitude coefficients in dB. (b) Phase coefficients in degrees.	30
2.15	Comparing the far-fields of the umbrella reflector with the focal plane conjugate matched array (directivity=49.06 dB) with the ideal reflector (directivity=50.58 dB) and the umbrella reflector with a single cosine-q feed at F_{opt} (directivity=43.77 dB).	31
3.1	Illustration of the novel 1m antenna developed for the next generation CubeSat precipitation radars. (a) An artist illustration of the antenna in space, (b) the reflector antenna system stowed in 3U volume and (c) deployed reflector [122,123].	35
3.2	Deployment sequence developed for the 1m reflector by Tendeg LLC [123].	38
3.3	Reflector antenna and horn feed with their respective coordinate systems. Note that the feed horn antenna has been enlarged to emphasize its location.	39
3.4	Compact horn antenna assembly comprising of a coaxial adapter, rectangular to circular adapter [128], and a spline-profiled horn antenna. The rectangular to circular adapter and a representative monotonic PCHIP spline profile are also illustrated.	41
3.5	Flow chart illustrating the key steps in the optimization process. The objective is to design a horn that achieves the requirements shown in Table 3.3 while ensuring minimum length.	42
3.6	Far field radiation patterns of the optimized horn feed compared to a standard conical horn at 35.75 GHz. (a) E-plane pattern (b) D-plane pattern (c) H-plane pattern. Note the significant performance improvement of the optimized horn. The solid lines and dotted lines denote copol and xpol respectively.	46
3.7	Electric field aperture distributions of (a) conical horn and (b) optimized horn. Note the reduced curvature of the field lines towards the edge of the aperture for the optimized horn.	47

3.8	Far field reflector patterns with the simulated patterns of the optimized horn at 35.75GHz. Solid and dotted lines represent copol and xpol respectively (peak directivity=50.21 dB).	47
3.9	Simulated far-field patterns for the optimized spline profiled horn for RainCube at different frequencies. (a) Normalized copol patterns (in dB) at 35.5 GHz. (b) Normalized xpol patterns (in dB) at 35.5 GHz and (c) E, D and H-plane patterns at 35.5 GHz. (d), (e) and (f) similarly represent patterns at 35.75 GHz (design frequency) and (g), (h) and (i) represent patterns at 36 GHz. The dotted lines indicate the subtended angle over which 10 dB taper is desired. Note the stable performance of the horn.	48
3.10	Optimized horn along with the rectangular to circular adapter and the coax adapter. The horn has a profile of length 48.2mm (5.74λ) and an exit aperture diameter of 19.6mm (2.33λ).	49
3.11	Measured reflection performance of the fabricated horn antenna assembly.	49
3.12	An overview of the bipolar planar measurement process.	50
3.13	Measurement of the fabricated horn at 35.75 GHz using UCLA’s tabletop planar bipolar near field chamber. 3-D printing was used to manufacture customized brackets for alignment. Note that the brackets and the base plate were covered with absorbers during actual measurement.	50
3.14	Measured near field aperture distributions after OSI interpolation at 35.75 GHz (a) Normalized copol amplitude distribution (in dB) (b) Normalized xpol amplitude distribution (in dB) (c) Copol phase distribution (in degrees) (d) Xpol phase distribution (in degrees).	51
3.15	Comparison between measured and simulated far field pattern for the optimized horn at 35.75 GHz (a) E-plane pattern (b) D-plane pattern (c) H-plane pattern. The valid angle for the measurement is chosen to be 70°	52
3.16	Simple wire-grid model analyzed by Astrakhan.	55

3.17	A representative complex tricot knit pattern utilized to construct mesh reflectors [141]. (a) Mesh structure. (b) Equivalent strip model with strip width W , scaled according to the OPI. (c) Equivalent wire grid model of wire diameter $D=W/2$.	56
3.18	Comparisons between the gain loss (ΔG) of the complex knit mesh surface via full wave simulations and the equivalent wire grid model for oblique incidence ($\phi = 0^\circ$) using Astrakhan's formulations (a) 20 OPI. (b) 40 OPI.	56
3.19	Photograph of the mesh used for the RainCube 1m antenna surface.	58
3.20	Modeling the complex mesh surface. We investigated two forms of contact: hard contact (top) and soft contact (bottom). The simplified unit cell was then analyzed using periodic boundary conditions.	58
3.21	Important angle of incidences to be considered for evaluating mesh performance.	59
3.22	Simulation setup to model chassis integration. (a) Proposed CAD model. (b) Simulation setup to model the CubeSat chassis and the reflector support structure. (c) Simplified model viable for full wave simulation.	60
3.23	Impact of chassis interaction on the reflector illumination fields. (a) Simplified CAD model showing aperture on which the electric fields are observed. (b) Feed copolar field amplitude without chassis. (c) Feed copolar field amplitude with chassis interaction. (d) Feed cross polar field amplitude without chassis. (e) Feed cross polar field amplitude with chassis interaction.	61
3.24	Simulation setup for characterizing the impact of chassis using full wave simulation.	62
3.25	Representative E-Plane patterns showing the impact of chassis. (a) Wide angle far field patterns and (b) near boresight patterns. These results show the minimal impact of chassis.	62
3.26	Prototype reflector using deployment testing [123].	63
3.27	Comparison of the measured radiation patterns with simulated results when the feed is kept at the final optimized position at 35.75 GHz [122]. (a) E-Plane and (b) H-Plane.	64

3.28	Measured directivity vs gain plot for the RainCube 1m reflector. The measurements were made with and without the support structures (side panels) to assess the impact of chassis. The reflector antenna achieved a gain of 49.18 dB at 35.75 GHz, which matched closely with simulated predictions [122].	65
3.29	Measured 3D normalized copol far fields (in dB) of the RIC-6U mesh deployable reflector, that shows the appearance of multiple grating lobes [122].	66
3.30	Construction of the hexagonal facets of the mesh.	67
3.31	Reflector surface with hexagonal facets created by UCLA to study the appearance of grating lobes. (a) 3D view and (b) view in the aperture (XY) plane.	68
3.32	3D far fields (copol component, in dB) of the reflector surface with hexagonal facets shown in Figure 3.31. The approximate location and level of the grating lobe is also illustrated. Note that the grating lobes show similar features to that of the RIC-6U surface (Figure 3.29).	69
3.33	Near field distribution of the CAD reflector surface with a hexagonal distribution of the facets. (a) Amplitude distribution (in dB) and (b) phase distribution (in degrees).	69
3.34	Reflector surface with phyllotactic facets created by UCLA to study the appearance of grating lobes. (a) Distribution of points on the aperture. (b) 3D view and (b) view in the aperture (XY) plane for the constructed CAD model by Delaunay triangulation.	71
3.35	Near field distribution of the CAD reflector surface with a phyllotactic distribution of the facets. (a) amplitude distribution (in dB) and (b) phase distribution (in degrees).	72
3.36	3D far fields (copolarized component, in dB) of the reflector surface with phyllotactic facets as shown in Figure 3.34. Note that compared to the hexagonal facets (Figure 3.32), the grating lobes almost disappear and a marginally high sidelobe envelope is seen.	72

3.37	Far field comparison in various planes between the hexagonal faceting and the phyllotactic arrangement of the facets. (a) $\phi=0^\circ$ plane, (b) $\phi=90^\circ$ plane. Note the drastic reduction in grating lobe in the $\phi=90^\circ$ plane. The solid lines denote copol and the dotted lines denote cross-pol. The directivity for the ideal reflector is 50.47 dB. The hexagonal and phyllotactic faceting results in directivities of 50.37 dB and 50.33 dB respectively.	73
3.38	Horn geometry designed to reduce reflector xpol at 35.75 GHz. (a) Profile of the horn showing the location of the screws that generate the TE_{21} mode and tunes the input impedance of the horn and (b) view from the mouth of the horn. . . .	75
3.39	(a) Reference coordinate system chosen for the optimization routine. Note that the screw points towards the bottom edge of the reflector. (b) Final optimized far field patterns of the feed horn and (b) corresponding far-fields of the 1m RainCube reflector. Note the drastic reduction in the crosspolarization of the reflector compared to using a conventional feed (which is approximately 22 dB).	76
3.40	Comparison of reflector radiation patterns ($\phi=90^\circ$ plane) when the horn is oriented in its optimal position (screw at bottom) with the case when the horn is rotated so that the screw faces the top edge of the reflector (screw at top) and a conventional cosine-q feed at 35.75 GHz.	77
3.41	Sensitivity of the reflector cross polarized to variation in the screw distance z_s . (a) Feed geometry. (b) horn patterns and (b) reflector patterns as z_s increases.	78
3.42	Measured S_{11} of the horn. The center frequency of 35.75 GHz is denoted by dotted lines.	79
3.43	Horn mounted in UCLA bipolar planar near-field chamber.	80
3.44	Measured near-field of the horn. (a) Normalized copol magnitude (in dB), (b) copol phase (in degrees), (c) normalized xpol magnitude (in dB) and (d) xpol phase (in degrees).	81
3.45	measured far fields of the horn compared to simulation. (a) E-plane, (b) D-plane and (c) H-plane.	82

3.46	Reflector far-field patterns (a),(b) comparison of cosine-Q feed performance with the measured patterns. (c),(d) comparison of simulated feed performance (screw facing bottom) with the measured patterns. (e),(f) comparison of simulated feed performance (screw facing top) with the measured patterns. Patterns on the left and right represent XZ-plane and YZ-plane respectively.	83
4.1	Various architectures of low profile reflectors that have been under investigation [176].	87
4.2	Diagrammatic illustration of the stepped parabolic reflector concept with a depth of h_0 . Each section provides a modulo 2π phase at the exit aperture. Note that s must be an integer [176].	89
4.3	Profile of a symmetric stepped parabolic reflector with $h_0 = 1\lambda$ (0.839 cm at 35.75 GHz), $s = 2$, $D = 1\text{m}$ and $F/D = 0.5$ [176].	90
4.4	Inclined Flat Offset Stepped Reflector (IFOSR) construction. (a) 2-D profile (b) The process of generating the 3D geometry: The parent paraboloid is intersected by a cylinder of radius a_n and an offset distance of d_n , which are computed by solving (4.7) [176].	92
4.5	Perspective views of the two approaches to generate an offset stepped reflector discussed in this work. (a) HFOSR and (b) IFOSR. Note the large difference in θ_u and θ_l for the HFOSR [176].	93
4.6	Ring widths for symmetric stepped parabolic reflector and offset stepped parabolic reflector with an aperture diameter of $1m$, $h_0 = 1\lambda$ and $s = 2$ at 35.75 GHz. (a) Comparison between symmetric stepped reflector and conventional FZP. (b) Comparison between HFOSR and IFOSR [176].	96

4.7	Far field pattern comparison for a stepped symmetric reflector of depth $h_0 = 1\lambda$ (0.839 cm at 35.75 GHz) and $s = 2$ with a classical symmetric paraboloid. (a) E-plane pattern and (b) D-plane pattern. The peak directivities for the ideal parabolic reflector, symmetric stepped reflector and FZP reflector are 50.57 dB, 49.54 dB and 40.41 dB respectively [176].	98
4.8	Far field pattern comparisons for a stepped offset reflector of depth $h_0 = 1\lambda$ (0.839 cm at 35.75 GHz) and $s = 2$ (through both HFOSR and IFOSR approaches) and a classical paraboloid. (a) Wide angle E-plane pattern. (b) Near boresight E-plane pattern. (c) Wide angle H-plane pattern. (d) Near boresight H-plane pattern. The E-Plane is the plane of offset. The boresight directivities for ideal offset parabolic reflector, HFOSR and IFOSR are 50.45 dB, 48.95 dB and 49.92 dB, respectively [176].	100
4.9	Comparison between PO and MLFMM for stepped parabolic reflector design with $h_0 = 1\lambda$, $s = 2$ and $D = 1m$ at 35.75 GHz. H-plane results are shown here. (a) Symmetric stepped reflector with $F/D = 0.5$. (b) HFOSR with $F/D = 0.75$. (c) IFOSR with $F/D = 0.75$. The directivities are tabulated in Table 4.1.	101
4.10	Bandwidth performance of the symmetric stepped reflector configuration, where increasing the height h_0 can result in bandwidth increases. The different colors represent various F/D values as indicated in the figure [176].	103
4.11	Far-field patterns at different frequencies for the stepped offset reflector. (a) IFOSR and (b) HFOSR. The details are tabulated in Table 4.2 and 4.3 [176]. . .	104
4.12	(a)Simulation model and (b) profile for the fabricated stepped reflector at 19GHz. The stepped reflector has a diameter of 20 cm and an F/D of 0.5.	107
4.13	Fabricated prototype of the stepped reflector. The reflector surface was built via CNC machining and weighed approximately 800 grams.	108

4.14	Generation of the ‘connecting’ sections for the stepped reflector geometry. The section is essentially generated by ensuring only the part of the section that falls within the shadow region of the preceding section is removed to ensure minimal impact on performance.	108
4.15	(a) Fabricated prototype of the offset stepped reflector with an aperture diameter of 20 cm and F/D of 0.5 at 19 GHz. (b) Stepped reflector mounted in the UCLA spherical near-field chamber.	109
4.16	Simulation model which includes the CAD model of the fabricated reflector along with the back plate, which was a part of the bracket used to mount the reflector inside the near-field chamber. The simulation model for the feed horn (Narda-638) is also shown. A cosine-q feed that models the main beam of the feed horn was used for comparing simulated and measured results (see Figure 4.17).	110
4.17	Simulated far-fields of the simplified feed model at different frequencies, and the equivalent cosine-q feed that was used to compare simulated and measured results. (a) E-plane. (b) H-plane.	110
4.18	Comparing simulated results with the measured radiation patterns at 19 GHz. (a) E-plane copol, (b) E-plane xpol, (c) H-plane copol and (d) H-plane xpol.	111
4.19	Comparing simulated results with the measured radiation patterns at lower and upper frequency bounds. (a) E-plane copol at 17.88 GHz, (b) E-plane xpol at 17.88 GHz, (c) E-plane copol at 20.26 GHz and (d) E-plane xpol at 20.26 GHz.	112
4.20	Illustration of the beam scan as the frequency changes for the HFOSR. (a) Simulated results and (b) measured results.	113
4.21	Studying the behavior of the far-field patterns as the geometry scales. (a) x1 scaled version. (b) x2 scaled version. (c) x3 scaled version. (d) Comparison of the far-field patterns	115

4.22	Near-field distributions for the 20 cm (x1 scaled) stepped reflector simulated 2 cm away from the aperture. (a) Normalized copol magnitude distribution (in dB). The dotted red lines represent every individual section. (b) Copol phase distribution (in degrees). (c) Line-cut along x-axis with the blue lines denoting the approximate location of individual sections. Note the ripples in the amplitude coincide well with the position of each section.	116
4.23	Comparison of the results from Fourier transforming the near-field distributions along the x-axis for the stepped reflector as the geometry scales. Note that the number of cycles per unit length that make up the sidelobe envelope are almost the same, with similar levels.	117
4.24	Understanding the behavior of sidelobe envelope as the design scales to larger dimensions using analytical equations. (a) Simulated results and (b) Analytical obtained with $\alpha_i = 30, 31\dots, 55$, $F_i = 1$ and $F_{DC} = 30dB$. Note that the analytical model accurately recovers the trends seen for the sidelobe envelope.	119
5.1	Major contributions of this research.	122
A.1	Coordinate system reference for the umbrella reflector.	124
A.2	Surfaces created by different values of κ in (A.6). (a) $\kappa = 0$ - ideal paraboloid. (b) $\kappa = 1$ - Umbrella reflector, (c) $\kappa = 3$, (d) $\kappa = 5$. (e) Profile of the surface along the $\phi = \pi/N_g$ for various values of κ . Note that as the value of κ increases, the surface tends to bend more inward from the rib.	125
C.1	Modal field distributions for (a) TE_{11} mode, (b) TM_{11} mode and (c) TE_{21} mode assuming an aperture of diameter 2λ	129
C.2	Comparison between the far-fields resulting from the analytical equations and full-wave simulation for the TE_{11} mode. (a) Full-wave copol, (b) Analytical copol, (c) Full-wave xpol and (d) analytical xpol. All plots represent normalized amplitude in dB scale. The aperture is assumed to have a diameter of 2λ at 35.75 GHz.	132

C.3	Comparison between the far-fields resulting from the analytical equations and full-wave simulation for the TE_{21} mode. (a) Full-wave copol, (b) Analytical copol, (c) Full-wave xpol and (d) analytical xpol. All plots represent normalized amplitude in dB scale. The aperture is assumed to have a diameter of 2λ at 35.75 GHz.	133
C.4	Comparison between the far-fields resulting from the analytical equations and full-wave simulation for the TM_{11} mode. (a) Full-wave copol, (b) Analytical copol, (c) Full-wave xpol and (d) analytical xpol. All plots represent normalized amplitude in dB scale. The aperture is assumed to have a diameter of 2λ at 35.75 GHz.	134
C.5	Far-fields of modes combined to give desirable characteristics for illumination. (a) Copol and (b) xpol for $TE_{11} + 0.4TM_{11}$. (c) Copol and (d) xpol for $TE_{11} + 0.4TM_{11} + j0.15TE_{21}$. Note that the analytical formulations are used to generate these results. All plots represent normalized amplitude in dB scale.	135
C.6	Reflector patterns when illuminated by the far-fields corresponding to a combination of different cylindrical modes. (a) Reflector geometry showing the coordinate systems - the feed coordinate system is indicated by a subscript of 'f' and the reflector far-field radiation pattern coordinate system is indicated with subscript 'r'. (a) $\phi = 0$ plane ($x_r - z_r$ plane) and (b) $\phi = 90$ plane ($y_r - z_r$ plane). Note that the feed patterns are all polarized along the y_r axis.	136
D.1	A representative spline profile through the points (x_0, y_0) , (x_1, y_1) , (x_2, y_2) and (x_3, y_3) . These points are marked by red dots. The values of Δ_i and initial values of m_i are tabulated. These initial values must be corrected to ensure monotonicity as described in the text.	138
E.1	Coordinate definitions for reflector phase center estimation.	140
E.2	Analytically determined phase centers for two representative geometries. (a) Symmetric reflector with diameter of 0.5m and F/D of 0.5 and (b) offset reflector with diameter 1m and F/D of 0.75.	143

E.3	Phase center for symmetric parabolic reflector antenna with aperture diameter $D=0.5\text{m}$ and F/D of 0.5.	144
E.4	Comparison of the phase center locations got via analytical formulations (red +) and optimization (blue x).	146
E.5	Comparing the performance of the analytical phase center with the optimized phase center for $F/D=0.5$. (a) Far-field phase contour with the analytical phase center. (b) Far-field phase contour with the optimized phase center. (c) $\phi = 0$ line cut comparison. (d) $\phi = 90^\circ$ line cut comparison.	147
F.1	Focal plane fields (copolarized component) for a symmetric reflector of aperture diameter 1m and $F/D=0.5$ at 35.75 GHz. (a) Analytical focal plane fields, (b) simulated focal plane fields. All values are in dB. (c) and (d) show the comparison between the analytical and the simulated result along $x=0$ and $y=0$ axis. Note that the point $x=0$ and $y=0$ corresponds to the focal point of the reflector. . . .	149
F.2	Variation of the copolarized electric field magnitude along the reflector axis in the vicinity of the focal point for a symmetric reflector of diameter 1m and $F/D=0.5$ at 35.75 GHz. Note the excellent comparison between the analytical and simulated results.	150

LIST OF TABLES

1.1	Representative frequency bands that have been explored for current and future CubeSat missions [3].	5
1.2	Categorized list of references based on current CubeSat Antenna Designs [3]. . .	8
2.1	Dependency of grating lobe level and location on the number of gores N_g . The analytical equation used for predicting grating lobe location is given by (2.25). .	27
3.1	Antenna Specifications to Facilitate Radars that meet the demands of Global Precipitation Measurement Mission.	34
3.2	Antenna options available for small satellite platforms and its associated qualities for the desired aperture size (larger than 1m) at Ka band (<i>Courtesy: JPL</i>). . . .	36
3.3	List of specifications for the feed horn antenna. The geometry of the reflector antenna can be seen in Figure 3.3	40
3.4	Comparison between full wave simulated tricot knit mesh and the analytical simple wire grid model for normal incidence ($\theta_i = \phi_i = 0^\circ$) at 35.75 GHz. The parameters D , W and OPI are as defined in Figure 3.17.	57
3.5	Transmission loss (in dB) for the soft contact model at 35.75 GHz at representative angle of incidence.	59
3.6	Transmission loss (in dB) for the hard contact model at 35.75 GHz at representative angle of incidence.	59
3.7	Gain-Loss table at 35.75 GHz based on simulations [122].	65
3.8	Comparison of directivity and beamwidths for various kinds of faceting	73
4.1	Comparison of Directivity Values Calculated through PO and MLFMM at 35.75 GHz [176].	100
4.2	Frequency Performance for IFOSR [176].	105

4.3	Frequency Performance for HFOSR [176].	105
4.4	Comparison between simulated and measured results at 19GHz. The location of the peak of the main beam is denoted by θ_p and ϕ_p respectively.	110
4.5	Directivities at various frequencies for the HFOSR. The location of the beam peak is denoted by θ_p and ϕ_p in elevation and azimuth respectively.	111
E.1	Comparison of fitness value at the optimized phase center (PC) with the analytical phase center for various geometries.	146

ACKNOWLEDGMENTS

I take this opportunity to thank my advisor - Prof. Yahya Rahmat-Samii whose invaluable guidance has been instrumental for this research. This dissertation is a result of his strong belief in my capabilities and patiently guiding me in the right direction. I will remain indebted to him for the amount of time and effort he has spent in reviewing and analyzing the results presented in the research. I would also thank my committee members - Prof. T. Itoh, Prof. A. Babakhani and Prof. Y. E. Wang who have provided valuable guidance in shaping this research. Many aspects of this thesis is a result of a very successful collaboration with Jet Propulsion Laboratory and Tendeg LLC, and I gratefully acknowledge their support. I am also grateful to the guidance and support provided by Mr. Minji Zhu for many of the measurements described in this dissertation. This research is also a product of many fruitful discussions that I have had with my labmates, who have become my family over the years. I would especially like to acknowledge the mentorship provided by Dr. Joshua Kovitz during my initial years at UCLA. He has played a vital role in my growth personally and professionally. My PhD at UCLA could never have been so comfortable if it weren't for the constant support provided by Deena Columbia and Ryo Arreola from the Office of Graduate Student Affairs.

None of this work could be possible if it weren't for the constant support I received from my friends and family back in India. My parents and my wife have always stood beside me and have never let me doubt my capabilities, and have supported every decision I have taken. I remain eternally grateful to them.

VITA

- 1992 Born in Nagpur, Maharashtra, India.
- 2013 B.E. in Electronics and Telecommunication Engineering, University of Mumbai, Mumbai, India
- 2016 M.S. in Electrical Engineering, University of California Los Angeles, Los Angeles, CA

PUBLICATIONS

Y. Rahmat-Samii, **V. Manohar** and J.M. Kovitz, “Novel antenna concepts and developments for CubeSats,” in *Developments in Antenna Analysis and Design: Volume 2*, eds. Raj Mittra IET, 2018, ch 11.

Y. Rahmat-Samii, **V. Manohar**, J. M. Kovitz, R. E. Hodges, G. Freebury and E. Peral, “Development of Highly Constrained 1 m Ka-Band Mesh Deployable Offset Reflector Antenna for Next Generation CubeSat Radars,” *IEEE Transactions on Antennas and Propagation*, vol. 67, no. 10, pp. 6254-6266, October 2019.

V. Manohar and Y. Rahmat-Samii, “Revisiting the Appearance of Grating Lobes for Antennas With Circular Periodicity,” *IEEE Transactions on Antennas and Propagation*, vol. 67, no. 8, pp. 5723-5728, August 2019

V. Manohar, J.M Kovitz and Y. Rahmat-Samii, “Synthesis and Analysis of Low Profile, Metal-Only Stepped Parabolic Reflector Antenna,” *IEEE Transactions on Antennas and Propagation*, vol. 66, no. 6, pp. 2788-2798, June 2018.

Y. Rahmat-Samii, **V. Manohar** and J.M. Kovitz, “For Satellites, Think Small, Dream Big: A review of recent antenna developments for CubeSats,” *IEEE Antennas and Propagation Magazine*, vol. 59, no. 2, pp. 22-30, February 2017.

J. Wang, **V. Manohar** and Y. Rahmat-Samii, “Enabling Internet of Things with CubeSats - A Review on Beam Steerable Antennas,” *IEEE Antennas and Propagation Magazine* [Accepted].

V. Manohar and Y. Rahmat-Samii, “RF Effects of Umbrella Reflector Antenna Topology for CubeSats: Optimal Feed Point, Boresight Gain Loss and Grating Lobes,” in Proceedings of URSI International Symposium on Electromagnetic Theory (EMTS), pp. 1-4, San Diego, CA, USA, May 2019.

V. Manohar and Y. Rahmat-Samii, “Mimicking Antenna Near-Field Measurements using Full Wave Solvers For Error Characterization,” in Proceedings of the IEEE International Symposium on Antennas and Propagation and USNC-URSI Radio Science Meeting, pp. 1851-1852, Atlanta, GA, July 2019.

J.M. Kovitz, **V. Manohar** and Y. Rahmat-Samii, “Feed Horn Optimization Using Feed+Reflector Co-simulation for Advanced Reflector Antennas,” in *Proceedings of the International Applied Computational Electromagnetics Society Symposium*, pp. 1-2, Florence, Italy, March 2017.

V. Manohar, J. M. Kovitz, and Y. Rahmat-Samii, “A novel customized spline-profiled mm-wave horn antenna for emerging high performance CubeSats,” in *Proceedings of Antenna Measurements and Techniques Association (AMTA)*, October 2016.

CHAPTER 1

Introduction

High-performance satellites typically need to meet stringent RF requirements to deliver the desired quality-of-service (QoS) along with heavy payloads. This precluded the use of small-size satellites for many years. Conventional satellites typically operate at power levels near 10 kW with precise satellite pointing and sophisticated antennas. This results in costs ranging from \$100M – \$2B USD [1] with typical time frames greater than 5 years (from proposal to launch). While it is not possible to completely replace conventional satellite systems by small satellites, the vision and needs for future space concepts are beginning to evolve. As small satellites gain popularity space becomes more accessible to the public, and many grand missions can be envisioned at fractional costs.

The size and power consumption of electronics has been drastically reduced through the development of very large scale integrated circuits, microelectromechanical systems (MEMS), digital signal processing technologies, and low-power programmable systems. This scaling of onboard electronics to smaller dimensions has made it practical to shrink the size and weight of the satellite by orders of magnitude. As one might expect, a smaller weight and volume leads to direct cost reductions in the satellite launch. Though the size limits the multifunctional capabilities that a single satellite can offer, launching a small satellite constellation can offer innumerable possibilities. These small satellites are often abbreviated as *SmallSats*. The term SmallSats encompasses many different subclasses of small satellites, the most notable being the *CubeSat* as discussed subsequent section. The revolutionary idea behind the CubeSat concept was that designers could reduce the satellite volume to the size of a secondary payload on conventional launch vehicles, thereby reducing the launch costs considerably. This provides small universities, commercial companies, government

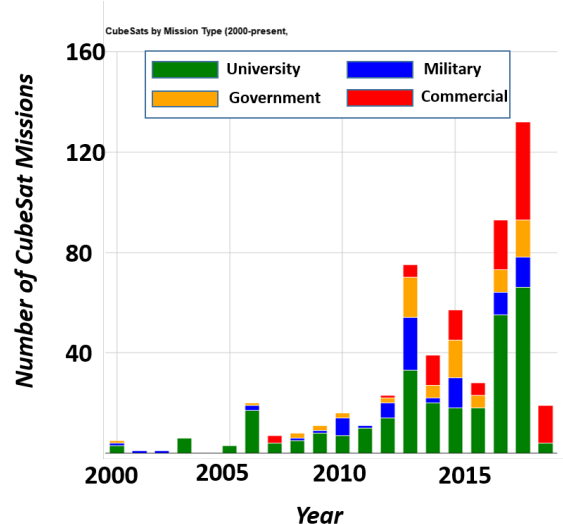


Figure 1.1: Number of CubeSat missions launched as a function of year by different sectors (adapted from [2]). Note that this does not include CubeSat constellations that are being developed for imaging, Internet of Things, etc.

organizations, and even hobbyists reasonable opportunities to access space.

While initial CubeSat missions were predominantly experimental missions launched by startups and universities, the potential of CubeSats has recently excited the defense and commercial sectors leading to several CubeSat missions being conceptualized on a large scale. In fact, it is clear from Figure 1.1 that there has been a consistent rise in the participation of the commercial sector in the development of CubeSats [2].

Antenna systems are key components for radar, remote sensing, and establishing a communication link between the CubeSat and Earth. The inherent proportionality between the antenna gain and antenna size leads to inevitable compromises between the size and weight and link quality for the CubeSat. The scientific community is actively working towards the development of novel antenna systems that can meet the specifications for data rate and resolution while optimizing the physical size of the antenna system [3–7]. With potential CubeSat missions operating over a broad range of frequencies from ELF band up to mmWave bands, many types of antennas have been investigated in the literature, as illustrated in Figure 1.2.

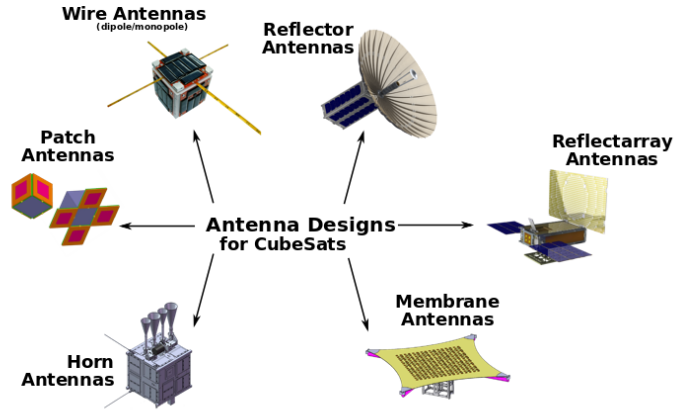


Figure 1.2: A graphical depiction of the various antenna types available to CubeSat designers [4].

1.1 Existing Standards for Small Satellites

The SmallSat family can be subdivided into various categories as shown in Figure 1.3. The “Cube” in CubeSat comes from a motivation to develop a standard chassis that would facilitate a growth in commercial off-the-shelf (COTS) components [8]. According to the standard, the cube chassis should be $10 \times 10 \times 10 \text{ cm}^3$ and weigh less than 1.33 kg. The CubeSat standard also designates this 1000 cm^3 volume as 1U, representing 1 CubeSat-volume.

The CubeSat program establishes a standard to which developers can adhere, thereby promoting widespread usage of miniaturized satellites. This standardization of size and weight allowed for the development of universal launch system for CubeSats, called the Poly-Picosatellite Orbital Deployer (P-POD). With a standard deployer module, researchers across the globe could easily collaborate to affordably participate in space missions through CubeSats. The P-POD launcher allows three 1U CubeSats to be launched simultaneously, potentially leading to the development of a 3U standard for advanced applications. The dimensions of a 3U CubeSat occupies a total volume of 3000 cm^3 and is identical to that of three 1U CubeSat stacked on top of each other. Currently, standards such as 6U, 12U and 27U have also begun to be considered. These standards are also shown in Figure 1.3,

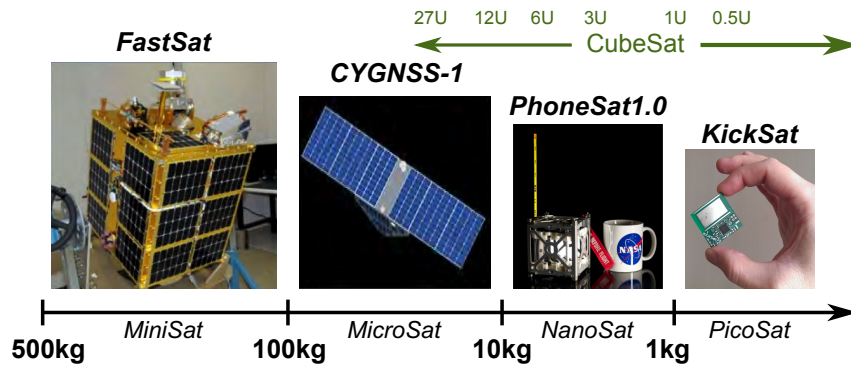


Figure 1.3: Illustration of the SmallSat family. Within this family, SmallSats can be classified by their mass as minisatellites, microsatellites, nanosatellites and picosatellites (adapted from [9]). CubeSats generally fall within the NanoSat and PicoSat classification.

where a mass of 1.33 kg per 1U volume is assumed. It is of interest to note that there is a slight inconsistency in the nomenclature for CubeSats. While the standard developed by Cal Poly SLO refers to CubeSats as PicoSats, some organizations (such as NASA) classify CubeSats within the NanoSat family [9], possibly due to the fact that the 1U CubeSat unit has a mass just slightly greater than 1kg [8], which falls right on the boundary of NanoSats and PicoSats.

1.2 Antenna Requirements for CubeSats

It has been widely accepted that the functionality of CubeSats are limited by the link budget between the satellite and the Earth [10]. Thus, the key to achieving high performance through CubeSats lies with the development of next generation antennas that can achieve the right balance between physical size and electromagnetic demands. The key points to consider while developing antennas for CubeSat missions are now discussed.

Table 1.1: Representative frequency bands that have been explored for current and future CubeSat missions [3].

Frequency	CubeSat Missions	Application
ELF band	QuakeSat [11]	Earthquake detection
VLF band	Firefly Cubesat [12]	Lightning detection
VHF band	Hit-Sat [13] PW-Sat [14] F-1 [15]	Communications
UHF band	RAX [16]	Understand ionospheric irregularities
	DICE [17]	Ionosphere electron density measurements
	AeroCube-4 [18] SwissCube [19]	Communications
S band	Aeneas [20]	Tracking cargo ships in sea
	Goliat [21] CINEMA [22]	Communications
X band	MarCO [23]	Deep space (Mars) communications relay
Ku band	KSat (Hayato) [24]	Moisture sensing for rain prediction
Ka band	RainCube [25]	Precipitation sensing
mmWave	PolarCube [26]	Tropospheric temperature profiling

1.2.1 Frequency

One of the major motives of the CubeSat standard is to use commercial off-the-shelf (COTS) components to construct a satellite. Given the availability of COTS components and the licensing for amateur space missions, the VHF, UHF and S bands are the most popular frequency ranges for CubeSat communications [27,28]. CubeSats have also been considered for a variety of space applications and earth sensing applications that require the system to process specific frequency bands as tabulated in Table 1.1. As CubeSats are being considered for advanced missions, evolving to higher frequency bands for communications has now become a necessity. With CubeSats being considered for deep space missions, the X and Ka bands are currently a major area of research for antenna engineers, as these are the bands used by the Deep Space Network (DSN) [29,30]. Several CubeSats for earth science missions at Ka band and mmWave bands have been conceptualized [25,26]. Although most futuristic missions rely on the launch of a CubeSat constellation into space, the bands for the intersatellite communication remain to be completely defined [31]. Ideas for establishing intersatellite links at S and V band are discussed in [32,33].

1.2.2 Antenna Radiated Power, Gain and Radiation Pattern

The power radiated by a CubeSat is limited by two dominant factors: (a) the amateur frequency bands restrict the power that can be transmitted and (b) the limited space within the CubeSat poses challenges to integrate high power electronic circuitry. Thus, most CubeSat missions that have been launched operate with low gain antennas (typically dipole antennas/patch antennas) with a typical power of 1W. This results typical data rates between 1200 and 9600 bps [27]. An advantage of low-gain antennas for CubeSats is that its broad radiation pattern avoids the need to integrate advanced pointing systems. As CubeSats are now being considered for advanced space applications like deep space missions and high resolution imaging, the needs for sophisticated antenna designs that can provide high gain and resolution, but meet the mechanical constraints of the CubeSat are beginning to evolve. It should be noted that the gain of an antenna system increases, its radiation pattern beamwidth

typically becomes narrower, necessitating the use of sophisticated pointing mechanisms that add cost and complexity to the CubeSat. The polarization of the antenna is also a critical consideration. The majority of the antenna systems that are developed for communications tend to be circularly polarized due to its reduced sensitivity to the relative orientation of the transmitting and receiving antennas [34]. Certain remote sensing missions require linearly polarized antennas [35].


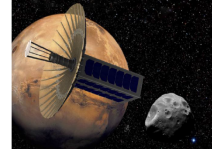
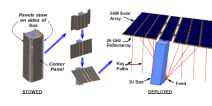
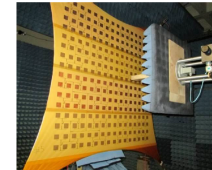


1.2.3 Antenna Material

Antennas in space must be capable of withstanding harsh environments. Depending on the orbit in which the satellite is deployed, the antenna is subjected to a variety of adverse environmental conditions like atomic oxygen, ionospheric plasma, trapped radiation, etc [36]. Current antennas available as COTS components (typically in the UHF/VHF bands) are most often wire antennas which are constructed from metallic tape springs [37, 38]. Antennas like these can be purchased from websites like www.cubesatshop.com. For S-band communications, patch antennas are typically preferred, which use commercially available space qualified substrate (such as Rogers RT/duroid) [34, 39]. For emerging CubeSat missions, high gain metal based deployable reflector antennas are attracting interest from the antenna community. For lower frequencies, where the surface RMS error can be contained to a fraction of wavelength, it is possible to use membrane based aperture antennas [40]. For higher frequencies, where the RMS surface tolerances are stringent, mesh-deployable reflectors are gaining popularity, and several recent investigations have explored their usage in CubeSats [20, 35]. Ideas to manufacture a solid deployable reflector antenna using composites are discussed in [41].

1.3 Representative Current Antenna Concepts for CubeSats

A variety of antenna architectures have been investigated for CubeSats in the literature. The different classes of antennas that have been investigated and developed for CubeSats, as summarized in [3, 4], are listed below.

Table 1.2: Categorized list of references based on current CubeSat Antenna Designs [3].

Antenna Type(s)	Reference	Image
Wire antennas	[13, 39, 42–56]	
Reflector antennas	[20, 35, 41, 57–63]	
Reflectarray antennas	[23, 64, 65]	
Membrane antennas	[40, 57]	
Planar and patch antennas	[34, 39, 66–102]	
Horn antennas and guided wave structures	[32, 58, 103–106]	

1. **Wire antennas:** Wire antennas typically involve monopoles, dipoles, Yagi-Uda arrays and helical antennas. They are common for low frequency applications (HF, VHF, and UHF bands), where the wavelength is long and achieving good radiation efficiency within a small volume is a challenge. The wire antennas are often stowed within the CubeSat volume during flight and deployed once in orbit. The omnidirectionality of dipoles also make them viable candidates for inter-CubeSat communications.
2. **Reflector Antennas:** The development of deployable reflector antennas for CubeSats has recently attracted significant interest in the scientific community. Reflector antennas offer the possibility of fine resolution and high gains, but they come with the need for accurate satellite pointing and increased mechanical complexity.
3. **Reflectarrays:** The reflectarray structure consists of resonant patches on a grounded dielectric substrate that emulate a curved reflector antenna. Reflectarrays can be manufactured in the form of flat panels, and can thus be folded and stowed on the CubeSat chassis .
4. **Membrane antennas:** The idea behind a membrane antenna is to implement the antenna on a fabric-like material. This enables the antenna to be folded and stowed in a compact volume. Membrane antennas are a feasible option for CubeSat applications at lower frequencies where the surface RMS error tolerance is reasonable.
5. **Planar and Patch antennas:** Planar antennas like patch and slot antennas have gained special attention for CubeSats since they can easily be seamlessly integrated with the CubeSat chassis, resulting in minimal space usage.
6. **Horn Antennas and Guided Wave Structures:** Horn antennas can provide reasonable gains and are amenable to fabrication and measurements, even at the university levels. Horn antennas can be a viable option for CubeSats at higher frequencies, where the dimensions of the horns are suitable for its integration with CubeSats.

Refer to Table 1.2 for a comprehensive collection of various works on the development of antenna technology for CubeSats and representative figures. The list is by no means exhaustive,

and readers are encouraged to explore the cited references for further reading.

1.4 Outline of this Work: Futuristic CubeSat Antenna Concepts

As is evident from the previous sections, a significant gap in the antenna technology for CubeSats is the absence of compact high gain antennas capable of meeting the requirements of data rates and spatial resolution for applications such as deep space communications and remote sensing. The fact that the gain of an antenna scales directly with its physical area poses a great difficulty for engineers while integrating high gain antennas with the small form factor of CubeSats. We attempt to close this gap by developing novel tools and antenna designs with the aim of facilitating the integration of high gain antennas with CubeSats. The organization of this prospectus is as follows: The first part analyzes the umbrella reflector in detail, which was amongst the first form of reflector antennas to be used for CubeSats at Ka-band [20]. The surface of umbrella reflectors consists of a discrete number of parabolic ribs that can fold itself into a compact volume for stowing. An important engineering decision is the number of ribs that must be used. While a large number of ribs improve the reflector performance, it increases the mechanical complexity for stowing and deployment. This work looks to provide guidelines to achieve this tradeoff. In the second part we present the development of one of the largest apertures for CubeSats at Ka-band - a *1m mesh deployable offset reflector* that can be stowed in a volume of $10 \times 10 \times 10$ cm³. This antenna was developed as a part of the RainCube project by NASA, which focuses on the development of CubeSat deployable radars for precipitation sensing [6]. Particular attention is given to the analysis of mesh surfaces with complex knits. This is critical for CubeSats since a denser mesh improves RF efficiency but makes it difficult to tension the mesh to maintain the parabolic profile. Further, we also develop an optimized feed to maximize the aperture efficiency. Representative antenna measurement results conducted at JPL are also presented. In the final part, we develop a novel metal-only, low-profile stepped parabolic reflector architecture that can easily be integrated with a flat chassis while providing efficiencies comparable to that of a classical reflector. Several theoretical

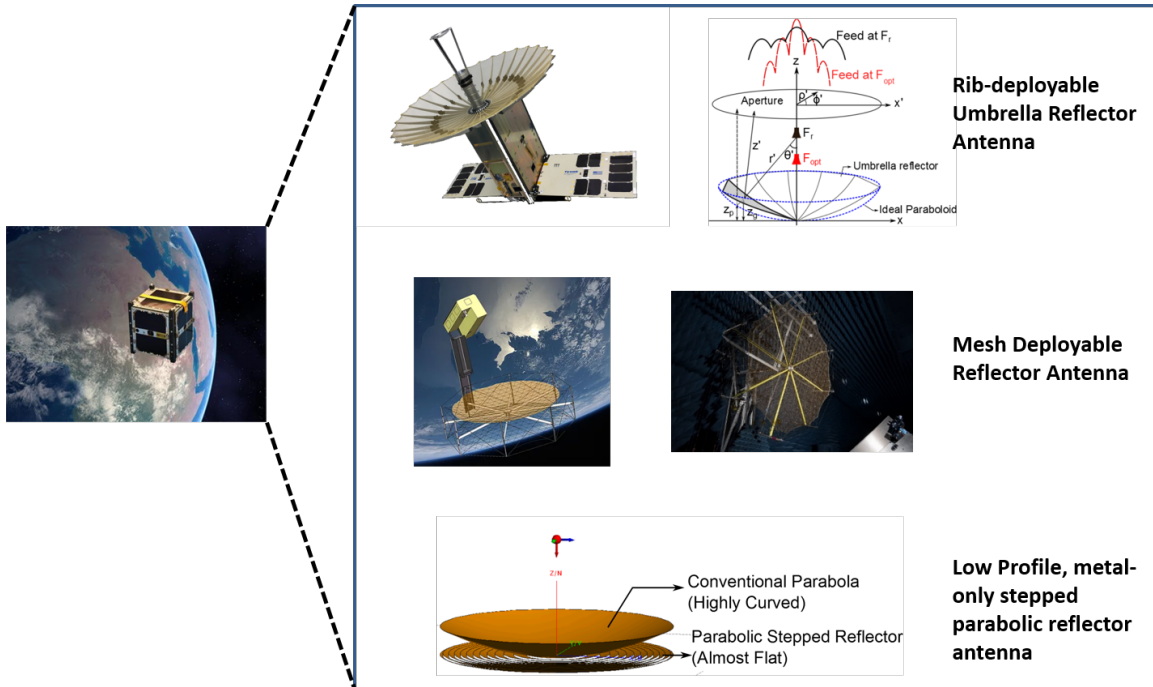


Figure 1.4: Outline of this dissertation.

equations that describe the antenna surface is presented and a complete electromagnetic analysis is carried out via full wave simulations. Most studies in this work are conducted at a frequency of 35.75 GHz due to the recent excitement of remote-sensing missions with CubeSats [6]. The outline of the work is diagrammatically illustrated in Figure 1.4.

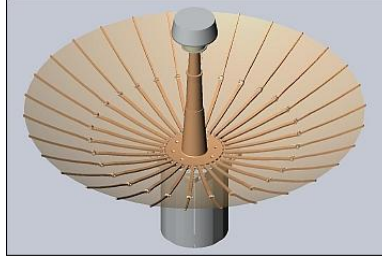
Part I

Umbrella Reflector Characterization

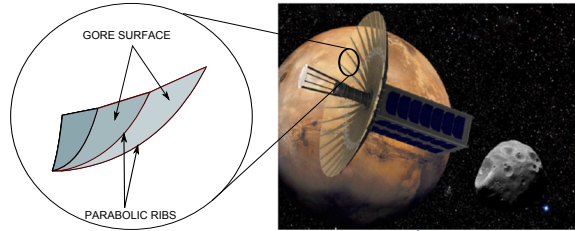
CHAPTER 2

Characterization of Umbrella Reflector Antennas: Analysis of Gain Loss and Estimation of Optimal Feed Point

The umbrella reflector is one of the most popular forms of deployable reflectors for satellite applications. One of the first CubeSats that used an umbrella reflector was the Aeneas CubeSat, which was launched in 2012 [20]. In the recent past, umbrella reflectors have been used to enable deep space missions and remote sensing with CubeSats [35, 107]. The umbrella reflector surface consists of a discrete number of parabolic ribs that are connected by surfaces called gores. Each gore surface is a section of a parabolic cylinder, bound between two parabolic ribs. In deployable reflector antenna systems, the gore surface can be formed by stretching a mesh between the two ribs. The gores cause the surface of reflector to deviate from a true paraboloid, resulting in ambiguity of optimal feed position and pattern degradation. As the number of ribs increase, the deviation of the umbrella reflector surface from an ideal paraboloid reduces, increasing the RF efficiency. However, packaging a large number of ribs into the small volume of the CubeSat bus can be a major challenge, making lower number of ribs attractive for CubeSat applications. In the case of dual reflector systems, as shown in Figure 2.1, the subreflector must be optimally positioned to account for the gores. Significant amount of work has been done in the past to characterize umbrella reflectors with larger amount of gores. This chapter revisits the determination of the optimum feed location and gain loss with an emphasis on a smaller number of gores. The underlying assumptions and analysis of previous approaches are reviewed. Furthermore, comparison with results from manually tuning using Physical Optics (PO)-based diffraction analysis is presented.



(a)



(b)

Figure 2.1: A representative example of umbrella reflector antenna that was used for previous CubeSat applications [20]. (a) The umbrella reflector model. (b) Illustration of the reflector being deployed in space.

These results pinpoint the cases in which the previous approximations are no longer valid, necessitating a manual tuning of the feed location for optimal gain. The effects of feed taper is also discussed, further extending previous works position. We also develop formulations that relate the gain loss due to gores to the diameter, frequency and number of ribs to provide several guidelines for the design of umbrella reflectors for CubeSats.

2.1 Mathematical representation of the gore surface

The surface of an umbrella reflectors consist of a discrete number of parabolic ribs, and a parabolic cylinder like surface connecting them, called gores. If there are N_g gores, with F_r being the focal length of each rib, the gore surface can be defined through two parameters A and t as:

$$x = t[\cos \phi'_m + A(\cos \phi'_{m+1} - \cos \phi'_m)] \quad (2.1)$$

$$y = t[\sin \phi'_m + A(\sin \phi'_{m+1} - \sin \phi'_m)] \quad (2.2)$$

$$z = t^2/4F_r \quad (2.3)$$

where, $0 \leq A \leq 1$, $0 \leq t \leq D/2$, $\phi'_m = 2\pi(m-1)/N_g$ and $m = 1, 2, \dots, N_g$. This parameterization is shown in Figure 2.2a. The three dimensional representation of the reflector surface is illustrated in Figure 2.2b.

These equations be converted into a single equation of the form of $z = f(x, y)$ as

$$z_g = \frac{\rho'^2}{4F_g(\phi')} \quad (2.4)$$

where

$$F_g(\phi) = \frac{F_r \cos^2(\pi/N_g)}{\cos^2 \frac{\phi_m + \phi_{m+1} - 2\phi}{2}} \quad (2.5)$$

$$\rho'^2 = x'^2 + y'^2 \quad (2.6)$$

$$\phi' = \tan^{-1}(y'/x') \quad (2.7)$$

An important observation from (2.4) and (2.5) is that the focal length of the umbrella reflector is now a function of ϕ . The variation of F_g with ϕ is plotted in Figure 2.3. An interesting interpretation of (2.4) and (2.5) is that the umbrella reflector can be viewed as a family of parabolic curves, each having a focal length between $F_r \cos^2(\pi/N_g)$ and F_r . Note the periodic variation of F_g . This periodicity manifests itself in aperture distributions as cyclical phase variations causing grating lobes. As the number of gores increase, the deviation of F_g from F_r begins to decrease. It is evident that there is no distinct focal point for the umbrella reflector and thus, the position of the feed is not obvious.

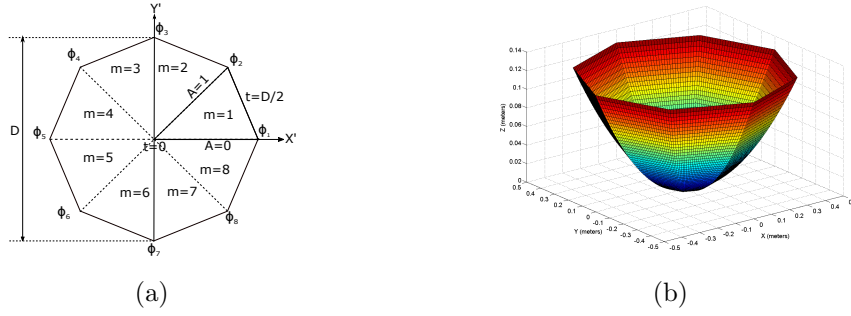


Figure 2.2: Mathematical representation of umbrella reflector surface with $N_g = 8$. (a) Parameterization in XY plane. (b) Actual 3D representation of the reflector surface.

2.2 Finding the optimum feed location

This section revisits the problem of finding the optimal feed position for umbrella reflectors with particular consideration for a low number of gores which are desirable for CubeSat applications. Two approaches reported in the literature include: (a) a Physical Optics (PO) approach combined with the parallel ray approximation and (b) finding the best-fit equivalent paraboloid through minimizing the RMS error between an ideal paraboloid and an umbrella reflector. The results from both these approaches are compared with manual tuning of the feed location using exact PO analysis, i.e. diffraction analysis with no approximations. For mmWave frequencies, considerable pattern degradation can occur with minor mechanical feed positioning errors. This makes the determination of the accurate optimal feed point critical. This study provides an effective way to judge the applicability of closed form expressions to determine the optimal feed position. Additionally, we also consider the effects of feed taper on the optimal feed location. The RMS deviation of the gores from the ideal paraboloid is related to the gain loss for various configurations.

2.2.1 Physical intuition behind the optimal feed location

The aperture field method of analysis can provide some intuition behind choosing the feed position. Consider the general equation for taper efficiency in (2.8). The numerator essentially represents the power of the radiated fields at boresight, which is proportional to the

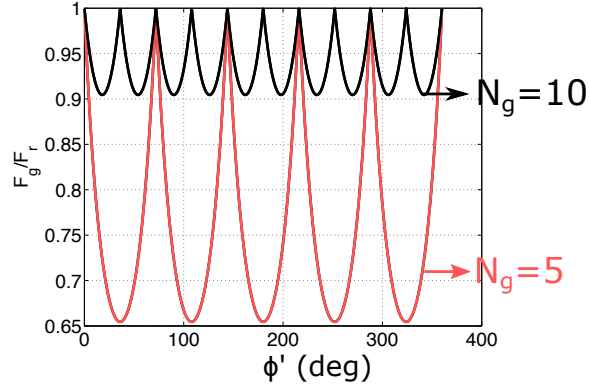


Figure 2.3: Variation of F_g as a function of ϕ for $N_g=5$ and 10. Note the periodic nature of F_g as a function of ϕ' . This periodicity results in cyclical variations in the amplitude and phase at the reflector aperture, causing an ambiguity in the optimum feed point, and far-field grating lobes.

aperture electric field E_a , where it is assumed that all fields are oriented in x or y direction. The denominator has two terms: The aperture area and the total power in the aperture. Since the total power in the aperture and aperture area can be assumed to be constant as the feed position changes, we focus on the numerator of the efficiency equation.

$$\eta = \frac{1}{A_a} \frac{|\iint_s E_a ds|^2}{\iint_s |E_a|^2 ds} \quad (2.8)$$

Referring to Figure 2.4, the aperture electric field can be described as

$$E_a = E_0(\rho', \phi') e^{jk(r'+z')} \quad (2.9)$$

The numerator of (2.8) can thus be written as (2.10).

$$\left| \iint_s E_a ds \right|^2 = \left| \iint_s E_0(\rho', \phi') e^{jk(r'+z')} ds \right|^2 \quad (2.10)$$

The aim is thus, to maximize (2.10). Moving the feed position for umbrella reflector will have minimal impacts on the amplitude distribution E_0 . The critical term that needs attention in the phase term $k(r' + z')$. For parabolic reflectors, $r' + z'$ is a constant, with a tapered amplitude distribution E_0 , resulting in uniform phase. This provides maximum directivity along boresight. However, this is not the case for umbrella reflectors since the gore surface

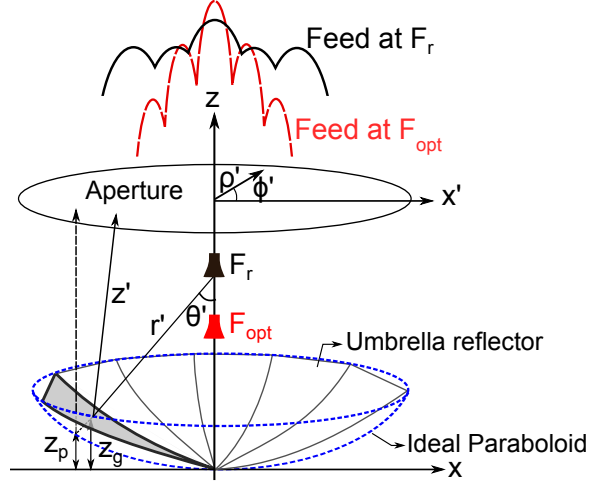


Figure 2.4: Finding the optimal feed position: The aim is to minimize the deviation in $r' + z'$. The dotted lines show the ray paths for an ideal parabolic reflector [60].

deviates from the paraboloid. Thus, the aim is to minimize the deviation of this phase term on the aperture. This can be carried out using multiple approaches, as will be discussed subsequently.

2.2.2 Physical Optics approach

In [108], the parallel ray approximation is used to express the phase term in the PO integral, (which bears resemblance to (2.10)) as $\Delta f(1 + \cos \theta')$ where Δf denotes the deviation of gore focal length F_g from the feed location and θ' denotes the incident ray angle. The problem, thus, reduces to simply finding a feed point that minimizes Δf . Since the feed point is a single point (independent of ϕ'), the optimal feed point just comes out to be the average value of F_g and is thus given as:

$$\frac{F_{opt}}{F_r} = \frac{N_g}{\pi} \int_0^{\frac{\pi}{N_g}} \frac{\cos^2 \pi/N_g}{\cos^2 \psi} d\psi \quad (2.11)$$

where $\psi = 0$ represents the parabolic curve passing through the center of the gore and $\psi = \frac{\pi}{N_g}$ represents the rib. The integral in (2.11) can easily be evaluated as

$$\frac{F_{opt}}{F_r} = \frac{N_g}{2\pi} \sin \frac{2\pi}{N_g} \quad (2.12)$$

For large values of N_g , (2.12) can be expanded into its Taylor series to yield

$$\frac{F_{opt}}{F_r} = 1 - \frac{2}{3} \left(\frac{\pi}{N_g} \right)^2 \quad (2.13)$$

2.2.3 Best Fit Paraboloid approach

A different approach to estimate the optimal feeding point was highlighted in [109]. This approach involved finding a best-fit paraboloid to the umbrella reflector through an RMS error minimization process. Intuitively, the focus of this best fit paraboloid will be the point that minimizes the phase deviation at the aperture and would be the optimal feed position for the umbrella reflector system. The RMS error is defined as

$$\Delta z_{rms} = \sqrt{\frac{1}{A_g} \int_0^{\frac{D}{2} \cos \phi_o} \int_0^{y \tan \phi_o} (z_g - z_{eq})^2 dx dy} \quad (2.14)$$

where,

$$z_g = \frac{x^2 + y^2}{4F_g(\phi')} \quad (2.15)$$

$$z_{eq} = \frac{x^2 + y^2}{4F_{eq}} \quad (2.16)$$

where $\phi_o = \pi/N_g$ and $A_g = \frac{1}{4}(\frac{D}{2})^2 \sin 2\phi_o$. Note the correction in the integration limits for x and y in [109]. The optimal focal length is then found by minimizing the RMS error defined in (2.14). This can be done analytically, leading to the equations for optimal focal length and the corresponding minimum RMS error.

$$\frac{F_{opt}}{F_r} = \cos^2 \phi_o \frac{1 + \frac{2}{3} \tan^2 \phi_o + \frac{1}{5} \tan^4 \phi_o}{1 + \frac{1}{3} \tan^2 \phi_o} \quad (2.17)$$

$$\Delta z_{rms} = 0.010758 \frac{D^2 \cos^2 \phi_o}{F_r} \frac{\tan^2 \phi_o (1 + \tan^2 \phi_o)}{\sqrt{(1 + \frac{2}{3} \tan^2 \phi_o + \frac{1}{5} \tan^4 \phi_o)}} \quad (2.18)$$

It is seen that for larger values of N_g , (2.17) can be approximated as (2.13). A comparison of the focal lengths got by (2.12), (2.13) and (2.17) is shown in Figure 2.5. It is interesting to note that none of these formulations for the optimal feed point directly involves the frequency or the diameter of the reflector. For the RMS minimization procedure, the diameter of the

reflector effects the RMS error but not the optimal focal length. It is worth noting that this approach is primarily geometry based. The inherent assumption in this approach is that the deviation of the umbrella reflector from the ideal paraboloid is small enough that minimizing the Δz between the gore and the paraboloid has the same effect as minimizing the phase deviation in the exit aperture. The authors in [109] report that this method was found suitable only when $\Delta z_{rms} < 0.08\lambda$.

2.2.4 Manual tuning of feed position

In this approach, the feed is moved along the axis of the reflector and the reflector antenna performance is observed for each feed location using an exact PO analysis, i.e. PO without any approximations. A cosine-q feed model is used to illuminate the reflector. The optimal feed location must result in minimizing the gain loss at boresight. This is an important investigation of the previous formulations, especially in the low gore regime, where the underlying assumptions may not be valid.

2.3 Results and discussions

A comparison between the optimal feed locations computed via the two approaches defined by (2.12), (2.17) and through manual tuning of the feed position is presented in Figure 2.5. It can clearly be seen that none of the theoretical approaches result in the optimal feed location for $N_g < 15$ for an aperture of diameter 1m and $F_r/D = 0.5$ at 35.75GHz.

In order to understand the importance of accurate feed positioning, we consider the case of $N_g = 10$, $D = 1m$, $F_r/D = 0.5$ for analysis. The boresight gain loss computed through exact PO analysis as a function of feed location for $N_g = 10$ is shown in Figure 2.6. The gain loss is measured relative to an ideal paraboloid illuminated with the same edge taper with feed at focus. Manual tuning predicts an optimal feed position of $0.4532m$ for uniform illumination ($0dB$ taper) and $0.4540m$ for optimal $-10dB$ taper. The optimal location predicted by (2.12), (2.17) and (2.13) results in the feed location being $0.4677m$, $0.4686m$ and $0.4671m$ respectively. Even though $N_g = 10$ also reduces the physical aperture area, it only accounts

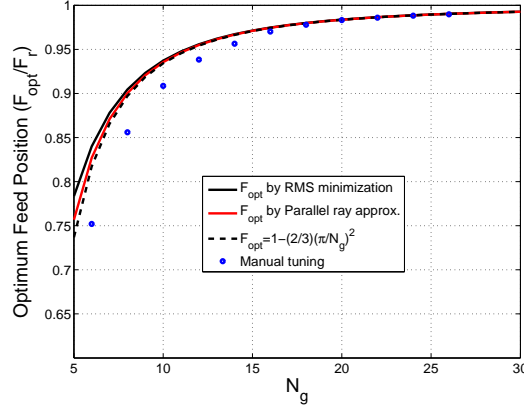


Figure 2.5: Comparison of the optimal feed positions got via (2.12), (2.17), (2.13) and manual tuning of feed position [60].

for 0.4dB loss for the 0dB taper. For small feed displacements, the change in the spillover and the taper losses are not significant. The surface deviation due to gores, thus, is the primary reason for the gain loss. Note that the results of these analytical formulations are independent of taper. This difference in the optimal feed positioning results in an additional loss of approximately 4.5dB with respect to keeping the feed at the position predicted by manual tuning. A significant observation here is also that the feed position does not heavily depend on taper as is predicted by both the theoretical approaches.

With $N_g = 10$ being studied in detail, a valid question that arises is the minimum value of N_g where the closed form expressions can be used. Figure 2.7 shows a comparison between the optimal feed point predicted by (2.13) with the feed point predicted by manual tuning and their corresponding gain loss. It is clearly seen that the closed form expressions can be used when $N_g > 15$ ($\Delta z_{rms} = 0.11\lambda$). Thus, for $N_g < 15$ one must resort to manually tuning the feed position to get the optimal performance.

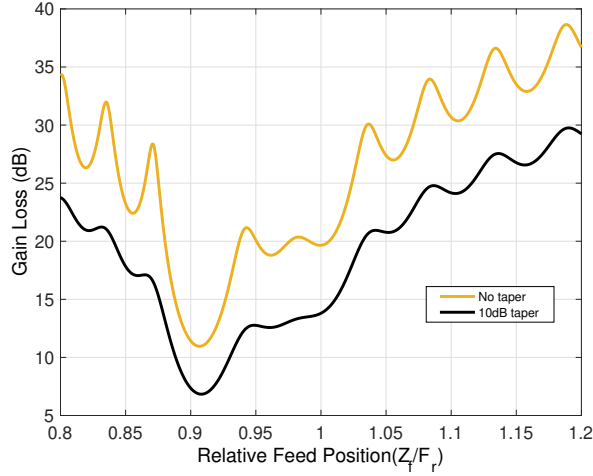


Figure 2.6: Gain loss variation relative to an ideal reflector as a function of feed position for $N_g = 10$, $D = 1m$ and $F_r/D = 0.5$ at 35.75GHz as predicted by PO diffraction analysis [60].

2.4 Gain loss as a function of Number of Gores

A significant advantage of the best-fit paraboloid method lies in the fact that it yields the RMS error between the umbrella reflector along with the optimal feed position. The RMS error can be used to estimate the gain loss through Ruze's equation, and ultimately result in a closed form expression that relates the gain loss to the parameters of the umbrella reflector. Starting from (2.18), the equation for the RMS error can be simplified using the following approximation for a reasonable amount of gores ($N_g > 20$):

$$\cos^2 \phi_o \frac{\tan^2 \phi_o (1 + \tan^2 \phi_o)}{\sqrt{(1 + \frac{2}{3} \tan^2 \phi_o + \frac{1}{5} \tan^4 \phi_o)}} \approx \left(\frac{\pi}{N_g} \right)^2 \quad (2.19)$$

This simplifies the expression for the RMS error significantly to:

$$\Delta z_{rms} = 0.010758 \frac{D}{F_r/D} \left(\frac{\pi}{N_g} \right)^2 \quad (2.20)$$

Substituting this into the Ruze's equation [110] yields

$$\Delta G(dB) = 685.811 \left(\zeta \frac{\Delta z_{rms}}{\lambda} \right)^2 = 7.73 \frac{\zeta^2}{\lambda^2} \frac{D^2}{(F_r/D)^2} \left(\frac{1}{N_g} \right)^4 \quad (2.21)$$

Where $\zeta = (4F_r/D) \sqrt{\ln[1 + 1/(4F_r/D)^2]}$. This leads to a very interesting result: for a given F_r/D , the gain loss scales as the $(\sqrt{D}/N_g)^4$, implying that the number of gores required for

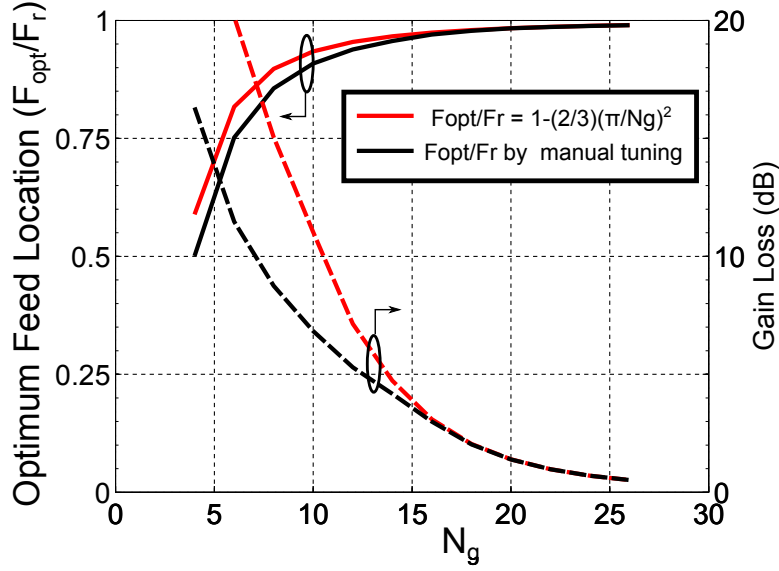


Figure 2.7: Comparison between optimal focal lengths predicted by (2.13), manual tuning, and the corresponding gain losses with reference to an ideal paraboloid [60].

the same gain loss scales only as the square root of the diameter.

It should be noted that if the amplitude distribution on the aperture of the reflector is tapered, the equation for the RMS error presented in (2.14) must be suitably modified to [111]:

$$\Delta z_{rms} = \sqrt{\frac{1}{A_g} \int_0^{\frac{D}{2} \cos \phi_o} \int_0^{y' \tan \phi_o} (z_g - z_{eq})^2 Q(\rho') dx' dy'} \quad (2.22)$$

Where $Q(\rho')$ and A_g are the taper function and the effective area respectively, given by [112]:

$$Q(\rho') = C + (1 - C) \left[1 - \left(\frac{\rho'}{D/2} \right)^2 \right]^p, \text{Edge taper}(ET) = 20 \log_{10} C \quad (2.23)$$

$$A_g = \int_0^{\frac{D}{2} \cos \phi_o} \int_0^{y' \tan \phi_o} Q(\rho') dx' dy' \quad (2.24)$$

The value of p in (2.23) governs the slope of the taper. Representative simulation results that highlight the dependency of gain loss on the number of gores for various aperture diameters D at 35.75 GHz is shown in Figure 2.8.

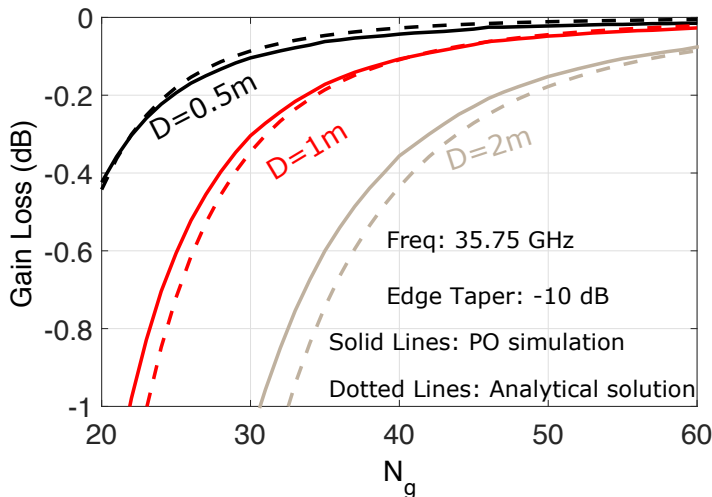


Figure 2.8: Variation of boresight gain loss as a function of N_g for various aperture diameters D with an F_r/D of 0.5. The analytical gain loss is calculated by numerically solving (2.22) and inserting the computed RMS error into Ruze’s equation.

2.4.1 Discussions on the Radiation Performance of Umbrella Reflectors

The discussion until this point was centered around finding the optimal feed position and estimating the gain loss that results due to deviations of the umbrella reflector surface from the ideal parabolic profile. In this section, we analyze the radiation patterns and the near field aperture distributions of an umbrella reflector. As a representative case, we assume an aperture diameter of 1m with an $F_r/D=0.5$ and $N_g=15$ at 35.75 GHz. Using Physical Optics, the near field aperture distribution for this system when the feed is kept at F_r is simulated, followed by moving the feed to F_{opt} . The near fields are shown in Figure 2.9. It is evident that moving the feed to the optimal position significantly improves the phase uniformity in the aperture leading to improved directivity, as seen in Figure. 2.10. It can also be observed that the amplitude distribution remains unaffected as was predicted. A striking feature of these near-field distributions is that they show a periodicity of π/N_g (as opposed to $2\pi/N_g$). This is expected due to the fact that each individual gore is symmetric about its center, and therefore the deviation of the gore surface is identical for the two halves of a single gore. This can also be seen from the variation of F_g with ϕ' in Figure 2.3. This periodicity manifests

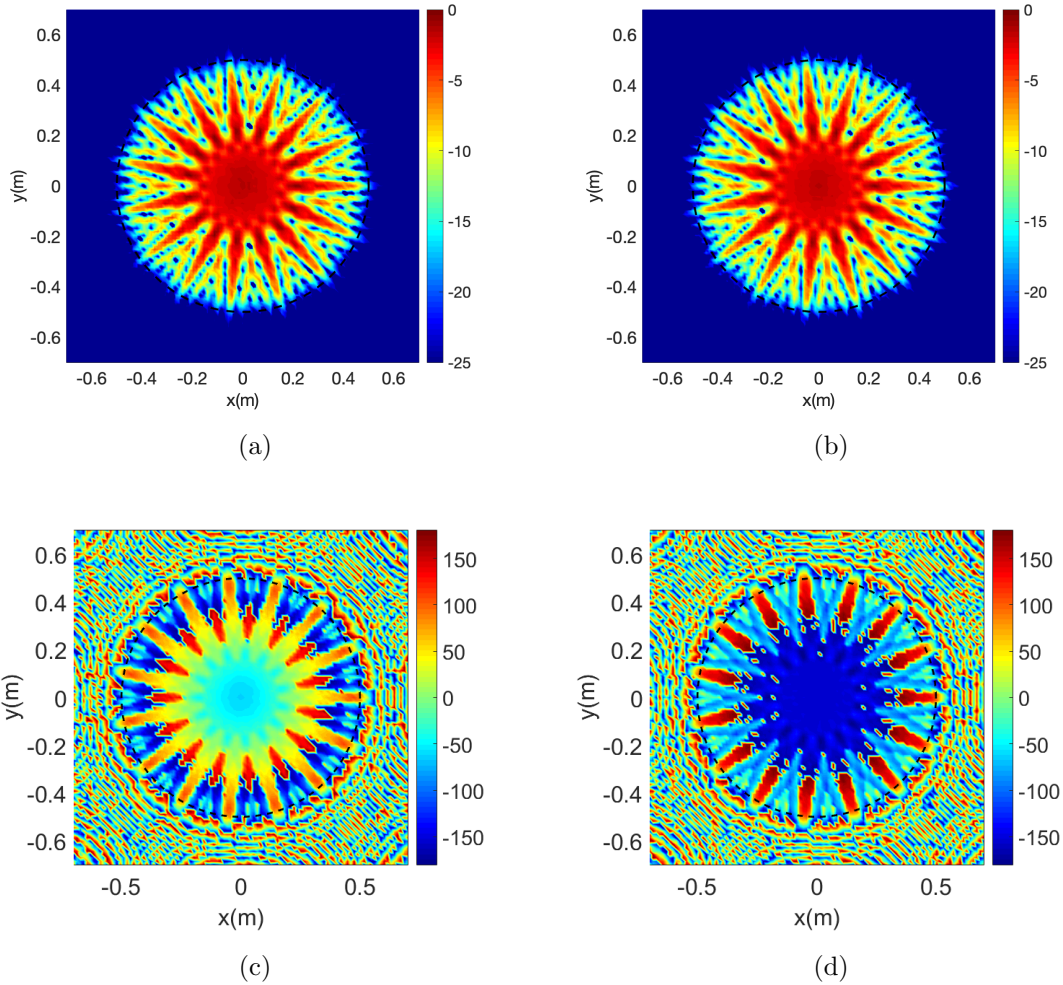


Figure 2.9: Aperture distributions of an umbrella reflector of $D = 1m$, $F_r/D = 0.5$ with $N_g = 15$ at 35.75GHz. (a) Normalized copol amplitude distribution when feed is at the reference focus F_r (in dB). (b) Normalized copol amplitude distribution when feed is at the optimal focus F_{opt} (in dB). (c) Copol phase distribution when the feed is at reference focus F_r (in degrees). (d) Copol phase distribution when the feed is at reference focus F_{opt} (in degrees). Note the uniformity of phase when the feed is kept at the optimum position.

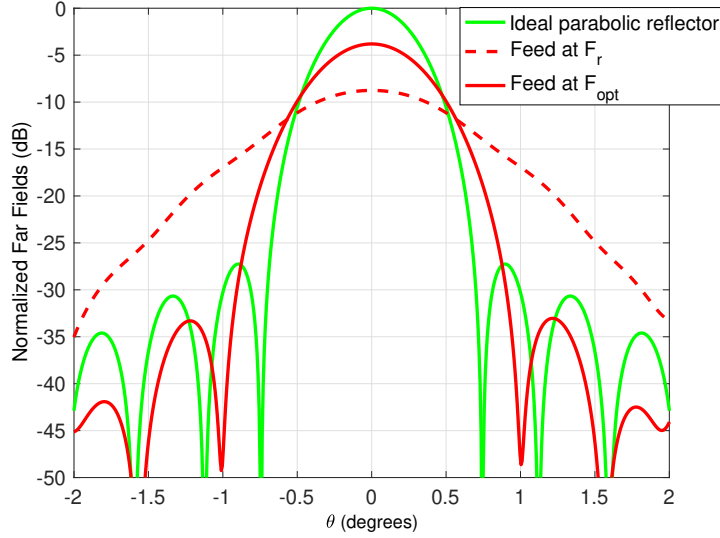


Figure 2.10: Comparisons between far field patterns for feed placed at F_r , F_{opt} and an ideal paraboloid for $N_g = 15$, $D = 1m$ and $F_r/D = 0.5$ at 35.75GHz.

itself in the far field as grating lobes, as seen in Figure 2.11. Note that 15 ribs result in 30 grating lobes in ϕ due to the periodicity in the aperture. These grating lobes can reduce the efficiency of the system [111, 113, 114]. An approximate expression that can be used to estimate the grating lobe location in the elevation plane can be given as [115, 116]:

$$\sin \theta_g = \frac{N_g}{\pi D/\lambda} \quad (2.25)$$

It is evident from (2.25) that as the value of N_g increases, the location of grating lobe move further away from the main beam, to a point where its level is insignificant. This is also verified through simulating the radiation patterns for an umbrella reflector of diameter 1m and F_r/D of 0.5 with various N_g at 35.75 GHz. The results are shown in Figure 2.12 and the details are tabulated in Table 2.1.

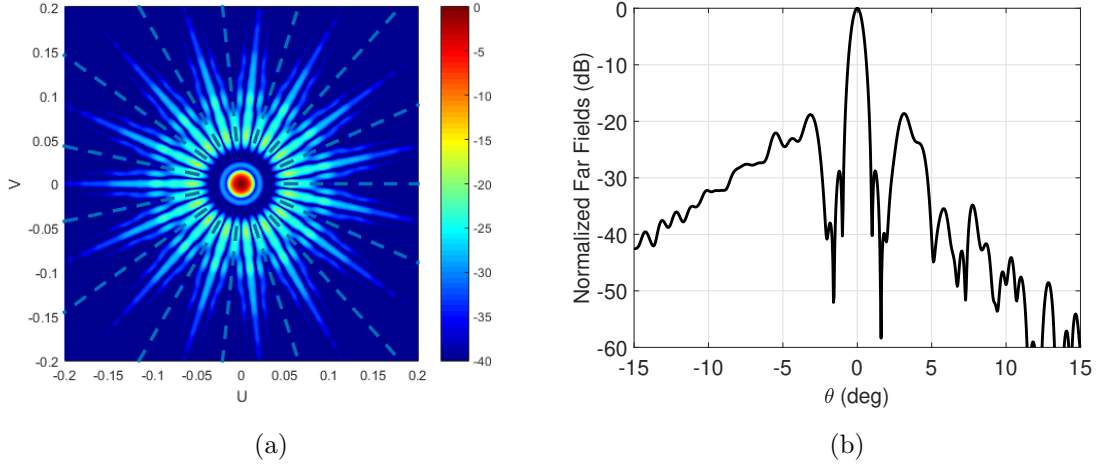


Figure 2.11: Far fields for $N_g = 15$, aperture diameter $D = 1m$ and $F/D = 0.5$ at 35.75 GHz. (a) 3D representation of the normalized copolarized fields (dB) and (b) E-Plane copol pattern.

Table 2.1: Dependency of grating lobe level and location on the number of gores N_g . The analytical equation used for predicting grating lobe location is given by (2.25).

N_g	Boresight directivity	Analytical grating lobe location	Simulated Grating lobe location	Grating Lobe Level
15	46.76 dB	2.29°	3.12°	-18.63 dB
20	49.19 dB	3.06°	3.84°	-24.01 dB
25	49.98 dB	3.83°	4.44°	-29.65 dB
30	50.28 dB	4.59°	5.52°	-33.58 dB

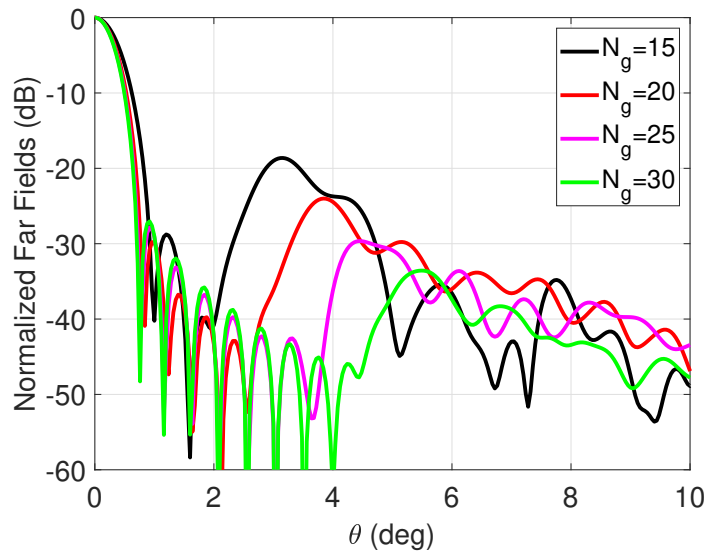


Figure 2.12: Far-fields of umbrella reflector as a function of N_g to illustrate the behavior of grating lobes as the number of gores increase. The details are tabulated in Table 2.1.

2.5 Compensating For Gain Loss due to Umbrella Reflector Topology - A Conceptual Study

The previous section described the details behind characterizing the radiation patterns of the umbrella reflector. In this section, we provide some conceptual insights into compensating for the pattern degradation caused by the umbrella reflector topology through the process of conjugate phase matching [117]. The process of conjugate field matching involves simulating the field distributions in the focal plane of the umbrella reflector when illuminated by a plane wave travelling parallel to the axis of the reflector followed by designing an array that can provide nearly the same amplitude distribution but a phase that is the *conjugate* of the phase of the focal plane fields of the reflector antenna. As a representative case, a 10 rib umbrella reflector is considered with an aperture diameter of 1m and an F_r/D of 0.5 at 35.75 GHz, which is identical to the geometry studied in detail in Section 2.2. The ‘focal plane’ for this reflector is assumed to be at the optimal feed position determined in the Section 2.2 as $F_{opt}=0.454\text{m}$. The magnitude and phase of the electric fields when the umbrella reflector is illuminated by a plane wave traveling along the axis of the reflector is shown in Figure 2.13. It can be observed that the focal plane distributions shows the presence of $2 \times N_g$ ‘grating lobes’, which are consistent with our observations about the far-field characteristics of umbrella reflectors in Section 2.4. In order to conjugate match this focal plane distribution, an array of 25 by 25 cosine-q point sources were used as feed. The separation between each of these elements was chosen to be $\lambda/2$ which results in a rectangular feed array of dimensions of 10 cm by 10 cm. The amplitude excitation for each of these elements were chosen to be identical to the amplitude of the electric fields got via simulation of the focal plane fields at the location of the element. The phase was chosen to be conjugate of the phase of the focal plane fields at the element’s location. The amplitude and phase excitations of the elements are shown in Figure 2.14. The ‘q’ for the cosine-q elements were chosen to be 1 to model a typical patch antenna.

Finally, the far-fields of the umbrella reflector are simulated by using this focal plane array as the feed. The far-field results are shown in Figure 2.15 where 3 cases are compared:

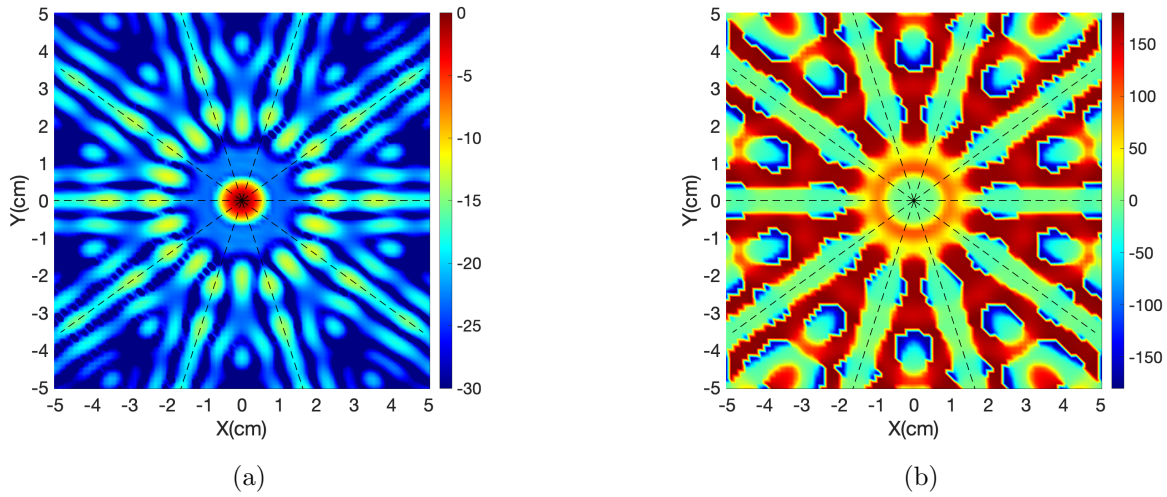


Figure 2.13: Focal plane fields at F_{opt} for $N_g = 10$, aperture diameter $D = 1m$ and $F_r/D = 0.5$ at 35.75 GHz. (a) Normalized copol amplitude distribution (dB) and (b) copol phase distribution. The dotted lines correspond to the location of the ribs, which are at $\phi = 0, 2\pi/N_g, 4\pi/N_g$ and so on.

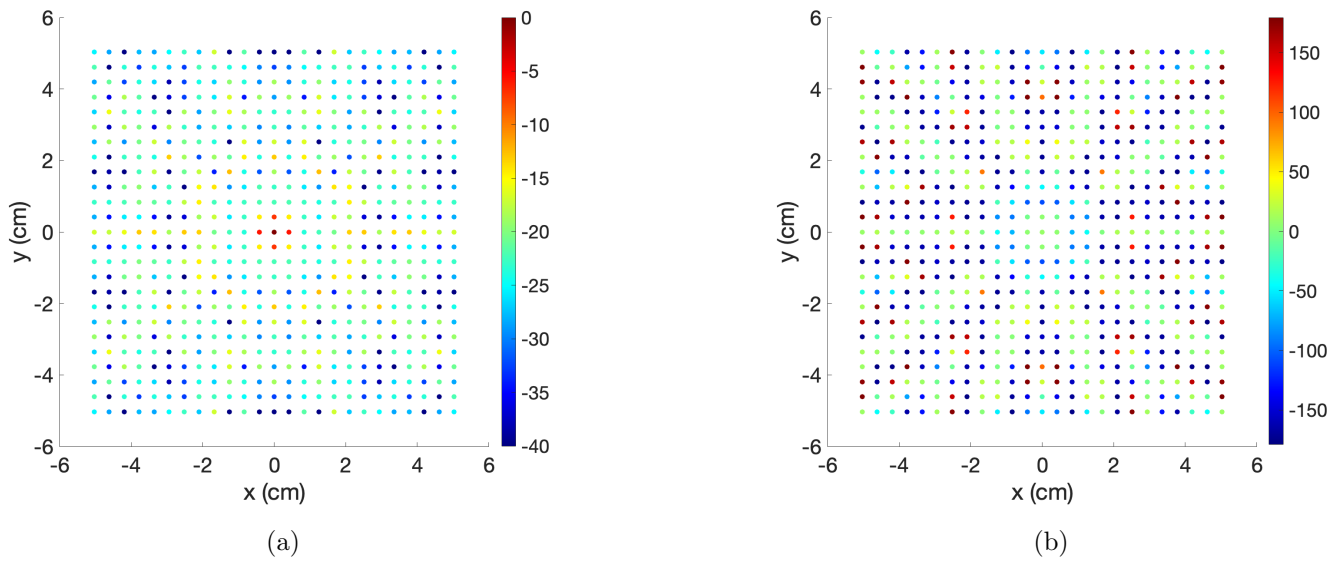


Figure 2.14: Excitation coefficients for the focal plane array to conjugate match the focal plane fields of the umbrella reflector. (a) Normalized amplitude coefficients in dB. (b) Phase coefficients in degrees.

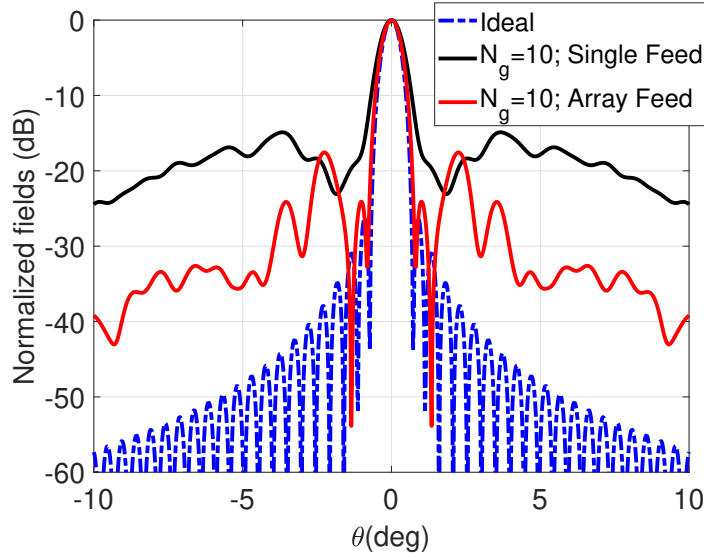


Figure 2.15: Comparing the far-fields of the umbrella reflector with the focal plane conjugate matched array (directivity=49.06 dB) with the ideal reflector (directivity=50.58 dB) and the umbrella reflector with a single cosine-q feed at F_{opt} (directivity=43.77 dB).

(a) far-fields of an ideal parabolic reflector with a single cosine-q feed at its focal point which provides a 10 dB edge taper, (b) far-fields of the umbrella reflector with a single cosine-q feed at F_{opt} which is configured to provide a 10 dB edge taper, and (c) far-fields of the umbrella reflector with the focal plane array got via conjugate field matching. It is evident that the conjugate field matching technique results in a more directive beam compared to using just a single cosine-q feed. The directivities for cases (a), (b) and (c) are 50.58 dB, 43.77 dB and 49.06 dB. Thus, the conjugate phase matching technique can recover almost 5 dB of directivity compared to its single feed counterpart. The challenge, however, is the design and fabrication of an array (or a subreflector) that can provide the required amplitude and phase variation in its aperture. This will be a subject of future research in the area.

Part II

Mesh Deployable Reflector Design for RainCube

CHAPTER 3

RainCube 1m Ka-Band Offset Mesh Deployable Antenna - Development and Characterization

3.1 RainCube Mission - Needs and Objectives

Remote sensing is one of the key application areas for satellites. Many conventional satellites have been launched to-date that use antennas to sense the power back-scattered by different molecules in the atmosphere [118–120]. However, one of the major technological gaps that we face today is the inability of such satellites to observe weather phenomenon that develops over a small time span (few seconds to minutes). This is primarily due to the fact that most conventional satellites have orbital periods of a much greater time span (few hours to a few days). These missions, therefore, are generally unable to observe the short-time evolution of weather processes, which is necessary to validate and improve existing numerical weather models. One possible solution is to deploy several radars (as convoy or constellation). This, however, is not economically feasible with conventional satellites. The arrival of the SmallSat and CubeSat platforms make this endeavor practical today due to their cost affordability. However, the challenge now shifts towards development of radars that can meet the desired RF specifications while being able to integrate with very small platforms, and be commercially viable. RainCube (Radar in a CubeSat) is a technology demonstration mission by the National Aeronautics and Space Administration (NASA) to enable such Ka-band precipitation radar technologies on a low-cost, quick-turnaround platform.

Radar instruments have often been regarded as unsuitable for small satellite platforms due to their traditionally large size, weight, and power. Recently, Jet Propulsion Laboratory (JPL), in collaboration with University of California, Los Angeles (UCLA), has developed

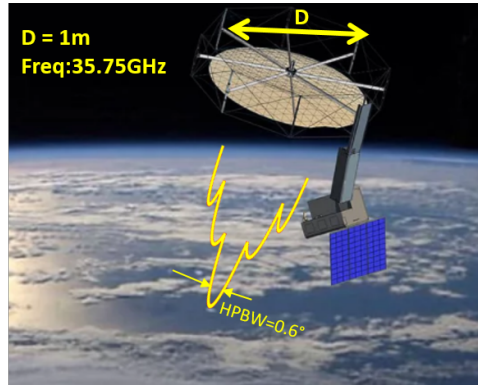
Table 3.1: Antenna Specifications to Facilitate Radars that meet the demands of Global Precipitation Measurement Mission.

Parameter	Value	Parameter	Value
Frequency	35.75 GHz	Stowage	10x10x30 cm ³
Polarization	linear	Antenna mass	2 kg
Return loss	15dB	Diameter	1 m
Sidelobe level	17 dB	Antenna Gain	45 dB
Bandwidth	20 MHz	Beamwidth	$\leq 0.7^\circ$

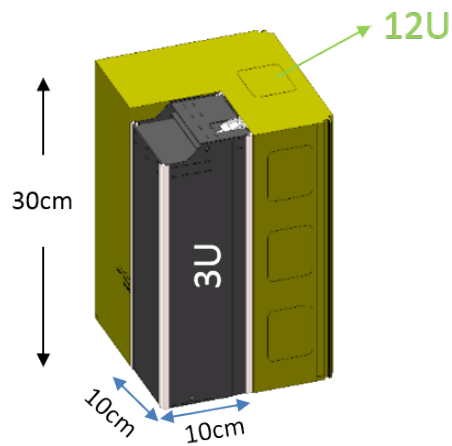
a novel architecture compatible with a 6U CubeSat platform. The antenna system consists of a 0.5m Cassegrain reflector antenna system, that can be stowed in a volume of 1.5U ($10 \times 10 \times 15$ cm³) [35]. While this architecture meets Global Precipitation Measurement mission’s specifications of +12 dBZ vertical sensitivity (which is sufficient to detect light rain and moderate snowfall), the 0.5m antenna aperture size is not sufficient for the horizontal resolution needed for science missions [6]. Thus, the development of a compact 1.0m antenna was envisioned to enable science missions which demand a constellation of low-cost small satellites providing global, distributed, and frequent coverage for global profiling of precipitation and breakthrough observation of precipitation processes [121]. An artist illustration of the novel 1m reflector concept, which can be stowed in a volume of 3U is shown in Figure 3.1.

3.2 Antenna Design for Next Generation RainCube Radar

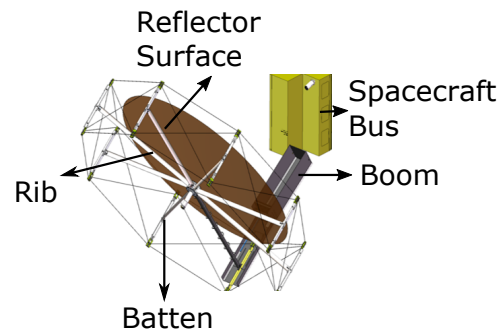
Table 3.1 shows preliminary performance requirements for the RainCube 1m antenna. The applicable antenna technologies are summarized in Table 3.2, which provides a qualitative assessment of how well each option meets the key requirements. Microstrip patch and waveguide slot array antennas require a bulky feed structure that makes them difficult to fold compactly (resulting in poor stowed volume) [124]. In contrast, reflectors provide a good balance between stowage efficiency and RF performance, as was noted in [35]. Even within



(a)



(b)



(c)

Figure 3.1: Illustration of the novel 1m antenna developed for the next generation CubeSat precipitation radars. (a) An artist illustration of the antenna in space, (b) the reflector antenna system stowed in 3U volume and (c) deployed reflector [122, 123].

Table 3.2: Antenna options available for small satellite platforms and its associated qualities for the desired aperture size (larger than 1m) at Ka band (*Courtesy: JPL*).

Technology	Mass	Stowed Volume	Surface tolerance (Ka-band)	Deployment Mechanism	Technology Readiness Level [125]
μ strip patch	High	Poor	Poor	Folded panels	2 (folding)
W/G slot array	High	Poor	Medium	Folded panels	2 (folding)
Shape memory reflector	Medium /High	Poor	Low	Ripple folding mechanism	2 (CubeSat)
Inflatable Membrane	Medium	Good	Medium	Rolled stowage mechanism	2 (CubeSat)
Reflectarray	Medium	Good	Medium	Folded panels	4
Mesh reflector	Low	Good	Medium	Folded ribs	3

the domain of reflector antennas, several options exist today. Inflatable or frame supported membrane reflectors show promise, but development of these antennas has not advanced beyond the research stage due to technical risks associated with inflation and membrane stability. Shaped memory composite reflectors do not achieve the demanding surface accuracy at Ka-band. A flat reflectarray can be deployed and can achieve relatively good efficiency ($\sim 50\%$), but mass will be relatively high for a 1m aperture [64]. Consequently, *deployable mesh reflector technology* appears to offer the best combination of mass, stowed volume and efficiency for this application. Moreover, in contrast to a reflectarray, the wide bandwidth of reflector class antennas could enable a multi-frequency radar or enable the antenna to support both the radar instrument, and a high data rate telecom downlink.

3.2.1 Reflector Configuration Selection

With the successful demonstration of the 0.5m reflector concept by JPL [107], we aimed to push the envelope further for the next generation of CubeSats. As described in the previous section, an aperture near 1 meter is desirable for achieving the required horizontal resolution. This led to a collaborative effort between NASA, JPL, Tendeg llc., and UCLA in targeting a 1 meter aperture for the next evolution of high-gain CubeSat reflector antennas. Mechanical constraints coupled with mm-Wave frequency sensitivities made it impossible to scale the previous 0.5m umbrella reflector design. Therefore, we developed a completely new reflector design—a *1 meter offset mesh reflector*—that stows in a 3U ($10 \times 10 \times 30$ cm³) volume within the CubeSat. The 0.5m Cassegrain reflector design could not be directly scaled for this application for the following reasons:

1. The gain loss for an umbrella reflector largely depends on the number of ribs. A 1m reflector would require greater than 30 ribs to maintain a reasonable deviation from an ideal surface and achieve a gain loss under 0.1dB as was seen in the previous chapter [63, 126]. This greatly increases the risk of rib jamming during deployment.
2. For Cassegrain systems, the number of deployment mechanisms used is decided by the distance between the vertex of the main reflector and subreflector. A direct scaling of the 0.5m design would thus add significant mechanical complexity to the system.
3. A larger subreflector would pose a greater mechanical constraint for packaging and further increase the weight of the reflector system. Further, dual reflector systems typically require larger feed dimensions to appropriately illuminate the small subreflector, increasing complexity of the system.

Though a symmetric single configuration has its advantages, the feed has to completely rotate to face the reflector, complicating the feed deployment mechanisms. To balance these tradeoffs, a single offset reflector configuration was chosen. The offset configuration alleviates some of the difficulties faced during the deployment of symmetric reflectors: it avoids feed blockage and facilitates feed positioning. The main disadvantages include an increased cross

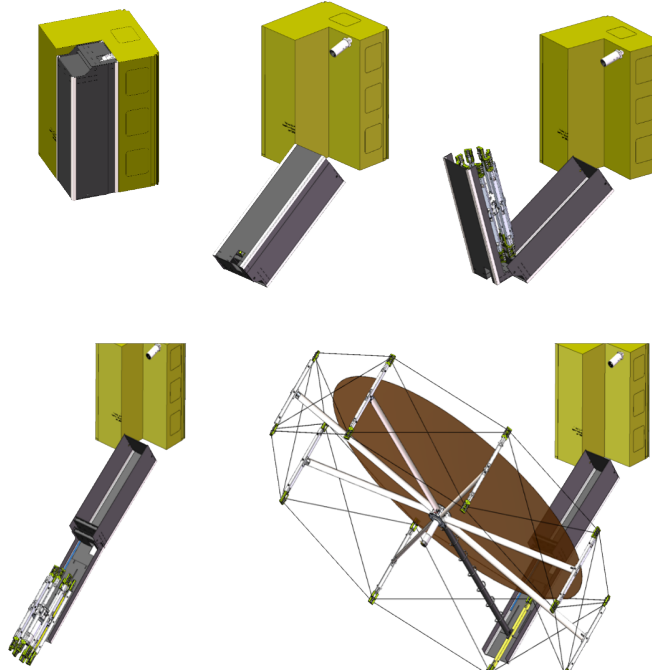


Figure 3.2: Deployment sequence developed for the 1m reflector by Tendeg LLC [123].

polarization and increased fabrication complexity, although a specialized feed horn can be designed to minimize reflector cross-polarization as is described towards the end of this chapter.

In the initial phases of the project, multiple reflector geometries were investigated that could meet the specifications for the RainCube [127]. This led to finalizing the 1m offset geometry. Once the geometry was known, a study on the impact of mesh and chassis on the reflector performance was conducted. Several tools were developed to analyze mesh surfaces with complex knits. Innovative ideas to design an optimized horn that maximizes reflector efficiency were developed. The feed horn was fabricated and measured at UCLA. Several reflector surfaces that were tested by Tendeg were characterized by UCLA to ensure that the RMS deviation was minimal and the desired specifications were met. Prior to measurement of the final surface, several tolerance studies relating the feed orientation and position were conducted. This new geometry necessitated a completely new deployment mechanism to be developed. The sequence is illustrated in Figure 3.2 and was developed by Tendeg LLC.

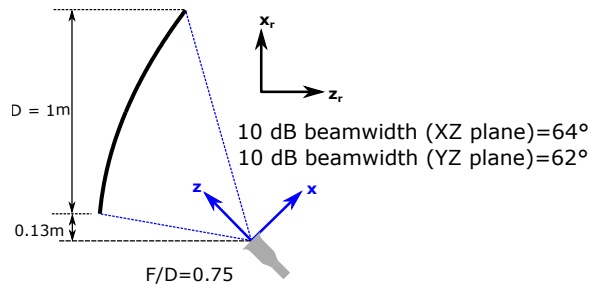


Figure 3.3: Reflector antenna and horn feed with their respective coordinate systems. Note that the feed horn antenna has been enlarged to emphasize its location.

3.3 Feed Horn Design

This section focuses on the development of a spline profiled optimized horn to illuminate the one meter mesh deployable RainCube reflector design. Particle Swarm Optimization (PSO) is used to design a horn capable of providing low cross polarization and sidelobe levels, while conforming to the mechanical constraints imposed by the CubeSat standard. The horn was fabricated by the UCLA machine shop using a 5-axis CNC milling machine and measured using the planar bipolar measurement technique. The final measured results of the horn were used as a feed model for subsequent reflector simulations to assess the performance of various reflector surfaces created by Tendeg and to assess tolerance required for feed positioning.

3.3.1 Reflector Antenna Design and Feed Horn Antenna Requirements

The RainCube 1m geometry uses an $F/D = 0.75$ as illustrated in Figure 3.3, resulting in half subtended angles of 32° and 31° in the XZ and YZ planes respectively. It is widely known that the feed horn must provide a taper of 10dB at the edge of the reflector for optimal aperture efficiency [112], leading to a 10dB beamwidth requirement of 64° and 62° in the XZ plane (E-Plane) and YZ plane (H-Plane) respectively. This requirement restricts the minimum diameter of the horn. In order to minimize the spillover from the feed, the backlobes and the sidelobes of the horn must be minimized. Further, the S_{11} must be as low as possible to effectively deliver the input power to the horn. A detailed list of specifications can be seen in Table 3.3.

Table 3.3: List of specifications for the feed horn antenna. The geometry of the reflector antenna can be seen in Figure 3.3

10dB Beamwidth (XZ-Plane)	64°
10dB Beamwidth (YZ-Plane)	62°
S_{11}	<-20dB
Cross polarization	<-25dB
Sidelobe Levels	<-25dB

Achieving these electromagnetic requirements while satisfying the mechanical constraints imposed by the RainCube architecture makes this design a major challenge. Pyramidal or conical horns, though inexpensive and simple to design, are limited in length by the quadratic phase error at its aperture. Potter horns are capable of providing low cross polarization at the cost of complexity of prototyping and reduced bandwidth. Corrugated horns are also capable of providing low cross polarization and sidelobes, but are typically heavier and expensive to fabricate. Optimization techniques enables the designer to put more emphasis on critical constraints and offers the possibilities of handling multiple design parameters. For the RainCube project, a novel spline-profiled smooth walled horn is designed that achieves the desired electromagnetic performance while satisfying the mechanical constraints of the CubeSat. Particle Swarm Optimization (PSO) was used to optimize the horn profile for the desired length, beamwidths, backlobe level and cross polarization level. A rectangular to circular adapter is required to connect the optimized horn to the coax adapter. Since the design uses commercially available coax adapters, the horn along with the rectangular to circular adapter was optimized to provide optimal electromagnetic performance with minimum length.

3.3.2 Horn Design Optimization Approach

Modern CAD simulation suites provide engineers the capabilities to simulate a full 3D antenna structure including any microwave components preceding the antenna. These 3D CAD

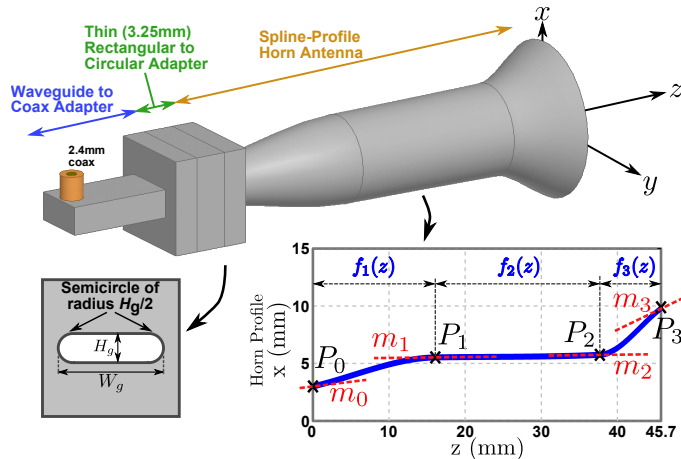


Figure 3.4: Compact horn antenna assembly comprising of a coaxial adapter, rectangular to circular adapter [128], and a spline-profiled horn antenna. The rectangular to circular adapter and a representative monotonic PCHIP spline profile are also illustrated.

modeling software suites can also be paired with optimization techniques to provide a design meeting important requirements, such as those shown in Table 3.3. Our aim was to utilize these engineering advances to develop a high-performance feed horn that optimally illuminates the 1m offset reflector antenna. In particular, HFSS was utilized to model and simulate the horn antenna assembly shown in Figure 3.4, and Particle Swarm Optimization was used to optimize the structure [129, 130]. An overview of the optimization process is shown in Figure 3.5.

The horn antenna is essentially a body of revolution applied to a curve created from a discrete number of splines. A representative set of splines are shown in Figure 3.4, where the points P_1 , P_2 , and P_3 are connected using splines. Since the length of the horn was an important parameter, the horn model was integrated with HFSS with the hope to optimize the performance parameters by tuning the geometry. To simplify the optimization problem, the horn profile was optimized separately from the rectangular to circular waveguide adapter. We refer to these as the horn optimization problem and the waveguide adapter optimization problem, respectively. The rectangular to circular waveguide adapter (seen in Figure 3.4) uses a semicircular shape adapted from [128]. For the waveguide to coax adapter,

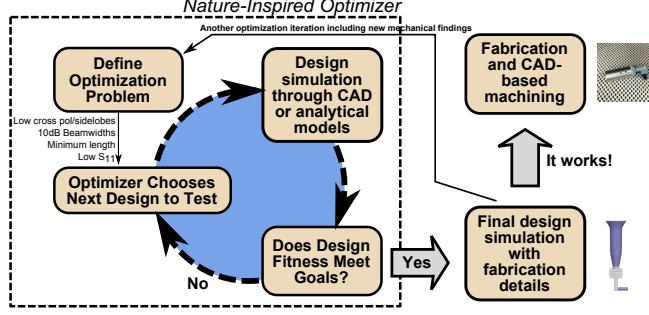


Figure 3.5: Flow chart illustrating the key steps in the optimization process. The objective is to design a horn that achieves the requirements shown in Table 3.3 while ensuring minimum length.

a commercial off-the-shelf component was purchased separately. For simulation purposes, a representative model was created in HFSS that was tuned for 35.75 GHz.

Referring to Figure 3.4, the spline profile can be shaped by adjusting the (z, x) positions of the spline points $\{P_0, \dots, P_k\}$. Each spline segment $\{f_1(z), \dots, f_k(z)\}$ is defined by the spline point positions $\{(z_0, x_0), \dots, (z_k, x_k)\}$ and the spline point slopes $\{m_0, \dots, m_k\}$ [131, 132]. The i th segment can be written by four Hermite basis functions as

$$f_i(z) = h_{00}(\bar{z})x_{i-1} + h_{01}(\bar{z})x_i + h_{10}(\bar{z})(z_i - z_{i-1})m_{i-1} + h_{11}(\bar{z})(z_i - z_{i-1})m_i \quad (3.1)$$

where \bar{z} represents the normalized independent variable z scaled as

$$\bar{z} = \frac{z - z_{i-1}}{z_i - z_{i-1}} \quad (3.2)$$

which maps z to the interval $[0, 1]$ for the i th segment. The Hermite basis functions can be defined as

$$h_{00}(\bar{z}) = 2\bar{z}^3 - 3\bar{z}^2 + 1 \quad (3.3)$$

$$h_{10}(\bar{z}) = \bar{z}^3 - 2\bar{z}^2 + \bar{z} \quad (3.4)$$

$$h_{01}(\bar{z}) = -2\bar{z}^3 + 3\bar{z}^2 \quad (3.5)$$

$$h_{11}(\bar{z}) = \bar{z}^3 - \bar{z}^2 \quad (3.6)$$

To facilitate fabrication, the splines were forced to be monotonic. This placed constraints on the slopes $\{m_0, \dots, m_k\}$ at each of the points. The monotonicity was achieved by using

a similar approach as was proposed in [133] and used in [132]. The process for finding $\{m_0, \dots, m_k\}$ is detailed in Appendix D. Assuming an X-polarized horn (refer to Figure 3.3), we quantified the performance using the fitness function

$$f(\mathbf{x}) = (BW_{E,10} - 64^\circ)^2 + (BW_{H,10} - 62^\circ)^2 + S_{11} + 0.2X_p + 0.2B_L + 0.5L_t \quad (3.7)$$

where \mathbf{x} is the vector of optimization variables, $BW_{E,10}$ and $BW_{H,10}$ are the E-plane and H-plane 10dB beamwidths of the horn design in degrees, S_{11} is the impedance matching in dB, and L_t is the total length of the horn antenna assembly in mm. The cross-polarization level, X_p , is defined as the ratio of the worst case cross-polarization component within the forward region of the D-plane (i.e. $-90^\circ \leq \theta \leq 90^\circ$, $\phi = 45^\circ$) to the boresight copolar component in dB. The backlobe B_L is defined as the worst-case component (copol or xpol) observed in the back region $|\theta| > 90^\circ$ for the E, D, and H-planes to the boresight copolar component in dB. The coefficients for each term in (3.7) are similar to a previous optimization study in [134].

The number of splines k is a tradeoff between the complexity of optimization and the degree of freedom. Small values simplify the optimization problem (less parameters to optimize) but might not give the optimizer enough degrees of freedom to find the optimal profile. We ran the optimization for $k = 3$ and $k = 5$ and achieved similar horn geometries. Thus, our initial observations have been that $k = 3$ was suitable for this optimization problem.

3.3.3 Simulated Results

This section details the simulation results of the optimized horn and analyzes its performance. As a reference, we compare the far field patterns of the optimized horn to the far field patterns of a conical horn designed to provide 10dB taper at the edge of the reflector. The patterns in the principal planes are illustrated in Figure 3.6. The key advantage of the optimized horn over the traditional conical horn is evident: the optimized horn provides nearly identical 10dB beamwidths in the E, D and H planes along with low cross polarization and sidelobe levels. This can be explained by studying the difference in aperture distributions of the two horns as shown in Figure 3.7. The fields at the exit aperture for a conical horn are similar to the TE_{11} mode of the cylindrical waveguide, resulting in relatively stronger fields

at the edges. This leads to increased cross-polarization, edge diffraction, and backlobes. The TE_{11} mode also comes with an increased presence of an E_y component leading to the higher cross polarization in the D-plane. Further, the TE_{11} mode for the conical horn produces different radiation patterns and beamwidths for the E-plane and H-plane. The optimized horn, however, provides a dual-mode $TE_{11} + TM_{11}$ distribution leading to a reduction in the curvature of the fields. This leads to low cross polarization and symmetric patterns. Further, the fields tend to be more concentrated near the center of the aperture resulting in the optimized horn having a diameter slightly greater than a conventional horn to provide identical 10dB beamwidths. An analytical study on the radiation characteristics of different modes in a cylindrical waveguide can be found in Appendix C.

The simulated results of the optimized horn was then used for reflector analysis using Physical Optics. The far field reflector patterns are shown in Figure 3.8. The peak directivity and half-power beamwidth are 50.21dB and 0.56° respectively, which satisfy the specifications for remote sensing. It should be noted that these simulation results do not include losses due to mesh and supporting structures, which will be investigated in subsequent sections.

An important consideration for such horns is the radiation performance over frequency, since the cancellation between the cross polarization of the TE_{11} and TM_{11} modes can, in general, be sensitive to frequency. The far-fields at 35.5 GHz, 35.75 GHz (center frequency) and 35.60 GHz are shown in Figure 3.9. It can be observed that the horn design provides a very stable radiation pattern, and the far-fields in the E, D and H planes are still very identical. Note that this bandwidth is much greater than the 20 MHz bandwidth required for the RainCube mission.

3.3.4 Fabrication and Measurement

We fabricated the optimized horn using a CNC lathe machine. The horn profile was bored out of a single piece of solid aluminum cylinder to ensure mechanical stability. The fabricated horn, along with the coax adapter and rectangular to circular adapter is shown in Figure 3.10. The S_{11} and the far field pattern measurements of the optimized horn was carried out to

validate our horn design. The measured S_{11} of the horn is shown in Figure 3.11. As desired, an S_{11} under -20dB is seen at 35.75GHz. In order to accurately measure the radiation patterns of the optimized horn, the table-top near field bipolar planar measurement chamber developed at UCLA [135, 136] was used. This technique involves measuring the near field data on a grid of concentric rings, with data points sampled along circular arcs. A major advantage of this technique is all major mechanical motions are rotational in nature, ensuring minimal cable bending. This results in stable RF measurements, especially phase. After the near field measurement, the data must be post processed to compute the far fields. First, the data measured in the bipolar grid is interpolated to a uniform rectangular grid using Optimal Sampling Interpolation (OSI). This interpolated data is then Fourier transformed to get the far field. An overview of the measurement process is shown in Figure 3.12. Alignment of the chamber is critical for mm-Wave frequency measurements since positioning tolerances are strict. To ensure proper alignment, customized brackets for the optimized horn were built using 3D printing.

The measurement setup is shown in Figure 3.13. The probe is positioned at a distance of 5.24λ above the aperture of the horn. The scan plane size (15.68λ diameter) is governed by the valid angle, chosen to be 70° . Figure 3.14 shows the measured near field data after OSI. A comparison between the measured and the simulated far field radiation patterns in the principal planes are shown in Figure 3.15. It can be seen that both measured and simulated results agree well within the 10dB taper region. Further, the measured results show low sidelobe and cross polarization levels as predicted by the simulation.

An important consideration for reflector antenna gain is the backlobe of the horn. Since the near field technique is only valid in the forward direction, it does not inherently account for backlobes. This issue is comprehensively discussed in [137], where methodologies to estimate the losses due to spillover caused by the backlobes of the horn are discussed.

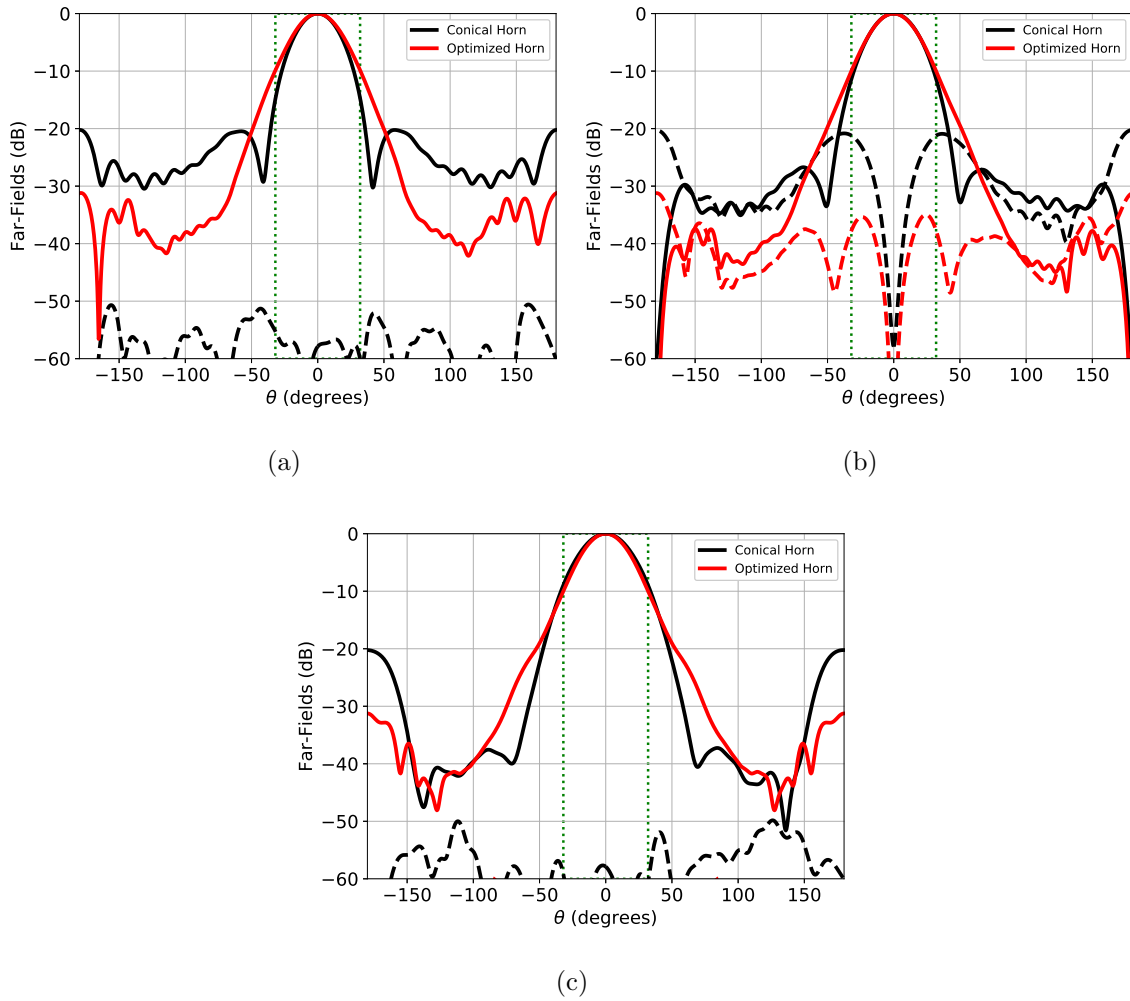


Figure 3.6: Far field radiation patterns of the optimized horn feed compared to a standard conical horn at 35.75 GHz. (a) E-plane pattern (b) D-plane pattern (c) H-plane pattern. Note the significant performance improvement of the optimized horn. The solid lines and dotted lines denote copol and xpolar respectively.

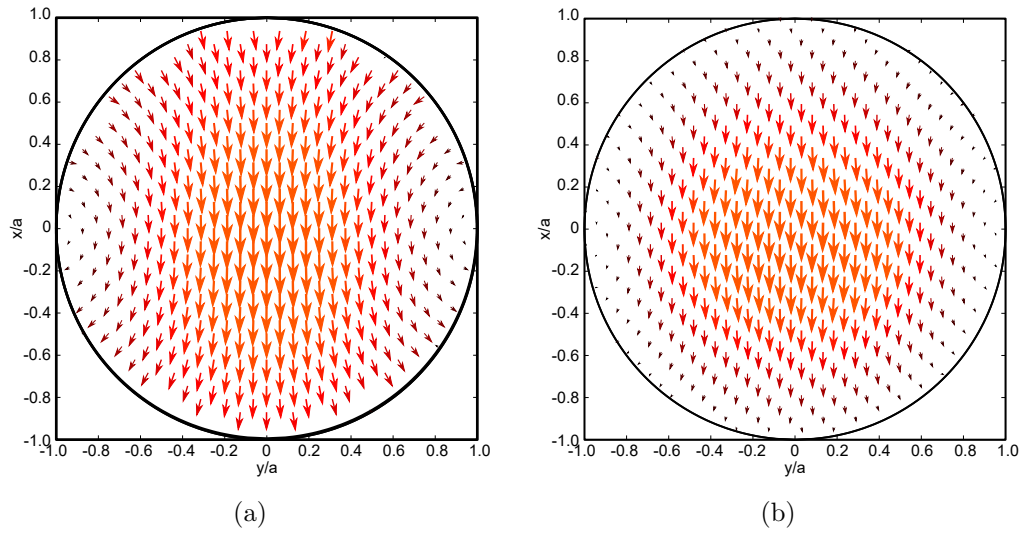


Figure 3.7: Electric field aperture distributions of (a) conical horn and (b) optimized horn. Note the reduced curvature of the field lines towards the edge of the aperture for the optimized horn.

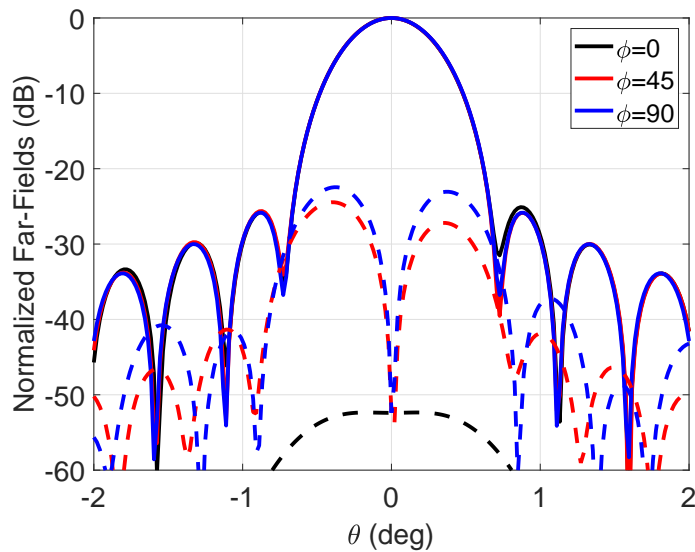


Figure 3.8: Far field reflector patterns with the simulated patterns of the optimized horn at 35.75GHz. Solid and dotted lines represent copol and xpol respectively (peak directivity=50.21 dB).

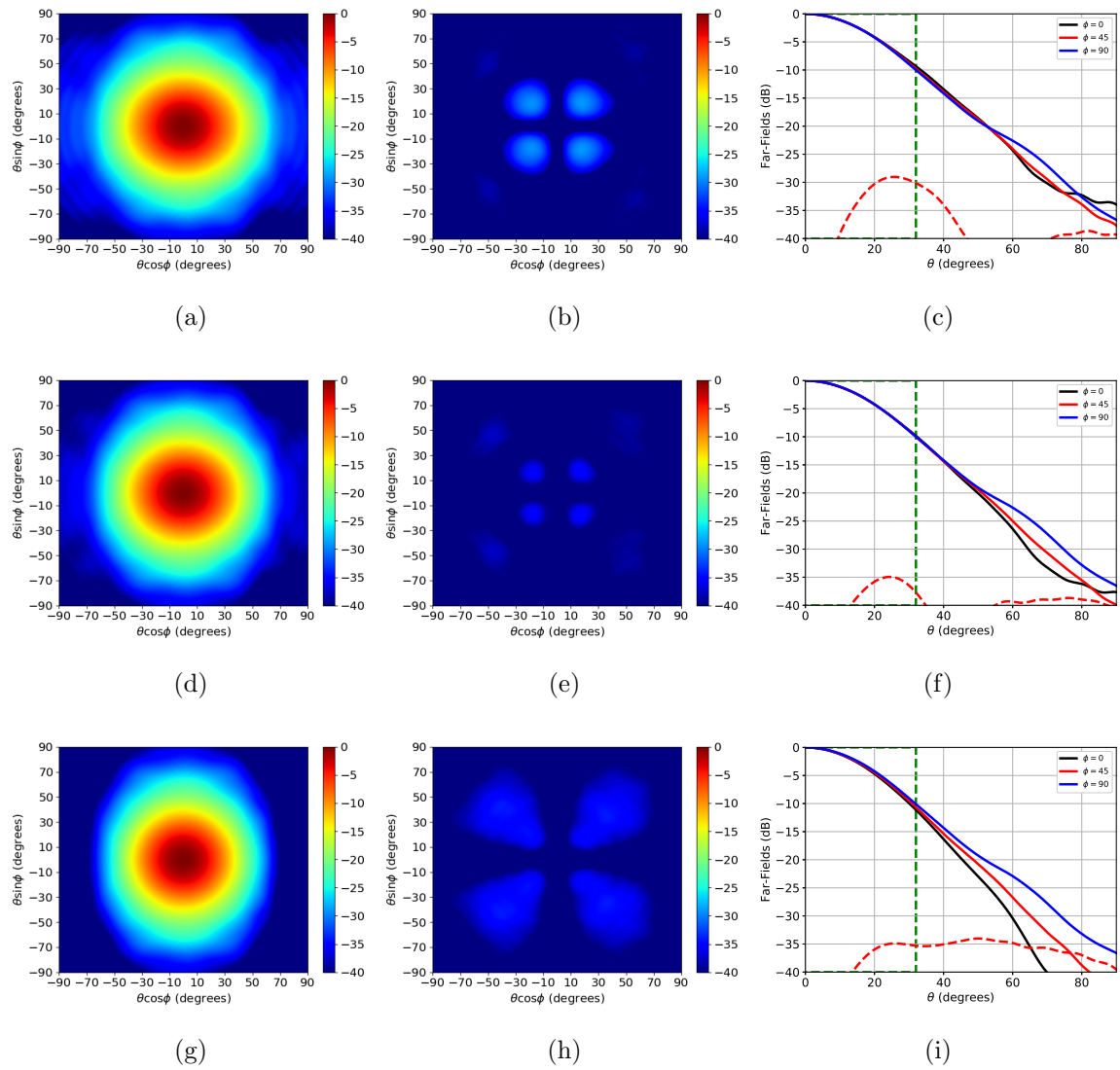


Figure 3.9: Simulated far-field patterns for the optimized spline profiled horn for RainCube at different frequencies. (a) Normalized copol patterns (in dB) at 35.5 GHz. (b) Normalized xpol patterns (in dB) at 35.5 GHz and (c) E, D and H-plane patterns at 35.5 GHz. (d), (e) and (f) similarly represent patterns at 35.75 GHz (design frequency) and (g), (h) and (i) represent patterns at 36 GHz. The dotted lines indicate the subtended angle over which 10 dB taper is desired. Note the stable performance of the horn.



Figure 3.10: Optimized horn along with the rectangular to circular adapter and the coax adapter. The horn has a profile of length 48.2mm (5.74λ) and an exit aperture diameter of 19.6mm (2.33λ).

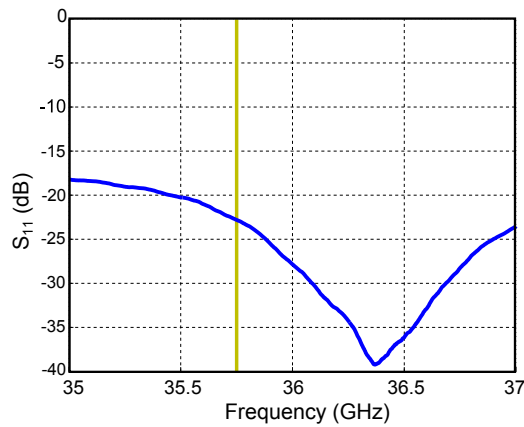


Figure 3.11: Measured reflection performance of the fabricated horn antenna assembly.

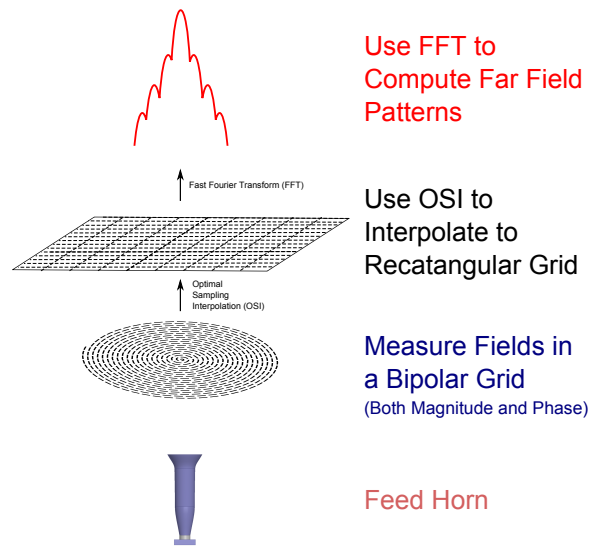


Figure 3.12: An overview of the bipolar planar measurement process.

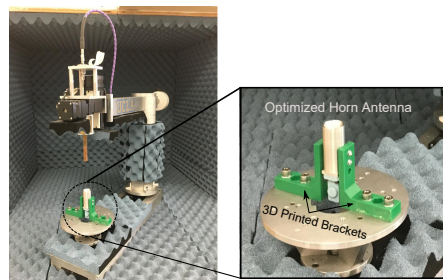


Figure 3.13: Measurement of the fabricated horn at 35.75 GHz using UCLA’s tabletop planar bipolar near field chamber. 3-D printing was used to manufacture customized brackets for alignment. Note that the brackets and the base plate were covered with absorbers during actual measurement.

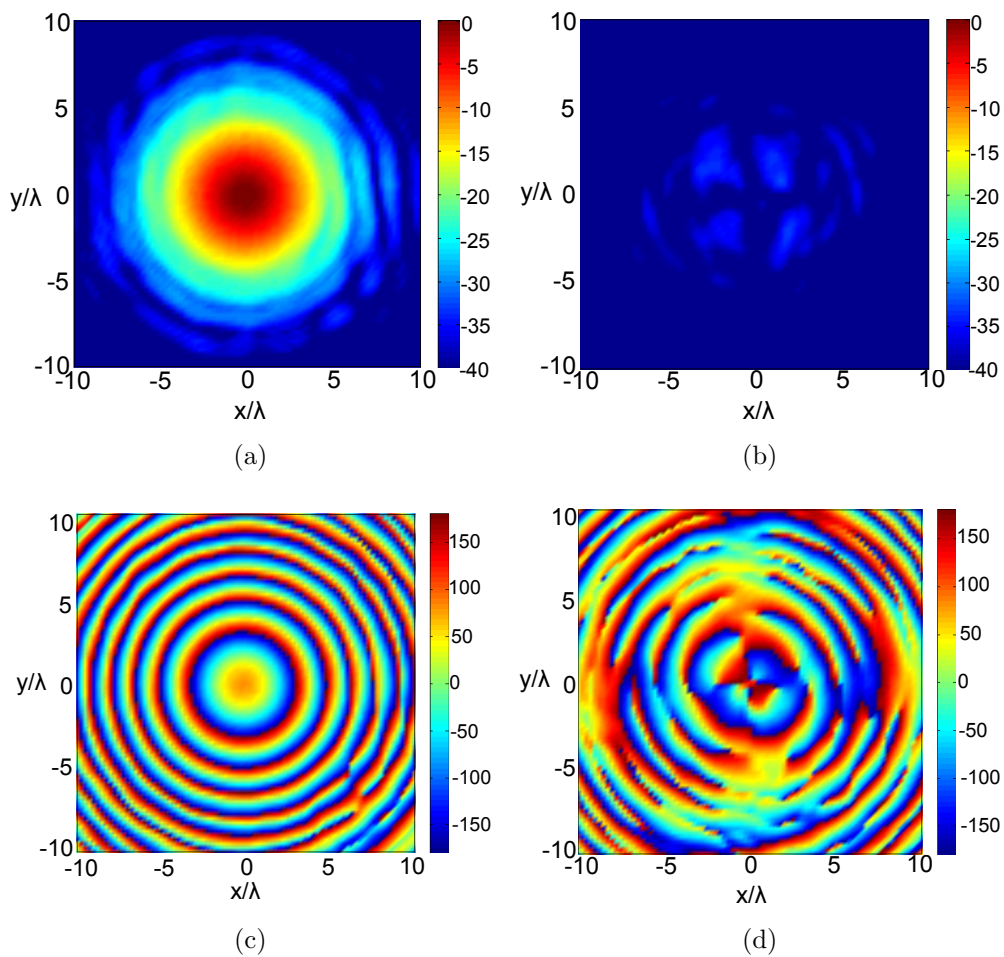


Figure 3.14: Measured near field aperture distributions after OSI interpolation at 35.75 GHz (a) Normalized copol amplitude distribution (in dB) (b) Normalized xpol amplitude distribution (in dB) (c) Copol phase distribution (in degrees) (d) Xpol phase distribution (in degrees).

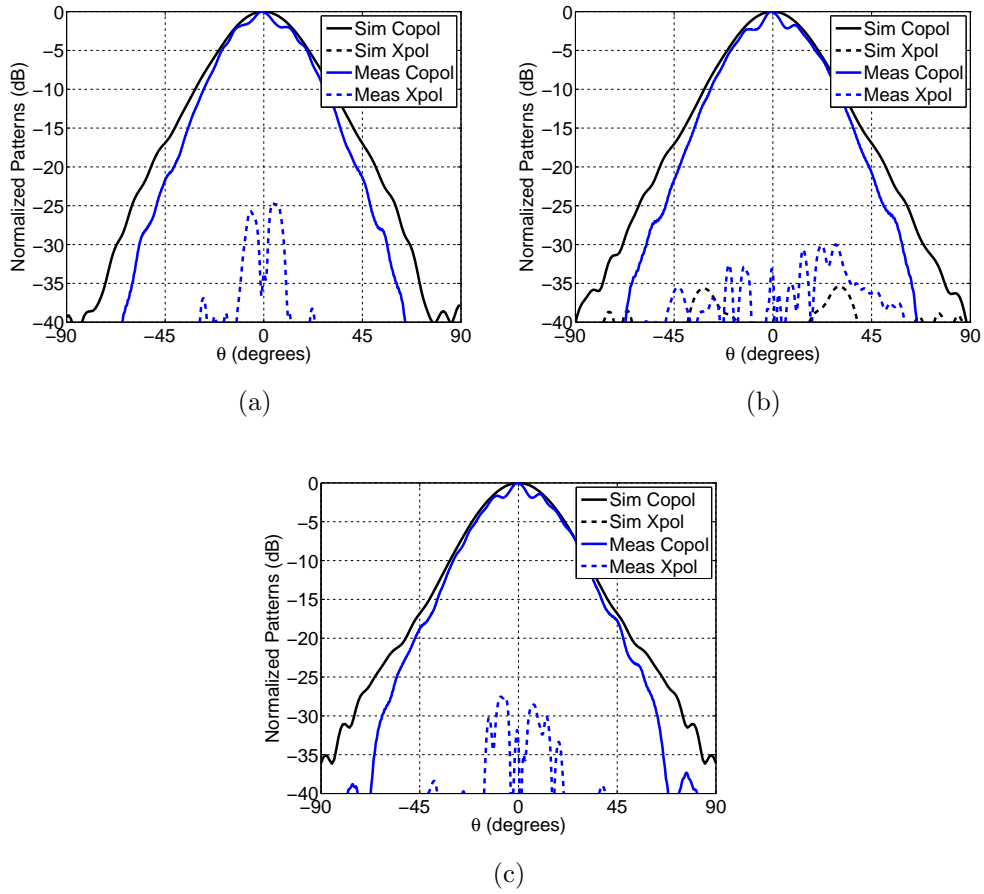


Figure 3.15: Comparison between measured and simulated far field pattern for the optimized horn at 35.75 GHz (a) E-plane pattern (b) D-plane pattern (c) H-plane pattern. The valid angle for the measurement is chosen to be 70° .

3.4 RainCube Reflector Characterizations

3.4.1 Mesh Characterization

To facilitate deployment and reduce weight, the RainCube 1m reflector design uses a knitted mesh surface. The mesh openings, however, cause transmission loss, resulting in reduced antenna gain. This is a critical consideration for CubeSats since power on board is limited. Further, the transmission losses at mm-Wave frequencies can be significant even for a tightly knit mesh. Mesh opening size is typically described in terms of the *Openings per Inch* (OPI). As the OPI increases, the mesh becomes denser, reducing transmission loss but increasing the mechanical complexity and weight. In general, the knit structure can be very complex (as visualized in Figure 3.17a), making direct full wave simulations unrealistic. Our aim within this project was to generate a simple equivalent model that can be easily analyzed and integrated with full wave solvers.

The analytical solution to the transmission coefficients of a simple wire grid model is known through the formulations by [138] (equations (3.8)-(3.18)). The reference coordinate system is given in Figure 3.16.

$$T_{TE-TE} = 1 - k_0 I_0^{-1} [\cos \theta_i + k_0 [\gamma_1 \cos^2 \phi_i + (\delta_2 - \delta_1) \sin \phi_i \cos \phi_i - \gamma_2 \sin^2 \phi_i]] \quad (3.8)$$

$$T_{TM-TE} = -k_0^2 \cos \theta_i I_0^{-1} [\delta_1 \sin^2 \phi_i - (\gamma_1 + \gamma_2) \sin \phi_i \cos \phi_i + \delta_2 \cos^2 \phi_i] \quad (3.9)$$

$$T_{TE-TM} = k_0^2 \cos \theta_i I_0^{-1} [\delta_1 \cos^2 \phi_i + (\gamma_1 + \gamma_2) \sin \phi_i \cos \phi_i + \delta_2 \sin^2 \phi_i] \quad (3.10)$$

$$T_{TM-TM} = 1 - k_0 \cos \theta_i I_0^{-1} (1 - k_0 \cos \theta_i [\gamma_2 \cos^2 \phi_i + (\delta_2 - \delta_1) \sin \phi_i \cos \phi_i - \gamma_1 \sin^2 \phi_i]) \quad (3.11)$$

$$\frac{I_0}{k_0} = \cos \theta_i (1 + k^2 \delta_1 \delta_2 - k_0^2 \gamma_1 \gamma_2) + k_0 \sin^2 \theta_i [\gamma_2 \cos^2 \phi_i + (\delta_2 - \delta_1) \sin \phi_i \cos \phi_i - \gamma_1 \sin^2 \phi_i] + k_0 (\gamma_1 - \gamma_2) \quad (3.12)$$

where

$$\alpha_1 = \frac{jb}{\pi} \ln \frac{b}{2\pi r_0} \quad (3.13)$$

$$\alpha_2 = \frac{ja}{\pi} \ln \frac{a}{2\pi r_0} \quad (3.14)$$

$$\gamma_1 = \alpha_1 \left[1 - \frac{\frac{a}{b}}{1 + \frac{a}{b}} \sin^2 \theta_i \cos^2 \phi_i \right] \quad (3.15)$$

$$\gamma_2 = -\alpha_2 \left[1 - \frac{\frac{b}{a}}{1 + \frac{b}{a}} \sin^2 \theta_i \sin^2 \phi_i \right] \quad (3.16)$$

$$\delta_1 = \alpha_1 \frac{\frac{a}{b}}{1 + \frac{a}{b}} \sin^2 \theta_i \sin \phi_i \cos \phi_i \quad (3.17)$$

$$\delta_2 = -\alpha_2 \frac{\frac{b}{a}}{1 + \frac{b}{a}} \sin^2 \theta_i \sin \phi_i \cos \phi_i \quad (3.18)$$

A comparison of the analytical Astrakhan's formulation with full wave simulation was presented in [139]. While the simple-wire grid model is well understood, the link between the complex mesh and the equivalent Astrakhan wire grid remains to be defined.

A detailed investigation of the Astrakhan formulations [140] reveal a strong dependency of the mesh transmission loss on the diameter of the constituent wires. This implies that while generating the equivalent model of the complex mesh, the equivalent diameter that represents the complex knit surface must be carefully chosen. As a representative example, a complex tricot knit structure that was previously analyzed in [141] is considered. This structure was simulated using Floquet analysis through full wave simulators. The knit structure is shown in Figure 3.17a. The constituent wires of the mesh are assumed to be of 0.0008" diameter, consistent with [58]. The mesh is assumed to be PEC for simplicity.

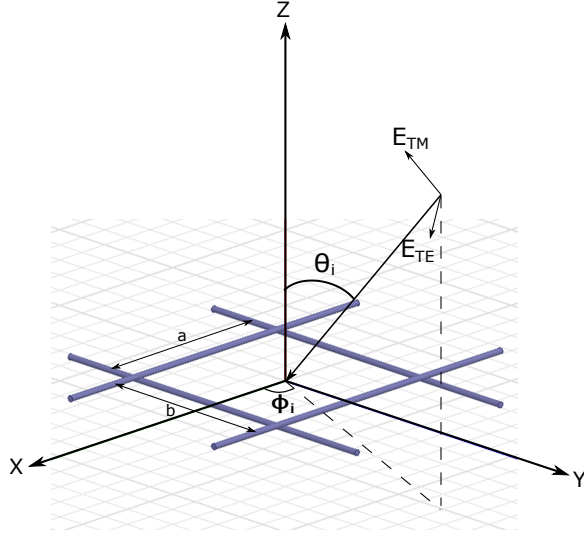


Figure 3.16: Simple wire-grid model analyzed by Astrakhan.

If the OPI is known, the critical step is to find the equivalent diameter. Dense meshes typically consist of intimate strands of wires that cross each other. These sections can be replaced by an equivalent strip since the spacing (in wavelengths) is small enough that the surface currents do not see the difference between the individual strands of wires and the thin strip. This leads to an equivalent strip model with a certain width W . Using this formation of the strip model, the wire grid model can be easily constructed using strip wire equivalence [140, 142]. For the knit geometry considered, the process is illustrated in Figure 3.17. The equivalent strip and wire grid model is illustrated in Figure 3.17b and 3.17c respectively. The performance comparison between the mesh loss for normal incidence for the complex knit (through full wave simulation) and the equivalent simple wire grid model (through analytical Astrakhan formulations) is shown in Table 3.4. The importance of choosing the right equivalent diameter can be clearly observed; if an equivalent wire grid model having the same diameter as the constituent wires is used, the difference between the simple model and the actual knit model is significant. Representative cases for oblique incidence for 20 and 40 OPI is shown in Figure 3.18. Note that TE and TM refers to electric field and magnetic field being oriented perpendicular to the plane of incidence, respectively. It is evident from the results that the accuracy of the equivalent model increases as the mesh gets denser, consistent with the previous hypothesis. In general, some knit

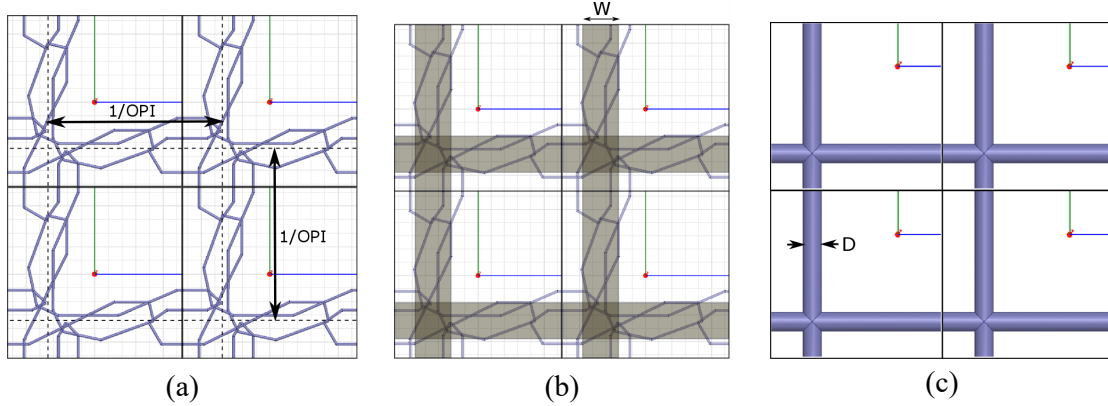


Figure 3.17: A representative complex triclot knit pattern utilized to construct mesh reflectors [141]. (a) Mesh structure. (b) Equivalent strip model with strip width W , scaled according to the OPI. (c) Equivalent wire grid model of wire diameter $D=W/2$.

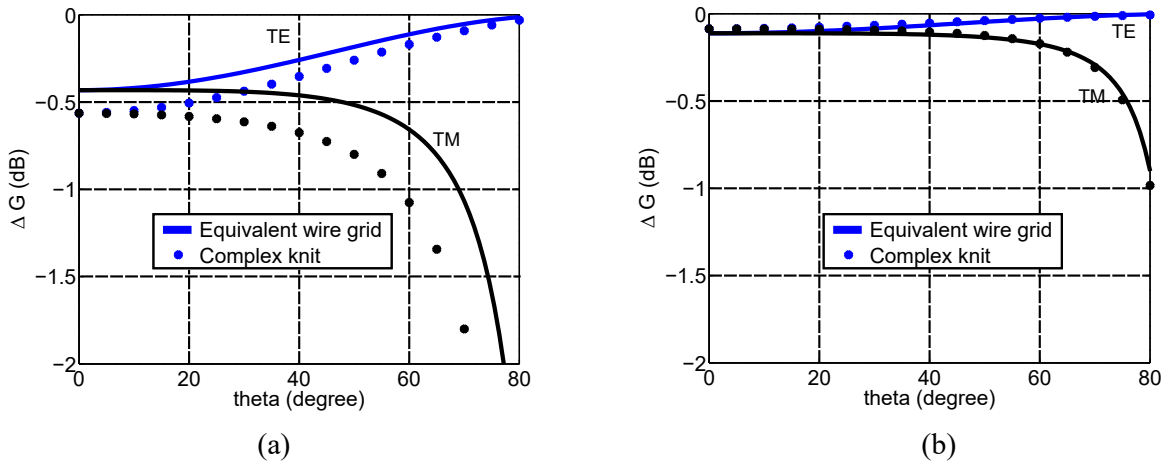


Figure 3.18: Comparisons between the gain loss (ΔG) of the complex knit mesh surface via full wave simulations and the equivalent wire grid model for oblique incidence ($\phi = 0^\circ$) using Astrakhan's formulations (a) 20 OPI. (b) 40 OPI.

structures could preclude the direct formation of the equivalent Astrakhan model. However, the methodology presented in this section can still be used as a tool to simplify complex knit structures to facilitate quick full wave simulation of complex knits. Thus, this section provided an analytical basis to simplify the analysis complex mesh surfaces, which is an important consideration for mesh reflectors.

Table 3.4: Comparison between full wave simulated tricot knit mesh and the analytical simple wire grid model for normal incidence ($\theta_i = \phi_i = 0^\circ$) at 35.75 GHz. The parameters D , W and OPI are as defined in Figure 3.17.

OPI	Gain Loss ΔG (dB)		
	Tricot Knit Mesh	Equivalent Wire Grid Model	
		$D_{eq} = D_{wire}$	$D_{eq} = W/2$
20	-0.56	-2.53	-0.43
30	-0.20	-1.01	-0.19
40	-0.09	-0.47	-0.11

3.4.1.1 Characterizing the RainCube Mesh

In this section, we use the foundations previously developed to characterize the mesh that was finally used for the RainCube 1m reflector surface. The geometry of the mesh is shown in Figure 3.19. This mesh provides an average of 30 OPI, with a wire diameter of 0.001” leading to potentially acceptable transmission losses at Ka-band. In order to evaluate the performance of this mesh, a simplified unit cell was created using EM simulation packages, as shown in Figure 3.20. For mesh reflectors, the strands of the mesh are tensioned to maintain the required profile. Since these strands can have multiple ways of crossing each other, the junction can be complex to model. Thus, we investigated two junction models. The first one (top figure in Figure 3.20) represents an ideal junction where all the strands are fused at the junction (we refer to this as ‘hard contact’), whereas the second model has a more practical junction, wherein the strands of the wire overlap each other at the junction (we refer to this as ‘soft contact’) [59]. Both these models were analyzed using the concept of periodic boundary conditions in conjunction with Finite Element Method (FEM). Based on the reflector geometry (shown in Figure 3.21), it is evident that the angle of incidence for the rays vary from $\theta_i = 5^\circ$ to $\theta_i = 37^\circ$. The mesh performance was thus evaluated at angle of incidences of $\theta_i = 0$, $\theta_i = 23^\circ$ and $\theta_i = 37^\circ$. We evaluate the performance for both TE and

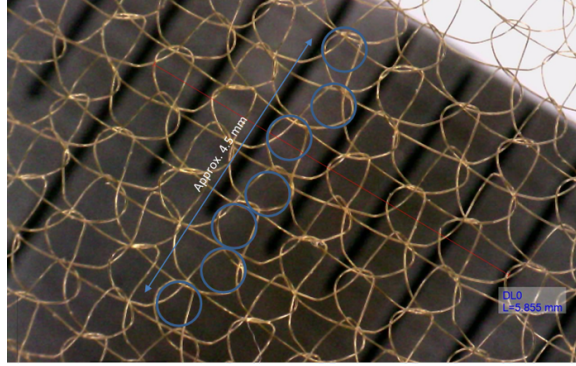


Figure 3.19: Photograph of the mesh used for the RainCube 1m antenna surface.

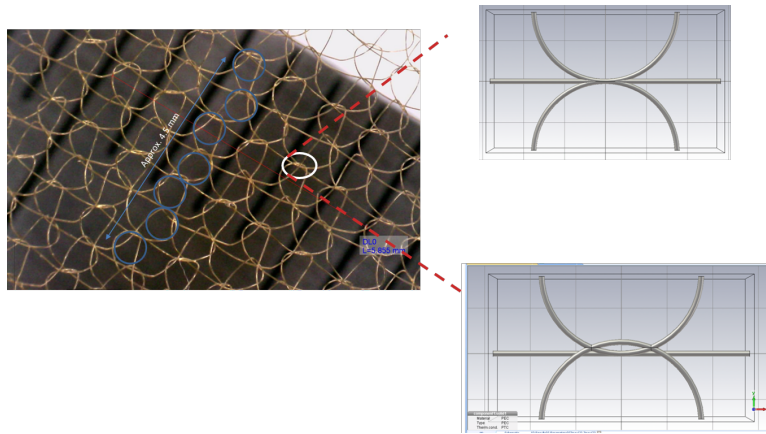


Figure 3.20: Modeling the complex mesh surface. We investigated two forms of contact: hard contact (top) and soft contact (bottom). The simplified unit cell was then analyzed using periodic boundary conditions.

TM polarizations. The results are tabulated in Tables 3.5 and 3.6. The simulations indicate that the mesh openings results in a loss of 0.3-0.4 dB, which is consistent with measurements of the mesh surface at JPL.

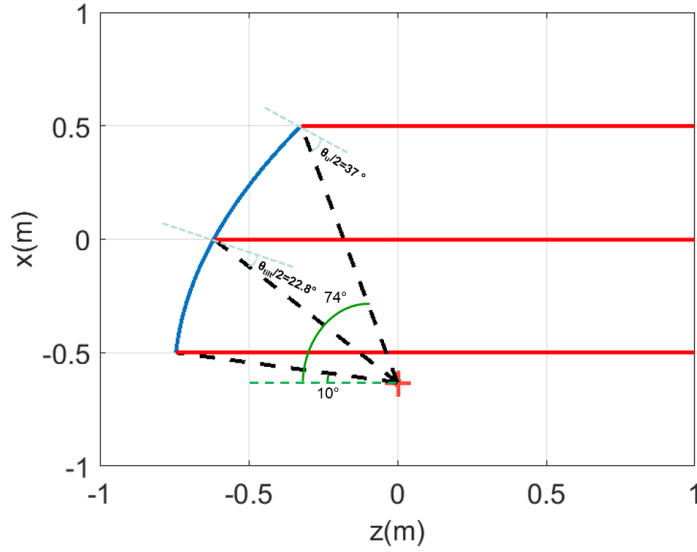


Figure 3.21: Important angle of incidences to be considered for evaluating mesh performance.

Table 3.5: Transmission loss (in dB) for the soft contact model at 35.75 GHz at representative angle of incidence.

$\theta=0^\circ$		$\theta=23^\circ$		$\theta=37^\circ$	
TE	TM	TE	TM	TE	TM
0.38	0.30	0.32	0.31	0.24	0.35

Table 3.6: Transmission loss (in dB) for the hard contact model at 35.75 GHz at representative angle of incidence.

$\theta=0^\circ$		$\theta=23^\circ$		$\theta=37^\circ$	
TE	TM	TE	TM	TE	TM
0.41	0.45	0.35	0.47	0.27	0.53

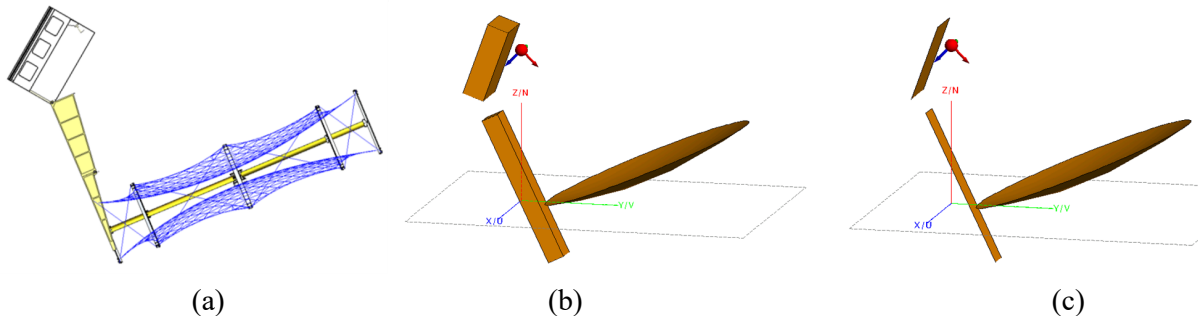


Figure 3.22: Simulation setup to model chassis integration. (a) Proposed CAD model. (b) Simulation setup to model the CubeSat chassis and the reflector support structure. (c) Simplified model viable for full wave simulation.

3.4.2 Chassis Characterization

The close proximity of the support structures with the radiating elements of the CubeSat system can affect the final reflector design performance. This makes characterizing the effects of the chassis interactions with the reflector system a critical design consideration. A significant challenge of mm-Wave frequency simulations for CubeSats is the large structure size in wavelengths. This section details the process by which the complex CAD was reasonably simplified to a model feasible for full wave simulation. The detailed CAD model of the reflector along with the chassis is shown in Figure 3.22a. Before attempting any simulation, the CAD model was simplified to make it feasible for full wave simulation. This simplification is done in two stages. First, the CAD model is simplified to model two major structures: CubeSat chassis and the reflector support structure as shown in Figure 3.22b. Second, any faces of the structure that are not directly lit by the feed pattern are removed, as shown in Figure 3.22c. The intuition behind this simplification is that the faces directly intercepting the feed radiation will dominate the changes to the radiation pattern. This setup can now be simulated within a reasonable timeframe. Since the feed pattern is much broader than the reflector pattern, the interaction of chassis with the feed will be much more pronounced than the interaction of the reflector pattern itself. This implies that the impact of the chassis interaction will be maximum on the field that illuminates the reflector. In order to assess the

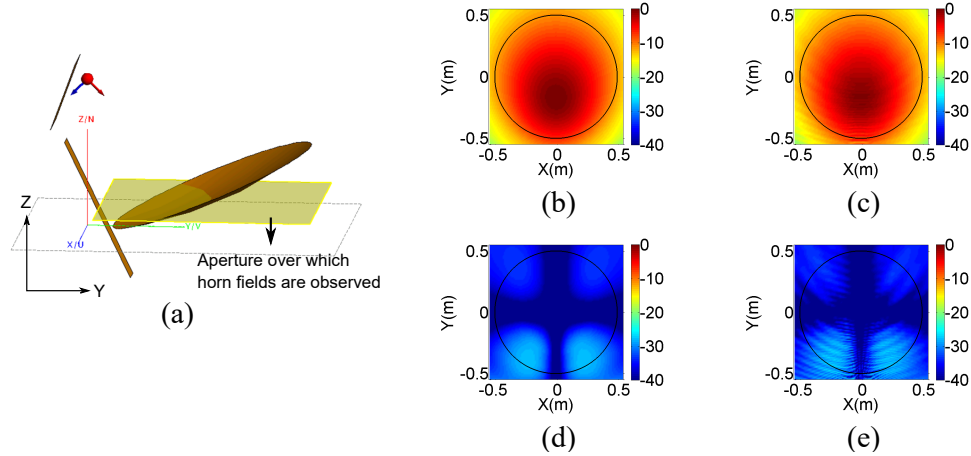


Figure 3.23: Impact of chassis interaction on the reflector illumination fields. (a) Simplified CAD model showing aperture on which the electric fields are observed. (b) Feed copolar field amplitude without chassis. (c) Feed copolar field amplitude with chassis interaction. (d) Feed cross polar field amplitude without chassis. (e) Feed cross polar field amplitude with chassis interaction.

distortion in the illuminating fields, the fields at a rectangular aperture that passes through the center of the projected aperture, as seen in Figure 3.23a, is observed. The results are shown in Figure 3.23b-3.23e. The chassis effects can be clearly seen in the form of small ripples in the distribution, and it stands to reason that the reflector pattern should be relatively unchanged in the main beam region, considering that the main beam of the feed pattern remains relatively unchanged. To verify our hypothesis, the feed+reflector system was integrated with a full wave electromagnetic simulation tool, as shown in Figure 3.24. The radiation pattern of the reflector when illuminated by the optimized horn with and without the chassis are compared in Figure 3.25. Minimal deviations are seen in regions away from boresight. It is evident that the chassis does not put any significant signature on the far field patterns and thus, the mechanical structure for the RainCube design was verified.

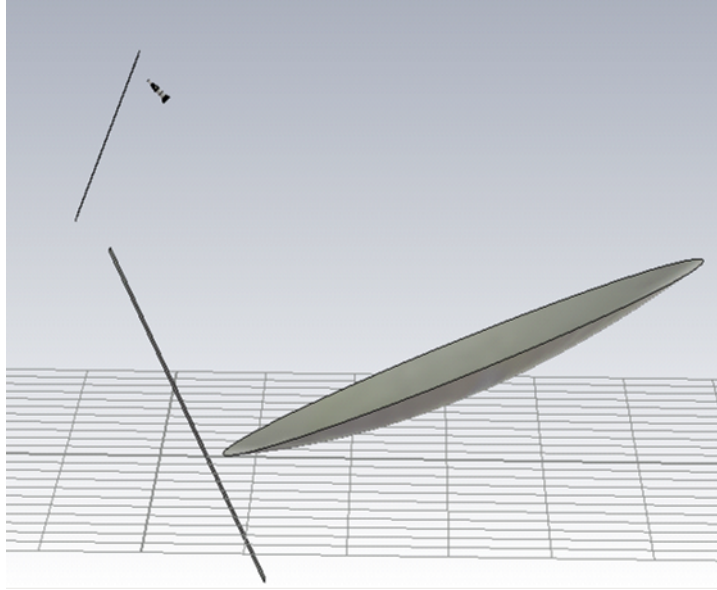


Figure 3.24: Simulation setup for characterizing the impact of chassis using full wave simulation.

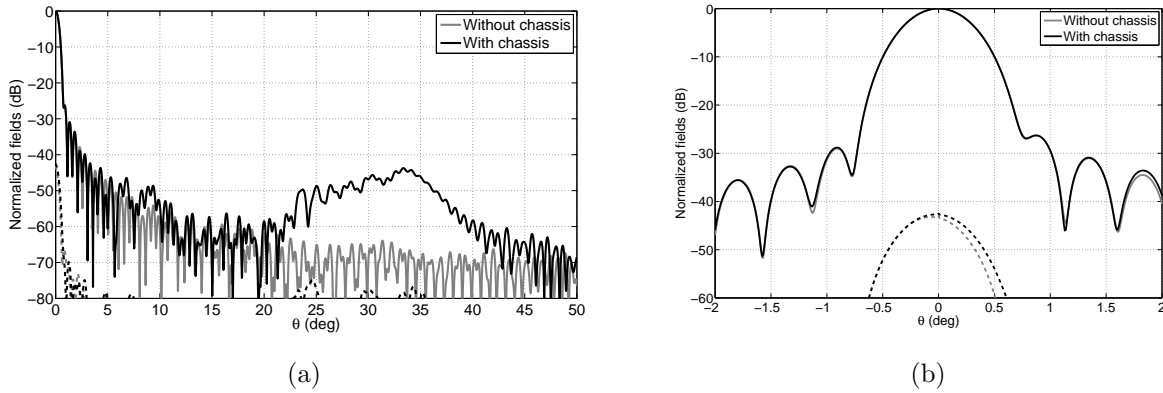


Figure 3.25: Representative E-Plane patterns showing the impact of chassis. (a) Wide angle far field patterns and (b) near boresight patterns. These results show the minimal impact of chassis.

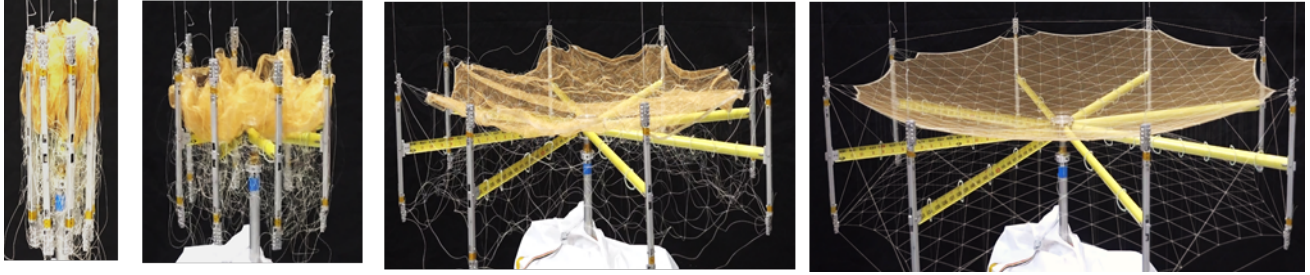


Figure 3.26: Prototype reflector using deployment testing [123].

3.5 Fabrication and Measurement of the RainCube 1m Reflector

The mesh reflector was fabricated by Tendeg LLC. The antenna surface consists of a mesh surface that is tensioned to achieve the required parabolic profile. The structure uses two opposing nets, which are supported by battens and ribs. The force reacted into each batten was balanced between the front and backside nets ensuring precision and repeatability. The reflector was put through multiple deployment cycles to ensure the reliability of the mechanical system. To confirm that the reflector surface maintains a reasonable RMS deviation after successive deployments, laser scanning of the surface was done, and a corresponding CAD model was created which could be incorporated into electromagnetic solvers for RF characterization. A representative diagram of the prototype reflector during deployment testing is shown in Figure 3.26. A detailed description of the fabrication process of the reflector surface is provided in [122]. After several iterations, the final fabricated reflector was mounted in the JPL Mesa near-field chamber [143] for radiation pattern and gain measurements. A comparison between the simulated and measured results are shown in Figure 3.27, where excellent agreements can be seen. The measured directivity was 49.95 dB. An important note here is that the near field measurement system only measures the pattern in the forward hemisphere ($0 \leq \theta \leq 90^\circ$), and thus the measured directivity is expected to be higher than the simulated directivity (which considers the radiation pattern over the complete sphere) [137]. The gain measurements are detailed in the subsequent section, which accounts for this ‘back’ radiation apart from other practical losses such as mesh loss and reflection loss. The measured half power beamwidth is 0.565° in the E-plane and 0.529° in the H-plane.

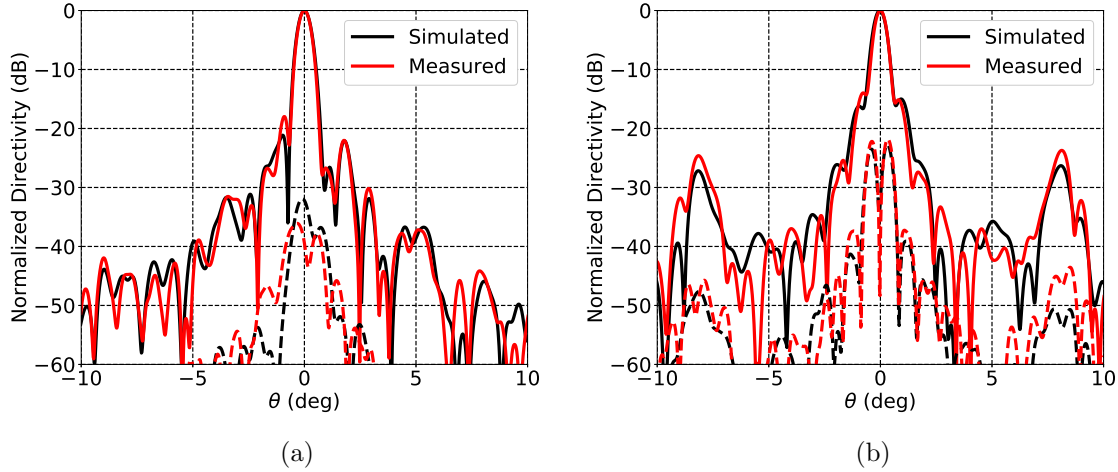


Figure 3.27: Comparison of the measured radiation patterns with simulated results when the feed is kept at the final optimized position at 35.75 GHz [122]. (a) E-Plane and (b) H-Plane.

Another critical parameter for antennas in radar and communication application is gain. The gain of an antenna finally determines how much power gets received by the receiver. Unlike the directivity, the gain includes all the loss sources that are present between the transmitter and receiver. A comparison between gain and directivity for different frequencies are shown in Figure 3.28. The predicted gain of 48.99 dB agrees well with the measured gain of 49.18 dB. The difference between prediction and measurement stems from uncertainties in measurement, and the fact that the simulation models used to predict the mesh transmission loss were simplified models suitable for full-wave simulation. This measured gain, which includes the spacecraft body panels, corresponds to an antenna efficiency of approximately 60%. It was found that the presence of the spacecraft body panels reduced the measured gain by about 0.05 dB, consistent with our simulated predictions. A detailed gain-loss table accounting for the various simulated losses is shown in Table 3.7 [122].

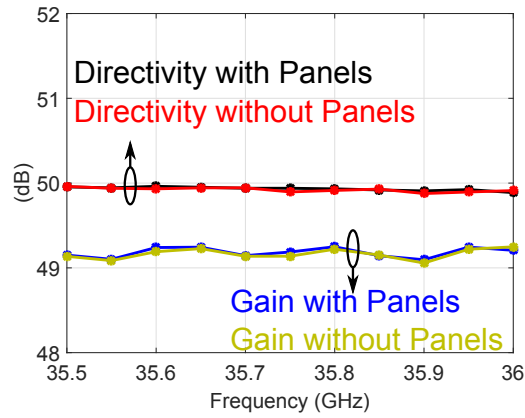


Figure 3.28: Measured directivity vs gain plot for the RainCube 1m reflector. The measurements were made with and without the support structures (side panels) to assess the impact of chassis. The reflector antenna achieved a gain of 49.18 dB at 35.75 GHz, which matched closely with simulated predictions [122].

Table 3.7: Gain-Loss table at 35.75 GHz based on simulations [122].

	Loss	Gain
Ideal Directivity	-	51.46 dB
Spillover+Taper	1.43 dB	50.03 dB
Surface	0.7 dB	49.33 dB
RMS		
Surface Mesh	0.3 dB	49.03 dB
Feed Mismatch	0.04 dB	48.99 dB
Total Gain (Simulated)	2.47 dB	48.99 dB

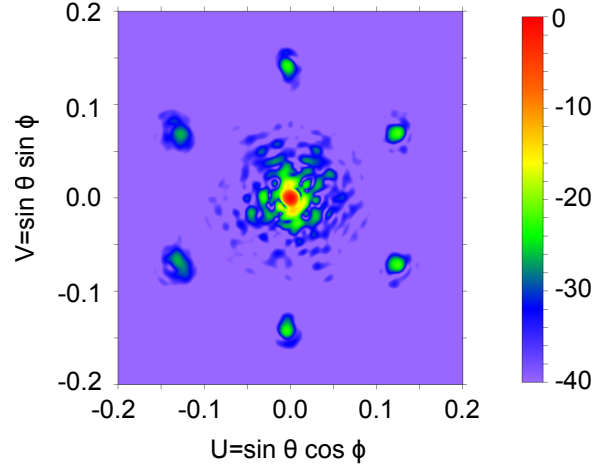


Figure 3.29: Measured 3D normalized copol far fields (in dB) of the RIC-6U mesh deployable reflector, that shows the appearance of multiple grating lobes [122].

3.6 Characterization and Reduction of Far-Field Grating Lobes

The previous sections detailed the measurement results of the 1m RIC-6U reflector, where excellent agreement between simulation and measured results were seen [122]. A detailed investigation of the measured far fields of the fabricated reflector revealed a set of six grating lobes as shown in Figure 3.29. In this section, we attempt to understand the appearance of these grating lobes and provide some potential techniques that can reduce the grating lobe levels.

3.6.1 Grating Lobe Appearance

Grating lobes are a manifestation of periodic variations in the aperture distributions of the antenna. If the length of the period is greater than a wavelength, the appearance of such grating lobes are expected. The smaller the period is, the farther the grating lobes occur, accompanied by a simultaneous reduction in their levels. For the RIC-6U mesh deployable reflector, the source of this periodic variation stems from periodic deviations of the reflector profile from an ideal paraboloid due to the tensioning of the mesh in between the support structure forming triangular facets. Typically, these facets are arranged to form hexagons in

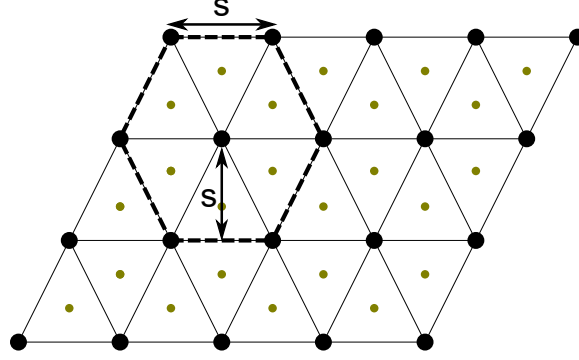


Figure 3.30: Construction of the hexagonal facets of the mesh.

the projected reflector aperture as shown in Figure 3.30. The vertices of each of the triangles are ‘pulled’ so that they lie on the true paraboloid. The triangular surface that connects these nodes, however, are planar in nature and thus deviate from the paraboloid. Since the majority of the triangles are identical in nature, and the curvature of the reflector is nominal, each triangle deviates almost identically from the reflector, and this leads to periodicity in the aperture of the reflector. The parameter s denotes the period of the deviations. As one can expect, the deviation of the triangles from an ideal paraboloid is maximum at the center and zero at the vertices, and thus distance between centers play a dominant role in the appearance of grating lobes. The geometry of the hexagonal faceting results in grating lobes in the planes corresponding to $\phi = 0^\circ, 30^\circ, 60^\circ, 90^\circ$ and so on. The value of elevation angle θ where the grating lobes appear depends on s and can be approximately found as [144]:

$$\sin \theta_g = 2 \frac{\lambda}{s} \text{ for } \phi = 0^\circ, 60^\circ, 120^\circ \text{ and so on} \quad (3.19)$$

$$\sin \theta_g = \frac{2\lambda}{\sqrt{3}s} \text{ for } \phi = 30^\circ, 90^\circ, 120^\circ \text{ and so on} \quad (3.20)$$

In order to model the RainCube 1m reflector surface, the value of s was chosen to be 8λ . This results in $\theta_g = 14.47^\circ$ for $\phi = 0^\circ, 60^\circ, 120^\circ$ and so on and $\theta_g = 8.29^\circ$ for $\phi = 30^\circ, 90^\circ, 120^\circ$ and so on. Since the grating lobes for $\phi = 30^\circ, 90^\circ, 120^\circ, ..$ are the nearest to the main beam, their levels are significantly higher. It is seen that these analytical results match the measured and simulated results presented previously.

In order to fully verify that it is indeed this hexagonal faceting that is causing these

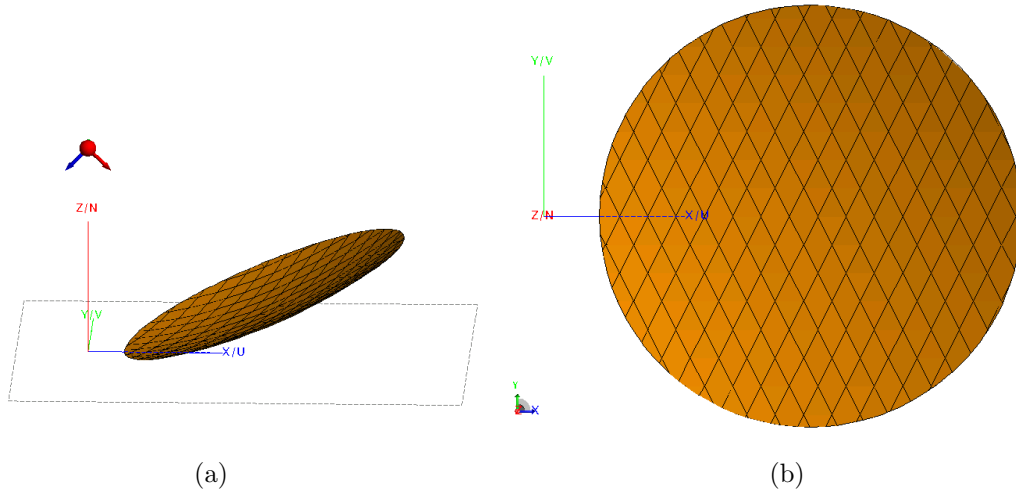


Figure 3.31: Reflector surface with hexagonal facets created by UCLA to study the appearance of grating lobes. (a) 3D view and (b) view in the aperture (XY) plane.

grating lobes to occur, computer codes were created that could create an STL file that generates a reflector surface with hexagonal facets similar to the one illustrated in Figure 3.30. The generated reflector is shown in Figure 3.31. This surface is then illuminated by a cosine- q feed to provide a 10dB taper at the edge of the reflector. The corresponding 3D far fields are shown in Figure 3.32. Note that the grating lobes occurring due to this surface is very identical to those shown by the measured results of the RIC-6U reflector surface as shown in Figure 3.29. The near-field aperture distributions can be seen in Figure 3.33 which clearly shows the periodicity in the amplitude distribution. This completely validates our hypothesis that the grating lobes are indeed a manifestation of the periodic deviations of the reflector surface from an ideal paraboloid.

3.6.2 Reduction of Grating Lobes

Now that it has been proved that the periodicity of the deviation of the reflector is the cause of the grating lobes, it is reasonable to expect that introducing a certain amount of randomness in the error distribution can bring the level of the grating lobes down. To prove this, we use a phyllotactic distribution of points in the aperture that are defined by the

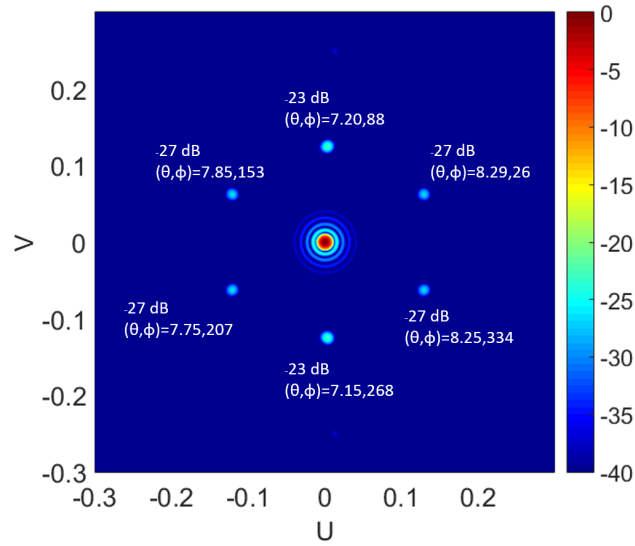


Figure 3.32: 3D far fields (copol component, in dB) of the reflector surface with hexagonal facets shown in Figure 3.31. The approximate location and level of the grating lobe is also illustrated. Note that the grating lobes show similar features to that of the RIC-6U surface (Figure 3.29).

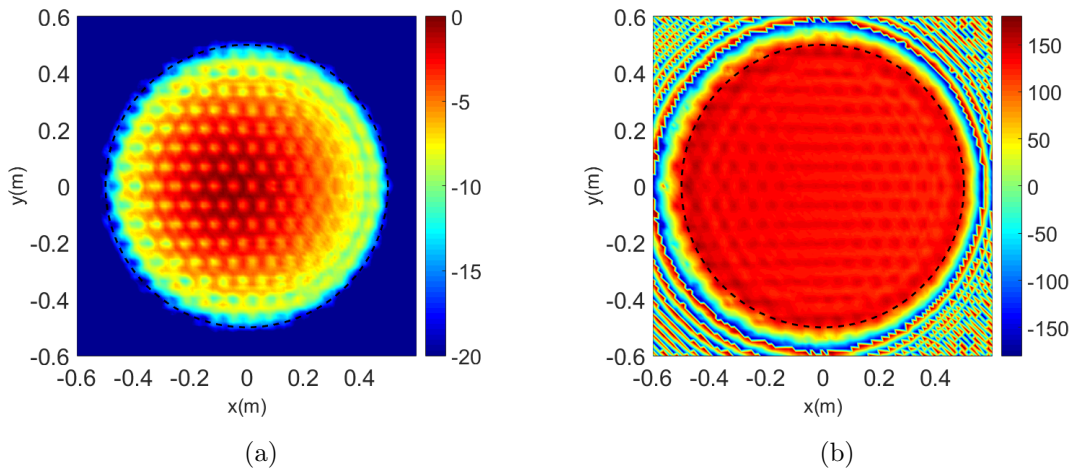


Figure 3.33: Near field distribution of the CAD reflector surface with a hexagonal distribution of the facets. (a) Amplitude distribution (in dB) and (b) phase distribution (in degrees).

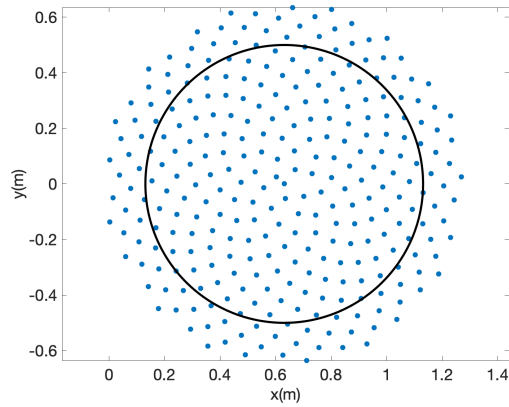
following equations [145]:

$$x_k = R\sqrt{\frac{k}{N-1}} \cos\left(\frac{\pi k}{\psi_{fib}}\right) + C_x \quad (3.21)$$

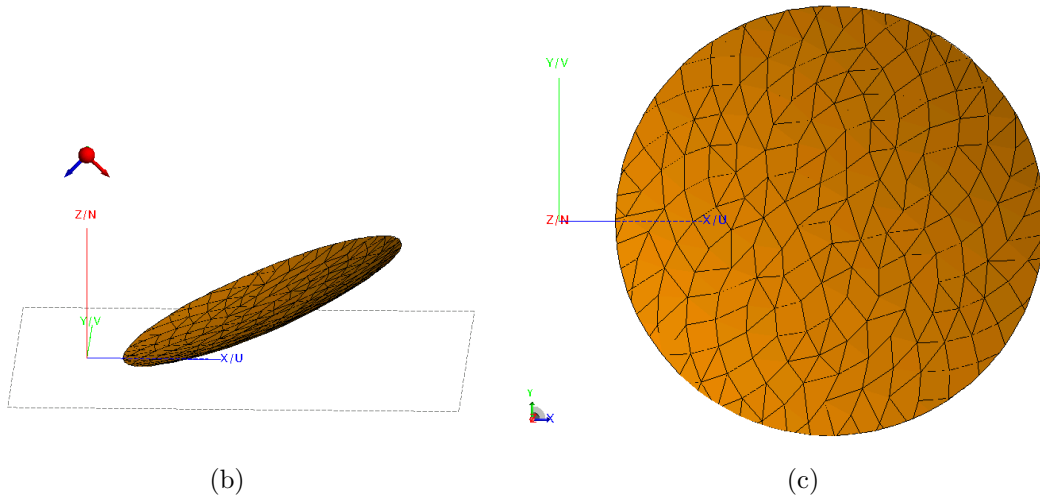
$$y_k = R\sqrt{\frac{k}{N-1}} \sin\left(\frac{\pi k}{\psi_{fib}}\right) + C_y \quad (3.22)$$

$$z_k = \frac{x_k^2 + y_k^2}{4F} \quad (3.23)$$

where N denotes the total number of points, $k = 0, 1, 2, \dots, N-1$, R denotes the radius of the reflector aperture and $\psi_{phyll} = \left(\frac{1+\sqrt{5}}{2}\right)^2$. The parameters C_x , C_y and F denote the offset of the aperture in the x and y directions and the focal length respectively. The distribution of the points is illustrated in Figure 3.34a. Once these points are obtained, a Delaunay triangulation is applied to generate the CAD model of the reflector surface [146]. In order to build an equivalent case to compare with the hexagonal mesh, $N = 300$ was chosen to generate the CAD surface as shown in Figure 3.34. The average length of the triangles for both the hexagonal and the phyllotactic mesh are kept almost identical (approximately 8λ in the aperture). An insight into the reason why this randomness reduces the grating lobes drastically can be got if the near field aperture distributions of this arrangement (shown in Figure 3.35) is compared with the aperture distributions of the hexagonally faceted reflector surface (shown in Figure 3.33). It is immediately obvious that the phyllotactic arrangement introduces enough randomness that the notion of the periodicity is lost, thus reducing the grating lobes. The corresponding 3D far fields are shown in Figure 3.36 where it can be clearly seen that the far-fields no longer show the discrete spots, but are more ‘spread’ so that its energy gets more distributed. This reduces the grating lobes by more than 15 dB in the planes that the hexagonal faceting showed grating lobes, at the cost of a marginal increase in the overall sidelobe envelope. Representative line cuts of the far field that illustrate the comparison of the performance of the hexagonal mesh with the phyllotactic arrangement is shown in Figure 3.37. An interesting observation is that the phyllotactic facets tend to show some signature of ‘lobes’ in planes that the hexagonal facets did not. However, the overall levels are much lower, and thus satisfies the sidelobe envelope constraints. The



(a)



(b)

(c)

Figure 3.34: Reflector surface with phyllotactic facets created by UCLA to study the appearance of grating lobes. (a) Distribution of points on the aperture. (b) 3D view and (b) view in the aperture (XY) plane for the constructed CAD model by Delaunay triangulation.

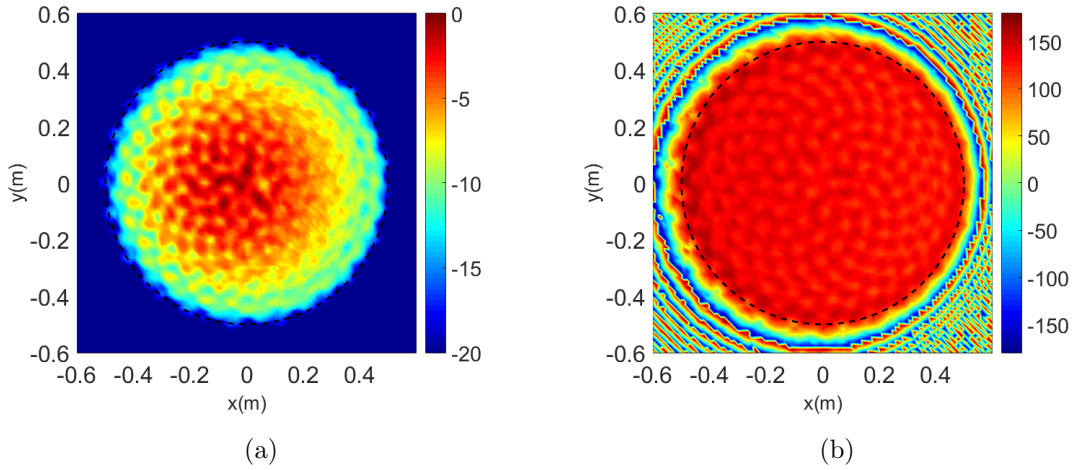


Figure 3.35: Near field distribution of the CAD reflector surface with a phyllotactic distribution of the facets. (a) amplitude distribution (in dB) and (b) phase distribution (in degrees).

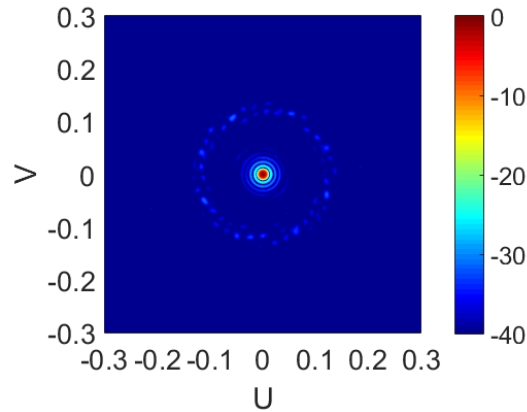


Figure 3.36: 3D far fields (copolarized component, in dB) of the reflector surface with phyllotactic facets as shown in Figure 3.34. Note that compared to the hexagonal facets (Figure 3.32), the grating lobes almost disappear and a marginally high sidelobe envelope is seen.

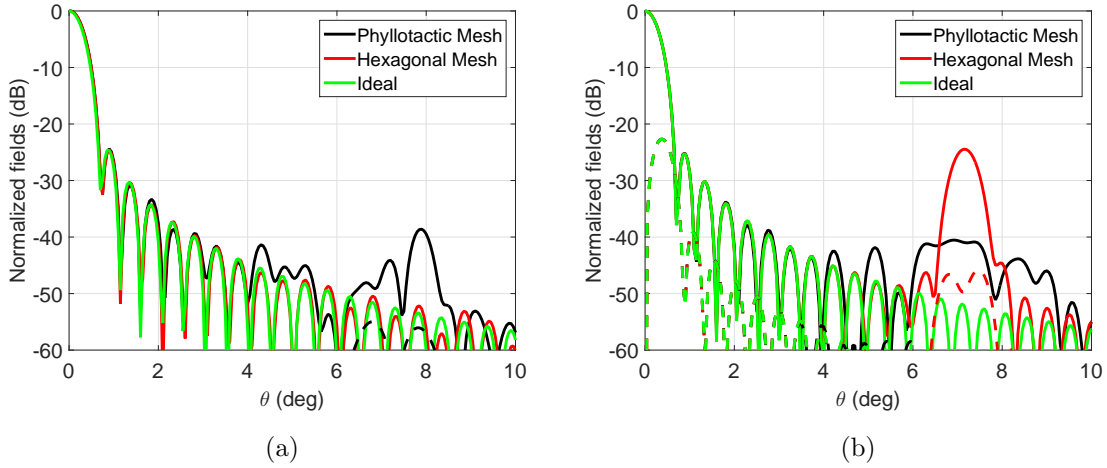


Figure 3.37: Far field comparison in various planes between the hexagonal faceting and the phyllotactic arrangement of the facets. (a) $\phi=0^\circ$ plane, (b) $\phi=90^\circ$ plane. Note the drastic reduction in grating lobe in the $\phi=90^\circ$ plane. The solid lines denote copol and the dotted lines denote cross-pol. The directivity for the ideal reflector is 50.47 dB. The hexagonal and phyllotactic faceting results in directivities of 50.37 dB and 50.33 dB respectively.

directivities and the beamwidths are compared in Table 3.8, where it can be seen that the phyllotactic arrangement has minimal impact on the boresight directivity and half power beamwidths. While these results are encouraging, the feasibility of practically implementing such an arrangement remains to be investigated. If required, the faceting algorithm can be paired with an optimization engine to achieve the desired faceting for the required sidelobe envelope [144, 147].

Table 3.8: Comparison of directivity and beamwidths for various kinds of faceting

	Phyllotactic Mesh	Hex Mesh	Ideal
Directivity (dB)	50.33	50.37	50.47
HPBW ($\phi=0^\circ$)	0.56°	0.56°	0.55°
HPBW ($\phi=30^\circ$)	0.56°	0.56°	0.56°
HPBW ($\phi=90^\circ$)	0.56°	0.56°	0.56°

3.7 Reduction of Linear Cross-Polarization for Offset Reflectors

While offset reflectors simplify deployment and result in compact geometries compared to symmetric reflectors, the asymmetry in the structure causes a high level of cross polarized fields in the plane perpendicular to the offset plane. This can also be seen in the simulated/measured results of the RainCube 1m reflector in Figure 3.27b. This can be a major consideration of remote sensing applications since the cross polarized fields can cause pollution of back-scattered data, or for communication applications since the cross polarized fields can reduce the boresight directivity of the system. Based on the research conducted for the RainCube 1m design, it is possible to develop a profiled horn so that it illuminates the reflector such that the reflector itself does not produce any cross polarized fields. In order to accomplish this, the profile of the horn is again discretized into three splines as was done in the previous case. However, an important difference in this design is that the horn must produce a cross polarization in one of its principal planes. This requires the generation of an additional TE_{21} mode within the geometry [148]. For details on the features of this mode, refer to Appendix C. The asymmetry of this mode requires some asymmetry in the physical cross-section of the horn. Thus, a screw was introduced as a part of the horn structure as seen in Figure 3.38. However, the inclusion of this screw can adversely impact the S_{11} of the horn, and thus an additional screw to tune the input impedance was incorporated. The screw diameters were chosen to be 1.85mm, which matches an ANSI 1-72 screw size.

Another significant difference between this horn and the previous horn for RainCube is the approach used for optimization. While the previously described horn optimizes its profile by considering the parameters of just the horn (for example, the S_{11} and horn far-field patterns), the approach for this horn involved a co-simulation of the feed and the reflector system. In other words, every run of the optimizer involved simulating the horn far-field patterns (with the desired profile and screw position chosen by the optimizer) and incorporating this into a PO based reflector simulation [149, 150]. The fitness function to be minimized was chosen to be:

$$f(\mathbf{x}) = S_{11} - 10D_0 + 3X_p \quad (3.24)$$

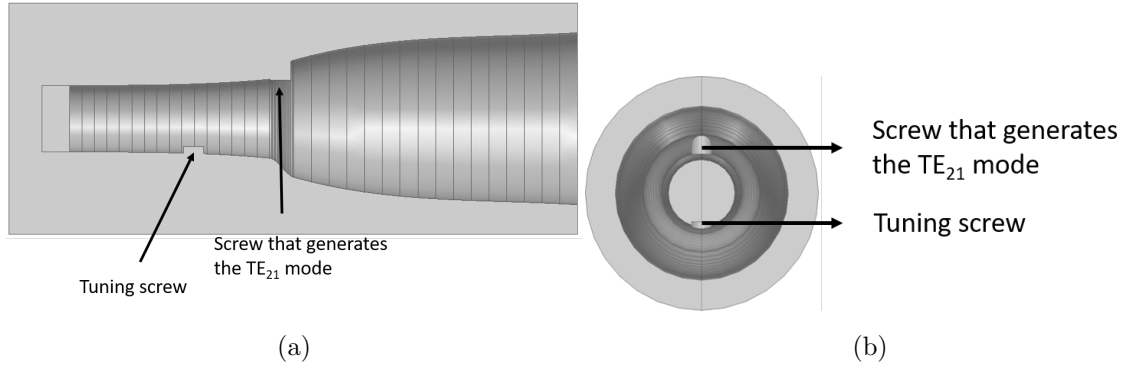


Figure 3.38: Horn geometry designed to reduce reflector xpol at 35.75 GHz. (a) Profile of the horn showing the location of the screws that generate the TE_{21} mode and tunes the input impedance of the horn and (b) view from the mouth of the horn.

where \mathbf{x} represents the vector of optimization variables (which include the start and end point of every spline and the position and depth of the two screws). D_0 is the boresight reflector directivity and X_p is the maximum reflector cross-pol found within the $\phi = 45^\circ$ and $\phi = 90^\circ$ planes. The final radiation patterns of the horn and reflector are shown in Figure 3.39. The simulated directivity of the reflector was 50.34 dB and the simulated S_{11} at 35.75 GHz was found to be -31 dB.

It is important to note the orientation of the horn relative to the reflector in Figure 3.39a. The screw position and depth was optimized so as to cancel out the reflector crosspol with the horn oriented such that the TE_{21} screw points towards the bottom edge of the reflector. If the horn gets rotated by 180° so that the screw now points towards the top edge of the reflector, the horn cross polarized can reinforce the cross polarized fields of the reflector resulting in a higher crosspol compared to a conventional cosine-q feed as shown in Figure 3.40.

3.7.0.1 Tolerance Studies

Since the basis of the horn design to reduce reflector crosspolarization is the cancellation of the reflector crosspolarized fields with that of the horn, it can be surmised that the design can be rather sensitive to the depth of the TE_{21} screw (which essentially controls the magnitude of TE_{21} mode relative to the other modes). The impact of varying the distance of the

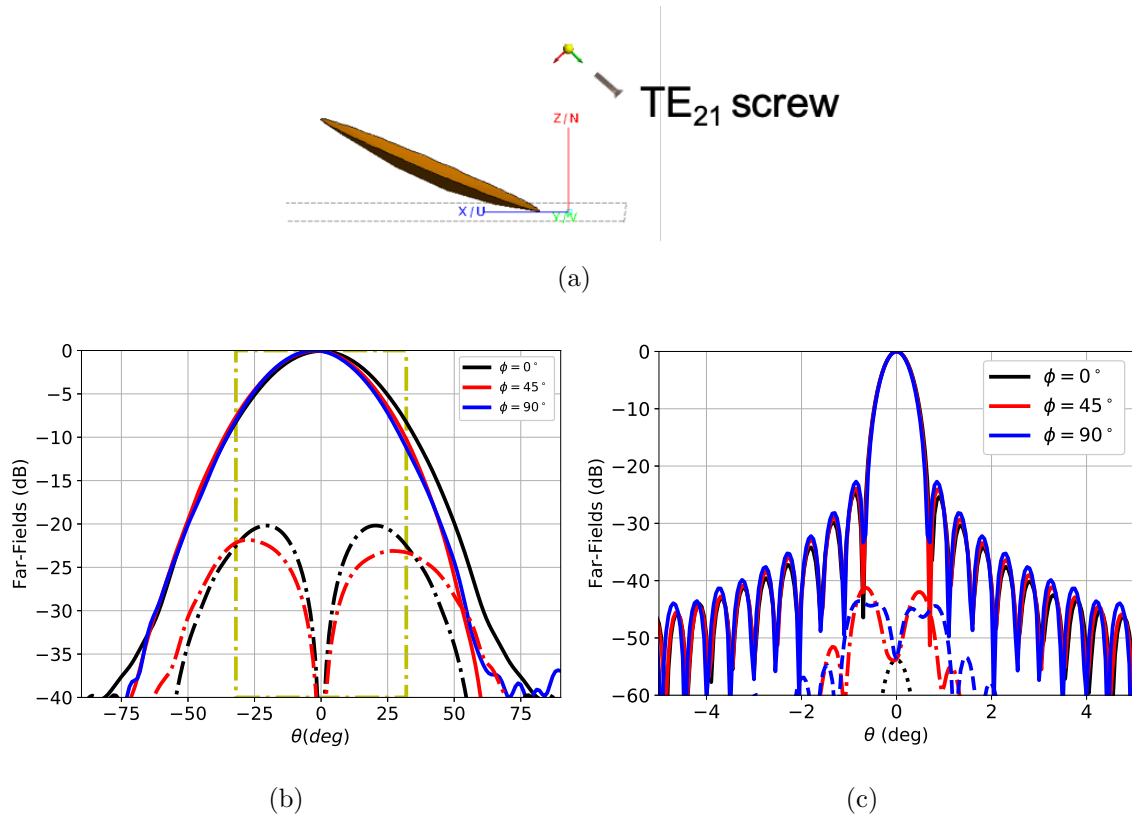


Figure 3.39: (a) Reference coordinate system chosen for the optimization routine. Note that the screw points towards the bottom edge of the reflector. (b) Final optimized far field patterns of the feed horn and (b) corresponding far-fields of the 1m RainCube reflector. Note the drastic reduction in the crosspolarization of the reflector compared to using a conventional feed (which is approximately 22 dB).

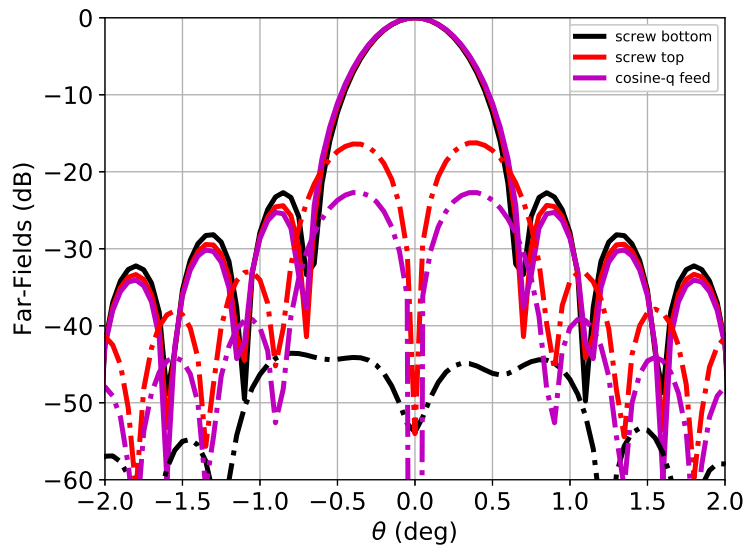


Figure 3.40: Comparison of reflector radiation patterns ($\phi = 90^\circ$ plane) when the horn is oriented in its optimal position (screw at bottom) with the case when the horn is rotated so that the screw faces the top edge of the reflector (screw at top) and a conventional cosine-q feed at 35.75 GHz.

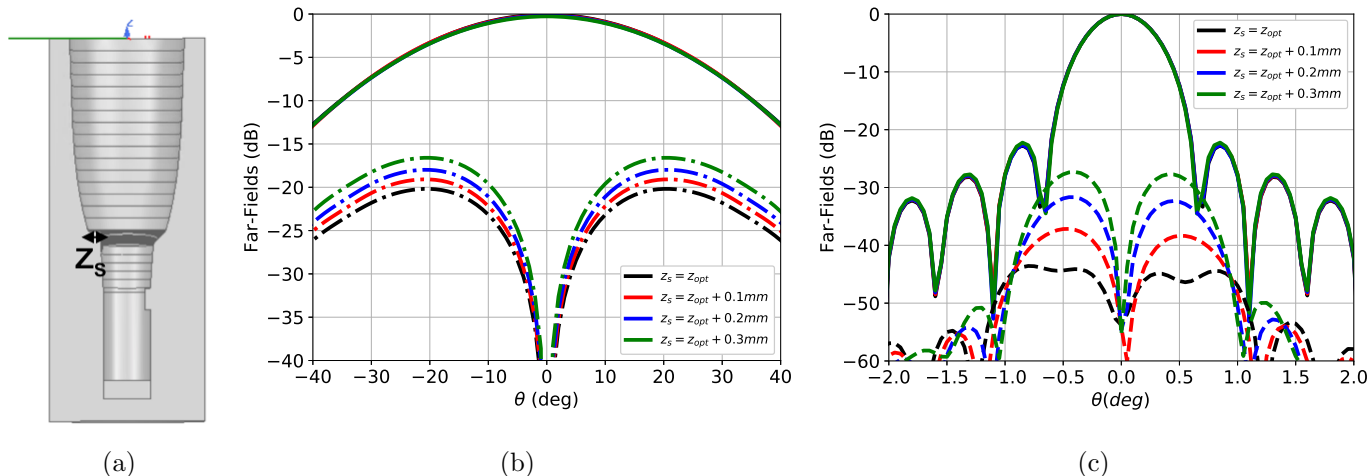


Figure 3.41: Sensitivity of the reflector cross polarized to variation in the screw distance z_s . (a) Feed geometry. (b) horn patterns and (c) reflector patterns as z_s increases.

screw (z_s) from its optimal position (z_{opt}) on the radiation pattern of the horn as well as the reflector antenna is shown in Figure 3.41. It can be observed that at 35.75 GHz, if the TE_{21} screw depth is increased by just 0.3mm, the cross polarization of the reflector increases by more than 15 dB making it comparable to the crosspolarization level seen when using a conventional horn design, even though the cross polarization level of the horn increases by only 4 dB. This makes the design very sensitive to fabrication errors and other errors that can arise while integrating the designed horn with the reflector antenna.

3.7.0.2 Fabrication and Measurement of the Horn

The advantage of the design philosophy described in this work is that the horn structure is still a body of revolution and thus can be manufactured using CNC lathe machines that can ensure the surface accuracy required for mmWave applications. The two screws (TE_{21} screw and the impedance tuning screw) are added through radial holes drilled after fabrication. The horn was fabricated by ProtoLabs, following which the screws were screwed in manually. However, it was extremely difficult to ensure that the depth of the screw was precise. The measured S_{11} of the horn is shown in Figure 3.42. The horn (along with the screws) was then mounted in the UCLA bipolar chamber (similar to the previously described horn).

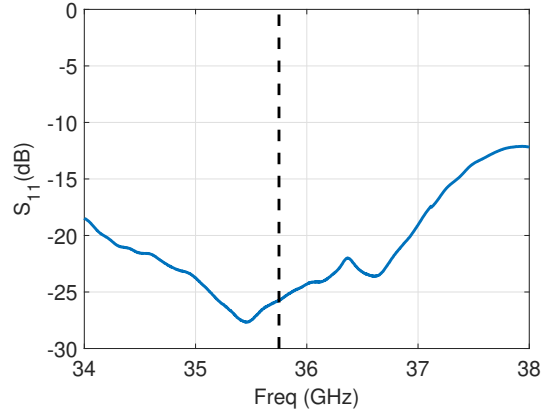


Figure 3.42: Measured S_{11} of the horn. The center frequency of 35.75 GHz is denoted by dotted lines.

The measured near-fields at distance of 5.24λ away from the mouth of the horn is shown in Figure 3.44. Note the appearance of the cross polarized fields in the horn pattern as expected. The far-field patterns are finally computed through the FFT of these measured near-fields and probe compensation. The measured and simulated far fields are compared in Figure 3.45. Note that the patterns agree reasonably well. However, the minor differences in the cross-polarized fields stemming from fabrication inaccuracies can potentially make cancelling the reflector cross-polarization difficult.

3.7.0.3 Measured Horn Patterns as Feed For Reflector

In this section, we integrate the *measured* far-field patterns from the previous section into the PO reflector analysis software and analyze its result. Figure 3.46a and 3.46b shows the radiation pattern when the measured radiation patterns are used for illumination compared to the conventional cosine-q feed. Both orientations of the horn are considered as was done in the previous study. It can be observed from these patterns that there is only a marginal reduction in the xpol level when the horn is positioned such that the screw faces the bottom edge, which is a result of the sensitivities of the cross pol cancellation to the depth of the screw. However, the fact that the cross pol increases beyond what is usually seen with a

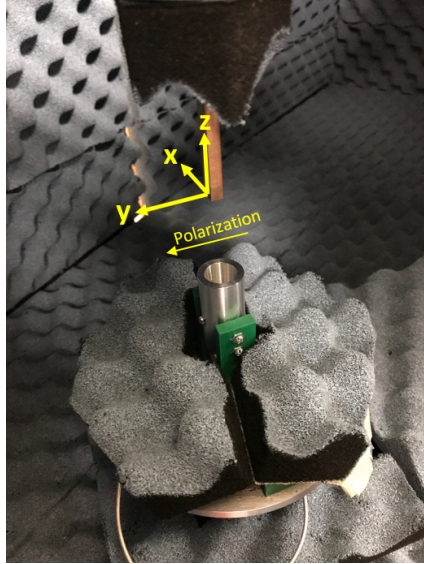


Figure 3.43: Horn mounted in UCLA bipolar planar near-field chamber.

cosine- q feed when the horn is rotated by 180 degrees is consistent with results in Figure 3.40. Figure 3.46c-f compare the performance of the measured feed patterns with the simulated feed patterns. An interesting note here is that the patterns agree very well for the case when the horn is oriented with screw pointing towards the top edge of the reflector (Figure 3.46f). This again suggests that while the horn's measured radiation pattern is reasonably close to the simulated patterns, the *cancellation* of the reflector cross polarization is rather sensitive. Future research in this area will involve the conceptualization of a feed design which is not as sensitive to design parameters. Also, measuring the feed along with the reflector can lead to a much better performance assessment since the errors that can be produced during post-processing can be avoided.

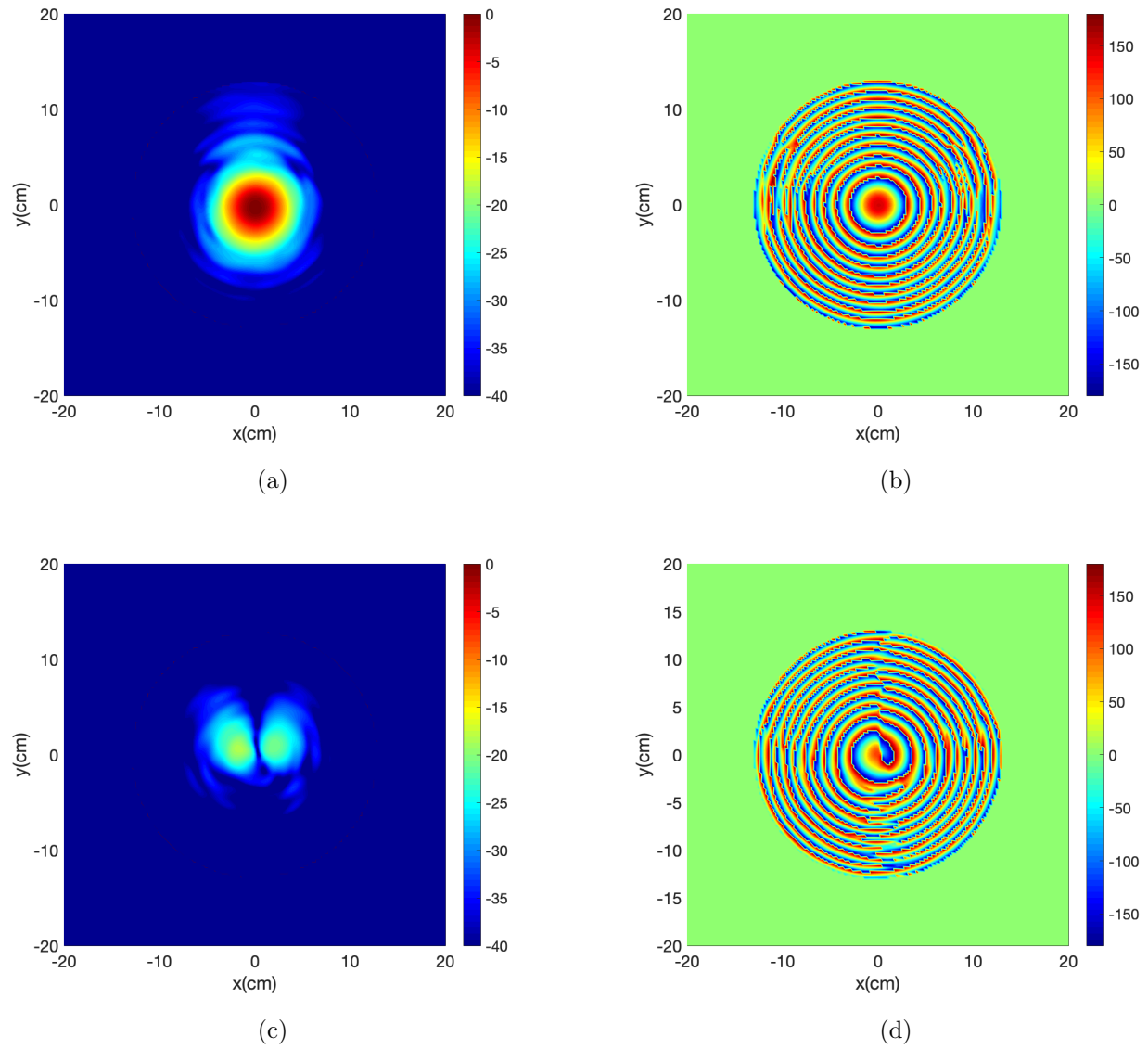


Figure 3.44: Measured near-field of the horn. (a) Normalized copol magnitude (in dB), (b) copol phase (in degrees), (c) normalized xpol magnitude (in dB) and (d) xpol phase (in degrees).

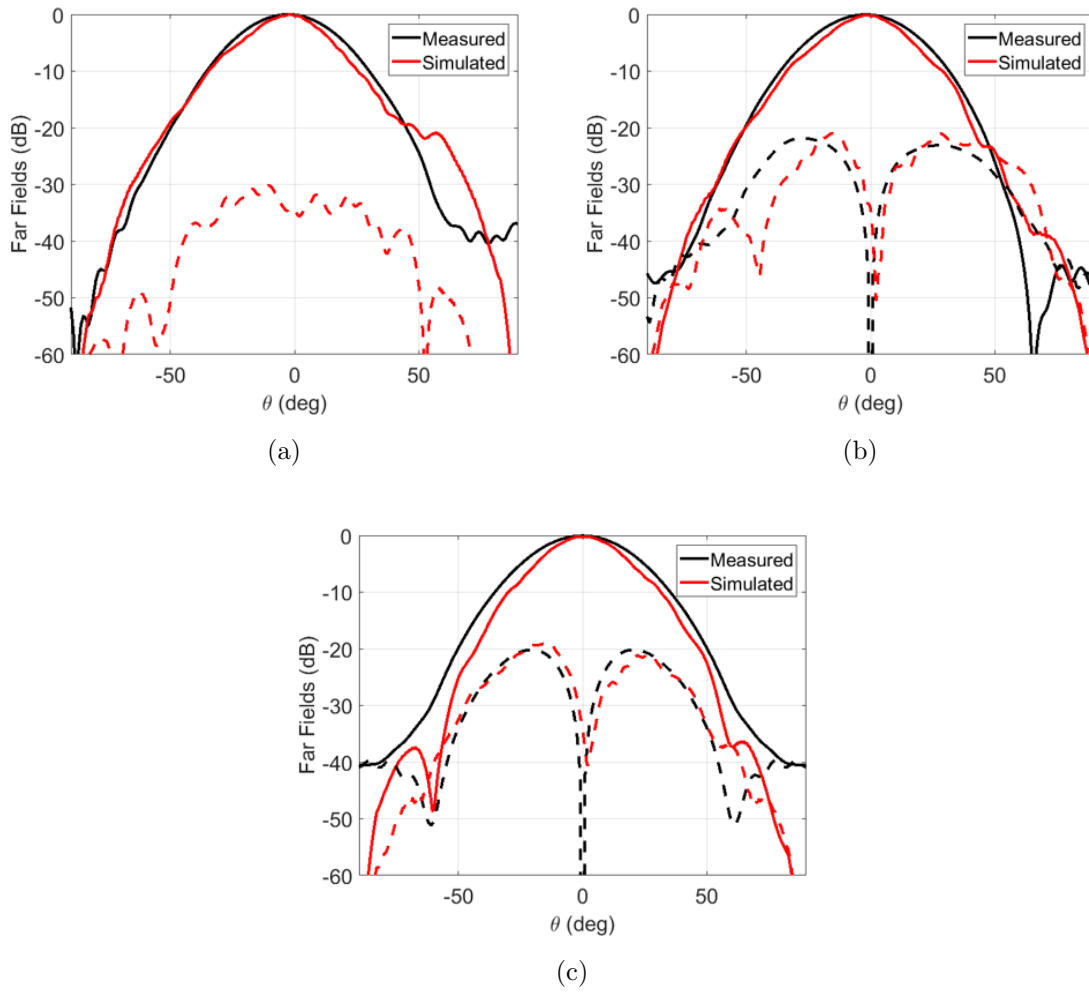


Figure 3.45: measured far fields of the horn compared to simulation. (a) E-plane, (b) D-plane and (c) H-plane.

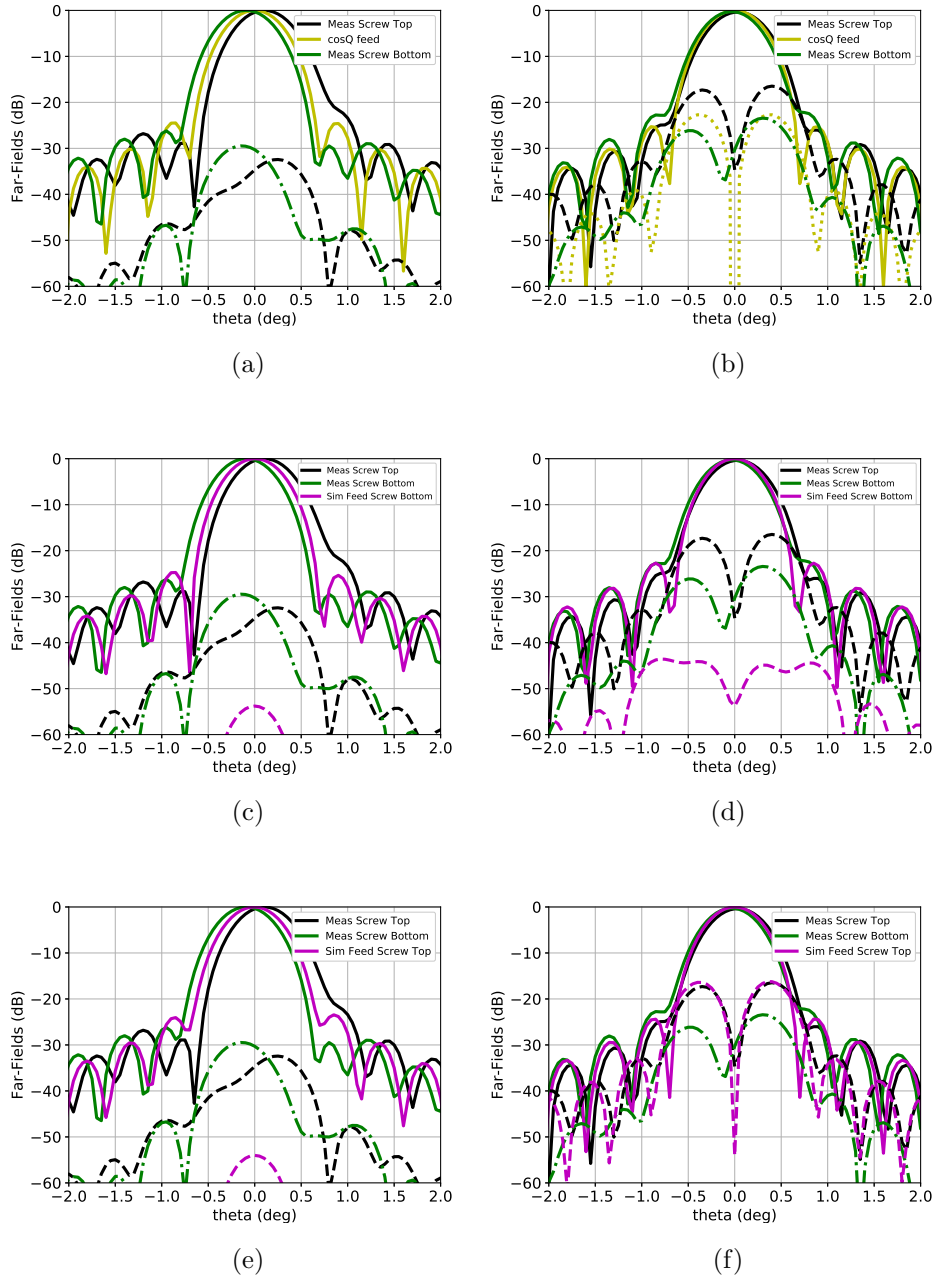


Figure 3.46: Reflector far-field patterns (a),(b) comparison of cosine-Q feed performance with the measured patterns. (c),(d) comparison of simulated feed performance (screw facing bottom) with the measured patterns. (e),(f) comparison of simulated feed performance (screw facing top) with the measured patterns. Patterns on the left and right represent XZ-plane and YZ-plane respectively.

Part III

Metal-Only, Low-Profile, Stepped Parabolic Reflector Antenna

CHAPTER 4

Synthesis and Analysis of High Gain, Metal-Only, Low Profile Stepped Parabolic Reflector Antenna

This chapter describes an intuitive approach for synthesizing low profile, metal-only high gain stepped reflector antennas that can aid emerging CubeSat missions for remote sensing and communications. The reflector surface consists of a discrete number of confocal parabolic sections which scatter in phase, ultimately resulting in a focused beam in the far field. The metal only structure avoids the need for dielectric characterization, which is essential for reflectarrays, transmitarrays, lenses, and other dielectric based antennas. Further, the parabolic sections provide a distinct advantage over the conventional Fresnel Zone Plate antenna (FZP) since parabolic sections ensure a greater uniformity of phase in the aperture of the antenna, and the radiation is unidirectional. Using this technique, it is possible to achieve depths of the order of one wavelength while ensuring performances comparable to conventional parabolic reflectors, making it very suitable for mmWave applications. Starting from a symmetric stepped reflector synthesis, two distinct approaches to synthesize offset stepped reflectors are explored in this chapter. Each of these approaches provide interesting tradeoffs between mechanical complexity and electromagnetic performance, as will be highlighted. A thorough analysis of the frequency performance of stepped parabolic reflectors is also presented, followed by a discussion on the prototyping and measurement of a stepped reflector prototype.

4.1 Existing Options for Low-Profile High Gain Antennas

Fresnel Zone Plate antenna (FZP) were one of the first antennas that were developed to achieve high gain from a low profile aperture. Investigations on microwave reflecting FZP's began as early as the 1930's [151–156] and continued into more recent investigations [157–159]. The original FZP concept began with investigations by Lord Rayleigh and Wood [160] in the 1800's, and interesting applications and new designs for FZP's are still continuing for optical frequencies and beyond [161–172]. Though FZP can take many forms, a typical design essentially uses a set of flat, metallic rings located in one plane, achieving significant reduction in volume of the antenna. The flat nature of the FZP causes the windloading force to be $1/8^{th}$ of conventional solid or wire meshed reflectors of similar size [173], making it a very suitable candidate for high gain applications from a mechanical standpoint. However, the low aperture efficiency of the FZP is often a concern for engineers, which arises from a higher sidelobe envelope compared to a conventional parabolic dish bidirectional radiation [174] and bidirectional radiation. For large apertures, the number of rings for an FZP can severely limit frequency response in terms of its 1dB gain bandwidth [175].

An alternative “flat reflector” design that has become popular within the antenna community is the reflectarray, which consists of resonant patches on a grounded dielectric substrate that provide the necessary phase correction to achieve a uniform phase at the exit aperture [177]. While this has demonstrated significant potential, the presence of dielectric material can pose concerns for certain applications, such as deployable spaceborne antennas. Dielectrics often increase losses and limits the power handling capacity and limit the bandwidth of the antenna. Another challenge for reflectarray analysis is the large computational time and resources needed to simulate the resonant structures. Recently, metal-only designs have become an interesting research focus for reflectarrays, especially for mmWave operation [178]. Several metal-only reflectarray concepts have been produced, providing decent aperture efficiencies at frequencies as high as 100 GHz [179–181]. The advancements in computer technology have aided another metal-only approach where a flat plate is deformed by optimizing the height of individual pixels. After optimizing the pixel heights, the sur-

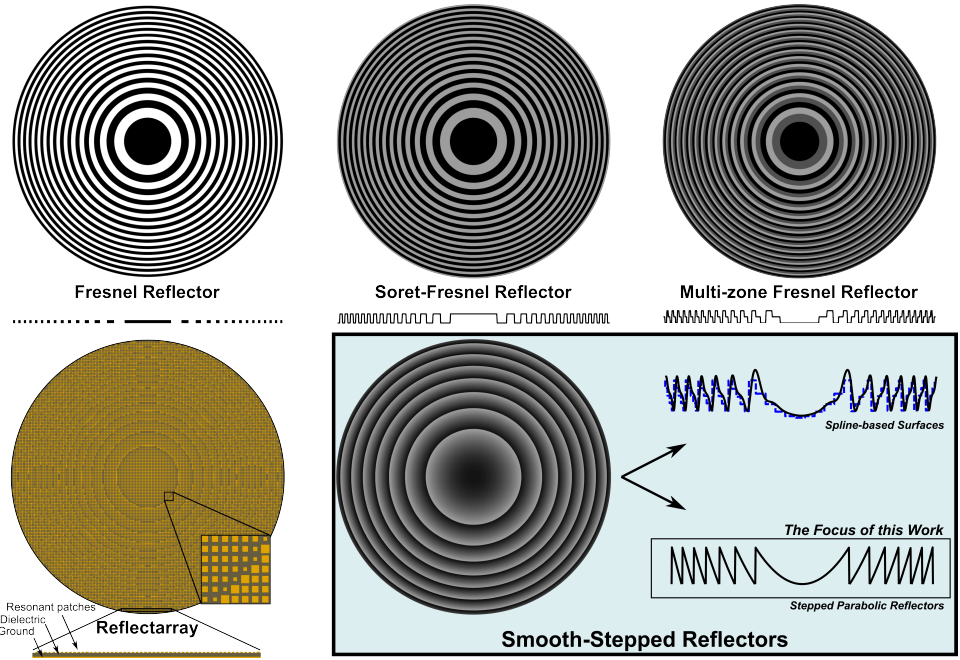


Figure 4.1: Various architectures of low profile reflectors that have been under investigation [176].

face profile is generated by smoothing the pixelated surface through B-splines to generate the surface profile [182, 183]. This process provides the flexibility to meet multiple constraints for specific applications. In this approach, a tradeoff is made between achieving improved efficiencies and computation complexity and time.

In this chapter, we revisit the notion of zoned reflectors to present an intuitive synthesis procedure to achieve a low profile, high-efficiency, metal-only reflector antenna that provides radiation efficiencies comparable to reflectarrays and deformed flat plate reflectors. The reflector aperture is constructed using a family of paraboloids such that the scattering from each individual section adds in-phase in the far field, resulting in high aperture efficiency. This technique is especially useful for mmWave frequencies and beyond, where a profile height of the order of 1 cm can easily be achieved. Engineers can thus retain the mechanical advantages of the FZP (like wind-loading), while achieving radiation efficiencies comparable to classical reflectors. For space applications, the stepped parabolic reflector can potentially be integrated with the chassis, thereby eliminating the need of complex deployment mecha-

nisms. Note that even though the reflector itself may not need deployment, the feed must still be deployed such that its phase center aligns with the focal point of the stepped reflector. This can be alleviated by using a dual reflector configuration as discussed in [184].

Recent trends in fabrication technology also make this investigation timely. The structure can possibly be printed using advanced 3D printers or machined using CNC tools, where fabrication time and cost for development can be significantly reduced [185].

Even though this architecture fits within the well-known zoned reflector category, a detailed characterization of this concept and an assessment of its full potential has not been done to the best of the author's knowledge (a brief description can be found in [173, 186]).

Figure 4.1 shows an illustration of the various options available for designing a high gain, low profile reflector antenna. All of these are symmetric designs. In many practical situations, however, an offset reflector geometry is desirable since it avoids feed blockage. In this chapter, we also discuss the development of a low profile, stepped offset reflector using multiple parabolic sections from a novel and practical point of view. Multiple techniques exist to generate an offset geometry as will be discussed subsequently. Each technique has its own special mechanical and RF characteristics. A detailed description of the frequency performance of the stepped parabolic reflector antenna (for both symmetric and offset configurations) is also provided and validated through measurements.

4.2 Surface Formulations

In this section, we elaborate on the formulations that describe the surface geometry for both symmetric and offset configurations. The synthesis technique is based on the fundamental geometric property of a paraboloid: the total path length for a ray that emanates from the focus and gets reflected off the reflector surface to the exit aperture is $2F$, with a corresponding phase of $2kF$, where $k = 2\pi/\lambda$ (λ being the wavelength). One can thus envision a family of N paraboloids of focal lengths F_n that can provide the same phase at

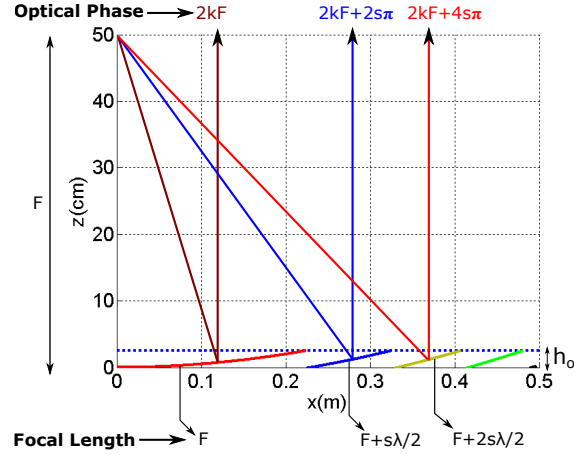


Figure 4.2: Diagrammatic illustration of the stepped parabolic reflector concept with a depth of h_0 . Each section provides a modulo 2π phase at the exit aperture. Note that s must be an integer [176].

its exit aperture if the following phase condition is met:

$$2kF_n = 2kF + 2(n - 1)s\pi \quad (4.1)$$

implying that $F_n = F + (n - 1)s\lambda/2$, where s is an integer and $n = 1, 2, 3, \dots, N$. This concept is illustrated in Figure 4.2.

As will be shown in the formulations that follow, it is this factor s that provides the flexibility to tradeoff mechanical complexity with radiation efficiency and bandwidth. An important note here is that as the focal length of the parabola changes, it must be shifted appropriately so that the feed remains at the focus for each of the sections.

4.2.1 Symmetric Stepped Reflector

Based on the concept introduced in the preceding section, we select a focal length of F , aperture diameter of D and a profile height of h_0 . The n^{th} parabolic section can then be expressed as:

$$z_n = \frac{\rho^2}{4 \left(F + (n - 1)s\frac{\lambda}{2} \right)} - (n - 1)s\frac{\lambda}{2} \quad (4.2)$$

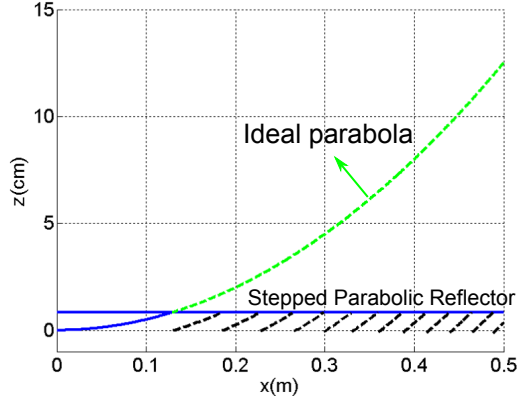


Figure 4.3: Profile of a symmetric stepped parabolic reflector with $h_0 = 1\lambda$ (0.839 cm at 35.75 GHz), $s = 2$, $D = 1\text{m}$ and $F/D = 0.5$ [176].

where ρ satisfies $a_{n-1} \leq \rho \leq a_n$ defined by

$$a_n = 2\sqrt{\left(h_0 + (n-1)s\frac{\lambda}{2}\right)\left(F + (n-1)s\frac{\lambda}{2}\right)} \quad (4.3)$$

or, in other words, between the $(n-1)$ th and n th section boundaries. Note that $a_0 = 0$. An example profile of a symmetric stepped reflector with aperture diameter $D = 1\text{m}$, $F/D = 0.5$, $s = 2$ and $h_0 = 1\lambda$ (0.839 cm at 35.75 GHz) is shown in Figure 4.3. In this case, the number of sections present is 13.

4.2.2 Offset Stepped Reflector

There can be multiple ways of extending the formulation developed for a symmetric reflector to an offset geometry. In this section, two interesting options are described to generate the geometry for an offset paraboloid. One can directly intersect the symmetric stepped reflector geometry by a cylinder of the required radius a at the desired offset height d , similar to the classical approach of generating an offset reflector [187]. Since this results in a geometry which is horizontal, we call this *Horizontal Flat Offset Stepped Reflector* (HFOSR). The other approach involves generating the offset reflector on an inclined plane tangential to the midpoint of the first section. We call this *Inclined Flat Offset Stepped Reflector* (IFOSR). The fundamental difference between these two approaches is that for HFOSR, the surface

is composed of incomplete circular arcs, whereas the IFOSR consists of complete elliptical rings. The fact that one has this flexibility of choosing between two totally different offset architectures is a distinct difference between this approach and the reflectarray approach or FZP [188] approach. Each architecture has its own unique electromagnetic and mechanical properties as is subsequently discussed. For the IFOSR case, the structure is constrained to lie between the two lines given by: $z_{l1} = \frac{d}{2F}(x - \frac{d}{2})$ and $z_{l2} = z_{l1} + h_0$ (Figure 4.4). The equation for the parent paraboloid for the n^{th} section is given by:

$$z_n = \frac{\rho^2}{4(F + (n-1)s\frac{\lambda}{2})} - (n-1)s\frac{\lambda}{2} \quad (4.4)$$

The intersecting cylinder that is used to generate the n th section has a radius a_n and offset d_n given by

$$a_n = \frac{\rho'_{n1} - \rho'_{n2}}{2} \quad (4.5)$$

$$d_n = \frac{\rho'_{n1} + \rho'_{n2}}{2} \quad (4.6)$$

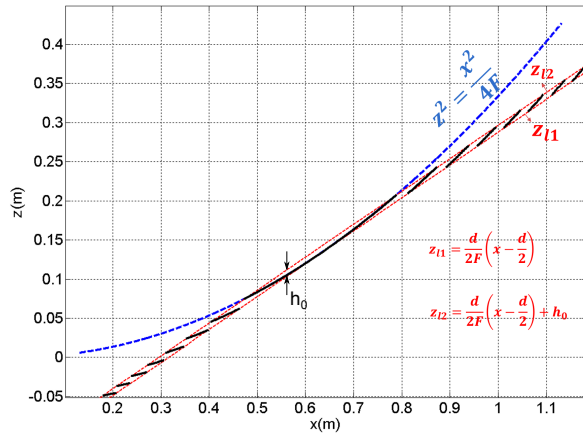
respectively, where ρ'_{n1} and ρ'_{n2} are the roots of the equation,

$$\rho'^2 \frac{1}{4(F + (n-1)s\frac{\lambda}{2})} - \rho' \frac{d}{2F} + \left[\frac{d^2}{4F} - h_0 - (n-1)s\frac{\lambda}{2} \right] = 0 \quad (4.7)$$

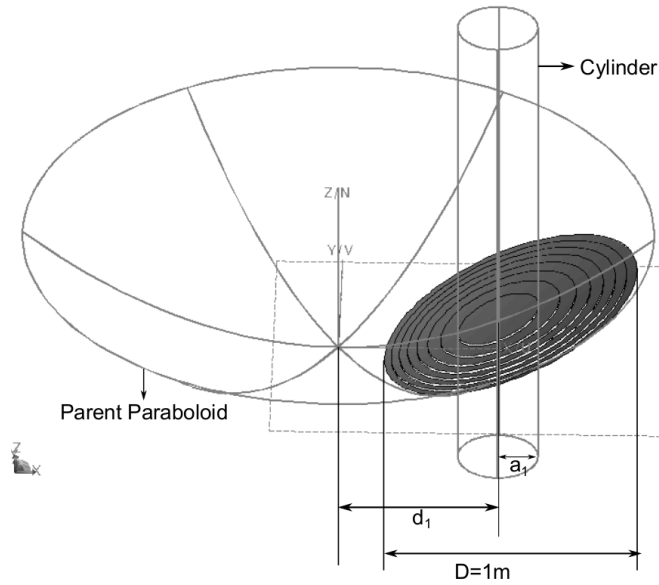
The quadratic equation presented in (4.7) is found by equating (4.4) with the equation defining z_{l2} . This is essentially finding the intersection between the parabolic surface and the line defined by z_{l2} . A 3D view of an offset stepped reflector with $h_0 = 1\lambda$, $s = 2$, $D = 1m$, $d = 0.6312m$ and $F = 0.75m$ using both approaches is shown in Figure 4.5.

4.3 Geometry Considerations

In this section, we detail the mechanical considerations for the stepped parabolic reflector approach, such as the ring width, number of rings, and feed positioning. It is important to note that there is always a tradeoff between the electromagnetic features that one desires and the depth that one can achieve with the stepped parabolic reflector approach. Increasing the number of rings can facilitate a lower profile while limiting the frequency performance and



(a)



(b)

Figure 4.4: Inclined Flat Offset Stepped Reflector (IFOSR) construction. (a) 2-D profile (b) The process of generating the 3D geometry: The parent paraboloid is intersected by a cylinder of radius a_n and an offset distance of d_n , which are computed by solving (4.7) [176].

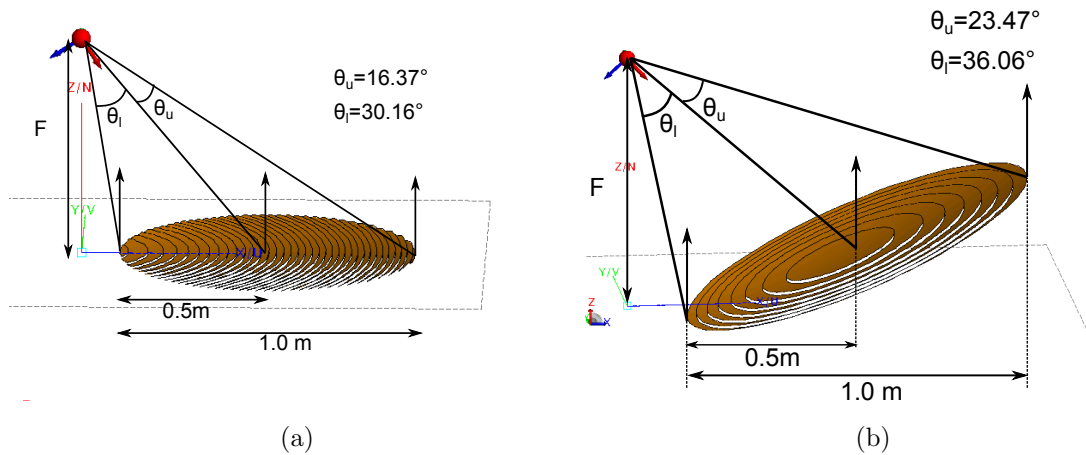


Figure 4.5: Perspective views of the two approaches to generate an offset stepped reflector discussed in this work. (a) HFOSR and (b) IFOSR. Note the large difference in θ_u and θ_l for the HFOSR [176].

increasing fabrication complexity due to reduction of ring widths. The ring width also plays a major role in deciding the simulation technique suitable for characterizing the antenna. If the rings that are heavily illuminated are lesser than a wavelength, the radiated fields would be diffraction dominated, necessitating the use of full wave techniques such as method-of-moments (MoM). However, if these rings are larger than 4 to 5 wavelengths, Physical Optics (PO) becomes a viable option for simulation, which can be significantly easier on computational resources than the conventional MoM approach.

4.3.1 Estimation of Number of Rings

Even though the method of synthesis for symmetric and offset reflectors stem from the same concept of achieving a modulo 2π phase at the exit aperture, the method of selecting the family of paraboloids differ for each approach. Thus, one expects the number of rings for each case to be different, as will be highlighted.

4.3.1.1 Symmetric Stepped Reflectors

For a reflector with N rings, the last ring must satisfy the following equation:

$$h_0 = \frac{(D/2)^2}{4(F + (N-1)s\frac{\lambda}{2})} - (N-1)s\frac{\lambda}{2} \quad (4.8)$$

Solving for N , one gets the number of rings as:

$$N = \frac{1}{s\lambda} \left(-(h_0 + F) + \sqrt{(F - h_0)^2 + \frac{D^2}{4}} \right) + 1 \quad (4.9)$$

Typically, one can assume that $h_0 \ll F$, leading to

$$N \approx \frac{1}{s\lambda} \left(-F + \sqrt{F^2 + \frac{D^2}{4}} \right) + 1 \quad (4.10)$$

Interestingly, the form in (4.10) is very similar to the number of rings for an FZP, which is given as [157]:

$$N_{FZP} = \frac{2}{\lambda} \left(-F + \sqrt{F^2 + \frac{D^2}{4}} \right) \quad (4.11)$$

Thus, the stepped parabolic reflector approach reduces the number of rings by a factor of approximately $2s$. It should be noted that the total number of rings for an FZP include both metallic rings (reflecting zones) and the gaps between them (transmitting zones).

4.3.1.2 Offset Stepped Reflectors

The number of rings for the two offset approaches can be very different. For the IFOSR, the number of rings can be expressed as $N = \frac{2N_0}{s} + 1$ where N_0 is the positive root of the equation

$$N_0^2 \left(\frac{d^2}{4F^2} + 1 \right) + N_0 \left(\frac{d^2}{4F\lambda} + \frac{F}{\lambda} + \frac{h_0}{\lambda} \right) + \left(\frac{Fh_0}{\lambda^2} - \frac{D^2}{16\lambda^2} \right) = 0 \quad (4.12)$$

For the HFOSR approach (a symmetric reflector intersected by an offset cylinder), the number of rings can be computed by subtracting the number of rings present in the clearance height ($0 \leq \rho \leq (d - D/2)$) from the number of rings required to make the parent paraboloid ($radius = d + D/2$). The approximate number of rings can be given as (assuming $h_0 \ll F$):

$$N = \frac{1}{s\lambda} \left(\sqrt{F^2 + \left(d + \frac{D}{2} \right)^2} - \sqrt{F^2 + \left(d - \frac{D}{2} \right)^2} \right) \quad (4.13)$$

For our particular case of $D = 1m$, $F/D = 0.75$ and $d = 0.6312m$ shown in Figure 4.5, the HFOSR results in 37 rings, whereas the IFOSR case only results in 8 rings for the same profile height of $h_0 = 1\lambda$. Based on these geometrical differences, it is reasonable to expect that the IFOSR and HFOSR would have very different electromagnetic performance. Further analysis, shown in a later section, confirms this expectation, where we observe a decreased efficiency and a frequency scanning property for the HFOSR.

4.3.2 Width of Ring

It is intuitive that the number of rings and the ring width have an inverse relationship. The greater the number of rings that are required to make the aperture, the narrower the individual rings are. The width of a ring n in the projected aperture can be expressed as:

$$w_n = a_n - a_{n-1} \quad (4.14)$$

where a_n and a_{n-1} can be calculated through the equations given previously in (4.3) and (4.5) for symmetric and IFOSR configurations respectively. The width for the HFOSR configuration uses the same equation form as the one for symmetric after suitably accounting for the number of rings that are present in the clearance height.

The ring width for the n^{th} section within the symmetric reflector ($D = 1m$, $F/D = 0.5$) is shown in Figure 4.6a, and that for an offset configuration with $D = 1m$, $d = 0.6312m$ and $F/D = 0.75$ is shown in Figure 4.6b. It should be noted that for the IFOSR, the average of the top and the bottom portion of the ring is plotted. Each ring has a vertical height of approximately λ , with the exception of the last ring. The last ring has a height lesser than wavelength so that the exact aperture diameter of 1m is achieved.

It is evident that the ring width for the HFOSR is narrower than the IFOSR due to higher number of rings. This makes the simulation and fabrication of the IFOSR more straightforward and scalable.

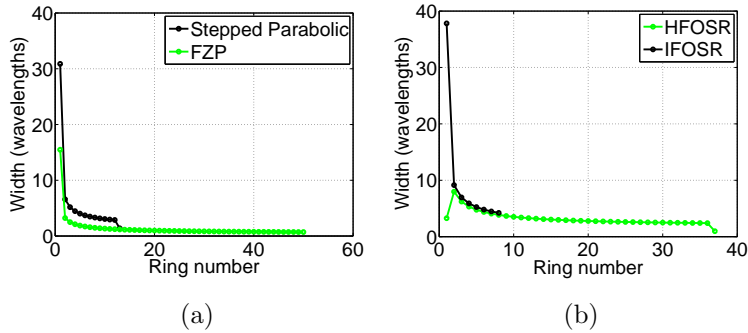


Figure 4.6: Ring widths for symmetric stepped parabolic reflector and offset stepped parabolic reflector with an aperture diameter of $1m$, $h_0 = 1\lambda$ and $s = 2$ at 35.75 GHz. (a) Comparison between symmetric stepped reflector and conventional FZP. (b) Comparison between HFOSR and IFOSR [176].

4.3.3 Feed Considerations

While the positioning of the feed for a symmetric configuration is intuitive, for the offset configuration, the tilt of the feed and the feed taper is not immediately obvious. For IFOSR, the tilt of the reflector plane provides a greater symmetry between the subtended angles of the feed (denoted as θ_l and θ_u in Figure 4.5). This makes balancing the feed spillover and taper relatively simpler than the HFOSR case. For classical horn feeds that provide symmetric patterns, the spillover plus taper efficiency for the HFOSR is expected to be lower than the IFOSR. This will be confirmed by simulations to follow.

4.3.4 Geometry Tradeoffs

It is evident that the geometry considerations differ between two approaches for generating offset stepped reflectors. This flexibility in synthesis technique allows one to achieve interesting tradeoffs between mechanical constraints and electromagnetic performance. For IFOSR, one can achieve a low profile reflector with a smaller number of rings, which reduces the frequency sensitivity of the structure. However, the IFOSR's main beam will be tilted at an angle with respect to the overall footprint of the reflector (see Figure 4.5b). This tilt

can be advantageous for certain applications, but it may complicate its integration with a flat chassis if a normal-directed beam is desired. The HFOSR, on the other hand, requires a larger number of rings to achieve the same profile height. While this structure can easily be integrated with the chassis structure, the increased number of rings increases its frequency sensitivity. Ultimately, the selection between the two approaches largely depends on the design constraints of the system and the desired antenna performance.

4.4 Simulation Results for the Stepped Parabolic Reflector Antenna

An endearing feature of the stepped parabolic reflector approach is that each section is a paraboloid, which are inherently smooth and monotonic. This leads to realizable computational meshing requirements, which results in reasonable simulation times. For this particular design, which is a 1m aperture at Ka band, the fact that the rings near the center (that are most illuminated) have a width of more than four wavelengths allows the structure to be solved using a Physical Optics engine, which significantly reduces simulation times. A comparison of results obtained via PO with the ones obtained via a full-wave MLFMM simulation for some representative cases is shown in the subsequent section. For this work, a cosine-q feed that provides a 10dB feed taper at the subtended angle of $\frac{\theta_u + \theta_l}{2}$ (see Figure 4.5) is used. An important consideration for such stepped reflector architectures is the shadowing of the outer rings by the higher edges of the preceding rings. The PO solver automatically takes this into account by forcing currents to zero in these shadow regions. The feed for the offset cases are tilted to the mean of the subtended angles from the edge of the reflector on the feed location (bisect angle).

4.4.1 Symmetric Configuration

Figure 4.7 shows the results for a symmetric stepped reflector with $D = 1m$ and $F/D = 0.5$. We also plot the patterns of an ideal parabolic reflector and an FZP, both having the same D

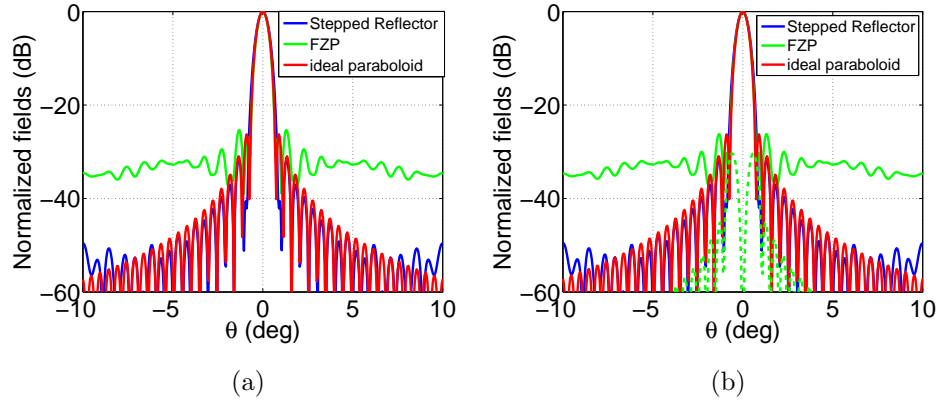


Figure 4.7: Far field pattern comparison for a stepped symmetric reflector of depth $h_0 = 1\lambda$ (0.839 cm at 35.75 GHz) and $s = 2$ with a classical symmetric paraboloid. (a) E-plane pattern and (b) D-plane pattern. The peak directivities for the ideal parabolic reflector, symmetric stepped reflector and FZP reflector are 50.57 dB, 49.54 dB and 40.41 dB respectively [176].

and F/D . The peak directivities for the ideal parabolic reflector, symmetric stepped reflector and FZP reflector are 50.57 dB, 49.54 dB and 40.41 dB respectively. It is evident that the stepped parabolic design is capable of achieving efficiencies much higher than conventional FZPs. The reason for the stepped parabolic reflector performing significantly better than the conventional FZP is twofold: (a) the FZP construction does not ensure that the rays that emanate from the focus are equiphase at the aperture, resulting in a higher sidelobe envelope and (b) the FZP radiates equally on both sides and It can be seen that the radiation pattern for the stepped parabolic reflector compares well with the ideal paraboloid, verifying the stepped parabolic reflector concept.

4.4.2 Offset Configuration

As discussed in the previous sections, there can be two approaches to design an offset stepped reflector, leading us to expect different performance for each case. The detailed geometries for each of these approaches are shown in Figure 4.5, and the corresponding radiation patterns are shown in Figure 4.8. The boresight directivities for ideal offset parabolic reflector, HFOSR and IFOSR are 50.45 dB, 48.95 dB and 49.92 dB, respectively. Some interesting ob-

servations emerge from these results. The HFOSR suffers from reduced efficiency. This can be justified from the fact that the geometry behaves similar to a uniformly excited phased array (see Figure 4.5a). Since the average width of the ring is greater than a wavelength, the far field pattern shows a grating lobe at approximately $\theta = \sin^{-1} \frac{1}{W/\lambda}$, where W is the average width of the ring, which evaluates to 18.10° for our geometry. The small ring width (compared to IFOSR) causes the grating lobe to be noticeably high, reducing the directivity of the system. The asymmetry of the structure also leads to suboptimal aperture efficiencies. The IFOSR does not suffer from the same issues since (a) the average ring width for the IFOSR is much larger. This results in potential grating lobes being pushed farther from the main beam, with a corresponding reduction in magnitude due to the element patterns of a parabolic section and (b) the main beam is not directed towards the normal of the surface (see Figure 4.5b).

4.5 Physical Optics vs Full Wave (MLFMM) comparison for stepped parabolic reflector

The patterns that were presented in the previous sections were based on Physical Optics (PO) approach, which minimizes computational resources and time. However, the PO technique does not fully account for the edge currents in the structure and ignores inter element interaction. In this section, we compare the results generated by PO with the ones generated through a full wave simulator (MLFMM) that fully accounts for edge diffraction and inter element interactions. A comparison of the radiation patterns for the symmetric stepped reflector, IFOSR and HFOSR are shown in Figure 4.9 and the directivity values are tabulated in Table 4.1. It is evident that both the approaches agree well. This is expected since the feed taper does not illuminate the outer rings (which are of the order of 1λ) strongly, causing diffraction effects to be minimal.

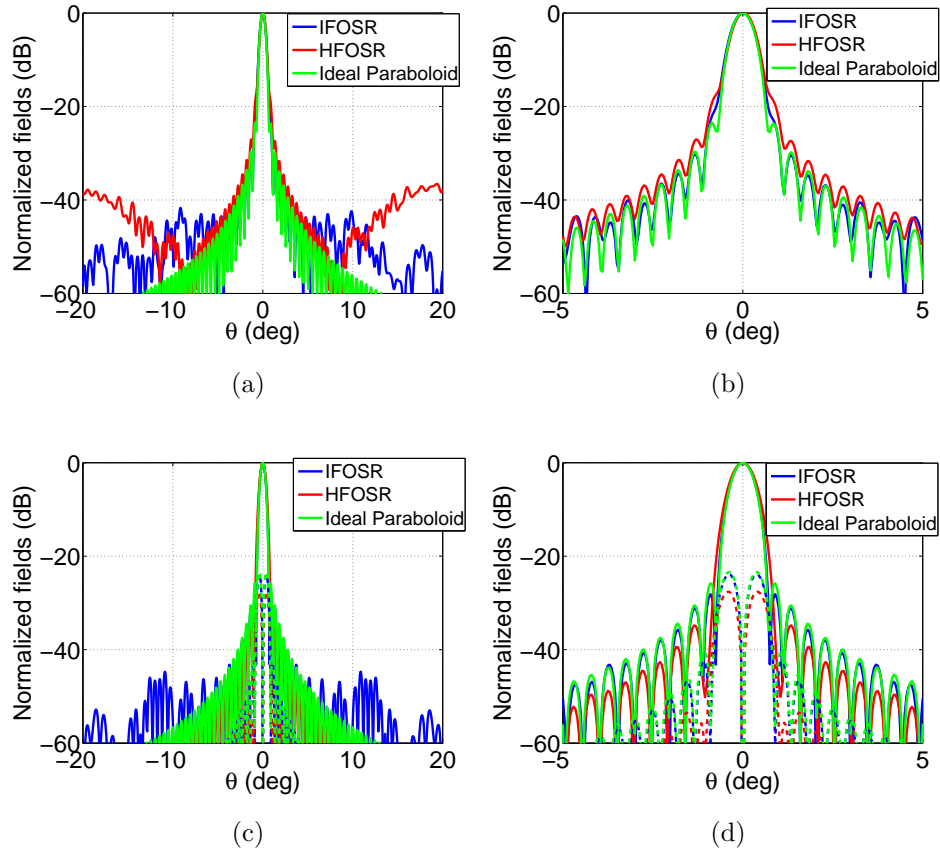


Figure 4.8: Far field pattern comparisons for a stepped offset reflector of depth $h_0 = 1\lambda$ (0.839 cm at 35.75 GHz) and $s = 2$ (through both HFOSR and IFOSR approaches) and a classical paraboloid. (a) Wide angle E-plane pattern. (b) Near boresight E-plane pattern. (c) Wide angle H-plane pattern. (d) Near boresight H-plane pattern. The E-Plane is the plane of offset. The boresight directivities for ideal offset parabolic reflector, HFOSR and IFOSR are 50.45 dB, 48.95 dB and 49.92 dB, respectively [176].

Table 4.1: Comparison of Directivity Values Calculated through PO and MLFMM at 35.75 GHz [176].

	PO	MLFMM
Symmetric Stepped	49.54 dB	49.95 dB
IFOSR	49.92 dB	50.10 dB
HFOSR	48.95 dB	49.43 dB

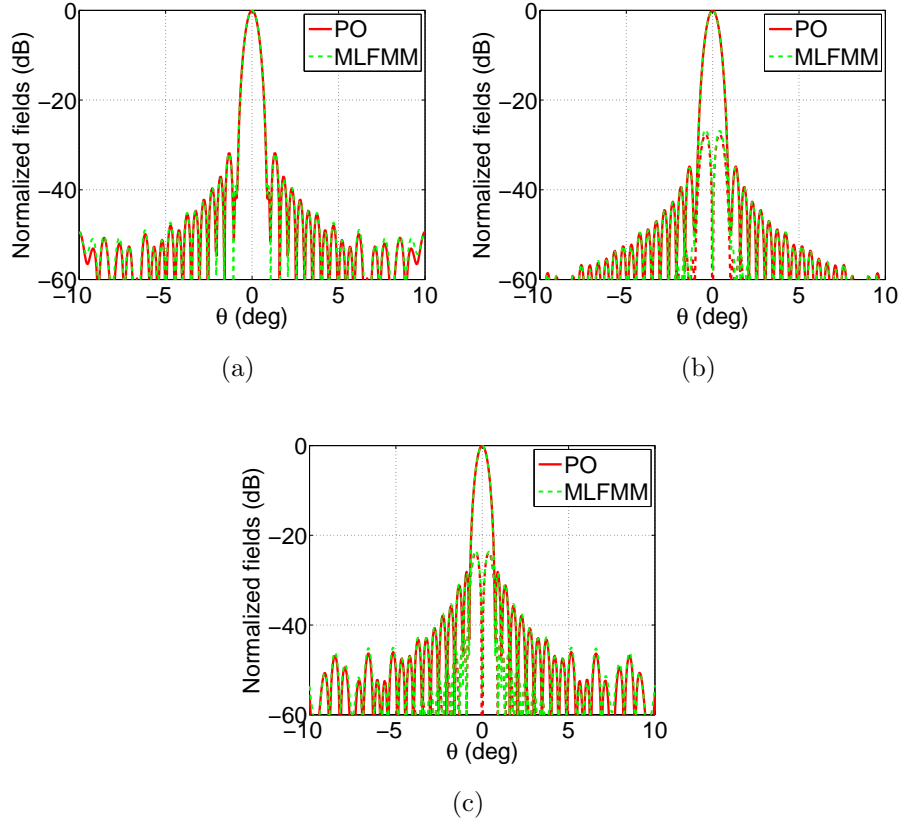


Figure 4.9: Comparison between PO and MLFMM for stepped parabolic reflector design with $h_0 = 1\lambda$, $s = 2$ and $D = 1m$ at 35.75 GHz. H-plane results are shown here. (a) Symmetric stepped reflector with $F/D = 0.5$. (b) HFOSR with $F/D = 0.75$. (c) IFOSR with $F/D = 0.75$. The directivities are tabulated in Table 4.1.

4.6 Frequency Response of Parabolic Stepped Reflector

Since the stepped reflector has dimensions which are based on a specific frequency of operation, its frequency response is an important consideration. It is intuitive that for a given wavelength λ , the phase at the center of the exit aperture and the edge of the exit aperture differ by δ , which is given by:

$$\delta = \frac{2\pi}{\lambda}(2F_{N-1} - 2F_0) - \frac{2\pi}{\lambda_0}(2F_{N-1} - 2F_0) \quad (4.15)$$

where λ_0 represents the central wavelength, which results in a uniform aperture phase distribution ($\delta = 0$). A good rule-of-thumb for the maximum phase difference that one can have across the aperture is π , which results in a reasonable gain drop. Thus, the value of δ is set to $\delta = \pm\pi$ for estimating the upper and lower bounds of frequency [189]. Thus, from (4.1) that $F_{N-1} - F_0 = s(N-1)\lambda_0/2$, the following equation can be derived:

$$f_{l,h} = \frac{f_0}{1 \pm \frac{1}{4N'}} \quad (4.16)$$

Where f_l and f_h represent the lower and higher bounds of frequency and $N' = s(N-1)/2$. For the case where $1/4N' \ll 1$, the two-sided bandwidth can be estimated as:

$$BW = \frac{f_h - f_l}{f_0} \approx \frac{1}{s(N-1)} \quad (4.17)$$

which is applicable for both offset and symmetric reflectors. One can see similarities between the classic FZP, which is given as $BW_{FZP} = 2/N_{FZP}$ [158] (if we assume a phase error of π rather than $\pi/2$). However, the factor s gives the designer a potentially added flexibility to get a larger bandwidth at the cost of an increased depth if desired. Below we describe several interesting insights specific for the symmetric and offset configurations.

4.6.1 Bandwidth Observations for Symmetric Configurations

There are two cases that are of interest to antenna engineers. The first case is stepped reflectors with a very low profile height ($h_0 \ll F$), where the two-sided bandwidth reduces to

$$BW \approx \frac{\lambda}{-F + \sqrt{F^2 + \frac{D^2}{4}}} \quad (4.18)$$

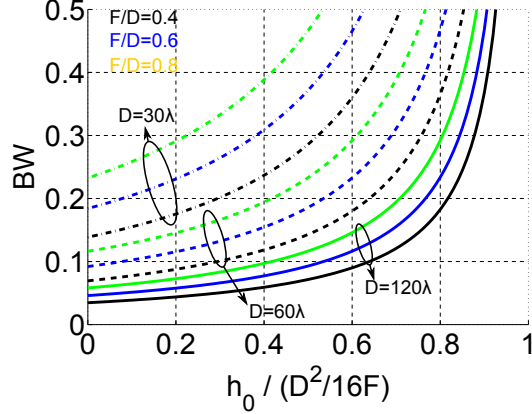


Figure 4.10: Bandwidth performance of the symmetric stepped reflector configuration, where increasing the height h_0 can result in bandwidth increases. The different colors represent various F/D values as indicated in the figure [176].

where (4.10) was inserted into (4.17). Interestingly, this expression exactly matches previous derivations for path length bandwidth of both FZP's and reflectarrays [157, 189]. This implies that for stepped reflectors with very low profile height, there are negligible bandwidth improvements over FZP's or reflectarrays (unless perhaps the element bandwidth is also considered).

In the case where one cannot assume $h_0 \ll F$, the bandwidth becomes

$$BW \approx \frac{\lambda}{\sqrt{(F - h_0)^2 + \frac{D^2}{4}} - (F + h_0)} \quad (4.19)$$

The bandwidth in this region monotonically increases with h_0 until $BW \rightarrow \infty$ at $h_0 = D^2/16F$, which is expected since this height is equal to that of an ideal parabolic reflector. This is illustrated for several representative values of F/D and aperture sizes in Figure 4.10, where it becomes clear that the bandwidth can be improved by increasing the reflector height. These results do reveal that these improvements are only useful for smaller aperture sizes with potentially larger F/D ratios.

It should also be emphasized that the aperture phase errors are circularly symmetric in the aperture. Thus, the beam will remain at broadside, and no scanning will be observed.

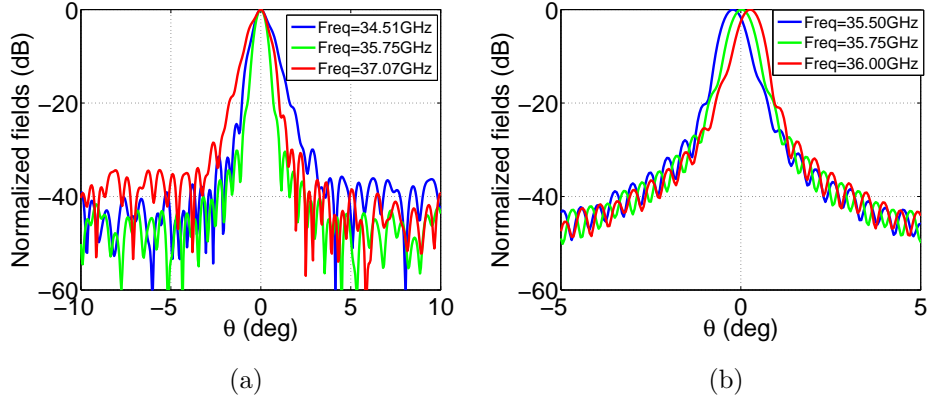


Figure 4.11: Far-field patterns at different frequencies for the stepped offset reflector. (a) IFOSR and (b) HFOSR. The details are tabulated in Table 4.2 and 4.3 [176].

4.6.2 Bandwidth Observations for Offset Configurations

The intuitive parabolic geometry for the offset design allows us to guess the distribution even before simulations: for the IFOSR, the reflector surface is composed of confocal parabolic sections with complete elliptical rims resulting in a phase distribution which is circularly symmetric at the exit aperture. This results in the broadside directed far field radiation pattern. With the aperture distribution phase errors for the IFOSR showing similarities to the symmetric configuration, many of the observations for the symmetric configuration are also applicable to the IFOSR. Increasing the height also enables the tradeoff between height h_0 and the bandwidth.

The situation for the HFOSR, however, becomes interesting. For the HFOSR, the reflector surface consists of rings that are only parts of a circle. For off-center frequencies, a phase gradient will develop along the plane of offset, leading to beam scanning as frequency changes. The extent to which the HFOSR scans can be estimated by array theory as:

$$\theta_{0,l} = -\sin^{-1} \frac{1}{\beta_l W} \frac{\pi}{(N-1)}, \quad \theta_{0,h} = \sin^{-1} \frac{1}{\beta_h W} \frac{\pi}{(N-1)} \quad (4.20)$$

where θ_0 represents the scan angle, W is the average ring width and $\beta_{l,h} = 2\pi/\lambda_{l,h}$, with $\lambda_{l,h}$ being wavelengths corresponding to f_l and f_h respectively. For our HFOSR geometry, the theoretical formula in (4.20) predicts a scan angle of approximately $\pm 0.25^\circ$, which is similar

Table 4.2: Frequency Performance for IFOSR [176].

Frequency	Max. Gain	Scan angle
34.51 GHz	45.57 dB	0
35.75 GHz	49.91 dB	0
37.07 GHz	45.20 dB	0

Table 4.3: Frequency Performance for HFOSR [176].

Frequency	Max. Gain	Scan angle
35.50 GHz	48.83 dB	-0.20°
35.75 GHz	48.95 dB	0
36.00 GHz	48.92 dB	+0.25°

to the scan values in Table 4.3. The far field patterns are shown in Figure 4.11.

A final note on these aperture antennas should emphasize that these apertures are bandwidth limited by the path delay bandwidth alone. Unlike reflectarrays, there are no resonant elements that further restrict the bandwidth.

4.7 Fabrication and Measurement of a Stepped Reflector Prototype

While the previous section focused on a comprehensive analytical formulation of the stepped reflector (both symmetric and offset configurations), this section will focus on the fabrication and measurement of a prototype of an offset stepped reflector (HFOSR). In order to ensure that the reflector can be readily fabricated and measured, a frequency of 19 GHz was chosen, and the aperture diameter was chosen to be 20 cm. The F/D was chosen to be 0.5 to ensure that the feed can be suitably positioned. The profile of the stepped reflector along with the 3D simulation model can be seen in Figure 4.12. The final CAD file that was created and sent for CNC milling can be seen in Figure 4.13. Two important points must be noted here:

(a) In order for this to be CNC milled effectively, each section had to be connected with a suitable slope. This connecting section is created in a way that the part of the section that is present in the PO-shadow region of the preceding section is removed as illustrated in Figure 4.14. This ensures that the impact of the connected sections on the radiated far-fields is minimal. For the dimensions under consideration, the last ring gets completely shadowed by the section before it and therefore gets removed from the CAD model. (b) Since the reflector was milled, a solid base for the reflector is essential. Thus, the reflector profile was subtracted from a cylinder that had an additional thickness of 0.5 mm. This adds weight to the reflector, however, as advanced techniques such as metal 3D printing are beginning to be explored, this additional height can be significantly reduced. The fabrication was done by Protolabs inc using a CNC mill machine. The final prototype is shown in Figure 4.15a. The stepped reflector was then mounted in the UCLA spherical near-field measurement range as shown in Figure 4.15b. A Narda 638 standard gain horn was used to feed the reflector. In order to estimate the performance of the stepped reflector via simulations, a cosine-q feed which models the main beam of the feed horn was used. The simulation model also incorporates a model of the extended back-plate which was a part of the mounting bracket. Both the feed model and the reflector model is shown in Figure 4.16.

A comparison of the measured far-fields at 19 GHz are shown in Figure 4.18. A comparison of the directivities and the beamwidths are shown in Table 4.4. Some key observations are:

1. **Directivity and beamwidths** : It can be observed that the measured directivity is approximately 0.6 dB higher than the simulated value. This can be attributed to the fact that the chamber does not accurately measure backlobes due to the presence of absorber. The measured patterns also exhibit marginally narrower beamwidths compared to simulation results. This could stem from the fact the horn profile is proprietary and thus cannot be exactly modeled in simulations.
2. **High sidelobe envelope** : A very interesting phenomenon that can be seen in both the measured and simulated data is the presence of a high-sidelobe envelope which was

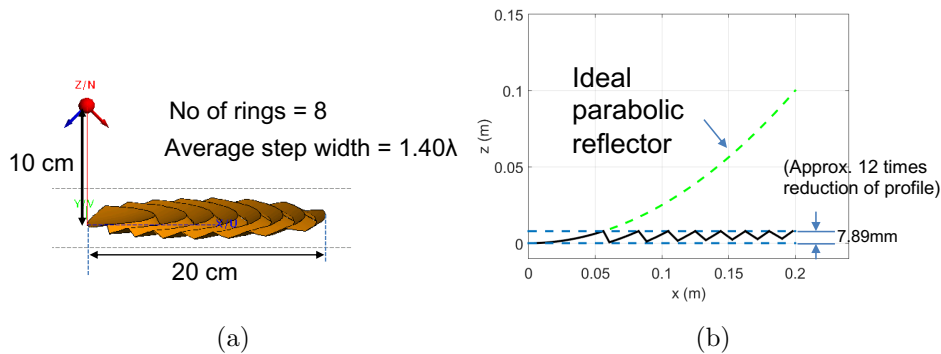


Figure 4.12: (a) Simulation model and (b) profile for the fabricated stepped reflector at 19GHz. The stepped reflector has a diameter of 20 cm and an F/D of 0.5.

not necessarily seen in the previous simulation results for the 1m reflector at 35.75 GHz. This arises dominantly due to the ripples in the amplitude distribution caused by the parabolic sections and will be a topic for detailed investigation in the next section. Note that the measured results do not recover the envelope fully on the negative side, which is most likely due to the presence of supporting structures.

For this particular architecture, the upper and lower frequency bounds were predicted using 4.16 at 17.88 GHz and 20.26 GHz, with a scan angle of approximately $\pm 0.25^\circ$, as predicted by (4.20). The stepped reflector was measured for both these frequencies and compared to simulations. The pattern comparisons are shown in Figure 4.19, and the details are tabulated in 4.5. The scanning of the beam can clearly be visualized through Figure 4.20.

Note that this particular geometry results in an efficiency of approximately 50% with a 12 time reduction in the profile of the reflector. However, if a larger F/D is used, efficiencies near 60% can be obtained. However, for this case, the reduction in profile height compared to ideal parabolic reflector will reduce.

4.8 Investigating High Sidelobe Profile for the Stepped Reflector

An interesting feature of stepped reflectors, especially the HFOSR, is a high sidelobe envelope that appears in the vicinity of the region where a grating lobe is expected. While this feature

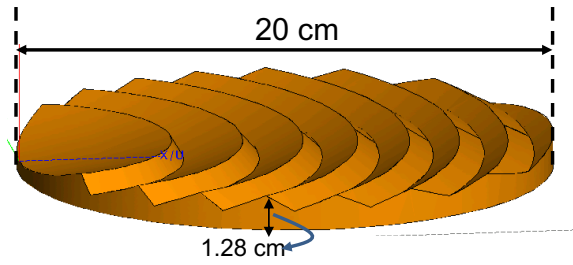


Figure 4.13: Fabricated prototype of the stepped reflector. The reflector surface was built via CNC machining and weighed approximately 800 grams.

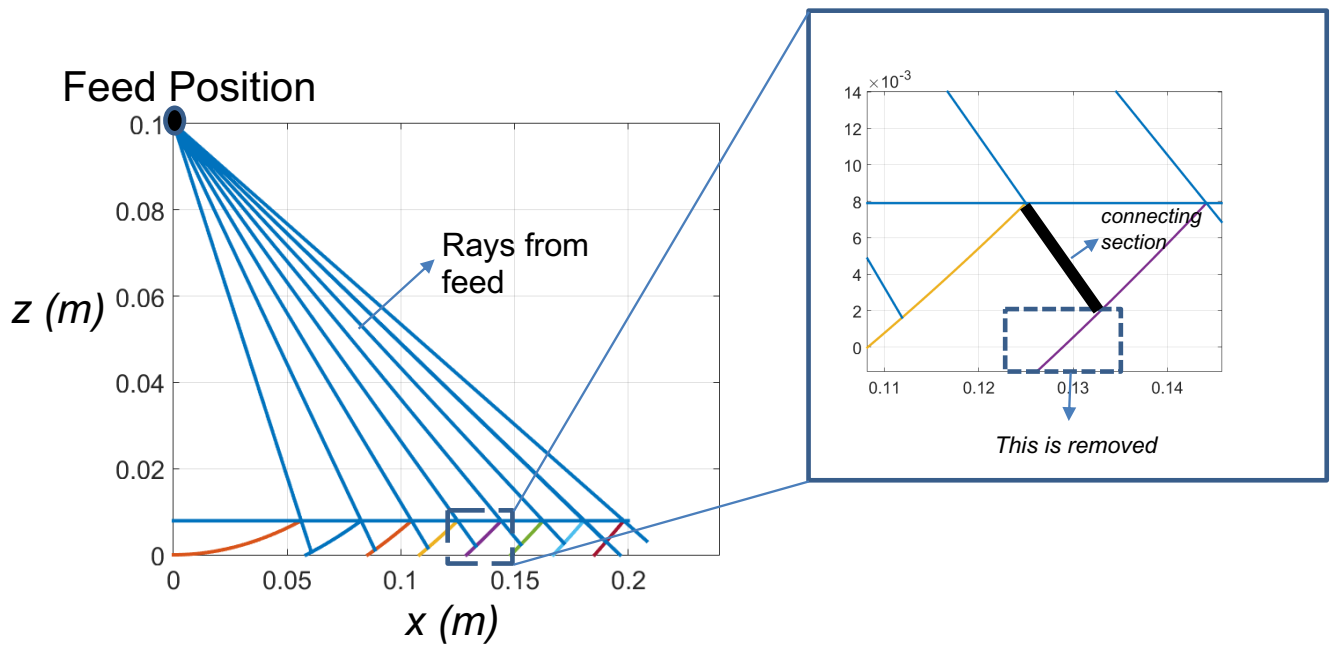
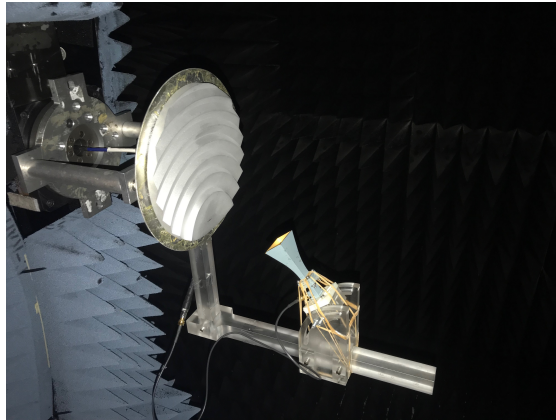


Figure 4.14: Generation of the ‘connecting’ sections for the stepped reflector geometry. The section is essentially generated by ensuring only the part of the section that falls within the shadow region of the preceding section is removed to ensure minimal impact on performance.



(a)



(b)

Figure 4.15: (a) Fabricated prototype of the offset stepped reflector with an aperture diameter of 20 cm and F/D of 0.5 at 19 GHz. (b) Stepped reflector mounted in the UCLA spherical near-field chamber.

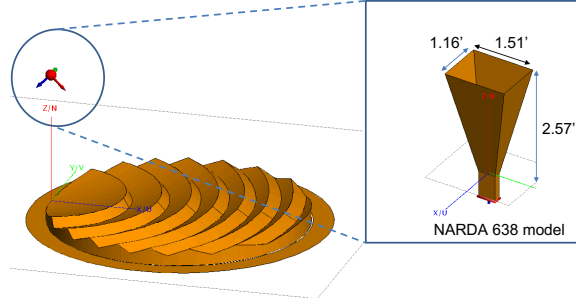


Figure 4.16: Simulation model which includes the CAD model of the fabricated reflector along with the back plate, which was a part of the bracket used to mount the reflector inside the near-field chamber. The simulation model for the feed horn (Narda-638) is also shown. A cosine-q feed that models the main beam of the feed horn was used for comparing simulated and measured results (see Figure 4.17).

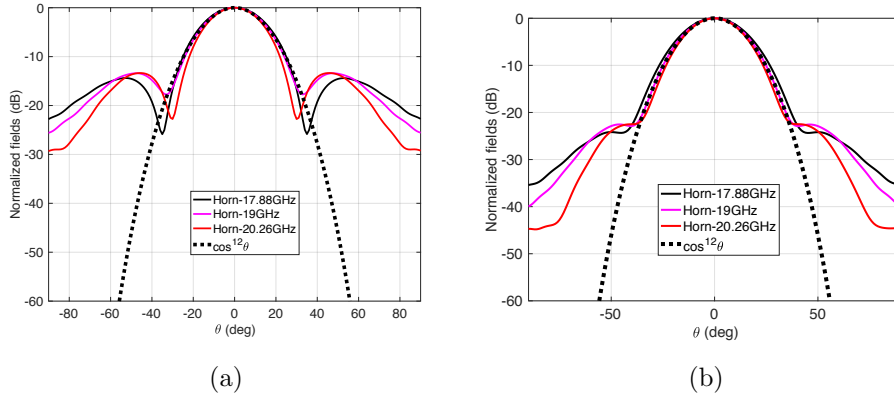


Figure 4.17: Simulated far-fields of the simplified feed model at different frequencies, and the equivalent cosine-q feed that was used to compare simulated and measured results. (a) E-plane. (b) H-plane.

Table 4.4: Comparison between simulated and measured results at 19GHz. The location of the peak of the main beam is denoted by θ_p and ϕ_p respectively.

	Simulated	Measured
Directivity	28.40 dB($\theta_p=0, \phi_p=0$)	29.04($\theta_p=-0.6, \phi_p=0$)
HPBW (E-Plane)	5.73	5.67
HPBW (H-Plane)	6.81	6.13

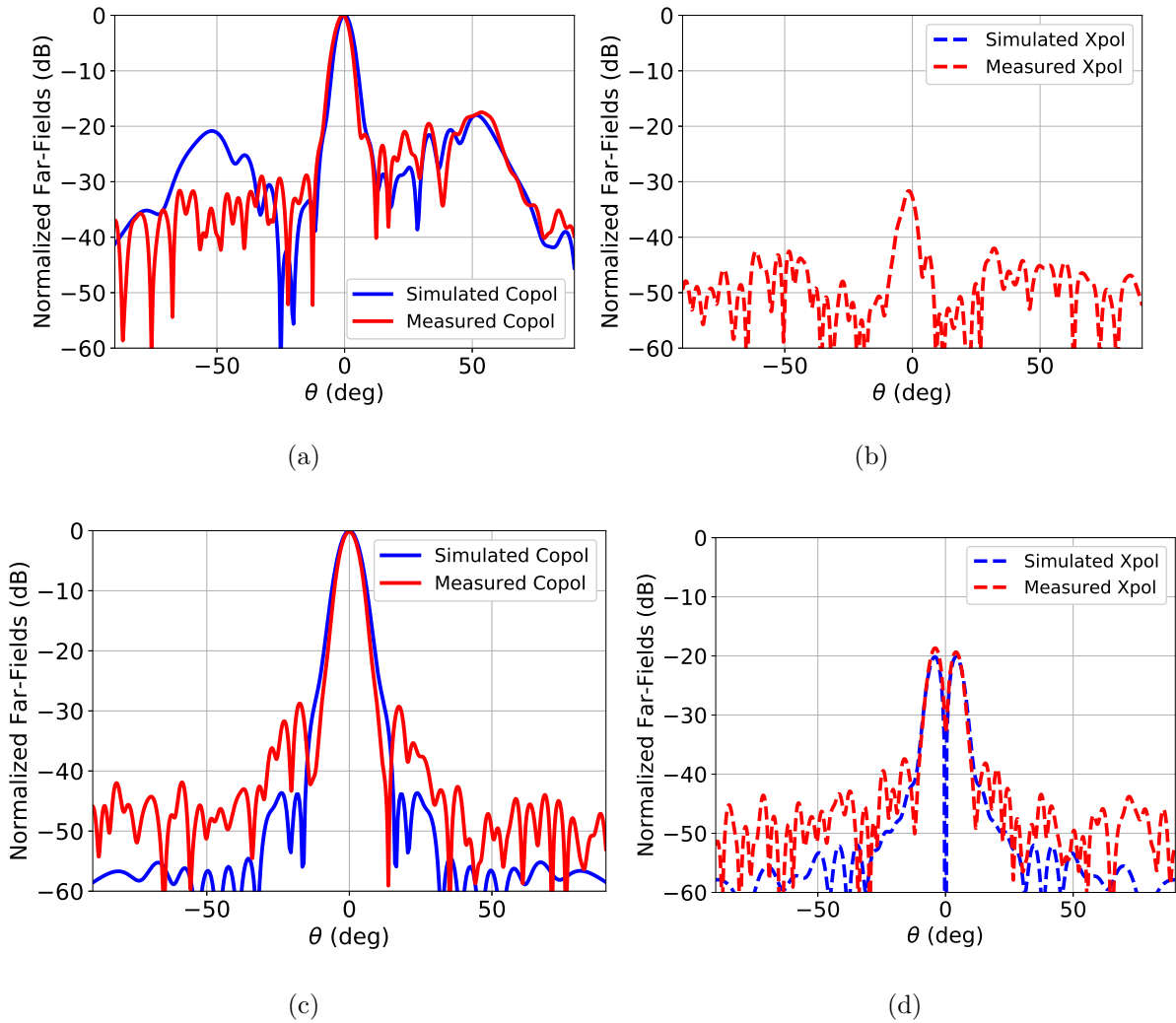


Figure 4.18: Comparing simulated results with the measured radiation patterns at 19 GHz. (a) E-plane copol, (b) E-plane xpol, (c) H-plane copol and (d) H-plane xpol.

Table 4.5: Directivities at various frequencies for the HFOSR. The location of the beam peak is denoted by θ_p and ϕ_p in elevation and azimuth respectively.

	Simulated	Measured
Directivity (17.88 GHz)	27.62 dB ($\theta_p = -2.5^\circ$, $\phi_p = 0^\circ$)	28.33 ($\theta_p = -3$, $\phi_p = 0$)
Directivity (19 GHz)	28.40 dB ($\theta_p = -0^\circ$, $\phi_p = 0^\circ$)	29.04 dB ($\theta_p = -0.6^\circ$, $\phi_p = 0$)
Directivity (20.26 GHz)	28.84 dB ($\theta_p = 2.5^\circ$, $\phi_p = 0^\circ$)	29.54 dB ($\theta_p = 2^\circ$, $\phi_p = 0^\circ$)

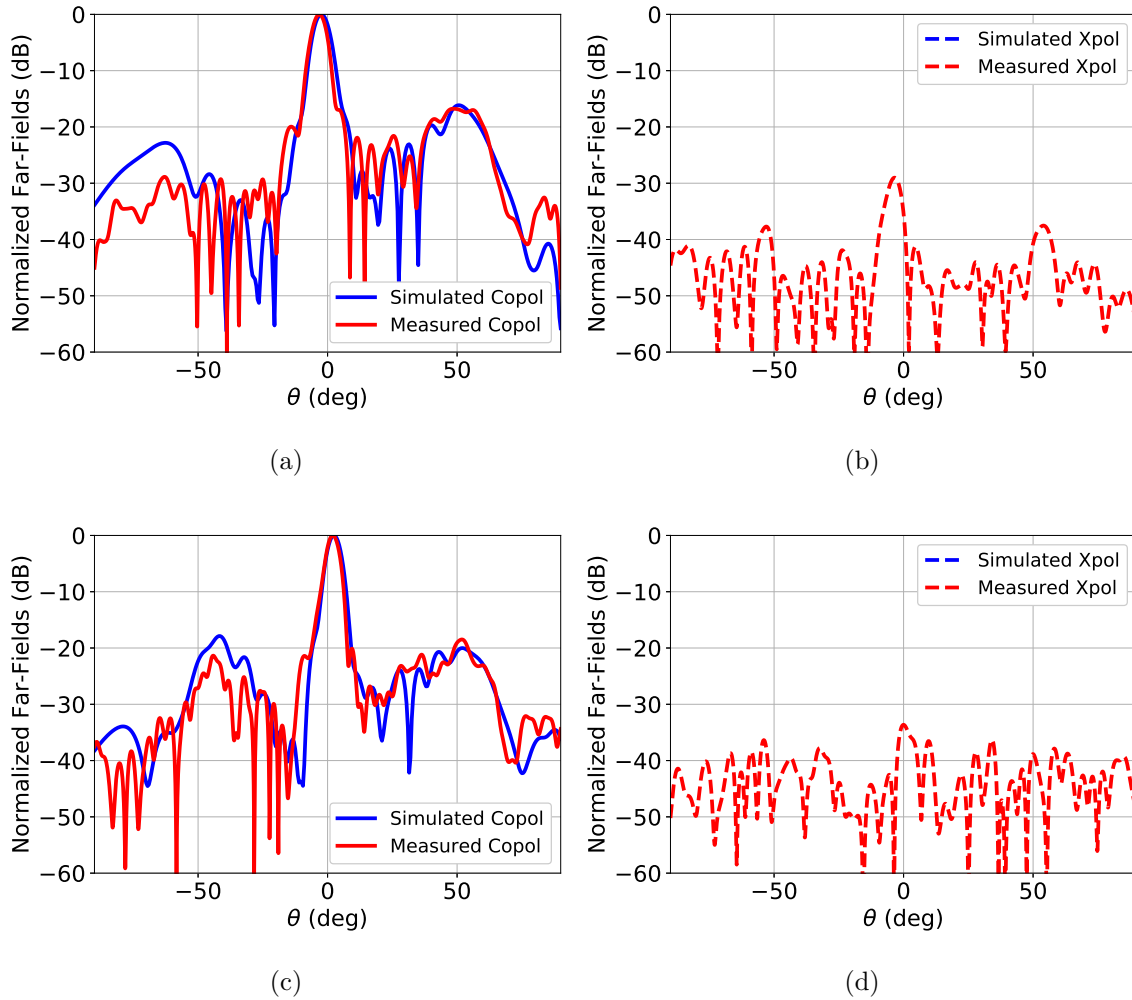


Figure 4.19: Comparing simulated results with the measured radiation patterns at lower and upper frequency bounds. (a) E-plane copol at 17.88 GHz, (b) E-plane xpol at 17.88 GHz, (c) E-plane copol at 20.26 GHz and (d) E-plane xpol at 20.26 GHz.

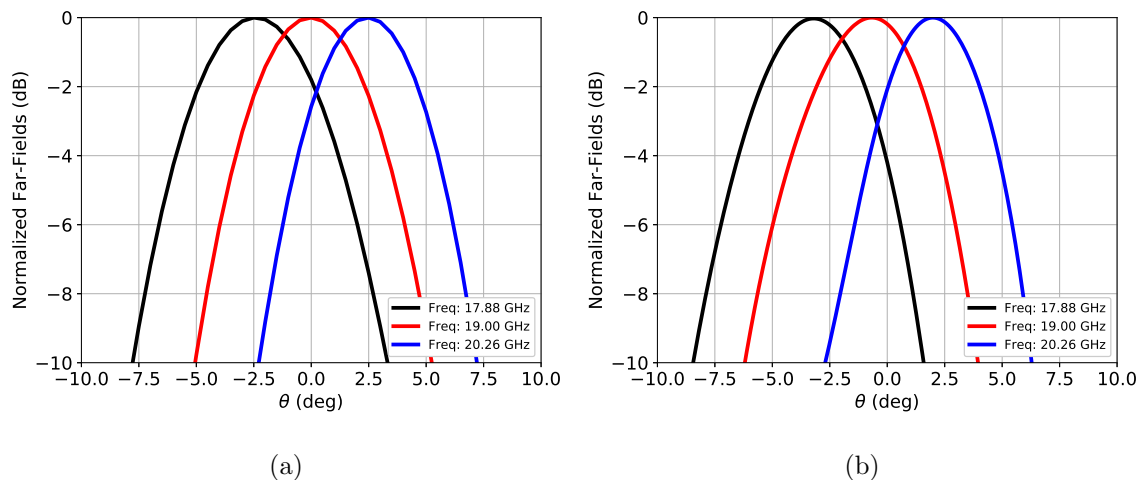


Figure 4.20: Illustration of the beam scan as the frequency changes for the HFOSR. (a) Simulated results and (b) measured results.

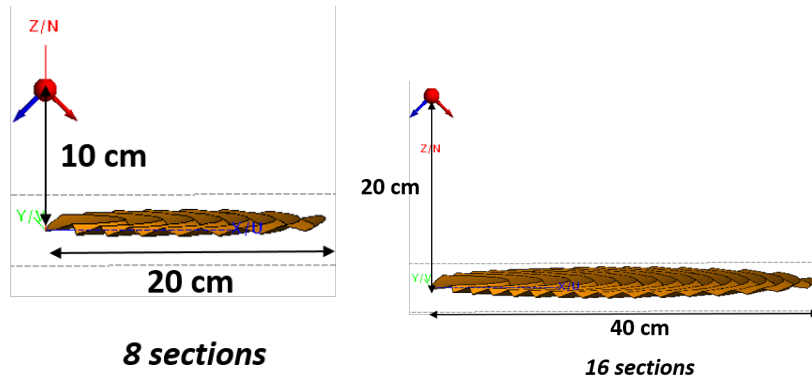
is always present, its level relative to the peak keeps reducing as the aperture size increases, making it insignificant for larger apertures. This can be seen from the results presented in the earlier sections of this chapter - simulations of the 1m reflector at 35.75 GHz (120λ diameter) had an envelope which was almost 40 dB down, whereas the 20 cm reflector at 19 GHz (12.6λ diameter) had an envelope which was approximately 20 dB down. This section looks to provide some theoretical insights into this and attempts to justify this behavior.

We start the analysis by taking the 20 cm reflector at 19 GHz as the reference case. First, to show that indeed scaling this aperture to larger dimension will reduce the envelope, the geometry is scaled by a factor of 2 and 3, keeping the F/D constant. This results in a set of three geometries as shown in Figure. 4.21a-c. The far-fields for each are shown in Figure 4.21d, where it is evident that as the aperture grows larger, the sidelobe envelope tends to reduce. Also note that the extent (width) of the sidelobe envelope is relatively unchanged as the geometry scales. This gives an indication that this envelope is a manifestation of the number of parabolic sections per unit length of the stepped reflector, since that remains unchanged as the geometry scales. If one looks at the near-field distributions for each of these geometries, one clearly sees that the amplitude distribution is not smooth, as one might expect from a parabolic reflector, but consists of ripples. Representative near-field

distributions for the 20 cm HFOSR is shown in Figure 4.22. A deeper look into this reveals that the ripples in the amplitude pattern seem to align well with the position of each individual parabolic sections, alluding to the fact that the far-field distribution can have several plane wave spectrum components that have spatial frequencies at and *near* the number of rings per unit length of the HFOSR design.

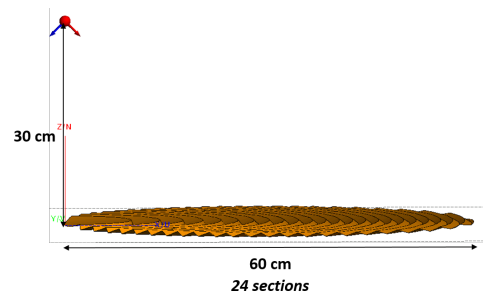
With this knowledge, one can intuitively understand the generation of this sidelobe envelope - the FFT of a single sinusoidal distribution which is finite in length is a sinc function whose peak is determined by the *frequency* of the sinusoid and a beamwidth which is decided by the *length* of the sinusoid. The HFOSR near-field distribution does not consist of just one sinusoid, but multiple of them whose frequencies are in the vicinity of the number of rings per unit length, each generating their own sinc functions. Thus, the final result will be an addition of the contribution of the sinc functions corresponding to each individual sinusoid. As the HFOSR scales, the periodicity of the sinusoids remain almost unchanged causing their respective peaks to be at the same location (resulting in an unchanged width of the sidelobe envelope). However, as these sinusoids extend over a larger length, the beamwidths of the corresponding sinc functions reduce so that the overlap between them also reduces ultimately reducing the *level* of the sinusoid. Conversely, for a smaller length, each sinc function will be relatively broad and thus would add up to a relatively large value. The following subsection will prove this quantitatively.

Note that the HFOSR geometry is much more susceptible to the generation of the high sidelobe level since it consists of multiple sections of almost the same width. The symmetric or the IFOSR configurations typically result in a significantly large first section which is much more illuminated than the steps that follow it, and thus the periodicity is not as strong.

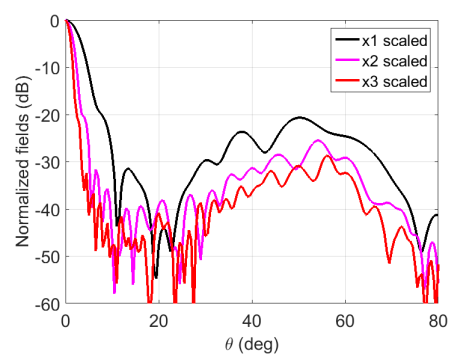


(a)

(b)



(c)



(d)

Figure 4.21: Studying the behavior of the far-field patterns as the geometry scales. (a) x1 scaled version. (b) x2 scaled version. (c) x3 scaled version. (d) Comparison of the far-field patterns

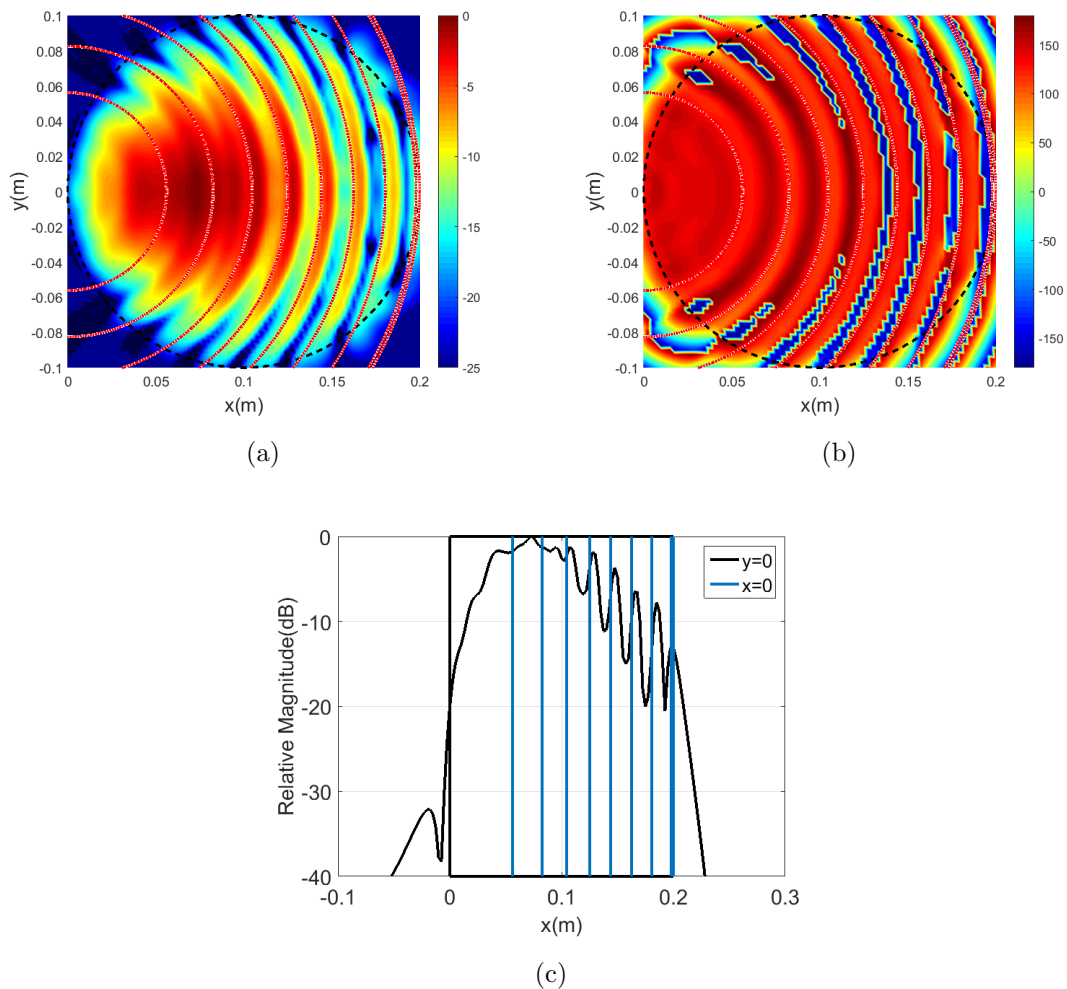


Figure 4.22: Near-field distributions for the 20 cm (x1 scaled) stepped reflector simulated 2 cm away from the aperture. (a) Normalized copol magnitude distribution (in dB). The dotted red lines represent every individual section. (b) Copol phase distribution (in degrees). (c) Line-cut along x-axis with the blue lines denoting the approximate location of individual sections. Note the ripples in the amplitude coincide well with the position of each section.

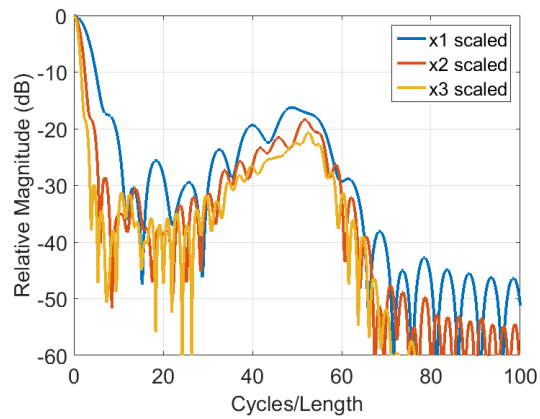


Figure 4.23: Comparison of the results from Fourier transforming the near-field distributions along the x-axis for the stepped reflector as the geometry scales. Note that the number of cycles per unit length that make up the sidelobe envelope are almost the same, with similar levels.

4.8.1 Analytical Model for the near Field Distribution

In this section, we attempt to provide a quantitative explanation for the high sidelobe envelope generated by the HFOSR, especially for apertures that are smaller. To begin, consider a 1D electric field distribution for simplicity expressed as:

$$E_x(x') = F_{DC} + \sum_{i=N_1}^{N_2} F_i \sin\left(\frac{2\pi i x'}{L}\right) \quad (4.21)$$

Where $0 \leq x \leq L$. The F_{DC} represents the magnitude of the DC component and the F_i corresponds to the amplitude of the i^{th} sinusoid that has N_i cycles over a length L . From an electromagnetic perspective, the number of cycles per unit length is an important parameter since it signifies the periodicity. Thus, one can write (4.21) as:

$$E_x(x') = F_{DC} + \sum_{i=N_1}^{N_2} F_i \sin(2\pi\alpha_i x') \quad (4.22)$$

where $\alpha_i = i/L$ is the number of cycles per unit length for the i^{th} sinusoid. Since the Fourier transform of each individual sine function provides a summation of two sinc functions, the Fourier Transform of this 1D line distribution (which gives us the plane wave spectrum) can be expressed as:

$$A_x(x') = F_{DC} L \text{sinc}\frac{k_x L}{2} + \frac{1}{2j} L \sum_{i=N_1}^{N_2} F_i \left[\text{sinc}(k_x + 2\pi\alpha_i) \frac{L}{2} - \text{sinc}(k_x - 2\pi\alpha_i) \frac{L}{2} \right] \quad (4.23)$$

Where $k_x = k \sin \theta$. Thus, one observes that each sine function of α cycles per unit length provides two sinc functions having a maxima at $\pm \sin^{-1}(\lambda\alpha)$. The fact that a sinusoid *amplitude* ripple results in a grating lobe for both positive and negative values of θ is also a good indication that the ripples in the amplitude is responsible for the high sidelobe envelope of the HFOSR. A deeper look into (4.23) reveals several interesting features:

1. As one incorporates a greater *range* of α_i into the distribution for the same length L , the corresponding sinc functions spread across a greater angular range, thereby increasing the *width* of the sidelobe envelope.
2. For a small L , the sinc function corresponding the each α_i will be broad enough that they overlap significantly. This causes the sidelobe envelope to rise significantly. How-

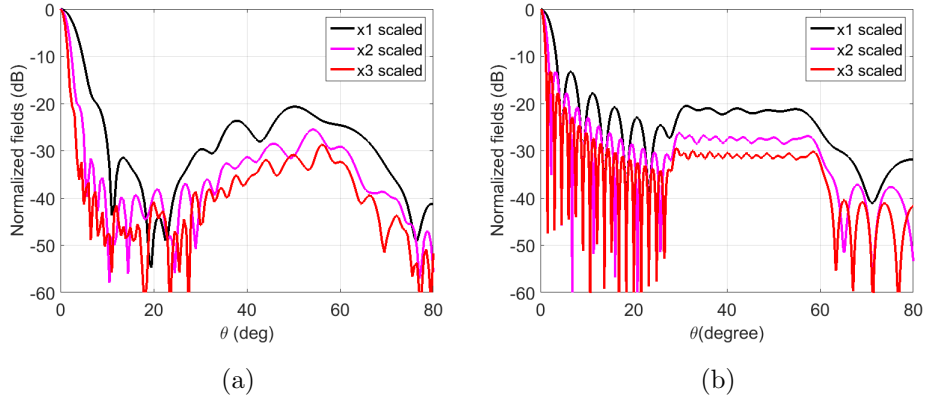


Figure 4.24: Understanding the behavior of sidelobe envelope as the design scales to larger dimensions using analytical equations. (a) Simulated results and (b) Analytical obtained with $\alpha_i = 30, 31 \dots, 55$, $F_i = 1$ and $F_{DC} = 30dB$. Note that the analytical model accurately recovers the trends seen for the sidelobe envelope.

ever, as L increases, the sinc functions will grow narrower and thus reducing the overlap, ultimately reducing the level of the sidelobe envelope.

3. The other factor that determines the relative level of the sidelobe envelope is the ratio between F_{DC} and the each of the F_i . If F_{DC} completely dominates, then the far field will not see any effect of the sinusoid ripples.

To relate this to the behavior of the stepped reflector, we first study the FFT of the near-fields of the 20 cm, 40 cm and 60 cm HFOSR designs each with an $F/D=0.5$. As one can see from Figure 4.23, the number of cycles per unit length (α_i) remain roughly constant as the design scales, resulting in similar width of the envelope. Now if one uses (4.21) such that α_i ranges from 30 to 55 in steps of 1, all F_i are chosen to be identical, and the F_{dc} is chosen to be 30 dB greater than F_{dc} , one can observe that one recovers an almost similar sidelobe envelope (width and level) as the design scales as. This is illustrated in Figure 4.24. From this exercise, it becomes clear that a diameter of around 50λ is desirable if one wants to ensure a lower sidelobe. Note that this is consistent with the 1m reflector simulations at 35.75 GHz (diameter of 120λ), where the sidelobe envelope was below 40 dB.

CHAPTER 5

Conclusions

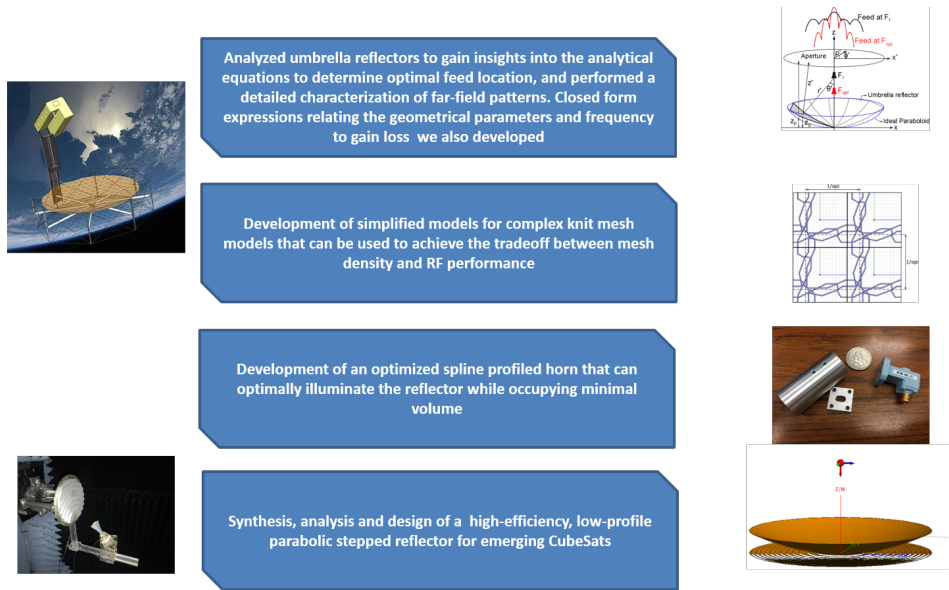
The recent advances in the field of VLSI and microelectronics has led to a drastic reduction in the size of electronic devices, while increasing its functionality. This massive scaling has resulted in the development of CubeSats, which are fully functional satellites but can be as small as a cube of volume $10 \times 10 \times 10 \text{ cm}^3$ and weight under 1.33 Kg. This significantly reduces the cost of developing and launching CubeSats, thereby enabling widescale access to space missions. While most CubeSat missions that have been launched use patch or wire antennas because of their ease of integration with the CubeSat, such antennas cannot meet the requirements for space missions that require high data rates and/or spatial resolution. The inherent proportionality between physical size of the antenna and its gain makes achieving the tradeoff between RF performance and mechanical complexity a major challenge.

This research addresses this very challenge. A significant aspect of this dissertation involved the development of one of the largest aperture antennas at Ka-band for NASA's RainCube mission – a 1m mesh deployable offset reflector antenna that can be stowed in a volume of just 3U ($10 \times 10 \times 30 \text{ cm}^3$). This project was a collaboration between UCLA, JPL and Tendeg LLC. The motivation behind this research was to enable a constellation of CubeSat based precipitation radars that can observe weather phenomenon that develops over a small time span. Some of the key contributions of this research were: (a) Studying the RF performance of complex knit mesh surfaces to establish the relation between number of openings, wire diameter and RF transmission loss, (b) development of an optimized horn feed using a combination of particle swarm optimization and finite element analysis, (c) fabrication and measurement of the feed horn and (d) assessing the impact of chassis on reflector radiation pattern. The dissertation also describes the RF analysis of the CAD reflector surface that

was generated through laser-scanning of the fabricated reflector. Further, the appearance of grating lobes that occur due to periodic errors caused by mesh faceting were studied, and recommendations were made to reduce their levels. The reflector antenna achieved a measured gain of 49.2 dB and beamwidths of 0.6° at 35.75 GHz. These results matched very closely with simulations, and marked a major milestone in the arena of high gain antennas for CubeSats.

The drive to develop antennas that can enable advanced CubeSat missions requiring high data rates also led to the analysis of well-known architectures from the point of view of its integration with the small CubeSat form factor. One class of reflector antennas that has been widely used for space applications is the umbrella reflector. The surface of an umbrella reflector consists of a discrete number of parabolic ribs which are connected through surfaces called gores. The gore surface has zero curvature in one direction, causing it to deviate from an ideal parabolic surface. While a large number of ribs improve the RF performance, it increases the mechanical complexity making it unsuitable for CubeSats. This dissertation revisited the previous works that have been published on this topic with the perspective of facilitating the integration of umbrella reflectors with CubeSats. In particular, the closed form expressions to determine the optimal feed location were studied, and their range of applicability was demonstrated through parametric tuning of feed position. Further, several closed form expressions were developed that related the boresight gain loss of the umbrella reflector to its geometrical parameters and frequency of operation. The periodic errors that stem from the umbrella reflector topology results in far-field grating lobes, which were characterized as a part of this work.

This research also develops a novel metal-only, low-profile architecture that can be integrated readily with CubeSats. The reflector surface consists of multiple parabolic sections that scatter in phase to provide a directive beam. Profile heights of the order of half a wavelength can be obtained using this technique, making it very suitable for CubeSat missions at mmWave frequencies. Since the antenna consists of discrete sections, it can be 3D printed making it an economical solution for CubeSats. A prototype of an offset stepped parabolic reflector was built and measured with very encouraging results. Since the reflector aperture



88

Figure 5.1: Major contributions of this research.

consists of discrete parabolic sections, the near-field amplitude distribution of such reflectors have periodic ripples, which can manifest themselves as a wide sidelobe envelope. Insights into this phenomenon were provided through the development of simplified numerical models that can represent this phenomenon.

The key contributions of this research are highlighted in Figure 5.1. As advanced space missions with CubeSats become a reality, we look forward to several futuristic missions with CubeSats that were impossible before, and the development of novel out-of-the-box antennas to support these missions.

APPENDIX A

Extending Formulation of Umbrella Reflectors for Controlling Surface Between Ribs

It was seen in chapter 2 that the equation of the umbrella reflector surface with a rib focal length of F_r could be derived as:

$$z_g = \frac{\rho'^2}{4F_g(\phi')} \quad (\text{A.1})$$

Where F_g is expressed as:

$$F_g(\phi) = \frac{F_r \cos^2(\pi/N_g)}{\cos^2 \frac{\phi'_m + \phi'_{m+1} - 2\phi'}{2}} \quad (\text{A.2})$$

where $\phi_m = 2\pi(m-1)/N_g$ and ρ' and ϕ' represent the polar aperture coordinates. The coordinate system can be seen in Figure A.1. Equations (A.1) and (A.2) can now be combined to yield:

$$z_g = \frac{\rho'^2}{4F_r/\alpha^2} = \frac{\rho'^2 \alpha^2}{4F_r} \quad (\text{A.3})$$

where α can be defined as:

$$\alpha = \frac{\cos \frac{\phi'_m + \phi'_{m+1} - 2\phi'}{2}}{\cos \pi/N_g} \quad (\text{A.4})$$

Thus, at points where ϕ' becomes 0, $2\pi/N_g$, $4\pi/N_g$ and so on, α becomes 1, so that equation A.3 reduces to the equation of a parabolic curve. These formulations, however, allows for the formulation of wider family of surfaces. This can be achieved by introducing a factor κ in the expression of α as follows:

$$\alpha' = \left[\frac{\cos \frac{\phi'_m + \phi'_{m+1} - 2\phi'}{2}}{\cos(\pi/N_g)} \right]^\kappa \quad (\text{A.5})$$

This results in a new surface whose features depend on κ , and can be defined as:

$$z_\kappa = \frac{\rho'^2}{4F_r/\alpha'^{2\kappa}} = \frac{\rho'^2 \alpha'^{2\kappa}}{4F_r} \quad (\text{A.6})$$

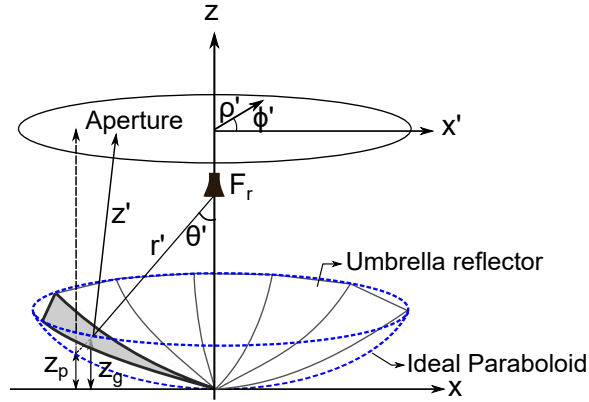


Figure A.1: Coordinate system reference for the umbrella reflector.

It is intuitive by an inspection of (A.6) that if $\kappa = 0$, the equation of the surface would reduce to the equation of an ideal paraboloid. For $\kappa = 1$, the equation would result in an umbrella reflector. Regardless of the value of κ , the value of α' will be 1 when ϕ' is on the ribs. Thus, the value of κ essentially modulates the surface between the ribs. Representative surfaces corresponding to various values of κ are shown in Figure A.2. Owing to the fact that a single parameter κ can modulate the surface between the ribs, this surface equation can be paired with an optimizer to optimize the surface geometry of the reflector for future applications.

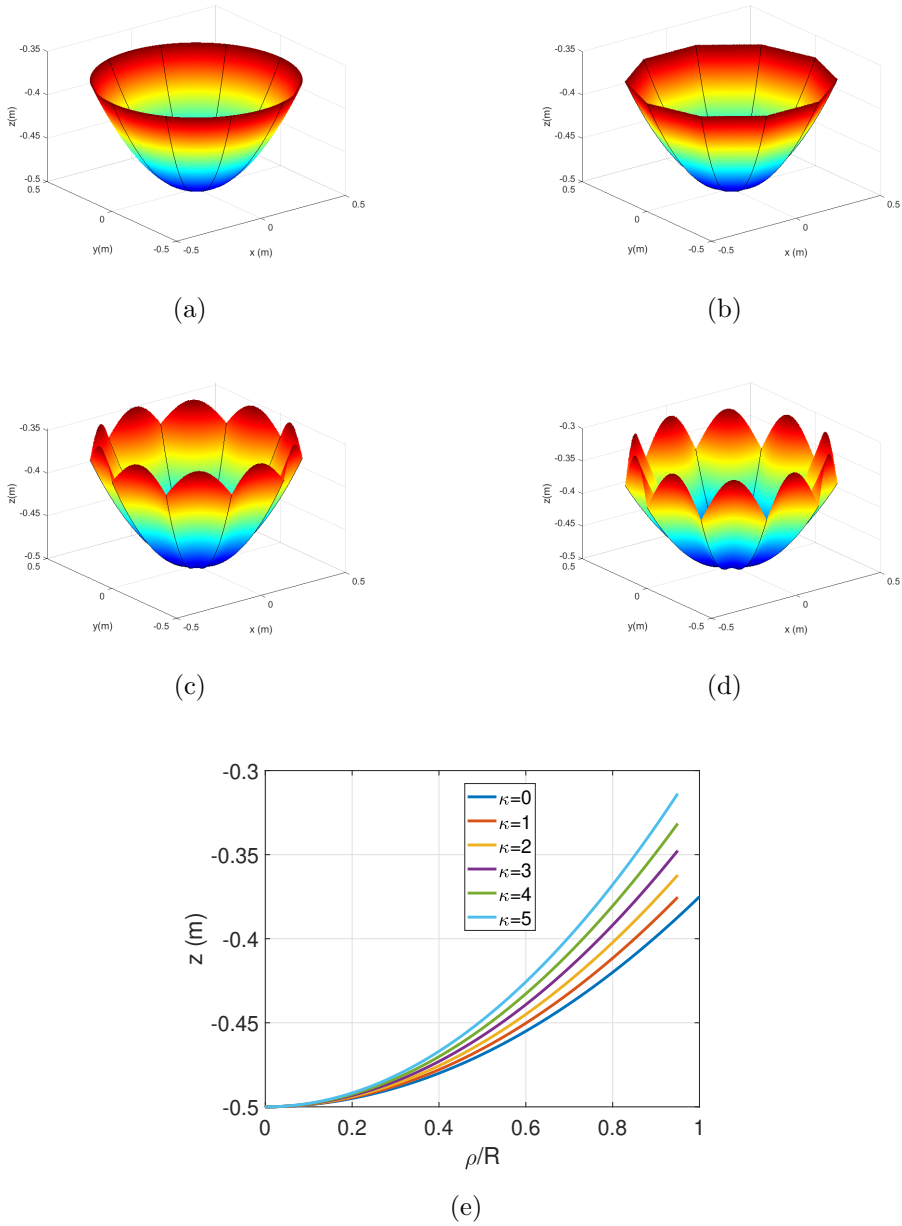


Figure A.2: Surfaces created by different values of κ in (A.6). (a) $\kappa = 0$ - ideal paraboloid. (b) $\kappa = 1$ - Umbrella reflector, (c) $\kappa = 3$, (d) $\kappa = 5$. (e) Profile of the surface along the $\phi = \pi/N_g$ for various values of κ . Note that as the value of κ increases, the surface tends to bend more inward from the rib.

APPENDIX B

Computing the Normals for an Umbrella Reflector Surface

In this appendix, we derive the equations of the normals to the umbrella reflector surface at the general point on its surface. This is especially useful when one does Physical Optics (PO) analysis of the reflector since the PO current J_{PO} at every point on the reflector can be expressed as $J_{PO} = 2\hat{n} \times \vec{H}_i$ where \hat{n} is the unit normal and \vec{H}_i is the incident magnetic fields. To start the derivation, we assume the general equation developed for the κ based surfaces in Appendix A. The normals for the umbrella reflector can be simply derived by substituting $\kappa=1$ in the general equations. The generic equation derived in Appendix A was:

$$z_\kappa = \frac{\rho'^2}{4F_r/\alpha'^{2\kappa}} = \frac{\rho'^2\alpha'^{2\kappa}}{4F_r} \quad (\text{B.1})$$

where

$$\alpha' = \left[\frac{\cos \frac{\phi'_m + \phi'_{m+1} - 2\phi'}{2}}{\cos(\pi/N_g)} \right]^\kappa \quad (\text{B.2})$$

The variables ρ' and ϕ' represent the polar aperture coordinates and can be related to rectangular coordinates as:

$$\rho' = \sqrt{x'^2 + y'^2} \quad (\text{B.3})$$

$$\phi' = \tan^{-1} \frac{y'}{x'} \quad (\text{B.4})$$

To compute the normal, we express the surface in the form $F(x, y, z) = z - f(x, y) = 0$. The equation for the normal can then be derived by taking the gradient of $F(x, y, z)$.

The function $F(x, y, z)$ can thus be expressed as:

$$F(x', y', z') = z_\kappa - \frac{\rho'^2\alpha'^{2\kappa}}{4F_r} = 0 \quad (\text{B.5})$$

The gradient of F can now be computed as:

$$\nabla F(x', y', z') = \frac{\partial F}{\partial x'} \hat{x} + \frac{\partial F}{\partial y'} \hat{y} + \frac{\partial F}{\partial z'} \hat{z} \quad (\text{B.6})$$

In order to compute the gradient, the following derivatives are necessary:

$$\rho \frac{\partial \rho}{\partial x} = x \quad (\text{B.7})$$

$$\rho \frac{\partial \rho}{\partial y} = y \quad (\text{B.8})$$

$$\frac{\partial \alpha'}{\partial x} = -K'(x', y') \frac{1}{\cos \frac{\pi}{N_g}} \sin \left(\frac{\phi'_m + \phi'_{m+1} - 2 \tan^{-1}(y'/x')}{2} \right) \frac{y'}{x'^2 + y'^2} \quad (\text{B.9})$$

$$\frac{\partial \alpha'}{\partial y} = K'(x', y') \frac{1}{\cos \frac{\pi}{N_g}} \sin \left(\frac{\phi'_m + \phi'_{m+1} - 2 \tan^{-1}(y'/x')}{2} \right) \frac{x'}{x'^2 + y'^2} \quad (\text{B.10})$$

$$K'(x', y') = \kappa \left[\frac{\cos \frac{\phi'_m + \phi'_{m+1} - 2\phi'}{2}}{\cos(\pi/N_g)} \right]^{\kappa-1} \quad (\text{B.11})$$

The components for ∇F can now be computed as:

$$(\nabla F)_x = -\frac{1}{4F_r} \left(2\rho' \frac{\partial \rho'}{\partial x} \alpha'^2 + 2\rho'^2 \alpha' \frac{\partial \alpha'}{\partial x} \right) \quad (\text{B.12})$$

$$(\nabla F)_y = -\frac{1}{4F_r} \left(2\rho' \frac{\partial \rho'}{\partial y} \alpha'^2 + 2\rho'^2 \alpha' \frac{\partial \alpha'}{\partial y} \right) \quad (\text{B.13})$$

$$(\nabla F)_z = 1 \quad (\text{B.14})$$

These equations can be readily used to compute the reflector normals for PO analysis.

APPENDIX C

Cylindrical Waveguide Modes and their Applications for Reflector Antenna Feed Development

In this appendix, we revisit the modes that can be excited within a cylindrical waveguide from the perspective of developing innovative feeds for reflectors. The TE and TM modes for an infinite cylindrical waveguide can be derived as [190]:

TE_{nm} modes:

$$E_\rho = \frac{-j\omega\mu n}{k_c^2 \rho} (A \cos n\phi - B \sin n\phi) J_n(k_c \rho) e^{-j\beta z} \quad (C.1)$$

$$E_\phi = \frac{-j\omega\mu}{k_c} (A \sin n\phi + B \cos n\phi) J'_n(k_c \rho) e^{-j\beta z} \quad (C.2)$$

TM_{nm} modes:

$$E_\rho = \frac{-j\beta}{k_c} (A \sin n\phi + B \cos n\phi) J'_n(k_c \rho) e^{-j\beta z} \quad (C.3)$$

$$E_\phi = \frac{-j\beta n}{k_c^2 \rho} (A \cos n\phi - B \sin n\phi) J_n(k_c \rho) e^{-j\beta z} \quad (C.4)$$

Where E_ρ and E_ϕ represent the components of the electric field in the cylindrical coordinate system, and $\beta = \sqrt{k^2 - k_c^2}$, where $k = \omega\sqrt{\mu\epsilon}$. k_c represents the cut-off wave number which is defined as:

$$k_c = \frac{P'_{nm}}{a} \quad \text{for } TE_{nm} \quad (C.5)$$

$$k_c = \frac{P_{nm}}{a} \quad \text{for } TM_{nm} \quad (C.6)$$

where P_{nm} and P'_{nm} represent the m^{th} root of J_n and J'_n respectively. A and B represent excitation coefficients and control the orientation of the mode. Feed horns for reflectors typically use 3 modes: TE_{11} (fundamental mode), TM_{11} and TE_{21} . The field distributions

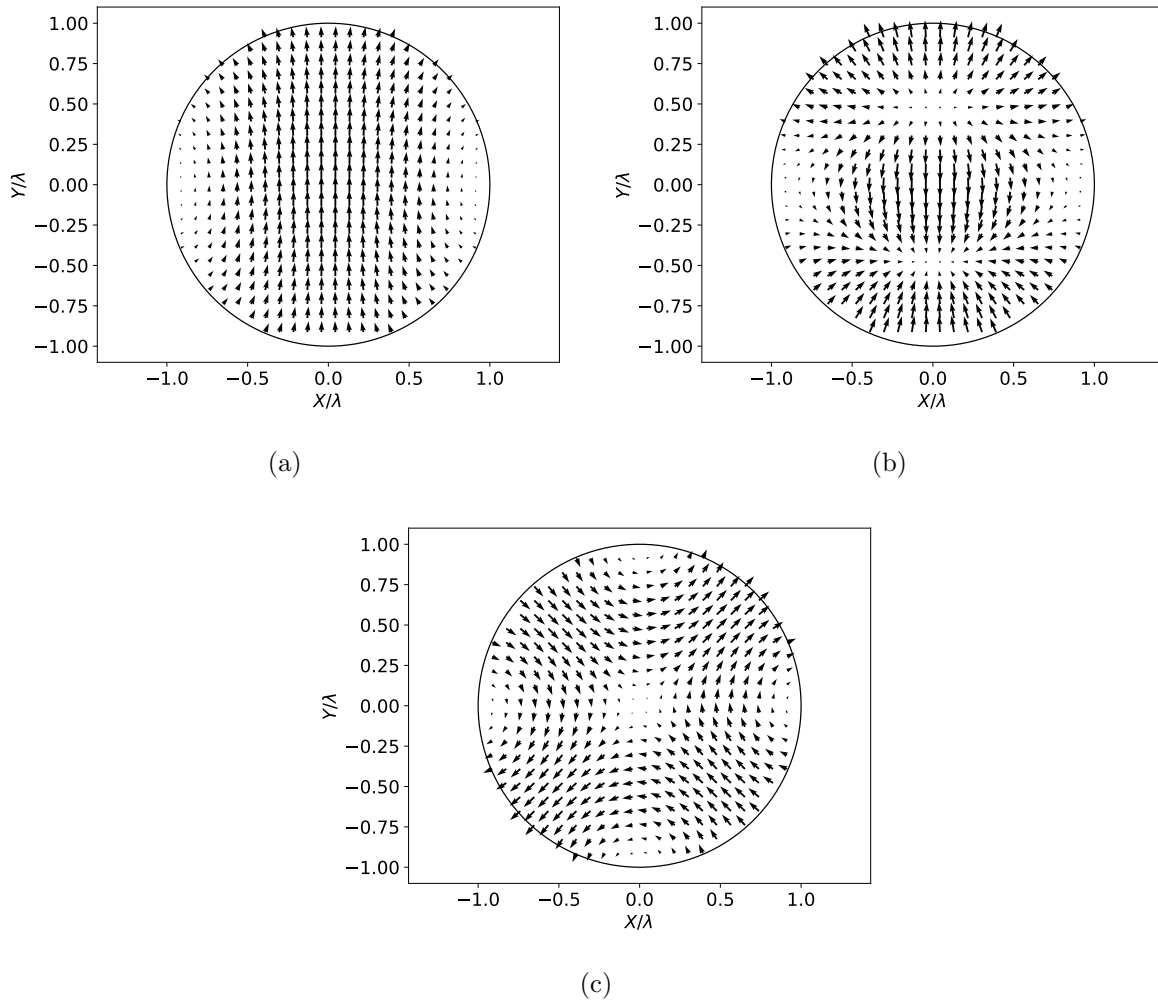


Figure C.1: Modal field distributions for (a) TE_{11} mode, (b) TM_{11} mode and (c) TE_{21} mode assuming an aperture of diameter 2λ .

for each of these modes are shown in Figure C.1 where an aperture diameter of $2a = 2\lambda$ is assumed for the horn. In a typical reflector design, the aperture diameter is chosen to get the required 10 dB beamwidths.

The equations for the far-field corresponding to the TE and TM modes are derived as [191]:

Far-fields for TE_{nm} mode:

$$E_\theta = j^{n+1} \frac{n\omega\mu}{2} \left[1 + \frac{\beta}{k} \cos \theta + \Gamma \left(1 - \frac{k_c}{k} \cos \theta \right) \right] \frac{J_n(k_c a) J_n(ka \sin \theta)}{\sin \theta} \sin n\phi \frac{e^{-jkr}}{r} \quad (\text{C.7})$$

$$E_\phi = j^{n+1} \frac{ka\omega\mu}{2} \left[\frac{\beta}{k} + \cos \theta - \Gamma \left(\frac{k_c}{k} - \cos \theta \right) \right] \frac{J_n(k_c a) J'_n(ka \sin \theta)}{1 - \left(\frac{k}{k_c} \sin \theta \right)^2} \cos n\phi \frac{e^{-jkr}}{r} \quad (\text{C.8})$$

Far-fields for TM_{nm} mode:

$$E_\theta = -j^{n+1} ka \frac{k_c}{\sin \theta} \left[\frac{k_c}{k} + \cos \theta + \Gamma \left(\frac{k_c}{k} - \cos \theta \right) \right] \frac{J'_n(k_c a) J_n(ka \sin \theta)}{1 - \left(\frac{k_c}{k \sin \theta} \right)^2} \cos n\phi \quad (\text{C.9})$$

$$E_\phi = 0 \quad (\text{C.10})$$

Where Γ represents the reflection coefficient at the aperture of the antenna. For this section, this is assumed to be 0, which can be justified by the fact that if the antenna aperture is of the order of a wavelength, the mismatch between the guided wave impedance and free space impedance is minimal. Note that these equations provide far-fields assuming that the TE_{nm} fields are oriented along y direction and the TM_{nm} fields are oriented along x direction. In order to ensure both modes are polarized along y , the ϕ in (C.9) can be substituted by $\phi + \pi/2$.

The first step in understanding how these equations can aid the design of horn feed antennas, the analytical far-field equations were compared to full-wave simulation results in CST where a cylinder of 1λ radius and height of 2λ was created and multiple modes were excited on one end via a waveport. A comparison between the results from the analytical formulations and full-wave simulations is shown for the TE_{11} , TE_{21} and TM_{11} in Figures C.2, C.3 and C.4 respectively. It is evident that the analytical equations provide results that closely match full-wave simulation results allowing us to use the analytical equation to develop and understand the radiation properties of different modes.

Now, from the TE_{11} far-field pattern (Figure C.2), it can be observed that the radiation patterns in the two principal planes are significantly different. The E-plane pattern is relatively narrower with higher sidelobe level, whereas the H-plane pattern is broader with lower sidelobe envelope. This asymmetric illumination results in reduced aperture efficiency of the reflector antenna. It is also intuitive from the TM_{11} radiation patterns (Figure C.4a,

C.4b) that if a small amount of TM_{11} is combined with the TE_{11} mode, it could potentially result in symmetric feed pattern. Further, it can be observed that the cross pol patterns of the TE_{11} and TM_{11} bear resemblance to each other and thus if the combined correctly, the resultant pattern can have almost zero cross polarization. Indeed, it can be seen from Figure C.5 that if the radiation patterns (electric field amplitude) of the TM_{11} is scaled by a factor of 0.4 and added to the TE_{11} radiation patterns, the resulting pattern has a very symmetric beam and a cross polarization under -40 dB. While this removes the *feed* cross pol, the inherent asymmetry in the offset reflector geometry architecture will result in the reflector radiation pattern having high cross polarization in the plane orthogonal to the offset plane. This can be counteracted by the feed itself producing a cross pol that can cancel the cross-polarized currents on the reflector surface. If one observes the TE_{21} far-field patterns (Figure C.3) it can be seen that this mode produce cross-pol that has a similar appearance to that seen from typical offset reflectors. Thus, if one adds a scaled version of these fields to the previous $TE_{11} + 0.4TM_{11}$ combination, it is possible to achieve an illumination which is symmetric as well as reduces the *reflector cross polarization*. Through tuning the excitation coefficients, it was seen that if the radiation pattern of the TE_{21} is scaled by a factor of $0.15j$ and added to the previous combination of TE_{11} and TM_{11} , the resulting pattern has a cross-polarization level similar to a typical offset reflector (Figure C.5c, C.5d). Note that for all these runs, the analytical formulations were used for computations.

The feed patterns thus generated were imported as a point source into a reflector simulation software, and the resulting patterns are shown in Figure C.6. It can be seen that the TE_{11} mode provides a broader beam and lower sidelobes in the $y_r - z_r$ plane due to an increased edge taper. This is corrected by adding the TM_{11} mode which provides symmetric illumination. However, this mode changes the cross polarization of the reflector antenna minimally. Finally, when TE_{21} mode is added, the reflector copol patterns are not significantly affected, however the reflector cross polarization reduced by almost 10 dB.

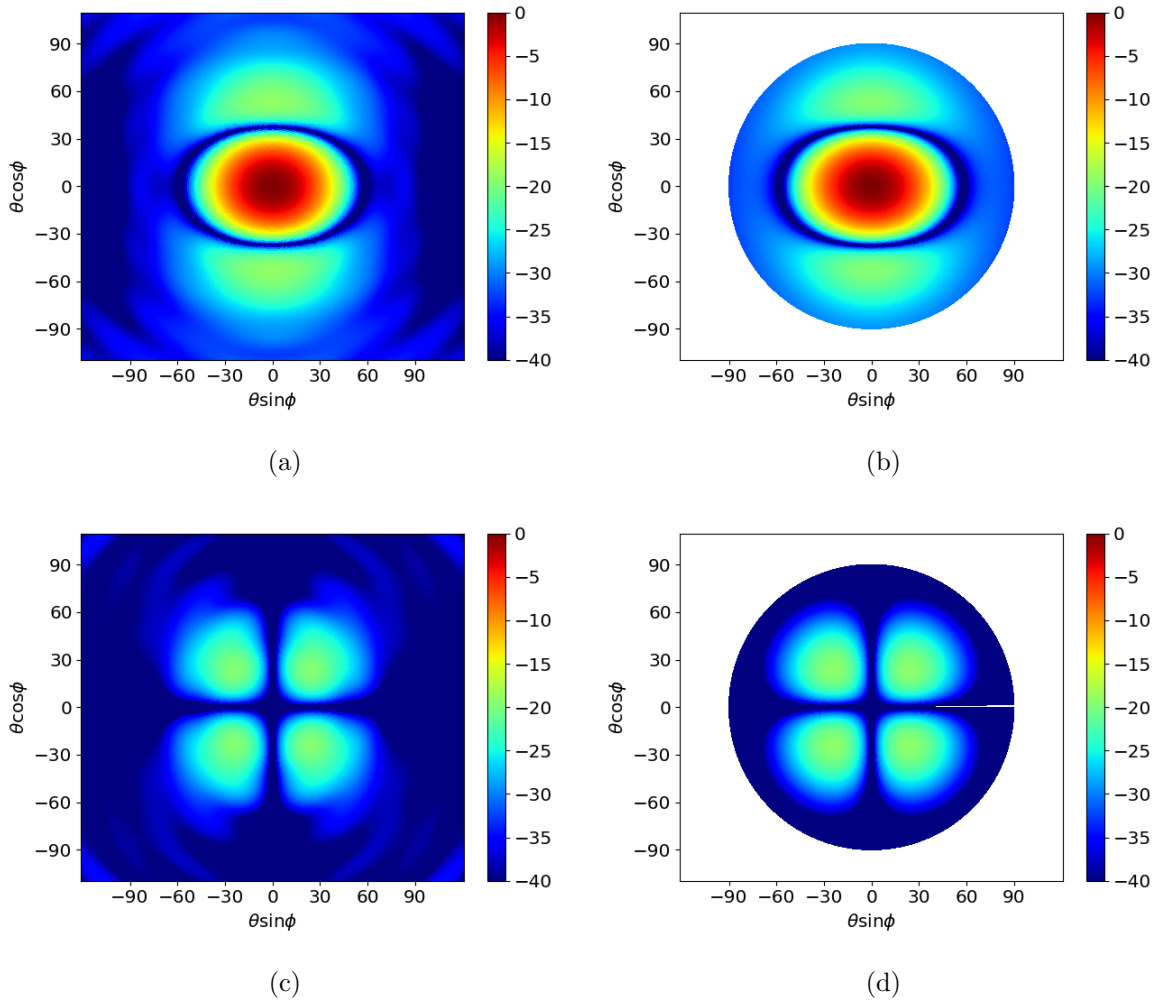


Figure C.2: Comparison between the far-fields resulting from the analytical equations and full-wave simulation for the TE_{11} mode. (a) Full-wave copol, (b) Analytical copol, (c) Full-wave xpol and (d) analytical xpol. All plots represent normalized amplitude in dB scale. The aperture is assumed to have a diameter of 2λ at 35.75 GHz.

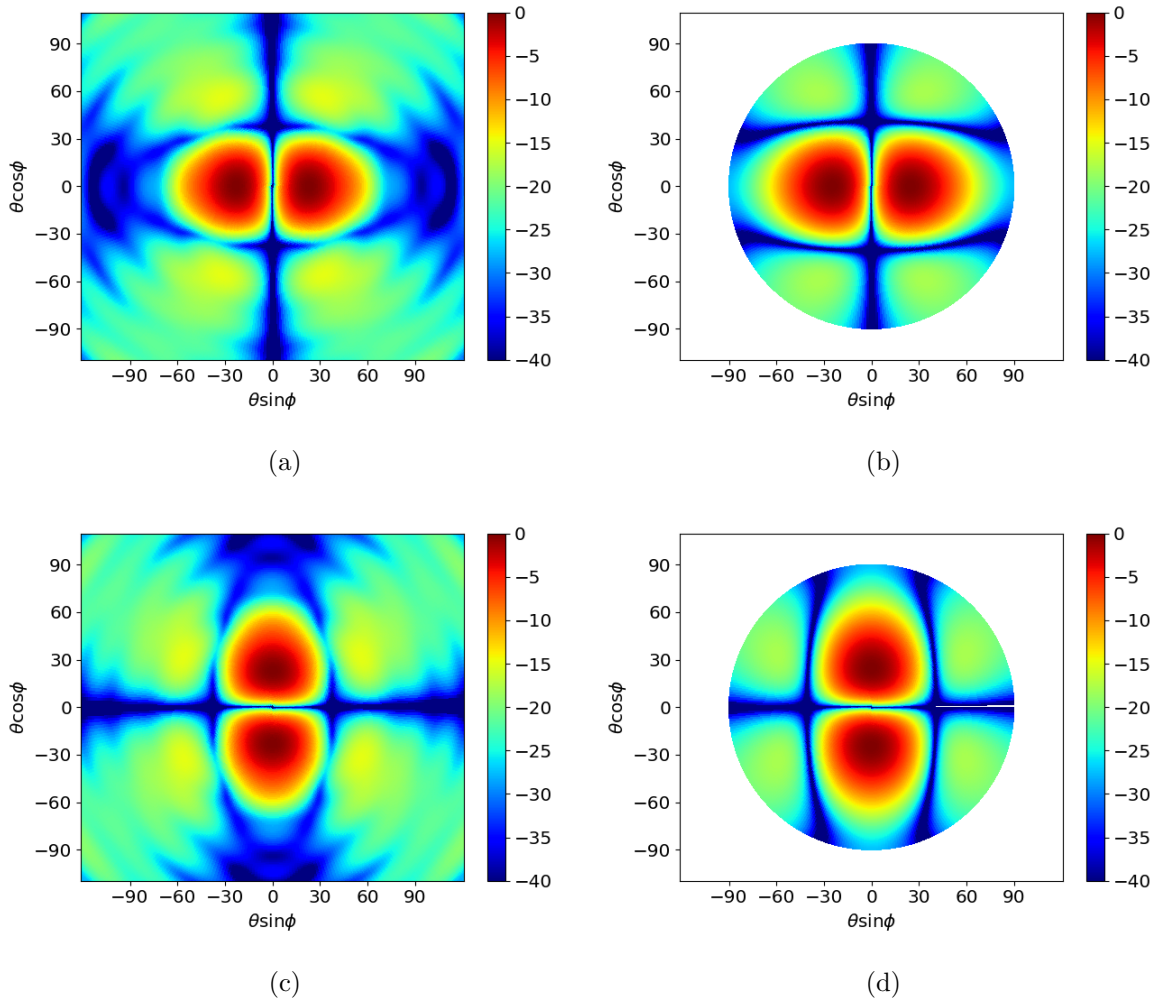


Figure C.3: Comparison between the far-fields resulting from the analytical equations and full-wave simulation for the TE_{21} mode. (a) Full-wave copol, (b) Analytical copol, (c) Full-wave xpol and (d) analytical xpol. All plots represent normalized amplitude in dB scale. The aperture is assumed to have a diameter of 2λ at 35.75 GHz.

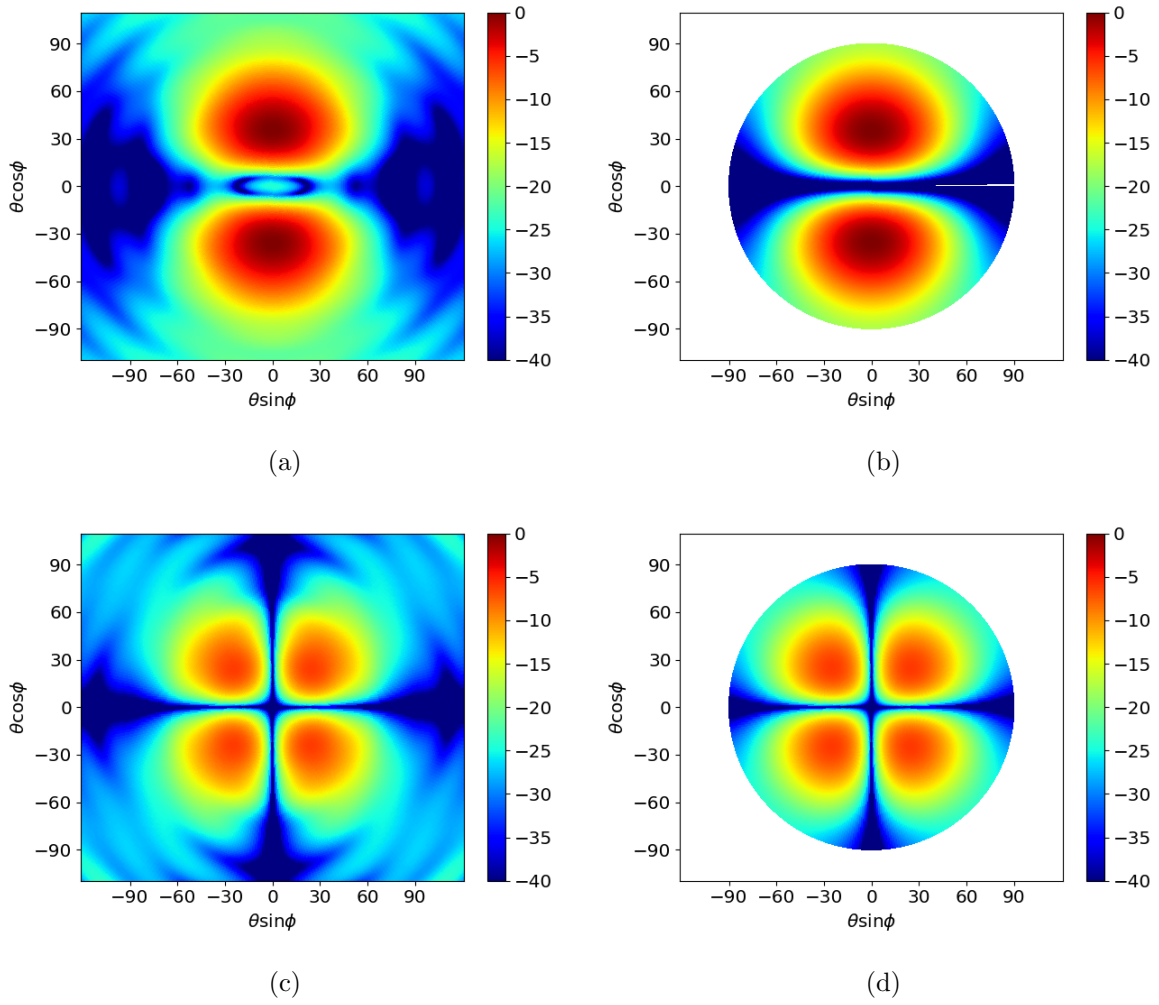


Figure C.4: Comparison between the far-fields resulting from the analytical equations and full-wave simulation for the TM_{11} mode. (a) Full-wave copol, (b) Analytical copol, (c) Full-wave xpol and (d) analytical xpol. All plots represent normalized amplitude in dB scale. The aperture is assumed to have a diameter of 2λ at 35.75 GHz.

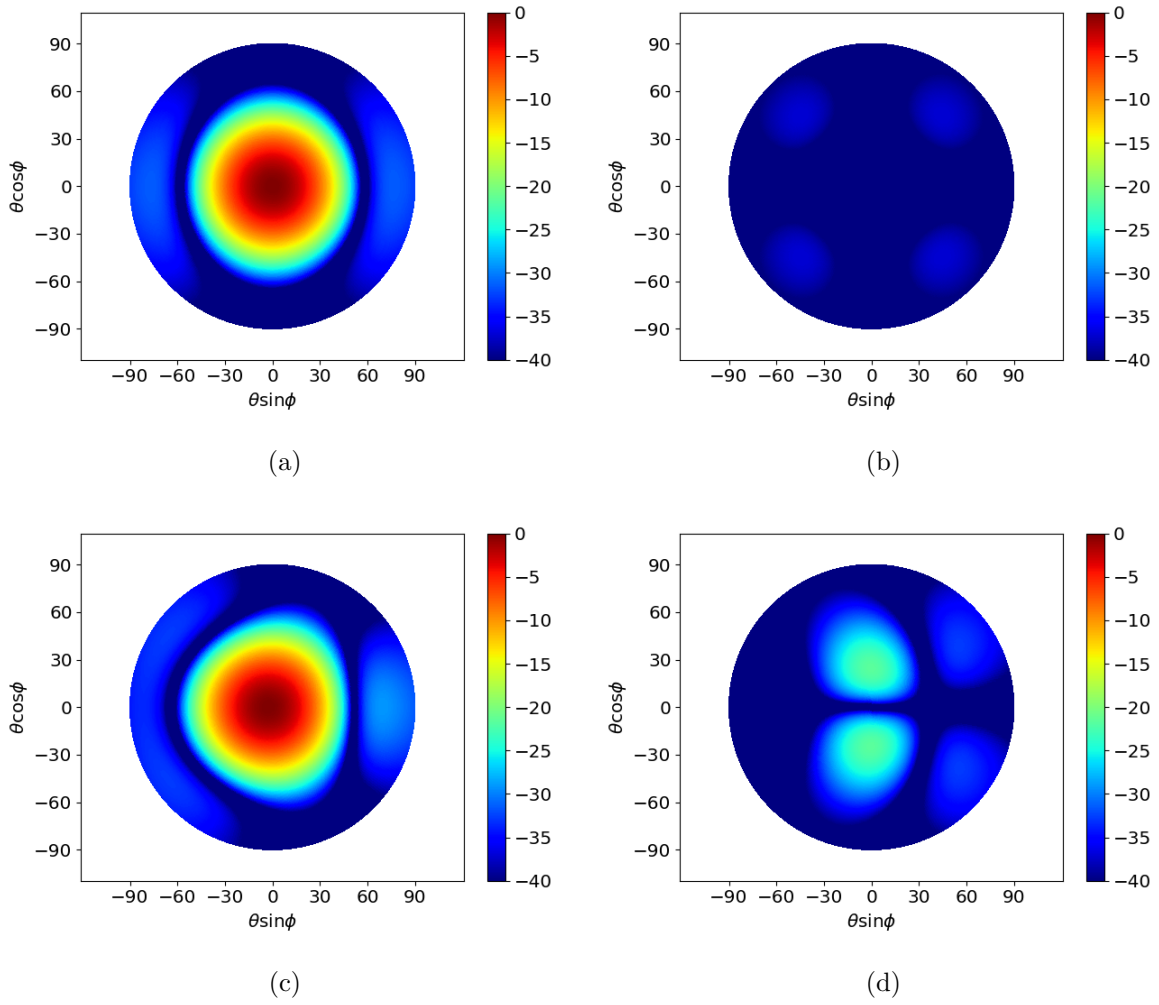
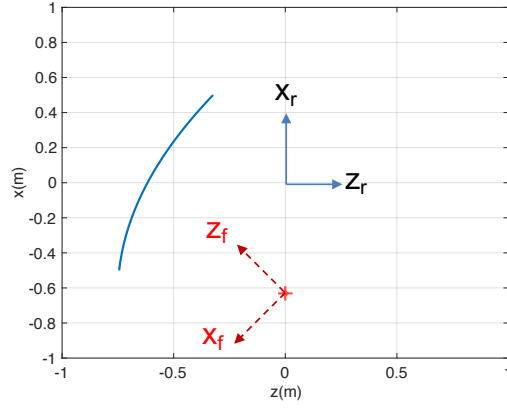
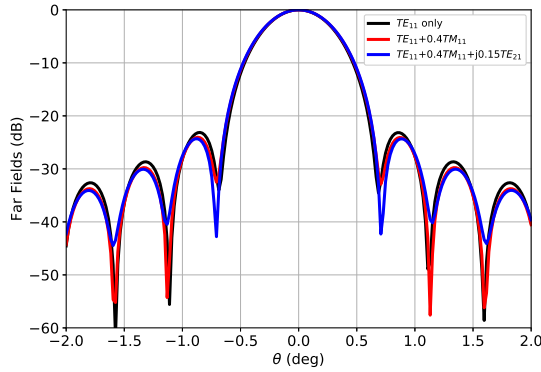


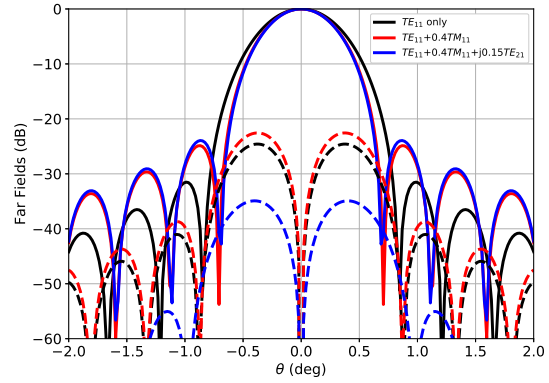
Figure C.5: Far-fields of modes combined to give desirable characteristics for illumination. (a) Copol and (b) xpol for $TE_{11} + 0.4TM_{11}$. (c) Copol and (d) xpol for $TE_{11} + 0.4TM_{11} + j0.15TE_{21}$. Note that the analytical formulations are used to generate these results. All plots represent normalized amplitude in dB scale.



(a)



(b)



(c)

Figure C.6: Reflector patterns when illuminated by the far-fields corresponding to a combination of different cylindrical modes. (a) Reflector geometry showing the coordinate systems - the feed coordinate system is indicated by a subscript of 'f' and the reflector far-field radiation pattern coordinate system is indicated with subscript 'r'. (a) $\phi = 0$ plane ($x_r - z_r$ plane) and (b) $\phi = 90$ plane ($y_r - z_r$ plane). Note that the feed patterns are all polarized along the y_r axis.

APPENDIX D

Determining the Slopes for Monotonic PCHIP spline

In this appendix, we describe the equation used to generate the spline profiled horn described in Chapter 3.

Given two points defined by (z_{i-1}, x_{i-1}) and (z_i, x_i) , the equation of the PCHIP spline $f_i(z)$ that connects them can be expressed as (refer to Figure D.1) [133]:

$$f_i(z) = h_{00}(\bar{z})x_{i-1} + h_{01}(\bar{z})x_i + h_{10}(\bar{z})(z_i - z_{i-1})m_{i-1} + h_{11}(\bar{z})(z_i - z_{i-1})m_i \quad (\text{D.1})$$

where \bar{z} represents the normalized independent variable z scaled as

$$\bar{z} = \frac{z - z_{i-1}}{z_i - z_{i-1}} \quad (\text{D.2})$$

which maps z to the interval $[0, 1]$ for the i th segment. The Hermite basis functions can be defined as

$$h_{00}(\bar{z}) = 2\bar{z}^3 - 3\bar{z}^2 + 1 \quad (\text{D.3})$$

$$h_{10}(\bar{z}) = \bar{z}^3 - 2\bar{z}^2 + \bar{z} \quad (\text{D.4})$$

$$h_{01}(\bar{z}) = -2\bar{z}^3 + 3\bar{z}^2 \quad (\text{D.5})$$

$$h_{11}(\bar{z}) = \bar{z}^3 - \bar{z}^2 \quad (\text{D.6})$$

Thus, the unknowns in (D.1) are m_{i-1} and m_i . The choice of these variable ultimately determine the monotonicity of the splines. In order to find the values of m_i , first define the slopes of a straight line that connects the two points. We denote this as Δ_i . Thus,

$$\Delta_i = \frac{z_{i+1} - z_i}{x_{i+1} - x_i} \quad (\text{D.7})$$

The process followed is as follows:

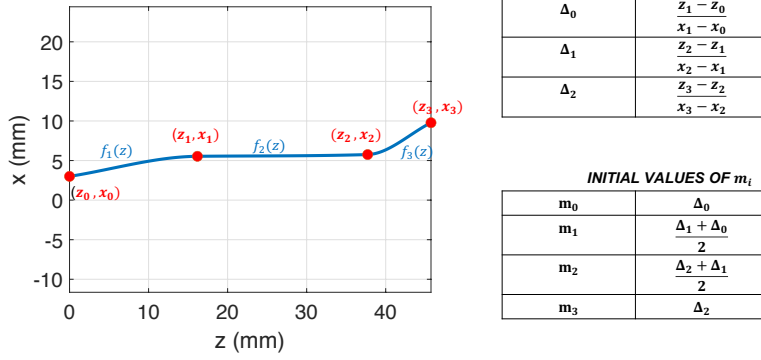


Figure D.1: A representative spline profile through the points (x_0, y_0) , (x_1, y_1) , (x_2, y_2) and (x_3, y_3) . These points are marked by red dots. The values of Δ_i and initial values of m_i are tabulated. These initial values must be corrected to ensure monotonicity as described in the text.

1. Initialize m_i . A good starting guess is to choose: $m_i = \frac{\Delta_i + \Delta_{i-1}}{2}$. The values of m corresponding to the starting point and ending point can be chosen to be the slope of the line following and preceding it respectively. If $\Delta_i = 0$, set $m_i = m_{i+1} = 0$.
2. Define $\alpha_i = m_i / \Delta_i$ and $\beta_i = m_{i+1} / \Delta_i$.
3. If α_i and β_i are such that $(\alpha_i^2 + \beta_i^2) < 9$, then retain the original values of m_i and m_{i+1} .
4. If α_i and β_i are such that $(\alpha_i^2 + \beta_i^2) > 9$, then define $m_i = \tau \alpha_i \Delta_i$ and $m_{i+1} = \tau \beta_i \Delta_i$, where $\tau = \frac{3}{\sqrt{\alpha_i^2 + \beta_i^2}}$.

APPENDIX E

Phase Center of Reflector Antennas

E.1 Phase Center Derivation

The position of the phase center, in general, is a complex function of geometry and excitation of the antenna. For reflector antennas, the dependency on the illumination of the feed antenna can make things even more unintuitive. However, through some simplifications and assumptions, one can find an *estimate* of the phase center, after which one can optimize. This work was motivated by the formulations presented in [192]. To start with, consider the well-known expression relating the current distribution to the far-field pattern:

$$\vec{E}_{far} = -\frac{j\omega\mu}{4\pi} \frac{e^{-jkr}}{r} \int \vec{J}(r') e^{jk\hat{r}\cdot r'} dr' \quad (\text{E.1})$$

where the vectors \hat{r} and r' are vectors that point from the far-field origin to the far-field direction and a specific point on the AUT respectively. The question of finding the phase center can thus be posed in the following manner: where should the far-field coordinate origin be positioned so that the integral itself results in a function which has a *phase* that is weakly dependent on the observation angle in the region of interest. For specific cases, one can find an analytical phase center for the entire radiation pattern. This usually arises as a consequence of the symmetry in the current distribution of the antenna - if one finds an origin such that $J(-r') = J(r')$ for all r' , the exponential factors combine to give a real function (sine or cosine). For complex geometries, such as reflector antennas, an *estimate* of the phase center can still be obtained if one finds a far-field origin such that the quantity $\sum_{r_i} r - \hat{r}\cdot r'_i$ is weakly dependent of θ and ϕ . Note that this does not account for any current asymmetry that could arise due to the fact that the reflector is offset, or a non-ideal feed illumination.

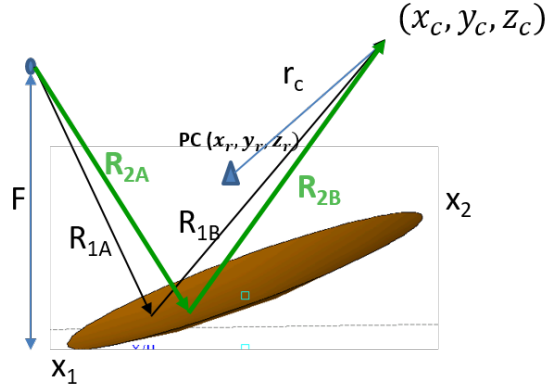


Figure E.1: Coordinate definitions for reflector phase center estimation.

E.2 Formulation

Consider the geometry shown in Figure E.1. The limits of the reflector aperture along x and y directions are denoted by (x_1, x_2) and (y_1, y_2) respectively. The location of the phase center is denoted as (x_r, y_r, z_r) . Assuming that the reference origin is located at the focal point, the problem of finding the phase center can be mathematically expressed as locating a point (x_r, y_r, z_r) such that the quantity r_ϵ expressed as (E.2)), is independent of far-field observation angles θ and ϕ .

$$r_\epsilon = \lim_{r_c \rightarrow \infty} \sum_i [(R_{iA} + R_{iB}) - r_c] \quad (\text{E.2})$$

If (x, y, z) refers to a point on the reflector, referring to Figure E.1, the point must satisfy the equation:

$$z = \frac{x^2 + y^2}{4F} - F \quad (\text{E.3})$$

The observation point (x_c, y_c, z_c) can be related to the phase center (x_r, y_r, z_r) and r_c through:

$$x_c = x_r + r_c \sin \theta \cos \phi \quad (\text{E.4})$$

$$y_c = y_r + r_c \sin \theta \sin \phi \quad (\text{E.5})$$

$$z_c = z_r + r_c \cos \theta \quad (\text{E.6})$$

The quantity $R_{iA} + R_{iB}$ can be generally written as:

$$r_t = R_{iA} + R_{iB} = \sqrt{x^2 + y^2 + z^2} + \sqrt{(x - x_c)^2 + (y - y_c)^2 + (z - z_c)^2} \quad (\text{E.7})$$

Since the reflector is a continuous, analytically defined surface, one can express (E.2) as:

$$r_\epsilon = \lim_{r_c \rightarrow \infty} \left[\frac{1}{A_p} \int_{x_1}^{x_2} \int_{y_1}^{y_2} r_t dx dy - r_c \right] \quad (\text{E.8})$$

where A_p is the area of the aperture expressed as $(x_2 - x_1)(y_2 - y_1)$, and r_t is expressed in (E.7). To evaluate this expression, we note that:

$$\sqrt{x^2 + y^2 + z^2} = \sqrt{4F(z + F) + z^2} = z + 2F = \frac{x^2 + y^2}{4F} + F \quad (\text{E.9})$$

Thus, the expression for r_t becomes:

$$r_\epsilon = \frac{x^2 + y^2}{4F} + F + \sqrt{(x - x_r - r_c \sin \theta \cos \phi)^2 + (y - y_r - r_c \sin \theta \sin \phi)^2 + (z - z_r - z_c \cos \theta)^2} \quad (\text{E.10})$$

Post some algebraic evaluations, and noting that one can use $\lim_{x \rightarrow 0} \sqrt{1 - x} = 1 - x/2$, we arrive at:

$$\begin{aligned} r_\epsilon = & \left[\frac{x_1^2 + x_1 x_2 + x_2^2}{12F} + \frac{y_1^2 + y_1 y_2 + y_2^2}{12F} + F \right] \\ & - \left[\frac{x_1 + x_2}{2} - x_r \right] \sin \theta \cos \phi - \left[\frac{y_1 + y_2}{2} - y_r \right] \sin \theta \sin \phi - \\ & \left[\frac{x_1^2 + x_1 x_2 + x_2^2}{12F} + \frac{y_1^2 + y_1 y_2 + y_2^2}{12F} - F - z_r \right] \end{aligned} \quad (\text{E.11})$$

Now, finding (x_r, y_r, z_r) such that r_ϵ is independent of (θ, ϕ) is straightforward. One can simply use

$$x_r = \frac{x_1 + x_2}{2} \quad (\text{E.12})$$

$$y_r = \frac{y_1 + y_2}{2} \quad (\text{E.13})$$

$$z_r = \frac{y_1^2 + y_1 y_2 + y_2^2}{12F} - F \quad (\text{E.14})$$

to ensure that the terms that depend on the far-field observation angles completely disappear. Conventionally, offset reflector defined in terms of aperture radii along x and y axis (denoted

as a and b respectively), focal distance F , offset height d and clearance H . These parameters can be related back to the variables in Figure E.1 through:

$$x_1 = d - a \quad (\text{E.15})$$

$$x_2 = d + a \quad (\text{E.16})$$

$$y_1 = -y_2 = b \quad (\text{E.17})$$

The equations (E.12-E.14) can thus be written in the following form:

$$x_r = d \quad (\text{E.18})$$

$$y_r = 0 \quad (\text{E.19})$$

$$z_r = \frac{a^2 + b^2}{12F} - \left(F - \frac{d^2}{4F}\right) \quad (\text{E.20})$$

These equations denote that the phase center is located in the XZ plane (plane of offset), on a line parallel to z-axis that passes through the center of the projected aperture. These results are consistent with the derivations in [192]. Again, it is important to note that this does not take into account any asymmetry present in the current distribution, which commonly occurs in offset reflectors. The illumination of the reflector surface in the plane of offset can be different due to unequal path lengths, causing the phase center to deviate from this analytical formulation. The phase center for a symmetric reflector can be got by substituting $d = 0$ in the equations for offset reflectors (E.18)-(E.20), which result in:

$$x_r = 0 \quad (\text{E.21})$$

$$y_r = 0 \quad (\text{E.22})$$

$$z_r = \frac{a^2 + b^2}{12F} - F \quad (\text{E.23})$$

It can be seen from these equations that the analytical phase center lies very near the vertex of the paraboloid. The positions of the analytical phase centers for two representative geometries are shown in Figure E.2. The first geometry is a symmetric reflector of diameter 0.5m and F/D of 0.5, whereas the other is an offset reflector of diameter 1m with an F/D of 0.75 and an offset height d of 0.6312m. Both these geometries are inspired by the reflector antennas developed for the RainCube mission [107, 122]. It can be seen that the position

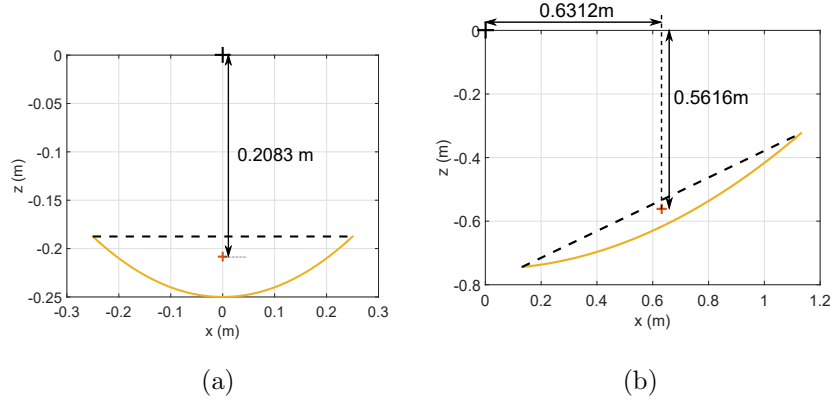


Figure E.2: Analytically determined phase centers for two representative geometries. (a) Symmetric reflector with diameter of 0.5m and F/D of 0.5 and (b) offset reflector with diameter 1m and F/D of 0.75.

of the phase center predicted via these analytical equations is somewhere in between the vertex and the rim along the axis of the reflector. The subsequent sections will analyze the effectiveness of these equations via comparison with full-wave simulations.

E.3 Simulation Results and Optimization of phase center

E.3.1 Finding the phase center through Particle Swarm Optimization

The pervious section elaborated on the analytical estimation of the phase center for symmetric and offset reflector. In this section, we use particle swarm optimization (PSO) to evaluate how effective the analytical equations are. In order to do this, we focus on the main-beam region (until the far-field magnitude decays to approximately 10 dB from its peak), and find the far-field reference that minimizes the phase variation in the $\phi = 0, 45, 90$ degree planes. The fitness function to minimize is given by the following equation:

$$f(x) = \frac{F(\phi = 0) + F(\phi = 45) + F(\phi = 90)}{3} \quad (\text{E.24})$$

where x represents the vector of optimization variables consisting of the displacement of the far-field coordinate system in the x, y and z directions. F represents the mean-square

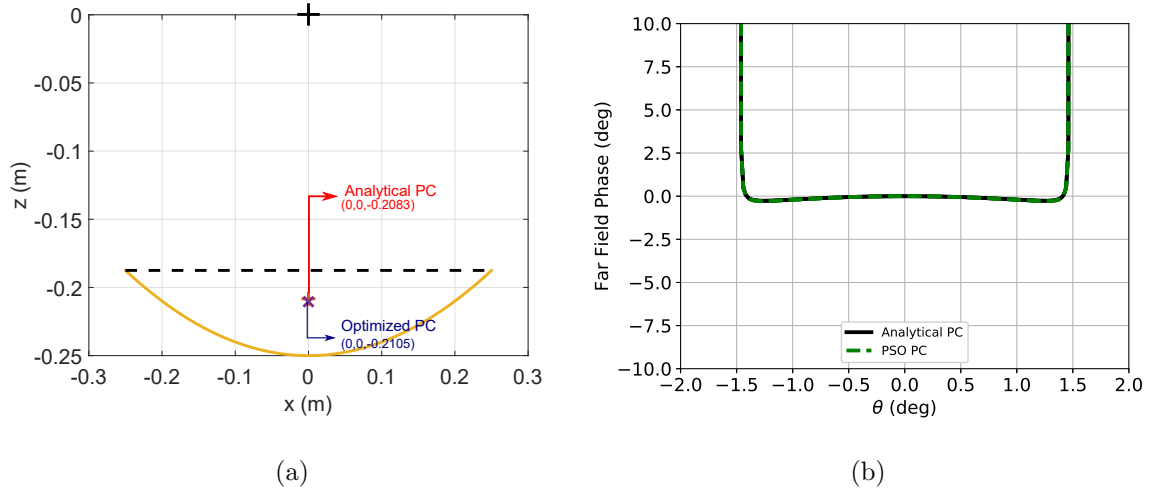


Figure E.3: Phase center for symmetric parabolic reflector antenna with aperture diameter $D=0.5\text{m}$ and F/D of 0.5.

deviation of the phase of the copol component, expressed as:

$$F(\phi) = \frac{1}{M} \sum_{m=1}^M [\angle E_{co}(\theta_m, \phi) - \angle \bar{E}_{co}(\phi)]^2 \quad (\text{E.25})$$

where M denotes the number of observation points in θ and \bar{E}_{co} represents the mean of the phase variation given as:

$$\bar{E}_{co}(\phi) = \frac{1}{M} \sum_{m=1}^M \angle E_{co}(\theta_m, \phi) \quad (\text{E.26})$$

An important point to note here is that moving of the far-field coordinate system does not necessitate a re-simulation of the entire reflector system - the effect can be mathematically modeled by multiplying the far-field with a phase factor of $\exp(-jk(\Delta x \sin \theta \cos \phi + \Delta y \sin \theta \sin \phi + \Delta z \cos \theta))$ where Δx , Δy and Δz represents the displacements in the far-field origin along the x , y and z direction respectively.

E.3.2 Symmetric Reflector

In this section, we investigate the case of a symmetric 0.5m reflector with an F/D of 0.5 as was used for a recent RainCube mission [107]. A cosine-Q feed which provides a 10 dB taper at the edges of the reflector and points along the axis of the reflector is used to simulate

the far-fields of the reflector. The positions of the analytical phase center and the optimized phase center is shown in Figure E.3a. The phase of the far-field with each of the phase center is compared in Figure E.3b. It is evident that for this case, the analytical equations predict the phase center very well. This is expected since the geometry of the reflector and the illumination are symmetric.

E.3.3 Offset Reflector

In this section, we consider the 1m offset geometry described (Diameter=1m, offset height $d=0.6312$). We consider the cases of F/D of 0.5, 0.75 and 1 to evaluate how close the analytical equations come to the optimized phase center. The position of the analytical and optimized phase center are shown in Figure E.4. Immediately, it can be seen that the difference in the analytical and optimized phase center reduces at the F/D increases. This is intuitive since the asymmetry in the reflector reduces as the F/D increases. Representative far-field phase results for $F/D=0.5$ are compared in Figure E.5. It is immediately evident that the analytical equations provide a very good estimation, however it may not necessarily be the best phase center especially in the offset plane where the reflector is not symmetric (and thus the current distributions are not fully symmetric). In the $\phi=0$ (XZ) plane, the analytical phase center provides a phase gradient, which can be corrected through optimization. For all the cases, the feed is tilted to point towards the center of projected aperture and a cosine-q feed which provides a 10 dB illumination at the subtended angle is used. A comparison of the fitness values for the analytical and optimized phase center are presented in Table E.1.

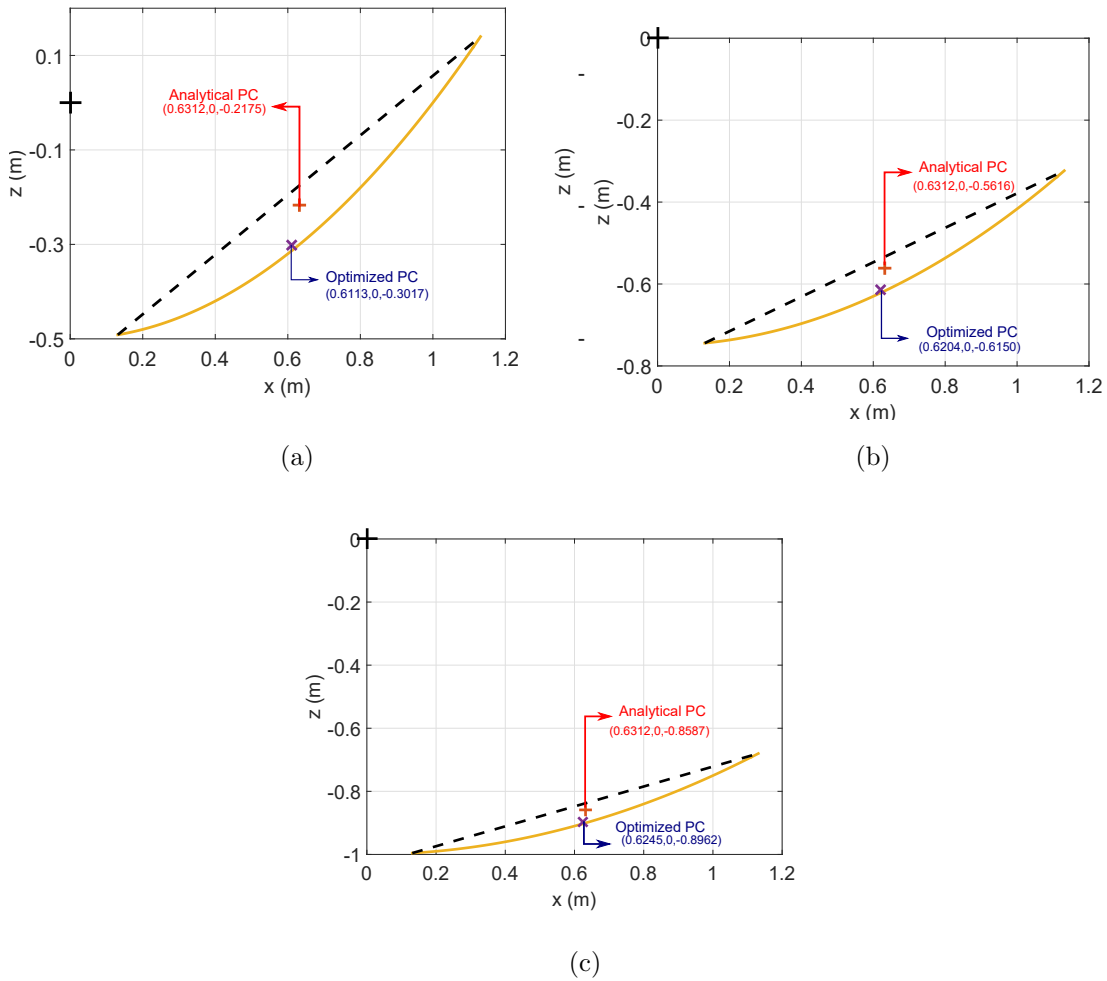


Figure E.4: Comparison of the phase center locations got via analytical formulations (red +) and optimization (blue x).

Table E.1: Comparison of fitness value at the optimized phase center (PC) with the analytical phase center for various geometries.

Case	Fitness at optimized PC	Fitness at analytical PC
Symmetric (D=0.5m, F/D=0.5)	0.0459	0.0463
Offset(D=1m, F/D=0.5)	0.5501	2.5682
Offset(D=1m, F/D=0.75)	0.2965	1.3759
Offset(D=1m, F/D=1)	0.1824	0.5443

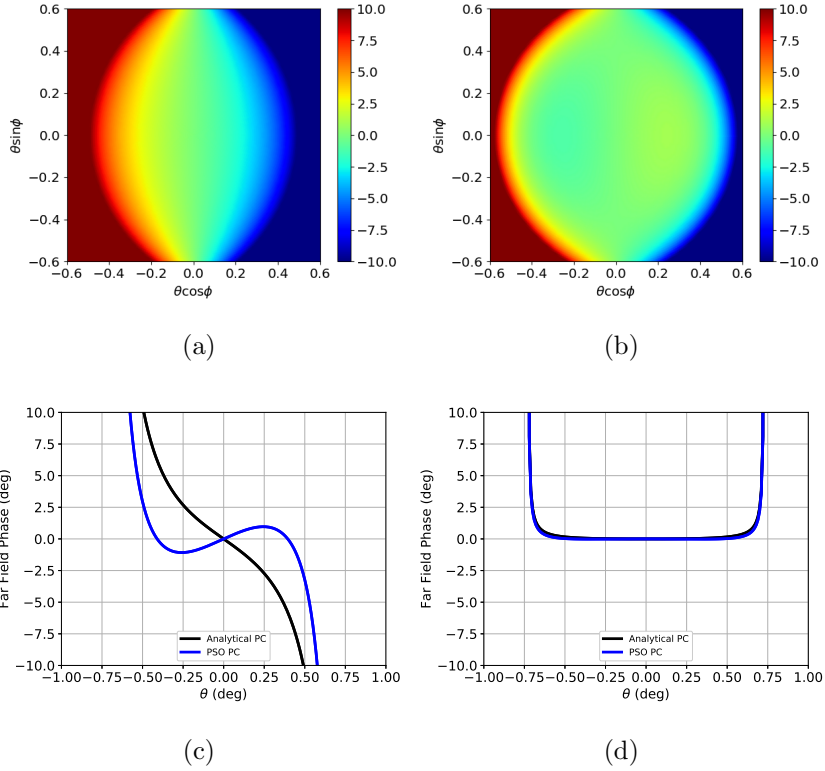


Figure E.5: Comparing the performance of the analytical phase center with the optimized phase center for $F/D=0.5$. (a) Far-field phase contour with the analytical phase center. (b) Far-field phase contour with the optimized phase center. (c) $\phi = 0^\circ$ line cut comparison. (d) $\phi = 90^\circ$ line cut comparison.

APPENDIX F

Focal Plane Distribution for Symmetric Reflectors

This appendix provides insights into the focal plane distribution of the electric fields for a symmetric parabolic reflector when illuminated by a plane wave. The closed form equations governing the focal plane copolarized electric field distribution for a symmetric reflector as well as the axial variation of the copolarized field along the reflector axis are derived in [193, 194] as:

$$E_{co}(t, \phi) = jk \sin^2 \theta_m \frac{J_1(kt \sin \theta_m)}{kt \sin \theta_m} \quad (\text{F.1})$$

$$E_{co}(z') = jk \sin^2 \left(\frac{\theta_m}{2} \right) \frac{\sin(k\Delta z \sin^2 \frac{\theta_m}{2})}{k\Delta z \sin^2 \frac{\theta_m}{2}} e^{jk\Delta z \cos^2 \frac{\theta_m}{2}} \quad (\text{F.2})$$

where t, ϕ and z represent the observation point in the cylindrical coordinate system and θ_m is the half-subtended angle of the reflector at the focal point which is related the F/D ratio of the reflector as:

$$\theta_m = 2 \tan^{-1} \left(\frac{1}{4F/D} \right) \quad (\text{F.3})$$

It should be noted that these equations are derived under the assumption that θ_m is small (implying a large F/D ratio). However, these equations still can be suitably applied for reflector geometries with reasonably small F/D ratios. As a representative example to evaluate the applicability of these equations, the focal plane fields of a symmetric reflector with an aperture diameter of 1m and an F/D of 0.5 are computed through (F.1) and (F.2) and compared to the results from full-wave PO simulation. This geometry results in a θ_m of 53.13° , and some differences between the analytical and simulation results are expected. The results are shown in Figure F.1 and F.2 where one can see that the analytical equations provide a very good approximation to the simulated results. One of the major difference between the analytical equations and simulated results from (F.1) is that the equation is

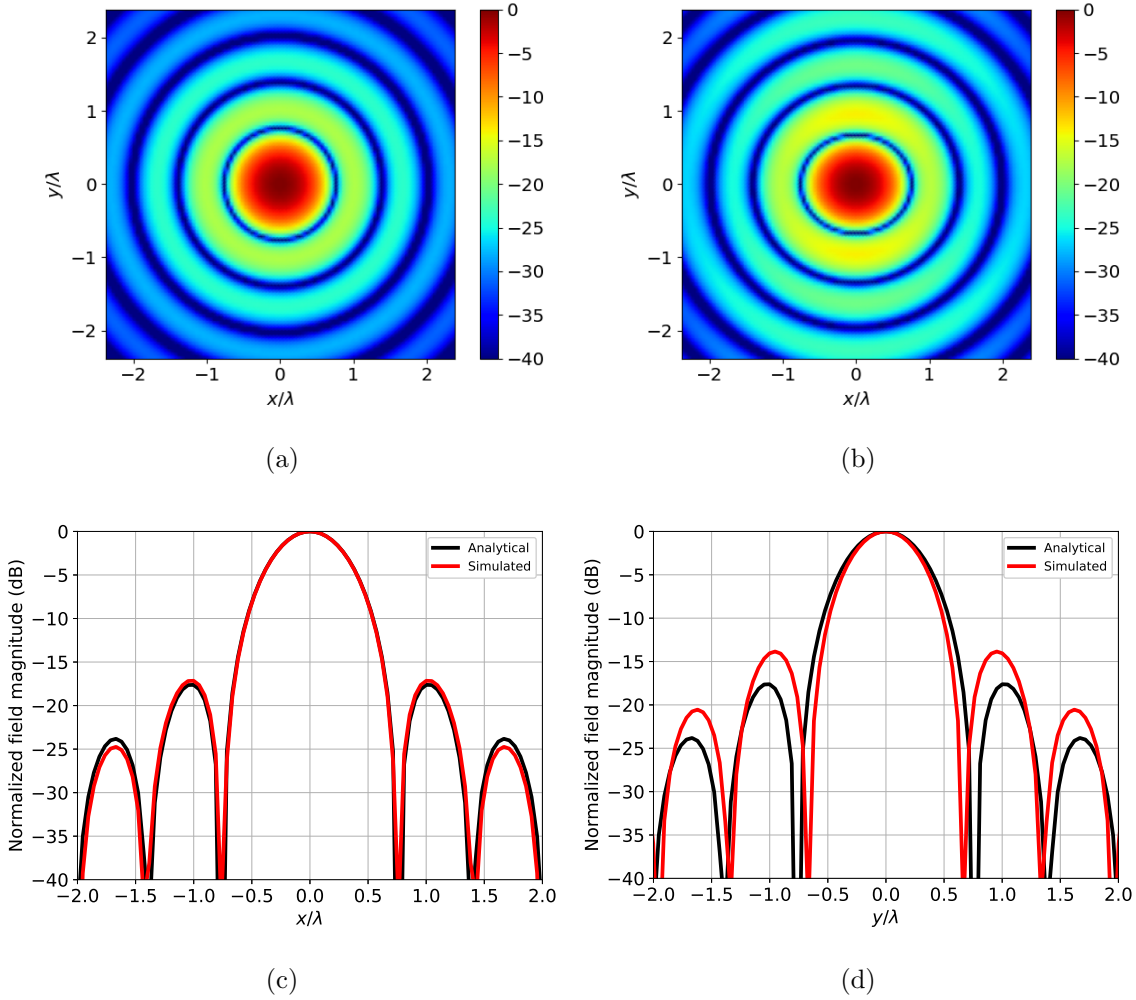


Figure F.1: Focal plane fields (copolarized component) for a symmetric reflector of aperture diameter 1m and $F/D=0.5$ at 35.75 GHz. (a) Analytical focal plane fields, (b) simulated focal plane fields. All values are in dB. (c) and (d) show the comparison between the analytical and the simulated result along $x=0$ and $y=0$ axis. Note that the point $x=0$ and $y=0$ corresponds to the focal point of the reflector.

independent of ϕ , whereas the simulated results show a dependence on ϕ . Nonetheless, it is evident that these equations are a very good approximation and can be used perform initial evaluations.

A very interesting point here is to note that the fields decay at a much slower pace axially than they do radially. This can be an important consideration for applications that require

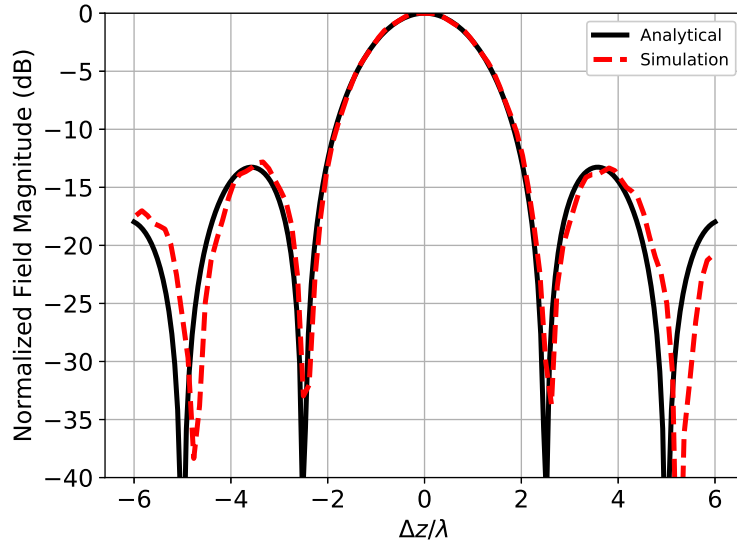


Figure F.2: Variation of the copolarized electric field magnitude along the reflector axis in the vicinity of the focal point for a symmetric reflector of diameter 1m and $F/D=0.5$ at 35.75 GHz. Note the excellent comparison between the analytical and simulated results.

the near-field energy to be confined within a very small volume. Also, a close examination of (F.2) and (F.2) reveal that the focal plane fields are strongly dependent of the *sine* of the half subtended angle θ_m and the wave number k (which is directly proportional to frequency). Since the dependence on θ_m is rather weak due to the fact that $\sin \theta_m$ changes only from 0.707 to 1 for θ_m changing from 45° to 90° , the only way to achieve a very focused spot in the near-field is to ensure a high frequency of operation.

REFERENCES

- [1] S. Gao, K. Clark, M. Unwin, J. Zackrisson, W. Shiroma, J. Akagi, K. Maynard, P. Garner, L. Boccia, G. Amendola, G. Massa, C. Underwood, M. Brenchley, M. Pointer, and M. Sweeting, “Antennas for modern small satellites,” *IEEE Antennas and Propagation Magazine*, vol. 51, August 2009.
- [2] M. A. Swartwout, “CubeSat Database.” <https://sites.google.com/a/slu.edu/swartwout/home/cubesat-database>. Accessed April 26, 2020.
- [3] Y. Rahmat-Samii, V. Manohar, and J. M. Kovitz, “Novel antenna concepts and developments for cubesats,” in *Developments in Antenna Analysis and Synthesis: Volume 2* (R. Mittra, ed.), ch. 11, IET, November 2018.
- [4] Y. Rahmat-Samii, V. Manohar, and J. M. Kovitz, “For satellites, think small, dream big: A review of recent antenna developments for cubesats,” *IEEE Antennas and Propagation Magazine*, vol. 59, pp. 22–30, April 2017.
- [5] S. Gao, Y. Rahmat-Samii, R. E. Hodges, and X. X. Yang, “Advanced antennas for small satellites,” *Proceedings of the IEEE*, vol. 106, pp. 391–403, March 2018.
- [6] E. Peral, E. Im, L. Wye, S. Lee, S. Tanelli, Y. Rahmat-Samii, S. Horst, J. Hoffman, S. H. Yun, T. Imken, and D. Hawkins, “Radar technologies for earth remote sensing from cubesat platforms,” *Proceedings of the IEEE*, vol. 106, pp. 404–418, March 2018.
- [7] N. Chahat, R. E. Hodges, J. Sauder, M. Thomson, and Y. Rahmat-Samii, “The deep-space network telecommunication cubesat antenna: Using the deployable ka-band mesh reflector antenna,” *IEEE Antennas and Propagation Magazine*, vol. 59, pp. 31–38, April 2017.
- [8] S. Lee *et al.*, “Cubesat design specification,” *The CubeSat Program*, vol. 8651, p. 22, 2009.
- [9] ARC Mission Design Division Staff, “Small spacecraft technology state of the art,” Tech. Rep. NASA/TP–2014–216648/REV1, NASA Ames Research Center, Moffet Field, CA, 2014.
- [10] D. Selva and D. Krejci, “A survey and assessment of the capabilities of cubesats for earth observation,” *Acta Astronautica*, vol. 74, pp. 50–68, May 2012.
- [11] T. Bleier, J. Cutler, E. Tapio, A. Lorenz, and B. Twigg, “Quakesat: Low cost university/commerical nanosatellite collaboration.” <http://mst1.atl.calpoly.edu/~workshop/archive/2004/Spring/04b-Bleier-QuakeSat.pdf>. Accessed: April 26, 2020.
- [12] D. E. Rowland, J. Hill, P. Uribe, J. Klenzing, F. Hunsaker, M. Fowle, K. Simms, H. Hancock, M. Saulino, D. Guzman, *et al.*, “The nsf firefly cubesat mission: Rideshare mission to study energetic electrons produced by lightning,” in *IEEE Aerospace Conference*, pp. 1–12, April 2011.

- [13] T. Sato, R. Mitsuhashi, and S. Satori, "Attitude estimation of nano-satellite "hit-sat" using received power fluctuation by radiation pattern," in *IEEE International Symposium on Antennas and Propagation*, June 2009.
- [14] Warsaw University of Technology, "Pw-sat2-polish student satellite soon on orbit." <http://pw-sat.pl/en/home-page/>. Accessed: April 26, 2020.
- [15] "F-1." <https://www.pe0sat.vgnet.nl/satellite/cube-nano-picosats/f1/>. Accessed: April 26, 2020.
- [16] H. Bahcivan and J. W. Cutler, "Radio aurora explorer: Mission science and radar system," *Radio Science*, vol. 47, no. 2, 2012.
- [17] C. Fish, C. Swenson, T. Neilsen, B. Bingham, J. Gunther, E. Stromberg, S. Burr, R. Burt, M. Whitely, G. Crowley, *et al.*, "Dice mission design, development, and implementation: Success and challenges," 2012.
- [18] D. Hinkley, "Aerocube 3 and aerocube 4." http://www.oh1sa.net/data/mirrors/bklofas_at_mst1.atl.calpoly.edu/Presentations/SummerWorkshop2012/Hinkley_AeroCube_3_4.pdf. Accessed: April 26, 2020.
- [19] G. Roethlisberger, F. Jordan, H. Shea, M. Borgeaud, and M. Noca, "Swiss-cube project." <http://mst1.atl.calpoly.edu/~workshop/archive/2007/Spring/02d-Roethlisberger-SwissCube.pdf>. Accessed: April 26, 2020.
- [20] M. Aherne, T. Barrett, L. Hoag, E. Teegarden, and R. Ramadas, "Aeneas-colony i meets three-axis pointing," in *25th Annual AIAA/USU Conference on Small Satellites*, pp. 1–11, 2011.
- [21] University of Bucharest, "Goliat - project overview." <http://mst1.atl.calpoly.edu/~workshop/archive/2006/Spring/07-Dumitru-GOLIAT.pdf>. Accessed: April 26, 2020.
- [22] "Cinema." <https://directory.eoportal.org/web/eoportal/satellite-missions/c-missions/cinema>. Accessed: April 26, 2020.
- [23] R. E. Hodges *et al.*, "ISARA-Integrated Solar Array and Reflectarray CubeSat deployable Ka-band antenna," in *IEEE International Symposium on Antennas and Propagation*, pp. 2141–2142, July 2015.
- [24] Gunter's space page, "Ksat (hayato)." http://space.skyrocket.de/doc_sdat/ksat.htm. Accessed: April 26, 2020.
- [25] E. Peral *et al.*, "RaInCube: a proposed constellation of precipitation profiling Radars In Cubesat," in *IEEE Symposium on International Geoscience and Remote Sensing*, pp. 1261–1264, July 2015.
- [26] L. Periasamy and A. J. Gasiewski, "Precision design, analysis and manufacturing of quasi-optic lens/reflector antenna systems for cubesat mmw/smmw radiometers," in *USNC-URSI Radio Science Meeting*, pp. 265–265, July 2015.

- [27] B. Klofas, J. Anderson, and K. Leveque, “A survey of cubesat communication systems,” in *5th Annual CubeSat Developers’ Workshop*, 2008.
- [28] J. Bouwmeester and J. Guo, “Survey of worldwide pico-and nanosatellite missions, distributions and subsystem technology,” *Acta Astronautica*, vol. 67, pp. 854–862, October 2010.
- [29] N. Chahat, R. E. Hodges, J. Sauder, M. Thomson, and Y. Rahmat-Samii, “The deep-space network telecommunication cubesat antenna: Using the deployable ka-band mesh reflector antenna.,” *IEEE Antennas and Propagation Magazine*, vol. 59, pp. 31–38, April 2017.
- [30] R. E. Hodges, N. Chahat, D. J. Hoppe, and J. D. Vacchione, “A deployable high-gain antenna bound for mars: Developing a new folded-panel reflectarray for the first cubesat mission to mars.,” *IEEE Antennas and Propagation Magazine*, vol. 59, pp. 39–49, April 2017.
- [31] P. Muri and J. McNair, “A survey of communication sub-systems for intersatellite linked systems and cubesat missions.,” *JCM*, vol. 7, pp. 290–308, April 2012.
- [32] C. J. Vourch and T. D. Drysdale, “Inter-cubesat communication with v-band “bull’s eye” antenna,” in *European Conference on Antennas and Propagation*, pp. 3545–3549, April 2014.
- [33] A. Budianu, T. J. W. Castro, A. Meijerink, and M. J. Bantum, “Inter-satellite links for cubesats,” in *IEEE Aerospace Conference*, pp. 1–10, March 2013.
- [34] F. E. Tubbal, R. Raad, and K.-W. Chin, “A survey and study of planar antennas for pico-satellites,” *IEEE Access*, vol. 3, pp. 2590–2612, December 2015.
- [35] N. Chahat, R. E. Hodges, J. Sauder, M. Thomson, E. Peral, and Y. Rahmat-Samii, “Cubesat deployable ka-band mesh reflector antenna development for earth science missions,” *IEEE Transactions on Antennas and Propagation*, vol. 64, pp. 2083–2093, June 2016.
- [36] J. Santiago-Prowald and L. S. Drioli, *Space Environment and Materials*, pp. 106–132. John Wiley and Sons, Ltd, 2012.
- [37] J. Costantine, Y. Tawk, C. G. Christodoulou, J. Banik, and S. Lane, “Cubesat deployable antenna using bistable composite tape-springs,” *IEEE Antennas Wireless Propagation Letters*, vol. 11, pp. 285–288, February 2012.
- [38] J. Ekelöw, “Design and manufacturing of thin composite tape springs.” <https://www.diva-portal.org/smash/get/diva2:805332/FULLTEXT01.pdf>, 2014. Accessed: 26 April, 2020.
- [39] M. T. Islam, M. Cho, M. Samsuzzaman, and S. Kibria, “Compact antenna for small satellite applications [antenna applications corner],” *IEEE Antennas and Propagation Magazine*, vol. 57, pp. 30–36, April 2015.

- [40] P. A. Warren, J. W. Steinbeck, R. J. Minelli, and C. Mueller, “Large, deployable S-Band antenna for a 6U CubeSat,” in *Annual AIAA/USU Conference on Small Satellites*, 2015.
- [41] R. Barrett, R. Taylor, P. Keller, D. Codell, and L. Adams, “Deployable reflectors for small satellites,” in *Annual AIAA/USU Conference on Small Satellites*, August 2007.
- [42] M. Deshpande and J. Piepmeier, “Design and development of vhf antennas for space borne signal of opportunity receivers for cubesat platforms,” 2015. Accessed from <http://ntrs.nasa.gov/>.
- [43] R. Lehmensiek, “Using the physical structure of a passive aerodynamic attitude-stabilization system as a multi-frequency antenna on nano-satellites,” *IEEE Antennas and Propagation Magazine*, vol. 54, pp. 39–49, June 2012.
- [44] T. J. Mizuno, J. D. Roque, B. T. Murakami, L. K. Yoneshige, G. S. Shiroma, R. Y. Miyamoto, and W. A. Shiroma, “Antennas for distributed nanosatellite networks,” in *IEEE/ACES International Conference on Wireless Communications and Applied Computational Electromagnetics*, pp. 606–609, April 2005.
- [45] E. S. Moghaddam, N. Aboutorabian, S. Amiri, S. Nikmehr, and P. Rezaei, “Design and analysis of a dualband antenna for small leo satellite applications,” in *International Conference on Computational Electromagnetics and Its Applications*, pp. 228–231, November 2004.
- [46] M. Nohmi, K. Oi, S. Takuma, and M. Ogawa, “Solar paddle antenna mounted on pico-satellite ”KUKAI” for amateur radio communication,” in *Second International Conference on Advances in Satellite and Space Communications*, pp. 31–36, June 2010.
- [47] A. Joseph, M. Deshpande, P. O’Neill, and L. Miles, “Development of VHF (240–270 MHz) antennas for SoOp (Signal of Opportunity) receiver for 6u cubesat platforms,” in *Progress in Electromagnetic Research Symposium (PIERS)*, pp. 2530–2531, August 2016.
- [48] C. E. Lesamu and A. Done, “Parasitic circular polarized vertical antennas,” in *International Conference on Development and Application Systems*, pp. 143–149, May 2016.
- [49] J. Costantine, Y. Tawk, A. Ernest, and C. Christodoulou, “Deployable antennas for cubesat and space communications,” in *European Conference on Antennas and Propagation*, pp. 837–840, March 2012.
- [50] J. Costantine, Y. Tawk, I. Maqueda, M. Sakovsky, G. Olson, S. Pellegrino, and C. G. Christodoulou, “UHF deployable helical antennas for cubesats,” *IEEE Transactions on Antennas and Propagation*, vol. 64, pp. 3752–3759, September 2016.
- [51] P. Rezaei, “Design of quadrifilar helical antenna for use on small satellites,” in *IEEE International Symposium on Antennas and Propagation*, vol. 3, pp. 2895–2898, June 2004.

- [52] P. Muri, O. Challa, and J. McNair, “Enhancing small satellite communication through effective antenna system design,” in *Military Communications Conference (MILCOM)*, pp. 347–352, November 2010.
- [53] G. Olson, S. Pellegrino, J. Costantine, and J. Banik, “Structural architectures for a deployable wideband uhf antenna,” in *Structural Dynamics and Materials Conference*, pp. 23–26, April 2012.
- [54] E. Pittella, S. Pisa, and A. Nascetti, “Design of an antenna system for cubesat satellites,” in *Proceedings of the 2nd IAA Conference on University Satellites Missions and CubeSat Winter Workshop*, 2013. Paper No. IAA-CU-13-13-05.
- [55] S. Liu, P. I. Theoharis, F. E. Tubbal, and R. Raad, “S-band steerable yagi antenna for cubesats,” in *2019 13th International Conference on Signal Processing and Communication Systems (ICSPCS)*, pp. 1–5, December 2019.
- [56] U. Garg and R. N. Jain, “Modelling and simulation of onboard wire antennas for a 3u cubesat,” in *Photonics Electromagnetics Research Symposium - Fall (PIERS - Fall)*, pp. 871–879, 2019.
- [57] A. Babuscia, M. Van de Loo, Q. J. Wei, S. Pan, S. Mohan, and S. Seager, “Inflatable antenna for cubesat: fabrication, deployment and results of experimental tests,” in *IEEE Aerospace Conference*, pp. 1–12, March 2014.
- [58] N. Chahat *et al.*, “CubeSat deployable Ka-band mesh reflector antenna development for Earth science missions,” *IEEE Transactions on Antennas and Propagation*, vol. 64, pp. 2083–2093, June 2016.
- [59] V. Manohar and Y. Rahmat-Samii, “Characterization of ka-band mesh surfaces for cubesat reflector antennas: From simple wire grid model to complex knits,” in *URSI National Radio Science Meeting*, pp. 1–2, January 2016.
- [60] V. Manohar, J. M. Kovitz, and Y. Rahmat-Samii, “Ka band umbrella reflectors for cubesats: Revisiting optimal feed location and gain loss,” in *International Conference on Electromagnetics in Advanced Applications*, pp. 800–803, September 2016.
- [61] L. Periasamy and A. J. Gasiewski, “Prelaunch antenna calibration of cubesat mmw/smmw radiometers with application to the polarcube 3u temperature sounding radiometer mission,” in *IEEE International Geoscience and Remote Sensing Symposium*, pp. 5565–5568, July 2016.
- [62] M. Takikawa, Y. Inasawa, and Y. Konishi, “One-dimensional beam scanning reflector antenna for small satellite applications,” in *IEEE-APS Topical Conference on Antennas and Propagation in Wireless Communications*, pp. 159–162, September 2012.
- [63] V. Manohar and Y. Rahmat-Samii, “Rf effects of umbrella reflector antenna topology for cubesats: Optimal feed point, boresight gain loss and grating lobes,” in *2019 URSI International Symposium on Electromagnetic Theory (EMTS)*, pp. 1–4, May 2019.

- [64] R. E. Hodges, N. Chahat, D. J. Hoppe, and J. D. Vacchione, “A deployable high-gain antenna bound for mars: Developing a new folded-panel reflectarray for the first cubesat mission to mars.,” *IEEE Antennas and Propagation Magazine*, vol. 59, April 2017.
- [65] A. K. Singh and S. Park, “A deployable metamaterial reflectarray antenna for microsatellite application,” in *2019 International Symposium on Antennas and Propagation (ISAP)*, pp. 1–2, October 2019.
- [66] T. Yasin and R. Baktur, “Circularly polarized meshed patch antenna for small satellite application,” *IEEE Antennas and Wireless Propagation Letters*, vol. 12, pp. 1057–1060, August 2013.
- [67] R. Montaña, N. Neveu, S. Palacio, E. Martinez, D. R. Jackson, J. Chen, P. W. Fink, and R. S. Provence, “Development of low-profile antennas for cubesats,” in *Annual AIAA/USU Conference on Small Satellites*, 2014.
- [68] B. K. Montgomery, S. K. Podilchak, and Y. M. Antar, “Circularly polarized meshed patch antenna for cubesats and other small satellites,” in *International Symposium on Antennas and Propagation*, pp. 1547–1548, 2016.
- [69] X. Liu, J. Liu, D. R. Jackson, J. Chen, P. W. Fink, and G. Y. Lin, “Broadband transparent circularly-polarized microstrip antennas for cubesats,” in *IEEE International Symposium on Antennas and Propagation*, pp. 1545–1546, 2016.
- [70] X. Liu, D. R. Jackson, J. Chen, J. Liu, P. W. Fink, G. Y. Lin, and N. Neveu, “Transparent and nontransparent microstrip antennas on a cubesat: Novel low-profile antennas for cubesats improve mission reliability.,” *IEEE Antennas and Propagation Magazine*, vol. 59, April 2017.
- [71] A. Budianu, A. Meijerink, M. J. Bentum, D. M. Smith, and A.-J. Boonstra, “Antenna architecture of a nano-satellite for radio astronomy,” in *IEEE Aerospace Conference*, pp. 1–10, June 2014.
- [72] G. F. Kurnia, B. S. Nugroho, and A. D. Prasetyo, “Planar inverted-f antenna (PIFA) array with circular polarization for nano satellite application,” in *International Symposium on Antennas and Propagation (ISAP)*, pp. 431–432, December 2014.
- [73] G. Dassano and M. Orefice, “The PICPOT satellite antenna systems,” in *IEEE International Symposium on Antennas and Propagation*, pp. 3029–3032, June 2007.
- [74] J. Padilla, G. Rosati, A. Ivanov, F. Bongard, S. Vaccaro, and J. Mosig, “Multi-functional miniaturized slot antenna system for small satellites,” in *European Conference on Antennas and Propagation*, pp. 2170–2174, April 2011.
- [75] J. Klein, J. Hawkins, and D. Thorsen, “Improving cubesat downlink capacity with active phased array antennas,” in *IEEE Aerospace Conference*, pp. 1–8, March 2014.

- [76] S. Tariq and R. Baktur, "Circularly polarized UHF up-and downlink antennas integrated with CubeSat solar panels," in *IEEE International Symposium on Antennas and Propagation*, pp. 1424–1425, July 2015.
- [77] R. M. Rodriguez-Osorio and E. F. Ramirez, "A hands-on education project: Antenna design for inter-cubesat communications," *IEEE Antennas and Propagation Magazine*, vol. 54, pp. 211–224, October 2012.
- [78] L. M. Hilliard, J. Mead, R. Rincon, and P. H. Hildebrand, "Lightweight linear broadband antennas enabling small UAV wing systems and space flight nanosat concept," in *IEEE International Geoscience and Remote Sensing Symposium*, vol. 5, pp. 3577–3580, September 2004.
- [79] E. Palantei, S. Syarif, B. Topalaguna, and Z. Ubaid, "Four elements array of lungs shape patch antenna for nanosatellite telemetry," in *IEEE International Symposium on Antennas and Propagation*, pp. 1808–1809, July 2013.
- [80] O. Ceylan, Y. Kurt, F. A. Tunc, H. B. Yagci, and A. R. Aslan, "Low cost S band communication system design for nano satellites," in *5th International Conference on Recent Advances in Space Technologies*, pp. 767–770, June 2011.
- [81] W. N. Saputra, B. Prasetya, and Y. Wahyu, "Design and realization of two array triangle patch of microstrip antenna with gold plat at frequency 2400–2450 mhz for hexagonal nanosatellite," in *International Conference of Information and Communication Technology*, pp. 322–327, March 2013.
- [82] C. A. Bergsrud and S. Noghianian, "Microstrip aperture-coupled antenna design for in-space power reception experiment using nano-sized satellite," in *USNC-URSI Radio Science Meeting*, pp. 25–25, July 2015.
- [83] J. Fouany, M. Thévenot, E. Arnaud, F. Torres, T. Monediere, N. Adnet, R. Manrique, L. Duchesne, J. Baracco, and K. Elis, "Circularly polarized isoflux compact X band antenna for nano-satellites applications," in *European Radar Conference*, pp. 381–384, September 2015.
- [84] M. P. Magalhaes, M. V. Heckler, J. Mota, A. S. Sombra, and E. C. Moreira, "Design and analysis of microstrip antenna arrays for meteorological nano-satellites for UHF uplink," in *International Telecommunications Symposium*, pp. 1–5, August 2014.
- [85] M. K. Watanabe, R. N. Pang, B. O. Takase, J. M. Akagi, G. S. Shiroma, and W. A. Shiroma, "A 2-D phase-detecting/heterodyne-scanning retrodirective array," *IEEE Transactions on Microwave Theory and Techniques*, vol. 55, pp. 2856–2864, December 2007.
- [86] T. Sreeja, A. Arun, and J. Jaya Kumari, "An s-band micro-strip patch array antenna for nano-satellite applications," in *International Conference on Green Technologies*, pp. 325–328, December 2012.

- [87] E. Arneri, L. Boccia, G. Amendola, and G. Di Massa, “A compact high gain antenna for small satellite applications,” *IEEE Transactions on Antennas and Propagation*, vol. 55, pp. 277–282, February 2007.
- [88] B. T. Murakami, J. D. Roque, S. S. Sung, G. S. Shiroma, R. Y. Miyamoto, and W. A. Shiroma, “A quadruple subharmonic phase-conjugating array for secure picosatellite crosslinks,” in *IEEE MTT-S International Microwave Symposium Digest*, vol. 3, pp. 1687–1690, June 2004.
- [89] C. Hamrouni, A. Abraham, and A. Alimi, “Both sides linked antenna array for ultra small satellite communication subsystem,” in *International Conference on Innovation Management and Technology Research*, pp. 230–235, May 2012.
- [90] J. R. Saberlin and C. Furse, “Challenges with optically transparent patch antennas for small satellites,” in *IEEE International Symposium on Antennas and Propagation*, pp. 1–4, July 2010.
- [91] J. Li, S. Gao, and J. Xu, “Circularly polarized high-gain printed antennas for small satellite applications,” in *International Conference on Microwave Technology and Computational Electromagnetics*, pp. 76–79, November 2009.
- [92] K. F. Warnick, “High efficiency phased array feed antennas for large radio telescopes and small satellite communications terminals,” in *European Conference on Antennas and Propagation*, pp. 448–449, April 2013.
- [93] F. E. Tubbal, R. Raad, K.-W. Chin, and B. Butters, “S-band shorted patch antenna for inter pico satellite communications,” in *8th International Conference on Telecommunication Systems Services and Applications*, pp. 1–4, October 2014.
- [94] P. R. Akbar, H. Saito, M. Zang, J. Hirokawa, and M. Ando, “X-band parallel-plate slot array antenna for sar sensor onboard 100 kg small satellite,” in *IEEE International Symposium on Antennas and Propagation*, pp. 208–209, July 2015.
- [95] G. Codispoti, M. Lisi, and V. Santachiara, “X-band SAR active antenna design for small satellite applications,” in *IEEE International Symposium on Antennas and Propagation*, vol. 1, pp. 666–669, June 1995.
- [96] S. Gunaseelan and M. Murugan, “High gain patch antenna for cubesat,” in *International Conference on Wireless Communications, Signal Processing and Networking*, pp. 52–54, March 2016.
- [97] Y. Yao, S. Liao, J. Wang, K. Xue, E. A. Balfour, and Y. Luo, “A new patch antenna designed for cubesat: Dual feed, L/S dual-band stacked, and circularly polarized.” *IEEE Antennas and Propagation Magazine*, vol. 58, pp. 16–21, April 2016.
- [98] E. Pittella, S. Pisa, M. Pontani, A. Nascetti, P. D’Atanasio, A. Zambotti, and H. Hadi, “Reconfigurable s-band patch antenna system for cubesat satellites,” *IEEE Aerospace and Electronic Systems Magazine*, vol. 31, pp. 6–13, May 2016.

- [99] P. Bouca, J. N. Matos, S. R. Cunha, and N. B. Carvalho, “Low-profile aperture-coupled patch antenna array for cubesat applications,” *IEEE Access*, vol. 8, pp. 20473–20479, 2020.
- [100] S. Zarbakhsh, M. Akbari, M. Farahani, A. Ghayekhloo, T. A. Denidni, and A. Sebak, “Optically transparent subarray antenna based on solar panel for cubesat application,” *IEEE Transactions on Antennas and Propagation*, vol. 68, pp. 319–328, January 2020.
- [101] G. Mishra, S. K. Sharma, and J. S. Chieh, “A w-band butterfly shaped series-fed circular polarized phased array antenna for cubesats,” in *IEEE International Symposium on Phased Array System Technology (PAST)*, pp. 1–8, 2019.
- [102] F. Tubbal, R. Raad, P. I. Theoharis, S. Iranmanesh, S. Abulgase, and M. U. A. Khan, “Dual band slot antenna with f-shaped slits for c-band and x-band applications,” in *13th International Conference on Signal Processing and Communication Systems (ICSPCS)*, pp. 1–4, December 2019.
- [103] M. Lucente, T. Rossi, A. Jebril, M. Ruggieri, S. Pulitanò, A. Iera, A. Molinaro, C. Sacchi, and L. Zuliani, “Experimental missions in W-band: A small leo satellite approach,” *IEEE Systems Journal*, vol. 2, pp. 90–103, March 2008.
- [104] J. M. Kovitz, V. Manohar, and Y. Rahmat-Samii, “A spline-profiled conical horn antenna assembly optimized for deployable ka-band offset reflector antennas in cubesats,” in *IEEE International Symposium on Antennas and Propagation*, July 2016.
- [105] V. Manohar, J. M. Kovitz, and Y. Rahmat-Samii, “A novel customized spline-profiled mm-wave horn antenna for emerging high performance cubesats,” in *Proceedings of the Antenna Measurements and Techniques Association Meeting*, November 2016.
- [106] J. King, J. Ness, G. Bonin, M. Brett, and D. Faber, “Nanosat ka-band communications—a paradigm shift in small satellite data throughput,” *26th Annual AIAA/USU Conference on Small Satellites*, 2012. Accessed from digitalcommons.usu.edu.
- [107] N. Chahat, R. E. Hodges, J. Sauder, M. Thomson, and Y. Rahmat-Samii, “Deep space network telecommunication cubesat antenna: Using the deployable ka-band mesh reflector antenna,” *IEEE Antennas and Propagation Magazine*, vol. 59, April 2017.
- [108] P. G. Ingerson and W. C. Wong, “The Analysis of Deployable Umbrella Parabolic Reflectors,” *IEEE Transactions on Antennas and Propagation*, vol. 20, pp. 409–414, July 1972.
- [109] F. L. Hai, “The Principle Error and Optimal Feed Point of Umbrella-Like Parabolic Reflector,” in *International Symposium on Antennas, Propagation and EM theory (IS-APE)*, pp. 697–700, August 2000.
- [110] J. Ruze, “Antenna Tolerance Theory - A Review,” *Proceedings of the IEEE*, vol. 54, pp. 633–640, April 1966.

- [111] Y. Rahmat-Samii, "Effects of Deterministic Surface Distortions on Reflector Antenna Performance," in *Annales des télécommunications*, vol. 40, pp. 350–360, July 1985.
- [112] Y. Rahmat-Samii, "Reflector antennas," in *Antenna handbook* (Y. Lo and S. Lee, eds.), ch. 15, New York: Van nostrand reinhold, 1993.
- [113] K. Bahadori and Y. Rahmat-Samii, "Effect of periodic and aperiodic surface distortions on membrane reflector antennas," in *IEEE Antennas and Propagation Society Symposium*, vol. 3, pp. 3031–3034, June 2004.
- [114] K. Bahadori and Y. Rahmat-Samii, "Characterization of effects of periodic and aperiodic surface distortions on membrane reflector antennas," *IEEE Transactions on Antennas and Propagation*, vol. 53, pp. 2782–2791, September 2005.
- [115] K. Pontoppidan, "Reflector Antennas - An Overview of Surface Distortion Effects," in *Proceedings JINA*, pp. 82–93, 1986.
- [116] V. Manohar and Y. Rahmat-Samii, "Revisiting the appearance of grating lobes for antennas with circular periodicity," *IEEE Transactions on Antennas and Propagation*, vol. 67, pp. 5723–5728, August 2019.
- [117] Y. Rahmat-Samii, "Array feeds for reflector surface distortion compensation: concepts and implementation," *IEEE Antennas and Propagation Magazine*, vol. 32, pp. 20–26, August 1990.
- [118] S. Tanelli, S. L. Durden, E. Im, K. S. Pak, D. G. Reinke, P. Partain, J. M. Haynes, and R. T. Marchand, "Cloudsat's cloud profiling radar after two years in orbit: Performance, calibration, and processing," *IEEE Transactions on Geoscience and Remote Sensing*, vol. 46, pp. 3560–3573, November 2008.
- [119] G. L. Stephens, D. G. Vane, S. Tanelli, E. Im, S. Durden, M. Rokey, D. Reinke, P. Partain, G. G. Mace, R. Austin, T. L'Ecuyer, J. Haynes, M. Lebsock, K. Suzuki, D. Waliser, D. Wu, J. Kay, A. Gettelman, Z. Wang, and R. Marchand, "Cloudsat mission: Performance and early science after the first year of operation," *Journal of Geophysical Research: Atmospheres*, vol. 113, no. D8, pp. n/a–n/a, 2008. D00A18.
- [120] C. Kummerow, W. Barnes, T. Kozu, J. Shiue, and J. Simpson, "The tropical rainfall measuring mission (trmm) sensor package," *Journal of Atmospheric and Oceanic Technology*, vol. 15, pp. 809–817, June 1998.
- [121] "Radar in a cubesat (raincube)." <https://www.jpl.nasa.gov/cubesat/missions/raincube.php>. Accessed: 2018-07-27.
- [122] Y. Rahmat-Samii, V. Manohar, J. M. Kovitz, R. E. Hodges, G. Freebury, and E. Peral, "Development of highly constrained 1 m ka-band mesh deployable offset reflector antenna for next generation cubesat radars," *IEEE Transactions on Antennas and Propagation*, vol. 67, pp. 6254–6266, October 2019.

- [123] Tendeg, “KaTENna: Deployable high gain antenna for small satellites.” <http://tendeg.com/products>. Accessed: April 26, 2020.
- [124] J. M. Kovitz, J. P. Santos, Y. Rahmat-Samii, N. F. Chamberlain, and R. E. Hodges, “Enhancing communications for future mars rovers: Using high-performance circularly polarized patch subarrays for a dual-band direct-to-earth link.,” *IEEE Antennas and Propagation Magazine*, vol. 59, pp. 50–61, August 2017.
- [125] “Technology readiness level definitions.” https://www.nasa.gov/pdf/458490main_TRL_Definitions.pdf. Accessed: 26 April, 2020.
- [126] V. Manohar and Y. Rahmat-Samii, “Umbrella reflector characterization for cubesats: Analytical formulation for boresight gain loss,” in *United States National Committee of URSI National Radio Science Meeting (USNC-URSI NRSM)*, January 2018.
- [127] V. Manohar, “Electromagnetic Characterizations of Mesh Deployable Ka Band Reflector Antennas for Emerging CubeSats,” Master’s thesis, University of California, Los Angeles, USA, 2016. Accessed from <https://escholarship.org/uc/item/1rz3d95w>.
- [128] J. Pawlan, “Compact and easy to manufacture dual mode feed horn with ultra-low backlobes,” in *German Microwave Conference*, pp. 355–358, March 2015.
- [129] Y. Rahmat-Samii, J. M. Kovitz, and H. Rajagopalan, “Nature-inspired optimization techniques in communication antenna designs,” *Proceedings of the IEEE*, vol. 100, pp. 2132–2144, July 2012.
- [130] J. Robinson and Y. Rahmat-Samii, “Particle swarm optimization in electromagnetics,” *IEEE Transactions on Antennas and Propagation*, vol. 52, pp. 397–407, February 2004.
- [131] C. Granet, G. L. James, R. Bolton, and G. Moorey, “A smooth-walled spline-profile horn as an alternative to the corrugated horn for wide band millimeter-wave applications,” *IEEE Transactions on Antennas and Propagation*, vol. 52, pp. 848–854, March 2004.
- [132] P. S. Simon, P. Kung, and B. W. Hollenstein, “Electrically large spline profile smooth-wall horns for spot beam applications,” in *IEEE International Symposium on Antennas and Propagation*, pp. 915–918, July 2011.
- [133] F. Fritsch and R. Carlson, “Monotone piecewise cubic interpolation,” *SIAM Journal on Numerical Analysis*, vol. 17, no. 2, pp. 238–246, 1980.
- [134] S. Sinton, J. Robinson, and Y. Rahmat-Samii, “Standard and micro genetic algorithm optimization of profiled corrugated horn antennas,” *Microwave and Optical Technology Letters*, vol. 35, pp. 449–453, December 2002.
- [135] Y. Rahmat-Samii, L. I. Williams, and R. G. Yaccarino, “The UCLA Bi-polar Planar-Near-Field Antenna Measurement and Diagnostics Range,” *IEEE Antennas and Propagation Magazine*, vol. 37, pp. 16–35, December 1995.

- [136] T. Brockett and Y. Rahmat-Samii, “A novel portable bipolar near-field measurement system for millimeter-wave antennas: construction, development, and verification,” *IEEE Antennas and Propagation Magazine*, vol. 50, pp. 121–130, October 2008.
- [137] S. F. Razavi, S. Xu, T. Brockett, and Y. Rahmat-Samii, “The spillover effect on the directivity calculation of reflector antennas in planar near-field measurements [measurements corner],” *IEEE Antennas and Propagation Magazine*, vol. 51, pp. 124–134, December 2009.
- [138] M. Astrakhan, “Reflecting and Screening Properties of Plane Wire Grids,” *Telecommunications and Radio Engineer-USSR*, no. 1, p. 76, 1968.
- [139] V. Manohar and Y. Rahmat-Samii, “Characterization of Ka-Band Mesh Surfaces for CubeSat Reflector Antennas: From Simple Wire Grid Model to Complex Knits,” in *United States National Committee of URSI National Radio Science Meeting (USNC-URSI NRSM)*, pp. 1–2, January 2016.
- [140] Y. Rahmat-Samii and S.-W. Lee, “Vector Diffraction Analysis of Reflector Antennas with Mesh Surfaces,” *IEEE Transactions on Antennas and Propagation*, vol. 33, pp. 76 – 90, January 1985.
- [141] W. A. Imbriale, V. Galindo-Israel, and Y. Rahmat-Samii, “On the Reflectivity of Complex Mesh Surfaces,” *IEEE Transactions on Antennas and Propagation*, vol. 39, pp. 1352–1365, September 1991.
- [142] H. Rajagopalan, A. Miura, and Y. Rahmat-Samii, “Equivalent Strip Width for Cylindrical Wire for Mesh Reflector Antennas: Experiments, Waveguide, and Plane-Wave Simulations,” *IEEE Transactions on Antennas and Propagation*, vol. 54, pp. 2845–2853, October 2006.
- [143] “Mesa antenna measurement facility.” <https://mesa.jpl.nasa.gov/>. Accessed: 26 April, 2020.
- [144] C. Cappellin, J. R. de Lasson, R. R. M. Jorgensen, L. Datashvili, J. Pauw, N. Maghaldadze, M. Migliorelli, J. Crawford, and Angevain, “Large mesh reflectors with improved pattern performances,” in *Proceedings of 37th European Space Agency (ESA) Antenna Workshop*, 2016.
- [145] J. Angevain, G. Rodrigues, J. Santiago-Prowald, C. Mangenot, and L. Datashvili, “Phyllotactic arrangements of reflector mesh facets to decrease grating lobes,” in *European Conference on Antennas and Propagation (EuCAP)*, pp. 1–5, April 2015.
- [146] “Delaunay triangulation.” <https://www.mathworks.com/help/matlab/math/delaunay-triangulation.html>. Accessed: April 26, 2020.
- [147] Y. Zong, B. Duan, Y. Ban, W. Wang, W. Xu, C. Wang, and J. Du, “Surface configuration design of cable-network reflectors considering the radiation pattern,” *IEEE Transactions on Antennas and Propagation*, vol. 62, pp. 3163–3173, June 2014.

- [148] K. Bahadori and Y. Rahmat-Samii, "Tri-mode horn feeds revisited: Cross-pol reduction in compact offset reflector antennas," *IEEE Transactions on Antennas and Propagation*, vol. 57, pp. 2771–2775, September 2009.
- [149] J. M. Kovitz, V. Manohar, and Y. Rahmat-Samii, "Feed horn optimization using feed+reflector co-simulation for advanced reflector antennas," in *International Applied Computational Electromagnetics Society Symposium - Italy (ACES)*, pp. 1–2, 2017.
- [150] J. M. Kovitz, V. Manohar, and Y. Rahmat-Samii, "An end-to-end optimization approach to drastically reduce cross-polarization in offset mmwave reflector antennas," in *IEEE International Symposium on Antennas and Propagation USNC/URSI National Radio Science Meeting*, pp. 981–982, July 2017.
- [151] G. C. Andre and H. D. Rene, "Directional radio transmission system," June 9 1936. US Patent 2,043,347.
- [152] I. M. Jr., "Fresnel zone plate antenna," Tech. Rep. R-3293, Naval Research Lab, Washington, DC, June 1948.
- [153] M. L. Klein, *A re-radiating zone plate antennae system*. PhD thesis, Boston University, 1950.
- [154] P. A. Boivin, H. Koenig, and A. Dion, "Etude experimentale de la diffraction des microondes par des ouvertures a symetrie de revolution," *Canadian Journal of Physics*, vol. 34, pp. 166–178, February 1956.
- [155] L. Van Buskirk and C. Hendrix, "The zone plate as a radio-frequency focusing element," *IRE Transactions on Antennas and Propagation*, vol. 9, pp. 319–320, May 1961.
- [156] G. Sanyal and M. Singh, "Fresnel zone plate antenna," *IETE Journal of Research*, vol. 14, no. 6, pp. 265–281, 1968.
- [157] H. A. Malliot, "Zone plate reflector antennas for applications in space," in *IEEE Aerospace Applications Conference*, pp. 295–311, February 1994.
- [158] B. Khayatian and Y. Rahmat-Samii, "A novel antenna concept for future solar sails: application of fresnel antennas," *IEEE Antennas and Propagation Magazine*, vol. 46, pp. 50–63, April 2004.
- [159] Y. Guo and S. Barton, "On the subzone phase correction of fresnel zone plate antennas," *Microwave and Optical Technology Letters*, vol. 6, pp. 840–843, December 1993.
- [160] R. W. Wood, "LIII. phase-reversal zone-plates, and diffraction-telescopes," *The London, Edinburgh, and Dublin Philosophical Magazine and Journal of Science*, vol. 45, no. 277, pp. 511–522, 1898.

- [161] A. V. Baez, “Fresnel zone plate for optical image formation using extreme ultraviolet and soft x radiation,” *Journal of the Optical Society of America*, vol. 51, p. 405, April 1961.
- [162] G. S. Waldman, “Variations on the fresnel zone plate,” *Journal of the Optical Society of America A*, vol. 56, pp. 215–218, February 1966.
- [163] B. New, “Design, production and performance of circular fresnel zone plates,” *Applied Optics*, vol. 10, pp. 498–503, March 1971.
- [164] H. H. Barrett and F. Horrigan, “Fresnel zone plate imaging of gamma rays; theory,” *Applied Optics*, vol. 12, pp. 2686–2702, November 1973.
- [165] C. Pfeifer, L. Ferris, and W. Yen, “Optical image formation with a fresnel zone plate using vacuum-ultraviolet radiation.,” *Journal of the Optical Society of America*, vol. 63, pp. 91–95, January 1973.
- [166] J. Kirz, “Phase zone plates for X rays and the extreme UV.,” *Journal of the Optical Society of America*, vol. 64, pp. 301–309, March 1974.
- [167] G. Boivin, “Use of a fresnel zone plate for optical image formation with short wavelength radiations,” *Applied Optics*, vol. 16, pp. 1070–1073, April 1977.
- [168] A. N. Kurokhtin and A. V. Popov, “Simulation of high-resolution x-ray zone plates.,” *Journal of the Optical Society of America A*, vol. 19, pp. 315–24, February 2002.
- [169] Q. Cao and J. Jahns, “Modified fresnel zone plates that produce sharp gaussian focal spots,” *Journal of the Optical Society of America A*, vol. 20, pp. 1576–1581, August 2003.
- [170] F. Giménez, W. D. Furlan, A. Calatayud, and J. A. Monsoriu, “Multifractal zone plates,” *Journal of the Optical Society of America A*, vol. 27, pp. 1851–1855, August 2010.
- [171] Y. Ma, C. Ye, J. Ke, J. Zhang, J. Zhu, and Z. Ling, “Array illumination of a fresnel-dammann zone plate,” *Applied Optics*, vol. 55, pp. 7218–7221, September 2016.
- [172] A. Vijayakumar, B. Vinoth, I. V. Minin, J. Rosen, O. V. Minin, and C.-J. Cheng, “Experimental demonstration of square fresnel zone plate with chiral side lobes,” *Applied Optics*, vol. 56, pp. F128–F133, May 2017.
- [173] Y. Guo and S. Barton, *Fresnel Zone Antennas*. Springer US, 2013.
- [174] L. Leyten and M. Herben, “Vectorial far-field analysis of the fresnel-zone plate antenna: A comparison with the parabolic reflector antenna,” *Microwave and Optical Technology Letters*, vol. 5, pp. 49–56, February 1992.
- [175] J. Gutierrez-Rios and J. V. Sanz, “Simulated response of conic fresnel zone plate reflectors (CFZPS),” in *European Conference on Antennas and Propagation*, pp. 1–7, November 2006.

- [176] V. Manohar, J. M. Kovitz, and Y. Rahmat-Samii, "Synthesis and analysis of low profile, metal-only stepped parabolic reflector antenna," *IEEE Transactions on Antennas and Propagation*, vol. 66, pp. 2788–2798, June 2018.
- [177] J. Huang and J. Encinar, "Reflectarray antenna," ch. Development History, pp. 9–26, Wiley, 2007.
- [178] Y. H. Cho, W. J. Byun, and M. S. Song, "High gain metal-only reflectarray antenna composed of multiple rectangular grooves," *IEEE Transactions on Antennas and Propagation*, vol. 59, pp. 4559–4568, December 2011.
- [179] J. P. Gianvittorio and Y. Rahmat-Samii, "Reconfigurable patch antennas for steerable reflectarray applications," *IEEE Transactions on Antennas and Propagation*, vol. 54, pp. 1388–1392, May 2006.
- [180] W. An, S. Xu, and F. Yang, "A metal-only reflectarray antenna using slot-type elements," *IEEE Antennas and Wireless Propagation Letters*, vol. 13, pp. 1553–1556, 2014.
- [181] R. Deng, F. Yang, S. Xu, and M. Li, "A 100-ghz metal-only reflectarray for high-gain antenna applications," *IEEE Antennas and Wireless Propagation Letters*, vol. 15, pp. 178–181, 2016.
- [182] J. Gómez, A. Tayebi, J. de Lucas, and F. Catedra, "Metal-only fresnel zone plate antenna for millimetre-wave frequency bands," *IET Microwaves, Antennas & Propagation*, vol. 8, pp. 445–450, April 2014.
- [183] A. Tayebi, J. Gómez, I. González, and F. Catedra, "Influence of the feed location on the performance of a conformed fresnel zone reflector," *IEEE Antennas and Wireless Propagation Letters*, vol. 12, pp. 547–550, 2013.
- [184] Y. Rahmat-Samii, J. M. Kovitz, J. F. Budhu, and V. Manohar, "A novel near-field gregorian reflectarray antenna design with a compact deployment strategy for high performance cubesats," in *Proceedings of the Antenna Measurements and Techniques Association Meeting*, 2017.
- [185] L. G. Menéndez, O. S. Kim, F. Persson, M. Nielsen, and O. Breinbjerg, "3D printed 20/30-GHz dual-band offset stepped-reflector antenna," in *European Conference on Antennas and Propagation*, pp. 1–2, April 2015.
- [186] Y. Wang, W. Dou, and B. Bi, "W band axially displaced monopulse dual-reflector antenna for inter-satellite communications," *IET Microwaves, Antennas & Propagation*, vol. 10, pp. 742–747, May 2016.
- [187] V. Jamnejad-Dailami and Y. Rahmat-Samii, "Some important geometrical features of conic-section-generated offset reflector antennas," *IEEE Transactions on Antennas and Propagation*, vol. 28, pp. 952–957, November 1980.

- [188] G. León Fernández, L. F. Herrán Ontañón, M. Muñoz, F. L. Las Heras Andrés, and Y. Hao, “Millimeter-wave offset fresnel zone plate lenses characterization,” *Progress In Electromagnetics Research C*, 54, 2014.
- [189] D. Pozar, “Bandwidth of reflectarrays,” *Electronics Letters*, vol. 39, pp. 1490–1491, October 2003.
- [190] D. M. Pozar, *Microwave engineering; 3rd ed.* Hoboken, NJ: Wiley, 2005.
- [191] S. Silver, *Microwave Antenna Theory and Design*. [Massachusetts Institute of Technology. Radiation Laboratory Series. no. 12.], McGraw-Hill Book Company, 1949.
- [192] A. W. Doerry, “Just Where Exactly is the Radar? (a.k.a. The Radar Antenna Phase Center),” tech. rep., Sandia National Laboratory, December 2013.
- [193] H. C. Minnett and B. M. Thomas, “Fields in the image space of symmetrical focusing reflectors,” *Proceedings of the Institution of Electrical Engineers*, vol. 115, pp. 1419–1430, October 1968.
- [194] A. W. Rudge, “Focal-plane field distribution of parabolic reflectors,” *Electronics Letters*, vol. 5, pp. 510–512, October 1969.